Sheathed Cold-Formed Steel Wall Systems

by
Constantinos Kyprianou

May, 2021

A thesis submitted to Imperial College London
for the degree of Doctor of Philosophy

Steel Structures Group
&
Centre of Doctoral Training in Sustainable Civil Engineering

Department of Civil and Environmental Engineering
Imperial College London
London, UK

Statement of Originality

This thesis presents findings of my own research carried out in the Department of Civil & Environmental Engineering at Imperial College London. Any material from published or unpublished work from others is appropriately referenced. This thesis is submitted to Imperial College London for the degree of Doctor of Philosophy and has not been submitted for a degree or any other qualification at another university.

Constantinos Kyprianou

May 2021, London

Copyright Declaration

The copyright of this thesis rests with the author. Unless otherwise indicated, its contents are licensed under a Creative Commons Attribution-Non Commercial 4.0 International Licence (CC BY-NC).

Under this licence, you may copy and redistribute the material in any medium or format. You may also create and distribute modified versions of the work. This is on the condition that: you credit the author and do not use it, or any derivative works, for a commercial purpose.

When reusing or sharing this work, ensure you make the licence terms clear to others by naming the licence and linking to the licence text. Where a work has been adapted, you should indicate that the work has been changed and describe those changes.

Please seek permission from the copyright holder for uses of this work that are not included in this licence or permitted under UK Copyright Law.

Abstract

Cold-formed steel members are widely used in the construction industry due to their versatility, high strength-to-weight ratio and ease of assembly. Stud columns set in tracks, form the main members in cold-formed steel wall systems, which are typically sheathed with plasterboard or oriented strand board (OSB). The interaction between the cold-formed steel members and the sheathing, which can have a significant effect on the ultimate strength and flexural stiffness due to composite action and bracing, is currently not systematically taken into consideration in design.

More than 100 material and connection component tests have been performed to study the behaviour of plasterboard and OSB and their interconnection with cold-formed steel through screws acting in shear and tension. The obtained test results, along with a collected dataset totalling more than 400 physical tests, were used to develop analytical models to describe their load-deformation behaviour; these are suitable for use in numerical simulations and advanced design methods. A total of 17 full-scale sheathed wall stud tests were also performed, with varying connector spacing between either plasterboard or OSB sheathing panels and the steel members. Tests were performed under pure compression, pure bending and combined loading. Reducing the spacing of the connectors from 600 mm to 75 mm resulted in up to 30% increase in capacity while also preventing pull-through connector failure for specimens sheathed with plasterboard.

Sophisticated finite element models of wall studs were also developed, which, following successful validation against test results, allowed parametric studies to be undertaken, where the influence of the sheathing, connector spacing and section depth was investigated. Finally, a preliminary design guidance has been developed, where the beneficial effects of bracing, composite action and enhanced boundary conditions at the member ends are recognised, thus enabling more efficient design of sheathed cold-formed steel wall systems.

Acknowledgements

The research presented in this thesis was carried out under the supervision of Professor Leroy Gardner and Professor David Nethercot. I want to express my sincere gratitude to both of my supervisors. To Professor Leroy Gardner who has offered me the opportunity to work in his group, who has always been keen for a discussion, supportive all the way through and always pushing me for the best. To Professor David Nethercot for his continuous encouragement, for being supportive of my work in the meetings with the industrial sponsor, for showing genuine interest in my research and for his valuable advice from his wide breadth of knowledge.

This study was made possible through the co-funding from the Centre of Doctoral Training (CDT) in Sustainable Civil Engineering at Imperial College London and Ayrshire Metals Limited – the industrial partner. The funding from the CDT was received through the Engineering and Physical Sciences Research Council (EPSRC), under the award reference *1790029* for this project. In particular, from Ayrshire Metals Limited, I would like to thank Scott Reilly and Simon Collins for their support throughout the project.

The opportunity for starting my PhD was made possible by the continuous support from the team at the Steel Construction Institute (SCI) in Ascot, where I used to work prior my PhD studies. I would like to acknowledge the support I received, in the early days of my research, from Nancy Baddoo and David Brown, and in terms of technical advice, from Professor Mark Lawson and Andrew Way. I am also very grateful to Dr Graham Couchman who has showed trust in me and supported me in many ways and many times, for his continuous interest in my studies and comments on the thesis.

I want to also express my sincere thanks to Dr Pinelopi Kyvelou who has acted as an assistant to my supervisors and was always present in the meetings with our industrial sponsor. She has always been keen to help and advice. I consider her a friend and I would miss our lunchtime breaks at the university in the pre-Covid times, as well as our frequent video lunch breaks in the Covid times. Thank you Pinelopi for all of your support.

Special thanks are addressed to all of the technicians in the Structures Laboratory of the Department of Civil and Environmental Engineering at Imperial College London, but in particular to Les Clark for his significant help at the lab, for his ingenuity in coming up with practical solutions, which were often crucial in the success of the experimental studies.

I am grateful to the many colleagues and friends I made throughout my studies, where I was fortunate to share an office, or meet in the CDT, or in the Steel Structures Group over the years, including Adam Bekele, Dr Konstantinos Georgiadis, Dr Nicolas Hadjipantelis, Dr Merih Kucukler, Dr Craig Buchanan and Dr Xian Yun. Thank you all, for our talks, lunchtime breaks, tea brakes and coffee breaks, but overall, thank you for making my PhD studies memorable.

Finally, I am grateful to my mother who is responsible for who I became as a person, my father and brother for their love. This thesis could not have been completed without the continuous support, patience and love from Elli, thank you for bearing with me in this long journey.

Contents

Abstract **4**

Acknowledgements **5**

Contents **7**

List of Figures **15**

List of Tables **32**

Nomenclature **44**

Chapter 1. Introduction **45**

1.1 Background 45

1.2 Cold-formed steel 46

1.3 Stud columns 46

1.4 Sheathed wall stud systems 49

1.5 Motivation 50

1.6 Aim and objectives 50

1.7 Methodology 52

1.8 Thesis outline 55

1.9 Publications 57

Chapter 2. Literature review **58**

2.1 Introduction 58

2.2 Cold-formed steel members 58

2.2.1 Material behaviour 59
2.2.1.1 Stress-strain behaviour 59
2.2.1.2 Material models for cold-formed steel 60
2.2.1.3 Cold-forming effects and enhanced strength in corner regions 62
2.2.1.4 Residual stresses 63
2.2.2 Service hole openings in the web of the member 64
2.2.3 Buckling behaviour 66
2.2.3.1 Cross-sectional buckling 66
2.2.3.1.1 Local buckling 66
2.2.3.1.2 Distortional buckling 68
2.2.3.2 Global buckling 68
2.2.4 Geometric imperfections 69
2.2.4.1 Initial studies 70
2.2.4.2 Categorising imperfections and imperfection amplitudes . . . 70
2.2.4.3 Simulating imperfections 72
2.3 Sheathed wall stud systems 74
2.3.1 Sheathed studs under compression 75
2.3.2 Sheathed studs under combined compression and bending 77
2.3.3 Studies on components of wall stud systems 79
2.4 Existing design methods 81
2.4.1 Effective width method (EWM) 81
2.4.2 Direct strength method (DSM) 82
2.4.2.1 DSM calculation procedure 83
2.4.2.2 Beam-column interaction 84
2.4.3 Comparisons between the EWM and the DSM 86
2.4.4 Considering sheathing into the design of wall studs 87
2.5 Concluding remarks 89

Chapter 3. Experimental study on components of sheathed cold-formed steel wall systems 91

3.1 Introduction . . . 91
3.2 Material and component testing . . . 92
3.2.1 Cold-formed steel . . . 92
3.2.1.1 Testing tensile cold-formed steel coupons . . . 93
3.2.1.2 Results of tensile cold-formed steel coupons . . . 93
3.2.2 Plasterboard . . . 95
3.2.2.1 Tensile and compressive plasterboard tests . . . 96
3.2.2.2 Results of material tests on plasterboard . . . 98
3.2.3 Oriented strand board (OSB) . . . 103
3.2.3.1 Tensile and compressive tests on OSB material . . . 104
3.2.3.2 Results of OSB material tests . . . 105
3.2.4 Screw connectors . . . 109
3.2.4.1 Tensile and shear tests on screws . . . 110
3.2.4.2 Results of tensile and shear tests on screws . . . 111
3.3 Pull-through behaviour of sheathing-to-steel screws . . . 112
3.3.1 Pull-through tests . . . 113
3.3.2 Results of pull-through tests . . . 116
3.4 Shear behaviour of sheathing-to-steel screw connectors . . . 121
3.4.1 Push-out tests . . . 123
3.4.2 Results of push-out tests . . . 123
3.5 Assemblage of experimental database . . . 132
3.5.1 Data on material behaviour . . . 132
3.5.1.1 Plasterboard . . . 132
3.5.1.2 OSB . . . 134
3.5.2 Shear behaviour . . . 136
3.6 Conclusions . . . 139

Chapter 4. Analytical modelling of components of sheathed cold-formed steel wall systems 141

4.1 Introduction . . . 141

4.2 Review of key existing formulations . . . 142
4.2.1 Ramberg-Osgood model . . . 142
4.2.2 Mander model . . . 143
4.2.3 Discussion . . . 144
4.3 Material modelling . . . 145
4.3.1 Cold-formed steel . . . 145
4.3.2 Sheathing material . . . 147
4.3.2.1 Plasterboard . . . 147
4.3.2.2 Oriented Strand Board . . . 149
4.4 Modelling of interaction between components . . . 152
4.4.1 Pull-through load-deformation response . . . 152
4.4.1.1 Pull-through load-deformation model . . . 153
4.4.1.2 Calculation of key parameters for pull-through load-deformation model . . . 154
4.4.1.3 Assessment of proposed pull-through model against experimental data . . . 157
4.4.2 Shear load-slip response . . . 160
4.4.2.1 Shear load-slip model . . . 160
4.4.2.2 Calculation of key parameters for shear load-slip model . . . 162
4.4.2.2.1 Shear capacity predictions $F_{u,po}$ for screwed connections in plasterboard . . . 164
4.4.2.2.2 Shear capacity predictions $F_{u,po}$ for screwed connections in OSB . . . 167
4.4.2.2.3 K_o, $\delta_{u,po}$ and $F_{1,po}$ estimations . . . 169
4.4.2.3 Assessment of proposed shear model against experimental data 170
4.5 Summary of proposals . . . 174
4.6 Conclusions . . . 176

Chapter 5. Sheathed cold-formed steel beam-columns experiments 178

5.1 Introduction . . . 178

5.2 Material tests . . . 179
5.2.1 Cold-formed steel . . . 179
5.2.2 Sheathing material tests . . . 181
5.3 Member tests . . . 182
5.3.1 Geometric properties . . . 182
5.3.2 Stub column tests . . . 183
5.3.3 Imperfections . . . 184
5.3.4 Screws types and arrangements . . . 189
5.3.5 Test rig . . . 190
5.3.6 Boundary and loading conditions . . . 193
5.4 Experimental results . . . 195
5.4.1 Pure compression test results . . . 197
5.4.1.1 Boundary conditions under pure compression . . . 198
5.4.1.2 Load-displacement curves under pure compression . . . 199
5.4.2 Compression and bending test results . . . 204
5.4.2.1 Load-displacement curves . . . 205
5.4.2.2 Load-rotation curves . . . 208
5.4.2.3 Strain distributions . . . 210
5.5 Comparison with existing findings and code provisions . . . 211
5.5.1 Comparison with previous experimental findings in the literature . . . 211
5.5.2 Comparison with Eurocode 3 design provisions . . . 212
5.6 Conclusions . . . 215

Chapter 6. Finite element study on sheathed cold-formed steel beam-columns 217

6.1 Introduction . . . 217
6.2 Beam-column wall system . . . 218
6.3 Finite element modelling . . . 219
6.3.1 Element type . . . 220
6.3.2 Meshing scheme . . . 223

6.3.3 Material modelling . . . 225
6.3.3.1 Cold-formed steel . . . 225
6.3.3.2 Plasterboard . . . 227
6.3.3.3 OSB . . . 229
6.3.4 Modelling of screwed connections . . . 230
6.3.4.1 Sheathing-to-steel connection . . . 230
6.3.4.2 Steel-to-steel connection . . . 232
6.3.5 Geometrical imperfections . . . 233
6.3.6 Boundary and loading conditions . . . 235
6.3.7 Contact interaction and solution scheme . . . 239
6.4 Validation . . . 242
6.4.1 Bare cold-formed steel columns with ideal boundaries . . . 243
6.4.2 Bare and sheathed cold-formed steel columns set in tracks . . . 244
6.4.3 Sheathed cold-formed steel beam-columns with a horizontal load at mid-height . . . 246
6.4.4 Sheathed cold-formed steel beam-columns loaded with four horizontal point loads . . . 250
6.5 Parametric study . . . 262
6.5.1 Effect of sheathing . . . 262
6.5.2 Effect of connector spacing and section depth . . . 264
6.5.2.1 Pure compression results . . . 265
6.5.2.2 Pure bending results . . . 268
6.5.2.3 Combined loading results . . . 271
6.5.3 Commentary on the effect of the track . . . 275
6.6 Conclusions . . . 277

Chapter 7. Preliminary design recommendations for sheathed cold-formed steel beam-columns 279

7.1 Introduction . . . 279
7.2 Existing design methods . . . 280

7.2.1 Design of cold-formed steel sections to Eurocode 3 280
7.2.1.1 Effective section properties 281
7.2.1.1.1 Local buckling 282
7.2.1.1.2 Distortional buckling 283
7.2.1.2 Design resistances 289
7.2.1.2.1 Compression resistance 289
7.2.1.2.2 Bending resistance 292
7.2.1.2.3 Shear buckling resistance 295
7.2.1.2.4 Combined compression and bending 295
7.2.1.3 Comparison with the beam-column test results of the present study 296
7.2.2 Design of sheathed studs with DSM and recommendations from the literature 299
7.2.2.1 Comparison with the beam-column test results of the present study 301
7.3 Design recommendations 306
7.3.1 Restraint in minor axis 306
7.3.2 End fixity in compression 310
7.3.3 Composite action 314
7.3.3.1 Degree of shear connection 315
7.3.3.2 Moment capacity 318
7.3.3.3 Interaction between bending and shear 322
7.3.3.4 Final bending capacity 322
7.3.4 Interaction curve profile 325
7.3.5 Connector limits 327
7.3.5.1 Sheathing-to-column 328
7.3.5.1.1 Required demands for axial stability bracing 328
7.3.5.1.2 Required demands to resist torsion 331
7.3.5.2 Column-to-track 332
7.3.6 Deflection checks 333

7.4 Concluding remarks 333

Chapter 8. Conclusions and future research **336**

8.1 Summary and conclusions 336

8.2 Potential impact 341

8.3 Future research 341

8.3.1 Directly related to the present study 341

8.3.2 Further areas of research 342

References **344**

Appendix A. **363**

List of Figures

1.1 Typical C-section shapes used for walls 47

1.2 Load bearing cold-formed steel frame for a modular unit (Davison & Owens 2012) 48

1.3 Typical sections used as floor joists and roof purlins 48

1.4 One-sided sheathed wall frame in a test rig (Grubb et al. 2003) 49

1.5 Order of executions for the finite element analyses 54

2.1 Stress-strain curve for structural steel with sharp yielding 59

2.2 Stress-strain curve for structural steel with gradual yielding 60

2.3 A typical lipped channel section with a service hole in the web 65

2.4 Longitudinal distribution of: (a,b) cross-sectional and (c-e) global buckling modes 67

2.5 Local and distortional buckling 67

2.6 Local (δ_L) and distortional (δ_D) imperfections with flanges buckling inwards . 71

2.7 Local (δ_L) and distortional (δ_D) imperfections with flanges buckling outwards 71

2.8 Signature curve and deformed shapes using CUFSM (Li & Schafer 2010) . . 74

2.9 Illustrations of (a) stud wall with lateral bracing (b) stud wall with sheathing (c) single sheathed column 75

2.10 Observed axial and horizontal failure loads of the same size stud of length 2.4 m, set in track, with various sheathing configurations on the two stud flanges (B=bare, O=OSB, G=gypsum). From Peterman & Schafer (2014). 78

2.11 The effective width concept applied to a plate. Adapted from Trahair et al. (2008) 82

2.12 Comparison between the current DSM linear interaction equations (with light grey) and the difference with the proposed beam-column interaction DSM for a single symmetric channel lipped section which is indicated with dark grey; from Torabian & Schafer (2018) 85
2.13 Local stiffness approach by Green et al. (1947), Winter (1952, 1960). Adapted from Vieira & Schafer (2013). 88
2.14 Illustrating the use of springs in elastic buckling analysis (CUFSM Li & Schafer (2010)) for determining enhanced capacities. From Vieira (2011). 90

3.1 Nominal dimensions of steel tensile coupons (in mm) 93
3.2 Test setup for cold-formed steel tensile coupons 94
3.3 Stress-strain curves of tensile coupons of (a) 1.2 mm and (b) 2.0 mm thickness 95
3.4 Dimensions of (a) tensile and (b) compressive plasterboard coupons 97
3.5 Test setup for (a) tensile and (b) compressive material tests on plasterboard . 97
3.6 Typical plasterboard tensile coupon (a) before and (b) after test 98
3.7 Stress-strain curves obtained from plasterboard tensile coupon tests in (a) the longitudinal and (b) the transverse directions 99
3.8 Failure modes observed in compressive coupon tests on plasterboard in (a) the longitudinal and (b) the transverse directions 101
3.9 Stress-strain curves obtained from compressive coupon tests on plasterboard in (a) the longitudinal and (b) the transverse directions 102
3.10 Notation defining key points on material stress-strain curves 103
3.11 Test setup for OSB coupons in (a) tension and (b) compression 104
3.12 Stress-strain curves obtained from OSB tensile coupon tests in (a) the longitudinal and (b) the transverse directions 105
3.13 Typical OSB tensile coupon (a) before and (b) after test. 106
3.14 Stress-strain curves obtained from OSB compressive coupon tests in (a) the longitudinal and (b) the transverse directions 107

3.15 Failure modes observed in the OSB compression tests in (a) the longitudinal and (b) the transverse directions 108
3.16 Types of screws considered (a) 3.5 mm (b) 4.8 mm and (c) 5.5 mm in diameter and (d) notations of the dimensions 110
3.17 Jig for tensile testing of screw connectors 110
3.18 Test setup for double-shear tests on screw connectors, applying force F at each shear plane 111
3.19 Schematic illustration of pull-through test arrangement 113
3.20 Pull-through test setup: (a) overall arrangement, (b) employed instrumentation and (c) bottom view 114
3.21 Load-displacement curves from pull-through tests (a) from two LVDTs (one on screw and one on adjacent board) and (b) showing the net embedment δ_{pt} and key properties, where $F_{u,pt}$ is the ultimate pull-through resistance, $\delta_{u,pt}$ is the corresponding displacement and $K_{o,40}$ is the secant stiffness at $0.4F_{u,pt}$ 115
3.22 Failure of plasterboard pull-through specimens: (a) top view, embedded screw (b) bottom view of board failing (c) rupture of the underside of plasterboard forming a conical surface 116
3.23 Single board pull-through load-displacement curves for (a) PT-35-1P, (b) PT-55-1P and (c) PT-48-1O on a horizontal scale up to 2 mm (a1, b1, c1) and up to 0.5 mm (a2, b2, c2) 117
3.24 Two layer board pull-through load-displacement curves for (a) PT-35-2P and (b) PT-55-2P on a horizontal scale up to 8 mm (a1, b1), up to 2 mm (a2, b2) and up to 0.5 mm (a3, b3) 118
3.25 Standard tests for measuring the shear behaviour of a connector between two elements: (a) pull-test in EN 520 (2009) and (b) push-test in EN 1994-1-1 (2004) 122
3.26 Schematic views of push-out test arrangement in elevation and from above. All dimensions are given in mm. 124
3.27 Experimental arrangement for push-out tests 125
3.28 (a) Overview and (b) top view of push-out test specimens 125

3.29 Illustration of key aspects of failure modes (a) pull-through of screw for double board specimens, (b) bearing and tilting of screw for single board specimens and (c) typical failure surface on the back of the plasterboard 126
3.30 Single layer plasterboard push-out load-slip responses, averaged per screw, for (a) PO-35-1P-12, (b) PO-35-1P-20 and (c) PO-55-1P-12 over a horizontal scale up to 16 mm (a1, b1, c1) and up to 2.0 mm (a2, b2, c3) 127
3.31 Double layer plasterboard push-out load-slip responses, averaged per screw, for (a) PO-35-2P-12, (b) PO-35-2P-20 and (c) PO-55-2P-20 over a horizontal scale up to 16 mm (a1, b1, c1) and up to 2.0 mm (a2, b2, c3) 128
3.32 Typical load-slip curve per connector in shear and calculation detail for the initial stiffness K_o 129
3.33 Illustrations of the observed failure modes for (a) PO-35-1P-12, (b) PO-35-2P-12, (c) PO-35-1P-20, (d) PO-35-2P-20, (e) PO-55-1P-12 and (f) PO-55-2P-20 specimens 130

4.1 Generalised form of single stage Ramberg-Osgood model 143
4.2 Mander et al. (1988) model 144
4.3 Stress-strain curves predicted using (a) Equations (4.1) and (4.2) for the 1.2 mm thick coupons and (b) Equations (4.1) and (4.6) the 2.0 mm thick coupons 146
4.4 Comparison of the proposed model for plasterboard with normalised test curves for specimens of 12.5-15.0 mm thickness in (a-b) tension and (c-d) compression 149
4.5 The Ramberg-Osgood (R-O) and Mander models using the average measured material properties of plasterboard, with positive values of stress and strain signifying tension (where only the R-O model is used) and negative values signifying compression (where both models are shown) 150
4.6 Comparison of the proposed model for OSB with the obtained normalised test curves in both directions in (a-b) tension and (c-d) compression 151

4.7 The Ramberg-Osgood (R-O) and Mander models using the average measured material properties of OSB, with positive values of stress and strain signifying tension (where only the R-O model is used) and negative values signifying compression (where both models are shown) 152
4.8 Pull-through load-deformation model 153
4.9 Screw connector geometry and bearing pull-through areas 155
4.10 Comparison between experimental and calculated values of $F_{u,pt}$ 156
4.11 Comparisons of the proposed model using test and recommended predicted input parameters with test curves for single board specimens 158
4.12 Comparisons of the proposed model using test and recommended predicted input parameters with test curves for double-board specimens 159
4.13 Pull-through load-deformation curves from proposed model for different test groups 159
4.14 Proposed combined Ramberg-Osgood (R-O) model consisting of 2 single R-O curves for describing the shear load-slip behaviour of screw connections between cold-formed steel and sheathing 161
4.15 Failure modes for steel-to-timber connections in accordance with EN 1995-1-1 (2004): (a) tilting, (b) bending in board, (c) bearing, (d) bending at steel plate and (e) double bending 163
4.16 Comparisons between test and predicted $F_{u,po}$ values for all screwed connections in plasterboard, calculated using EN 1995-1-1 (2004), with Equation (4.21) for embedment strength and interpolation between critical values from Equations (4.18) and (4.20) for cases when $0.5 < t/d \leq 1.0$ 165
4.17 Comparisons between test and predicted $F_{u,po}$ values calculated using Equation (4.18) Mode a (screw tilting) with embedment strength (a) $f_{h,k,gen}$ (Equation (4.21)) and (b) $f_{h,k,gyp}$ (Equation (4.23)) for all screwed connections in plasterboard with the thin plate limit extended to $t/d \leq 0.75$ 166

4.18 Comparisons between test and predicted $F_{u,po}$ values for all screwed connections in OSB, calculated using EN 1995-1-1 (2004), with Equation (4.22) for embedment strength and interpolation between the critical values from Equations (4.18) and (4.20) for cases when $0.5 < t/d \leq 1.0$ 168
4.19 Comparisons between test and predicted $F_{u,po}$ values for all screwed connections in OSB, calculated using Equation (4.24) for cases $t/d \leq 0.5$ and interpolation between Equation (4.24) and the critical value from Equation (4.20) for cases when $0.5 < t/d \leq 1.0$ 168
4.20 Comparison between the proposed load-slip model and normalised test curves for specimens with one layer of plasterboard for (a) all collected tests, (b) tests with $d = 3.5$ or 5.5 mm and (c) tests with $d = 4.2 - 4.8$ mm 171
4.21 Comparison between the proposed load-slip model and normalised test curves for specimens with two layers of plasterboard 171
4.22 Comparison between the proposed load-slip model and normalised test curves for specimens with OSB 172
4.23 Model fitting of the average key properties presented in Table 4.11 and comparisons between the load-slip behaviour of a screw connector per shear plane when connected to (a) plasterboard and (b) OSB 174

5.1 Stud column test specimen showing arrangement of service openings 179
5.2 Stress-strain curves of tensile coupons extracted from (a) stud and (b) track . 181
5.3 Notation for cross-sectional geometry of stud 183
5.4 Stub column test results: (a) load-displacement curves and (b) failure modes 184
5.5 Illustrations of amplitudes of imperfection shapes for (a) local, (b) distortional, (c) flexural about the minor axis, (d) flexural about the major axis and (e) torsional modes 185
5.6 Positions of LVDTs mounted on the imperfection rig 186
5.7 Imperfection rig (a) elevation view (b) schematic and (c) detail of the rails and the LVDTs around the cross-section 186
5.8 Cross-sectional imperfections along column length 188

5.9 Global imperfections along the column length, with dashed lines marking the half-sine curves of best fit . . . 188
5.10 Types of connector used: (a) 3.5 mm diameter screw for plasterboard to steel (b) 4.8 mm diameter screw for OSB-to-steel (c) 4.8 mm diameter screw for steel-to-steel and (d) 6 mm diameter anchor bolt . . . 189
5.11 Connector arrangements for spacings of (a) 75 mm, (b) 150 mm, (c) 300 mm and (d) 600mm (dimensions in mm) . . . 190
5.12 Illustration of rig for beam-column tests . . . 191
5.13 (a) Photo and (b) schematic illustration of test rig with employed instrumentation . . . 192
5.14 (a) Top and (b) bottom tracks connected to the test rig . . . 194
5.15 Column-to-track connection . . . 194
5.16 Bending moment diagrams under 4-point loads and the equivalent uniformly distributed load for (a) pinned and (b) fixed boundary conditions . . . 195
5.17 Ultimate load plotted against connector spacing for specimens under pure compression . . . 197
5.18 Typical failure modes: (a) distortional buckling (and pull-through failure of connectors) for a member under compression and (b) local buckling at a service hole for a member under bending . . . 198
5.19 (a) Typical end failure mode for specimens under pure compression and (b) schematic illustration of end fixity arising due to the restoring moment from axial force. Note that the overall end rotation illustrated in (b) is prevented in the real system, as seen in (a), due to the action of the restoring moment. 199
5.20 Axial load-displacement curves of a typical specimen under pure compression 200
5.21 Adjustment of gradient for the results of axial load-displacement curves . . . 201
5.22 Axial load-displacement curves of specimens sheathed with OSB under compression . . . 201
5.23 Axial load-displacement curves of specimens sheathed with plasterboard under compression . . . 202

5.24 Comparison between the axial load-displacement curves of specimens sheathed with plasterboard and OSB under compression 202
5.25 (a) Failure modes of columns sheathed with plasterboard and tested under compression (from left to right – connectors spaced at 600 mm, 300 mm (2 repeated), 150 mm and 75 mm), (b) test specimen with 600 mm connector spacings, post failure (with the sheathing removed to observe the failure mode) 203
5.26 Ultimate compression (P_u) and horizontal (H_u) loads for beam-column specimens sheathed with OSB and connected at 600 mm and 75 mm intervals . . 204
5.27 Failure modes of all the tests specimens (from left to right – 100% compression to 100% bending) with OSB sheathing connected at (a) 600 mm spacings and (b) 75 mm spacings 205
5.28 Horizontal load versus mid-height displacement curves for beam-column specimens connected at 75 mm intervals 207
5.29 Horizontal load versus mid-height displacement curves for beam-column specimens connected at 600 mm intervals 207
5.30 Horizontal load versus mid-height displacement curves for all specimens over (a) full range and (b) initial stages of loading for comparison with the theoretical stiffness for fixed and pinned boundary conditions 208
5.31 Relative degree of fixity β with increase in compression level for beam-columns based on slope of horizontal load-mid-span deflection curves 208
5.32 Horizontal load versus rotation at $L/10$ curves for beam-column specimens connected at 75 mm spacings 209
5.33 Horizontal load versus rotation at $L/10$ curves for beam-column specimens connected at 600 mm spacings 210
5.34 Relative degree of fixity β_θ with increase in compression level for beam-columns based on the slope of horizontal load versus rotation at $L/10$ 210
5.35 Strain gauge results from beam-column tests showing (a) development of strain for specimen O-75-S600 and (b) position of strain gauges at mid-height of member 211

5.36 Comparisons between compression test results and EN 1993-1-3 (2006) resistance predictions with different assumptions made for $L_{cr,z}$ equal to (a) the full column length of 2400 mm (b) the connector spacing and (c) two times the connector spacing. $L_{cr,y}$ was taken as the full member length in all cases. 213
5.37 Comparison between tests results and EN 1993-1-3 (2006) resistance predictions assuming various effective lengths 215

6.1 Illustrations of (a) stud wall with sheathing (b) single sheathed stud column under compression and bending about the major axis (c) finite element model 219
6.2 Four-noded shell elements with (a) a reduced single integration point scheme and (b) a full 2×2 integration point scheme. Adapted from ABAQUS (2016). 220
6.3 Eight-noded brick (hexahedral) elements with (a) a reduced single integration point scheme and (b) a full $2 \times 2 \times 2$ integration point scheme. Adapted from ABAQUS (2016). 221
6.4 (a) Spring element notation and (b) nonlinear spring force-displacement relationship (ABAQUS 2016). Adapted from Ellobody (2014). 222
6.5 Stud column cross-sectional discretisation and node numbers for various section depths 223
6.6 Cross-sectional notation of stud column and finite-element discretisation of sheathing 224
6.7 Adopted finite element mesh of the column with detail of the service hole mesh224
6.8 Stress-strain curves for use in FE modelling: (a) stud and (b) track 227
6.9 Uniaxial stress-strain behaviour of plasterboard adopted in finite element material model, with positive values signifying tension 228
6.10 Stress-strain behaviour of OSB adopted in finite element material model . . . 230
6.11 Simulation of screwed connection between sheathing and cold-formed steel using three 2-noded nonlinear springs in opposite directions 231
6.12 Adopted load-slip response for springs in the FE model for simulating sheathing-to-steel (a) shear and (b) pull-through screwed connection behaviour232

6.13 Adopted load-slip response for springs in the FE model for simulating steel-to-steel shear screwed connection behaviour 233
6.14 Shape of amplitude distribution along the length of the specimens for the different imperfection modes 234
6.15 Longitudinal distribution of: (a,b) cross-sectional and (c-e) global imperfections 234
6.16 Mode shape and amplitude notation of: (a,b) cross-sectional and (c-e) global imperfections 235
6.17 Idealised boundary implementation using MPCs 236
6.18 Column-to-track connection: (a) drawing and (b) FE model 237
6.19 Column-to-top-track detail and axial loading 238
6.20 FE model of the four-point loading scheme 239
6.21 Typical end deformation from FE model of column and track under compression; indicative load-displacement path for the top track springs when in compression 240
6.22 Typical FE model end deformation of column and track under combined loading at the (a) start of analysis (b) end of compression – Step 1 and (c) end of bending – Step 2 241
6.23 Typical comparison between the results from the developed FE model and the tests by Young (1997); example shown is L48F1500 244
6.24 Comparison between the ultimate compression P_u and horizontal H_u loads from the developed FE model and the tests by Peterman (2012) for beam-columns sheathed with OSB and connected at 300 mm intervals 248
6.25 Typical comparison between the results from the developed FE model and the tests by Peterman (2012); the example shown is OO-10-S300 249
6.26 Comparison between the ultimate compressive P_u and horizontal H_u loads determined from the developed FE and the tests from the present study for beam-column specimens (sheathed with OSB and connected at 600 mm and 75 mm intervals) 252

6.27 Comparison between the FE and test axial load-displacement curves for plasterboard sheathed specimens, connected with screws at a spacing of (a) 600 mm (b) 300 mm (c) 150 mm and (d) 75 mm, and for OSB sheathed specimens connected with screws at a spacing of (e) 600 mm and (f) 75 mm 253
6.28 Comparison between the FE and test horizontal load-displacement curves for OSB sheathed specimens, connected with screws at a spacing of (a) 600 mm and (b) 75 mm after being axially loaded at 75% of their compressive capacity 254
6.29 Comparison between the FE and test horizontal load-displacement curves for OSB sheathed specimens, connected with screws at a spacing of (a) 600 mm and (b) 75 mm after being axially loaded at 50% of their compressive capacity 254
6.30 Comparison between the FE and test horizontal load-displacement curves for OSB sheathed specimens, connected with screws at a spacing of (a) 600 mm and (b) 75 mm after being axially loaded at 25% of their compressive capacity 255
6.31 Comparison between the FE and test horizontal load-displacement curves for OSB sheathed specimens, connected with screws at a spacing of (a) 600 mm and (b) 75 mm subjected to pure bending 255
6.32 Comparison between the FE (left images) and test (right images) failure modes of specimens under pure compression sheathed with plasterboard screw connected at every (a) 600 mm, (b) 300 (mm), (c) 150 mm and (d) 75 mm (yielding in FE models is marked by grey) 256
6.33 Comparison between the FE and test failure modes of specimens screw connected at every 600 mm with OSB under (a) pure compression, (b) 75%, (c) 50%, (d) 25% and (e) 0% in compression followed by bending until failure (yielding in FE models is marked by grey) 257
6.34 Comparison between the FE and test failure modes of specimens screw connected at every 75 mm with OSB under (a) pure compression, (b) 75%, (c) 50%, (d) 25% and (e) 0% in compression followed by bending until failure (yielding in FE models is marked by grey) 258

6.35 Illustration of pull-through connector failure of the screw at mid-height of specimen G-100-S600, where A to C stages are indicated on (a) an axial load-displacement FE curve of the column, (b) a combined graph of two curves consisting of the pull-through screw load and the axial load of the column, both plotted against the pull-though displacement of the screw and (c) an FE model of the relevant screw at failure 260

6.36 Illustration of shear connector failure of the screw at mid-height of specimen O-0-S75, where A to C stages are indicated on (a) a horizontal load-displacement FE curve of the column, (b) a combined graph of two curves consisting of the shear screw load and the horizontal load of the column, both plotted against the shear slip of the screw and (c) an FE model of the relevant screw at failure 261

6.37 Comparisons of FE load-axial shortening curves for bare steel stud and plasterboard sheathed systems 263

6.38 Comparisons of FE load-axial shortening curves for bare steel stud and OSB sheathed systems 264

6.39 FE parametric axial load-displacements curves: (a) full spectrum and (b) initial detail 266

6.40 Influence of connector spacing on ultimate compression capacity: (a) absolute values and (b) normalised by the compression capacity of the equivalent system with 300 mm spacing 267

6.41 Influence of connector spacing on measured initial axial stiffness: (a) absolute values and (b) normalised by the stiffness of the equivalent system with 300 mm spacing 267

6.42 FE parametric results of horizontal load vs mid-height at mid-depth deflections: (a) full spectrum and (b) initial detail 268

6.43 Influence of connector spacing on ultimate bending capacity in terms of horizontal loads H_u: (a) absolute values and (b) normalised by the loads of the equivalent system with 300 mm spacing 269

6.44 Influence of connector spacing on flexural stiffness for the examined systems under pure bending: (a) absolute values and (b) normalised by the stiffness of the equivalent system with 300 mm spacing 269
6.45 Case study results of specimen 15015-S300 under pure bending modelled with (i) perfectly elastic and (ii) actual nonlinear material behaviour 270
6.46 Influence of connector spacing on bending capacity for specimens initially compressed at 50% of their compression capacity, in terms of horizontal loads H_u: (a) absolute values and (b) normalised by the loads of equivalent systems with 300 mm spacing 271
6.47 Summary of interaction curves of the FE parametric results in terms of (a) P_u vs H_u and (b) normalised capacities with effective cross-sectional properties determined using EN 1993-1-3 EN 1993-1-3 (2006) 273
6.48 Interaction curves of FE parametric results in terms of (1) P_u vs H_u and (2) normalised capacities with effective cross-sectional properties determined using EN 1993-1-3 EN 1993-1-3 (2006) for specimens with section depths of: (a) 70 mm, (b) 100 mm, (c) 150 mm, (d) 200 mm and (e) 250 mm 275
6.49 Failure modes for specimens in pure bending with 75 mm screw spacing and a section depth of (a) 68 mm, (b) 100 mm, (c) 150 mm (d) 201 mm and (e) 252 mm 276

7.1 Mid-line theory for a C-lipped section where (a) is the actual section, (b) is the idealised section and (c) is a detail of the rounded corner. Adapted from EN 1993-1-3 (2006) 281
7.2 The (a) local and (b) distortional buckling modes of a C-lipped section under compression and (c) the theoretical effective cross-section 284
7.3 The (a) local and (b) distortional buckling modes of a C-lipped section under bending about major axis and (c) the theoretical effective cross-section 284
7.4 Equivalent linear spring model assumed by EN 1993-1-3 (2006) to replicate the distortional mode at (a) an edge lip, (b) an edge double lip and (c) an intermediate stiffener 285

7.5 Equivalent dimensions for a flange with a single edge stiffener in compression. Adapted from EN 1993-1-3 (2006). 285
7.6 Effective properties of an edge stiffener, Step 1. Adapted from EN 1993-1-3 (2006). 287
7.7 Effective properties of an edge stiffener, Step 2. Adapted from EN 1993-1-3 (2006). 288
7.8 Effective properties of an edge stiffener, Step 3. Adapted from EN 1993-1-3 (2006). 288
7.9 Buckling curves a, b and c. Adapted from EN 1993-1-3 (2006). 290
7.10 Comparison between the beam-column test results from Chapter 5 and EN 1993-1-3 (2006) predictions assuming various effective lengths in a normalised format, in terms of $P_u/N_{c,Rd}$ vs $H_u/H_{c,y,Rd}$ 298
7.11 Comparison between the beam-column test results from Chapter 5 and EN 1993-1-3 (2006) predictions assuming various effective lengths in a normalised format, in terms of $P_u/N_{c,Rd}$ vs $M_u/M_{c,y,Rd}$ 298
7.12 Spring on cross-section to simulated the effect of sheathing for use in elastic buckling analysis 301
7.13 Signature curve and deformed shapes for the specimen with geometries and properties tested in Chapter 5 using CUFSM; illustrating critical compression loads versus length for different stiffnesses in accordance with the properties given in Table 7.1 303
7.14 Signature curve and deformed shapes for the specimen with geometries and properties tested in Chapter 5 using CUFSM; illustrating critical moments versus length for different stiffnesses in accordance with the properties given in Table 7.1 303
7.15 Comparisons between linear interaction curves predicted with DSM and Table 7.1 spring stiffnesses in elastic buckling analysis with the beam-column test results from Chapter 5 in terms of axial loads P_u vs horizontal loads H_u . . . 304

7.16 Comparisons between linear interaction curves predicted with DSM and Table 7.1 spring stiffnesses in elastic buckling analysis with the beam-column test results from Chapter 5 in a normalised format, in terms of $P_u/N_{c,Rd}$ vs $H_u/H_{c,y,Rd}$ 304

7.17 Comparisons between linear interaction curves predicted with DSM and Table 7.1 spring stiffnesses in elastic buckling analysis with the beam-column test results from Chapter 5 in a normalised format, in terms of $P_u/M_{c,Rd}$ vs $M_u/M_{c,y,Rd}$ 305

7.18 Column with intermediate elastic restraints. Adapted from Gardner (2011). . 306

7.19 Comparisons between normalised compression test results with EN 1993-1-3 (2006) resistance prediction limits assuming $L_T = L_{cr,z}$ and $L_{cr,z}$ is equal to (a) the connector spacing s and (b) two times the connector spacing s. $L_{cr,y}$ was taken as the full member length for both cases. 308

7.20 Comparisons between normalised compression test and FE results with EN 1993-1-3 (2006) flexural-torsional buckling curve assuming $L_T = L_{cr,z}$ and $L_{cr,z}$ is equal to (a) the connector spacing s and (b) two times the connector spacing s. $L_{cr,y}$ was taken as the full member length L for both cases. 308

7.21 Comparisons between normalised bending test and FE results with EN 1993-1-3 (2006) lateral-torsional buckling curve assuming L_{LT} is equal to (a) the connector spacing s and (b) two times the connector spacing s 309

7.22 Effective lengths L_{cr} of columns with various end boundary conditions. From Trahair et al. (2008). 310

7.23 Comparisons between normalised compression test results with EN 1993-1-3 (2006) resistance prediction limits assuming $L_T = L_{cr,z}$ and $L_{cr,z}$ is equal to (a) the connector spacing s and (b) two times the connector spacing s. $L_{cr,y}$ was taken as the half the member length for both cases. 311

7.24 Comparisons between normalised compression test and FE results with EN 1993-1-3 (2006) flexural-torsional buckling curves assuming $L_T = L_{cr,z}$ and $L_{cr,z}$ is equal to (a) the connector spacing s and (b) two times the connector spacing s. $L_{cr,y}$ was taken as the half member length $0.5L$ for both cases. . . 311

7.25 Comparisons between normalised compression test results with EN 1993-1-3 (2006) flexural-torsional buckling curve assuming $L_T = L_{cr,z}$ and $L_{cr,z}$ is equal to two times the connector spacing s. $L_{cr,y}$ was taken as $0.7L$. 312
7.26 Comparison between the beam-column test results from Chapter 5 and EN 1993-1-3 (2006) predictions assuming fixity in compression and effective lengths about the minor axis equal to connector spacing in a normalised format, in terms of $P_u/N_{c,Rd}$ vs $H_u/H_{c,y,Rd}$ 313
7.27 Comparison between the beam-column test results from Chapter 5 and EN 1993-1-3 (2006) predictions assuming fixity in compression and effective lengths about the minor axis equal to connector spacing in aa normalised format, in terms of $P_u/N_{c,Rd}$ vs $M_u/M_{c,y,Rd}$ 313
7.28 Relationship between moment resistance and degree of shear connection η in composite systems under bending in accordance with EN 1994-1-1 (2004) . . 318
7.29 Plastic stress distributions for full shear connection (Point C) and partial shear connection (Point B) 319
7.30 Variation of moment capacity of composite systems against degree of shear connection η according to the proposed method by Kyvelou et al. (2017*a*). Adapted from Kyvelou et al. (2017*a*). 321
7.31 Illustrating increase in bending for FE and test data with fixings spaced at 300 mm 323
7.32 Illustrating increase in bending for FE and test data with fixings spaced at 150 mm 324
7.33 Illustrating increase in bending for FE and test data with fixings spaced at 75 mm 324
7.34 Interaction curve fitted to the FE and test data with fixings spaced at 300 mm326
7.35 Interaction curve fitted to the FE and test data with fixings spaced at 150 mm327
7.36 Interaction curve fitted to the FE and test data with fixings spaced at 75 mm 327
7.37 Assumed final location of horizontal load for twisting. From Peterman & Schafer (2014) 331

8.1 Screw connectors with a large flat head 342

List of Tables

2.1 Imperfection amplitudes provided by Zeinoddini & Schafer (2012) 72

3.1 Material properties obtained from tensile coupon tests on cold-formed steel . 94

3.2 Average material properties obtained from tensile coupon tests on cold-formed steel 95

3.3 Key tensile material properties from plasterboard coupon tests 100

3.4 Key compressive material properties from plasterboard coupon tests 103

3.5 Key measured tensile material properties from OSB tests 106

3.6 Key measured compressive material properties from OSB tests 109

3.7 Average measured dimensions of screw connectors 110

3.8 Results of tensile tests on screws 111

3.9 Results of shear tests on screws 112

3.10 Details of pull-through test specimens 113

3.11 Experimental results from pull-through tests with single boards 119

3.12 Experimental results from pull-through tests with two layers of board 120

3.13 Average measured results from pull-through tests 121

3.14 Combinations of parameters investigated in push-out tests 122

3.15 Measured results from push-out tests on single board specimens 130

3.16 Measured results from push-out tests on double board specimens 131

3.17 Average measured results from push-out tests 131

3.18 Summary of key average material properties from the present study and the literature on standard plasterboard 133

3.19 Summary of key average material properties from the present study and the literature on OSB . . . 135
3.20 Summary of key average results from shear behaviour tests from the present study and the literature . . . 138

4.1 Averaged material properties of cold-formed steel reported in Chapter 3 for use in models . . . 146
4.2 Averaged measured material properties of plasterboard . . . 148
4.3 Averaged measured material properties of OSB . . . 151
4.4 Pull-through screw properties and comparison between calculated and test capacity $F_{u,pt}$ . . . 155
4.5 Average measured properties for tested screws expressed in terms of screw diameter d, overall board thickness t_b and $F_{u,pt}$; recommended representative values for the key model parameters are also provided. . . . 156
4.6 Average measured values of model parameters, as determined from pull-through tests . . . 157
4.7 Comparisons between predictions of $F_{u,po}$ for shear tests with plasterboard using Equation (4.18) for Mode a (tilting) with embedment strength calculated using Equations (4.21) and (4.23) . . . 167
4.8 Comparisons between test and predicted $F_{u,po}$ values for groups of screwed connections in OSB with similar characteristics, calculated using Equation (4.24) for cases $t/d \leq 0.5$ and interpolation between Equation (4.24) and the critical value of Equation (4.20) for cases when $0.5 < t/d \leq 1.0$ . . . 169
4.9 Average measured values for key properties derived from full load-slip $F_{po}-\delta_{po}$ curves obtained from shear tests, grouped by common arrangement properties 169
4.10 Average values of the parameters required as input for the proposed models (t_b - board thickness, t - steel thickness, d - screw diameter) . . . 172
4.11 Average measured values of key properties of screw connectors per shear plane for different steel-to-sheathing connections (t_b - board thickness, t - steel thickness, d - screw diameter) . . . 173

4.12 Summary of models and associated parameters for each material and system interaction system 175

5.1 Material properties of cold-formed steel coupons extracted from columns (CS15) 180
5.2 Material properties of cold-formed steel coupons extracted from tracks (CS12) 180
5.3 Average measured material properties of sheathing 182
5.4 Average measured cross-sectional dimensions 183
5.5 Summary of initial geometric imperfection amplitude measurements 187
5.6 Summary of details of the tested specimens and observed failure loads 196

6.1 Averaged material properties of stud and track reported by Kyprianou et al. (2021*c*) and used in the FE model 226
6.2 Material properties of plasterboard adopted in FE models 228
6.3 OSB material model characteristics 229
6.4 Properties adopted to describe the load-slip response model by Kyprianou et al. (2021*b*) for the shear behaviour of the springs for the given type of board and screw diameter 231
6.5 Properties adopted to describe the load-displacement response model by Kyprianou et al. (2021*b*) for the pull-through behaviour of the springs for the given type of board and screw diameter 231
6.6 Summary of studies and type of specimens used for validation 242
6.7 Comparison between FE and test results reported in Young (1997) 243
6.8 Comparison between FE and test results reported by Vieira et al. (2011) . . . 245
6.9 Comparison between FE and test results presented in Peterman & Schafer (2014) 248
6.10 Comparison between FE and test results for experiments carried out as part of the present study, as described in Chapter 5 251
6.11 Comparison between the observed FE and test failure modes 259
6.12 Description of parametric examined systems and obtained FE results. 263
6.13 Results of parametric studies 265

7.1 Spring stiffnesses for different screw spacings for use in CUFSM of a steel-to-OSB 4.8 mm in diameter screw connection 302
7.2 Axial member predictions using CUFSM (Li & Schafer 2010) and DSM . . . 302
7.3 Flexural member capacity predictions using CUFSM (Li & Schafer 2010) and DSM 302
7.4 Recommended effective lengths in compression 314
7.5 Empirically determined power coefficients ω and the refined ω_1 and ω_2 when fitting the employed interaction curves to the FE data 326
7.6 Summary of pull-through $F_{u,pt}$ and bearing $F_{u,po}$ capacities for certain configurations determined in Chapter 4 329
7.7 Comparison between the proposed formula for pull-through demand, calculated based on the test results and the resistances; a value above one in the last column indicates a valid prediction of pull-though connector failure . . . 330
7.8 Comparison between the axial resistance calculations, based on the design recommendation from the previous sections N_{Rd}, the axial resistance from the pull-though screw resistance $N_{Rd,pt,fixing}$ and the test results P_u 330

A.1 Section dimensions 364
A.2 Gross section properties 365
A.3 Effective section properties 366

Nomenclature

A	Gross cross-sectional area of steel
A_{eff}	Effective cross-sectional area of steel member
A_{pt}	Bearing area of a screw
$A_{s,eff}$	Effective bearing area around $A_{s,hd}$
$A_{s,hd}$	Bearing area below the screw head
$A_{s,thr}$	Bearing area of the screw threads
A_s	Area of a stiffener
$C_{y,eff,comp}$	Effective centroid from midline of web (due to bending)
C_y	Centroid from midline of web
$C_{z,eff,comp}$	Effective centroid from midline of bottom flange (due to compression)
C_z	Centroid from midline of bottom flange
E	Young's modulus
$E_{0.2}$	Tangent modulus (stiffness) at 0.2% proof
F	Force
$F_{1,po}$	Push out load at 1 mm of slip
$F_{u,po}$	Ultimate shear resistance of a screw in a board-to-steel component
$F_{u,pt,0.8}$	Post peak pull-through resistance of a screw into a board at 80% of $F_{u,pt}$

$F_{u,pt,2}$	Second peak pull-through resistance of a screw into a board
$F_{u,pt}$	Ultimate pull-through resistance of a screw into a board
$F_{u,s}$	Ultimate tensile resistance of a screw
$F_{u,v}$	Ultimate shear resistance of a screw
H	Horizontal load
$H_{c,y,Rd}$	Cross-sectional resistance in major axis bending in terms of horizontal force
H_u	Ultimate horizontal load (determined from test or FE results)
I	Second moment of area
I_{eff}	Effective second moment of area
I_t	Torsion constant
I_w	Warping constant
$I_{y,eff}$	Effective second moment of area about the major axis
I_y	Second moment of area about y-y axis (major axis)
I_z	Second moment of area about z-z axis (minor axis)
K	Stiffness of a spring
$K_{o,40}$	Secant stiffness at 40% of ultimate F_u force
K_o	Initial stiffness for a highly non-linear curve
L	Length of a member
$L_{cr,y}$	Effective length about major axis
$L_{cr,z}$	Effective length about minor axis
L_{crd}	Critical wavelength for distortional buckling
L_{cre}	Critical wavelength for global buckling

L_{crl}	Critical wavelength for local buckling
L_{cr}	Effective length
M_n	Bending moment
M_n	Nominal bending resistance
M_{Rd}	Bending resistance with partial shear connection
M_R	Restoring moment
$M_{c,Rd}$	Cross-sectional resistance in bending
$M_{c,y,Rd}$	Cross-sectional resistance in major axis bending
$M_{comp,Rd}$	Bending resistance with partial shear connection for cold-formed steel members (Class 4 as non-composite)
M_{crd}	Elastic critical moment for distortional buckling
M_{cre}	Elastic critical moment for global buckling
M_{crl}	Elastic critical moment for local buckling
M_{cr}	Critical moment for lateral-torsional buckling
M_{cr}	Elastic critical moment
$M_{pl,Rd}$	Bending resistance of a fully composite system
$M_{pl,a,Rd}$	Plastic bending resistance of a bare steel member
M_u	Ultimate bending moment (determined from test or FE results)
$M_{y,screw}$	Yield moment of screw
M_y	yield moment
$N_{b,Rd}$	Buckling resistance in compression
$N_{c,Rd}$	Cross-sectional resistance in compression

$N_{c,board}$	Compressive strength of board
$N_{cr,FT}$	Elastic critical flexural-torsional buckling resistance
$N_{cr,T}$	Elastic critical torsional buckling resistance
N_{cr}	Elastic critical flexural buckling resistance (Euler load)
N_c	Total longitudinal force transferred by the shear connectors
$N_{pl,a}$	Axial strength of a member (determined with gross properties)
P	Axial load
P_n	Nominal axial compressive resistance
P_{Rd}	Resistance of a shear connector
P_b	Bearing strength of screw in design
P_{crd}	Elastic critical axial load for distortional buckling
P_{cre}	Elastic critical axial load for global buckling
P_{crl}	Elastic critical axial load for local buckling
P_{cr}	Elastic critical axial load
P_u	Ultimate compressive load (determined from test or FE results)
P_v	Shear strength of screw
P_y	Squash (yield) load
T_{Ed}	Required torsion
T_{Rd}	Torsional resistance
$V_{b,Rd}$	Shear buckling resistance
$W_{y,eff}$	Effective elastic section modulus for major axis
W_y	Elastic section modulus for major axis

$W_{z,eff}$	Effective elastic section modulus for minor axis
W_z	Elastic section modulus for minor axis
Φ	Value to determine the reduction factor χ
β	Relative degree of fixity based on deformations at mid-length
β_θ	Relative degree of fixity based on rotations
χ	Reduction factor for relevant buckling mode
χ_d	Reduction factor for distortional buckling
δ	Displacement or deformation
δ_D	Distortional imperfection amplitude
δ_L	Local imperfection amplitude
$\delta_{G,maj}$	Major axis flexural imperfection amplitude
$\delta_{G,min}$	Minor axis flexural imperfection amplitude
δ_f	Mid-length deformation for member with fixed ends
δ_{po}	Push-out slip of a screw in shear in a board-to-steel component
δ_{pt}	Pull-through deformation of a screw into a board (net embedment)
δ_p	Mid-length deformation for member with pinned ends
δ_{true}	Corrected (true) axial deformation for columns under compression
$\delta_{u,po}$	Ultimate shear slip of a screw in a board-to-steel component
$\delta_{u,pt,0.8}$	Post peak pull-through deformation of a screw into a board at $F_{u,pt,0.8}$
$\delta_{u,pt,2}$	Deformation of a screw into a board at $F_{u,pt,2}$
$\delta_{u,pt}$	Ultimate pull-through deformation of a screw into a board
η	Degree of shear connection

$\overline{\lambda}$	Non-dimensional slenderness
$\overline{\lambda}_d$	Non-dimensional slenderness for distortional buckling
$\overline{\lambda}_p$	Non-dimensional slenderness for local buckling of a plate
$\overline{\lambda}_{LT}$	Non-dimensional slenderness for lateral-torsional buckling
ψ	Stress ratio between the edges of a plate element
ρ	Reduction factor
σ	Stress
$\sigma_{0.2}$	0.2% proof stress
$\sigma_{1.0}$	1.0% proof stress
$\sigma_{cr,s}$	Critical buckling stress of a stiffener
σ_{true}	True stress for input in ABAQUS
σ_u	Ultimate stress
$\theta_{G,tor}$	Twist imperfection amplitude
θ_f	Rotation for member with fixed ends
θ_p	Rotation for member with pinned ends
ε	Strain
ε^{pl}_{true}	True plastic strain for input in ABAQUS
$\varepsilon_{0.2}$	Elastic strain at 0.2% proof stress
$\varepsilon_{1.0}$	Elastic strain at 1.0% proof stress
$\varepsilon_{c,u}$	Final strain post f_c
ε_c	Strain at f_c
ε_f	Elongation at fracture

ε_{sh}	Strain at the end of the yield plateau
$\varepsilon_{u,0.8}$	Post peak strain at 80% of f_u
ε_u	Ultimate strain
b	Width
b_{eff}	Effective width
c	Lip length
d	Screw diameter (nominal)
$d_{s,hd}$	Diameter of the head of a screw
$d_{s,sh}$	Diameter of the shank of a screw
$d_{s,thr}$	Screw diameter at the threads
e	Eccentricity
f_c	Compressive strength
$f_{h,k,OSB}$	Embedment strength for OSB
$f_{h,k,gen}$	Embedment strength for a general type of timber board
$f_{h,k,gyp}$	Embedment strength for gypsum (plasterboard)
$f_{h,k}$	Embedment strength
$f_{u,s}$	Tensile strength of a screw
f_u	Ultimate strength
f_y	Yield strength
h	Depth of a cross-section
h_{hole}	Depth of hole in a cross-section
$h_{s,hd}$	Depth of the head of a screw

i_y	Radius of gyration for major axis
i_z	Radius of gyration for minor axis
k	Stiffness of a spring
k_x	Lateral stiffness of a spring in direction x
k_y	Lateral stiffness of a spring in direction y
k_ϕ	Rotational stiffness of a spring
$k_{\theta,f}$	Stiffness from rotation for member with fixed ends
$k_{\theta,p}$	Stiffness from rotation for member with pinned ends
k_f	Stiffness from horizontal load - deformation for member with fixed ends
k_p	Stiffness from horizontal load - deformation for member with pinned ends
m	Compound Ramberg-Osgood exponent between $\sigma_{0.2}$ and σ_u
n	Number of shear connectors
n	Ramberg-Osgood strain hardening exponent up to $\varepsilon_{0.2}$
$n'_{0.2,1.0}$	Compound Ramberg-Osgood exponent between $\sigma_{0.2}$ and $\sigma_{1.0}$
n_1	Ramberg-Osgood exponent
n_f	Number of shear connectors needed for full shear connection
r	Internal radius
s	Spacing between sheathing-to-steel fixings
$s_{s,nonthr}$	Non-threaded length of the shank
$s_{s,thr}$	Pitch between threads of a screw
t	Core thickness of steel excluding any coating
t_b	Thickness of sheathing board

t_{nom}	Nominal thickness of steel including coating
t_{red}	Reduced thickness to account for the effects of distortional buckling
t_s	Thickness of steel member used in component calculations
u	Displacement in spring elements of finite element models
v	Poisson's ratio
w	Distributed load
y_0	Shear centre (horizontal distance) from centroid
z_0	Shear centre (vertical distance) from centroid

Chapter 1

Introduction

1.1 Background

COLD-FORMED members are manufactured from steel sheets, strips or plates by processes such as rolling, folding or pressing. The most common process is cold rolling using steel strips since it allows for larger volumes of production more efficiently (Rhodes 1991). There is a wide variety of applications of cold-formed steel members in numerous industries, with their use in the construction industry becoming increasingly common across a range of building types (Davison & Owens 2012).

Construction using cold-formed steel began in about the 1850s in both the United States and Great Britain but its wider application in buildings was not initiated until the 1940s. Since the 1940s, as reported by Yu & LaBoube (2010) and Miller & Peköz (1994), research by Professor George Winter and his colleagues at Cornell University funded by the American Iron and Steel Institute (AISI) accelerated the use of cold-formed steel in construction.

In 2019, as reported by the World Steel Association (2020), the world production of steel coil, sheet and strip of thickness less than 3 mm used for making cold-formed steel sections exceeded 35 million tonnes, while the production of hot-rolled steel coil, sheet and strip amounted to about 80 million tonnes. In Australia, since the early 2000s, the use of cold-formed steel structural elements has exceeded that of hot-rolled steel elements (Hancock

et al. 2005).

Within the construction industry, the importance of cold-formed steel members is clearly growing. This is due to better economies of scale, flexibility and speed of construction, recent growth of interest in modular construction (Heywood et al. 2012) and growing use of composite and hybrid systems.

1.2 Cold-formed steel

Both in practice and in the scientific literature, cold-formed steel structural sections are associated with vocabulary such as thin-walled (EN 1993-1-3 2006) (AISI S100 2016) (Yu & LaBoube 2010), thin-gauge (BS 5950-5 1998), light-gauge (Winter 1952), light weight or even simply light steel (Grubb et al. 2001) (Way & Heywood 2012) (Davison & Owens 2012) sections. These terms have been historically used to describe the same structural sections. Henceforth, for the purposes of this thesis, the term used will be 'cold-formed' and will refer to galvanised cold-formed steel sections of uniform thickness less than 3 mm for application in the construction industry.

The cold-rolled strip used in the manufacturing process comes as a pre-galvanised coil without any additional treatment. In the UK, the standard coating for construction products is 275 g/m^2, which translates into a uniform zinc coat (referred to as Z275) of 0.02 mm on either side. In section property calculations, the core thickness of steel considered is 0.04 mm less than the measured (or provided by section manual libraries) nominal thickness of the cold-formed steel members to account for the non-structural effect of galvanisation as per EN 1993-1-3 (2006).

1.3 Stud columns

Despite sharing similar physical properties with their hot-rolled counterparts, the structural behaviour of cold-formed steel products is significantly different, because of their much thinner nature. Therefore, due to their inherent high cross-sectional slenderness, cold-formed

steel products typically require utilisation of their post-buckling capacity to ensure efficient design.

Owing to the way in which cold-formed steel structural sections are manufactured, their cross-sectional shapes are typically singly- or non-symmetric. The most common families of cold-formed steel members for construction applications are C- and Z-shaped sections. Channel lipped sections are broadly manufactured since they are easy to roll, while the lips provide additional stiffness to the flanges, strengthening them against local buckling (Heywood et al. 2012). Channels tend to be used as the main vertical members in framing applications, acting as wall studs, connected at their top and bottom with simpler C-shaped, horizontal 'track' members. Typical C-sections used in wall frames are shown in Figure 1.1.

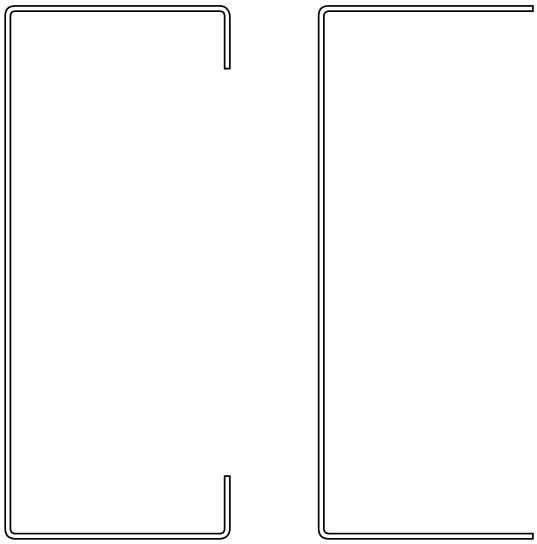


Figure 1.1: Typical C-section shapes used for walls

Often in cold-formed steel frames, additional secondary bracing elements known as bridging or noggins are required. These secondary elements connect the studs at intermediate heights, providing restraint to the minor axis and reducing their effective length for global buckling. Examples of load bearing frames with channel lipped sections used as the main vertical members along with other secondary bracing members, forming a prefabricated modular building unit, are shown in Figure 1.2.



Figure 1.2: Load bearing cold-formed steel frame for a modular unit (Davison & Owens 2012)

Variations of C-sections and Z-profiles, with or without stiffeners, are frequently used as horizontal members, including joists and purlins. Typical shapes of such members are shown in Figure 1.3.

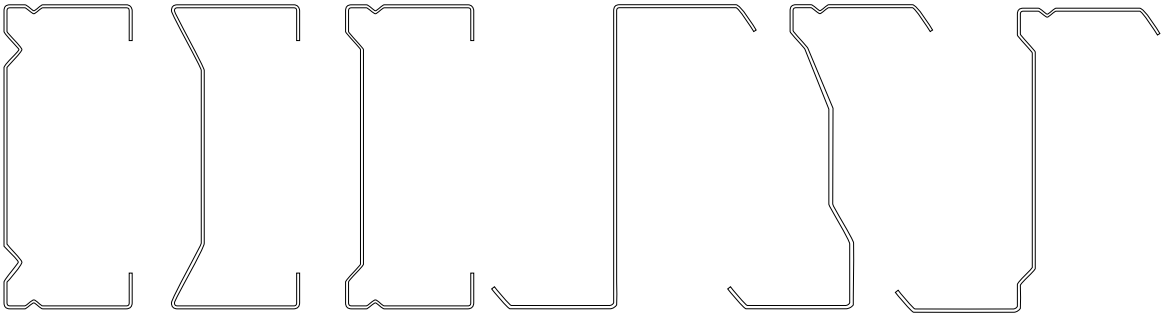


Figure 1.3: Typical sections used as floor joists and roof purlins

1.4 Sheathed wall stud systems

Wall systems made out of cold-formed steel channel lipped vertical members (studs) set in tracks and sheathed with various types of boards are becoming increasingly common in the construction industry. The versatility, practicality and economy associated with the quick construction process of these systems allows for their use both as non-structural and load-bearing wall systems. Some common boards used for sheathing include gypsum boards or plasterboards, cement particle boards and timber-based boards such as orientated strand board (OSB) and plywood. Gypsum boards are widely used since they also provide fire protection and are commonplace in medium rise buildings. In low rise residential buildings in North America, wall studs sheathed with OSB boards tend to also be common practice. An example of a cold-formed wall system, sheathed on one side, in a test rig setting, is shown in Figure 1.4.

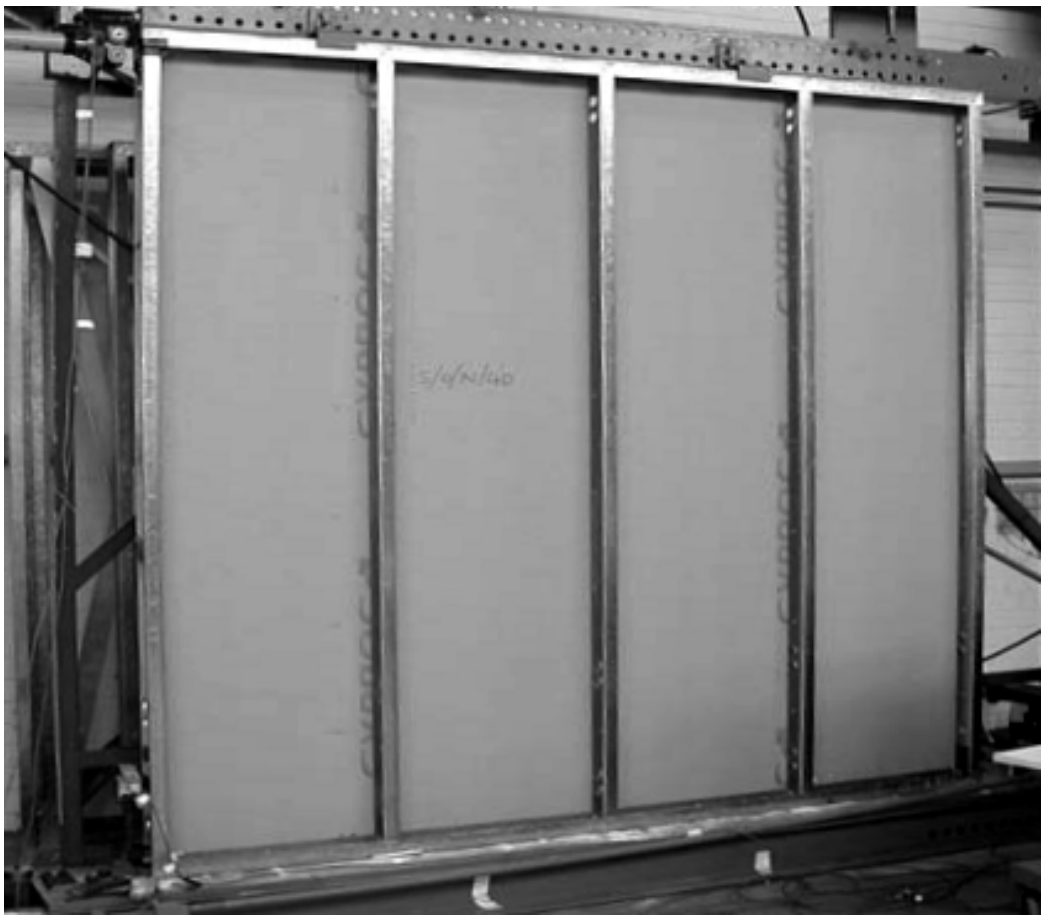


Figure 1.4: One-sided sheathed wall frame in a test rig (Grubb et al. 2003)

1.5 Motivation

Reducing the impact of the construction industry on the natural and built environment is crucial for tackling the environmental crisis of global warming, with its reformation being essential, for a more sustainable use of building materials (Allwood et al. 2012). Our world is also faced with a global housing crisis. From developing countries to leading economies, the lack of affordable housing worldwide has reached concerning levels, since not enough homes are being built at the scale, speed and quality that is needed (B1M 2020). Modular construction systems of sheathed cold-formed steel frames offer an elegant, fast and versatile solution for building low to medium-rise structures (Lawson & Ogden 2008), while emerging technological developments in the modular construction sector can allow for even higher economies of scale, safer and more precise construction.

Current North American design methodologies AISI S100 (2016) and AISI S211 (2012) are conservative in the design of sheathed wall studs, whereas in Europe, EN 1993-1-3 (2006) design code does not provide any specific guidance on the effect of sheathing to cold-formed steel columns. This thesis is funded by the Centre of Doctoral Training in Sustainable Civil Engineering of Imperial College and by Ayrshire Metals Ltd (a cold-formed steel manufacturer); therefore, it is in the interest of both parties for a solution of designing sheathed wall stud systems more efficiently. A more efficient sheathed wall stud design, which recognises the structural effects from the sheathing, can promote the modular construction sector, which can offer a solution to the global housing crisis, as well as the use of less materials and, as such, decrease of the carbon-footprint on the environment, aiding to transition towards a more sustainable construction industry.

1.6 Aim and objectives

The aim of the current study is to illustrate that the structural impact of sheathing on wall studs, which is typically ignored in design, should be structurally considered. As such, the thesis objectives are:

(i) To experimentally study typical components of sheathed cold-formed steel wall systems in order to establish their characteristic behaviour. The conducted experiments include material tests on cold-formed steel and various types of sheathing board, tests on screw connectors to determine their capacity and tests on steel-to-sheathing connectors in both shear and pull-through.

(ii) To collect all similar tests on components of sheathed cold-formed steel wall systems reported in the literature and compare them with the test data obtained by this study. Assessment and grouping of all these data are to be presented.

(iii) To develop analytical models that can describe the stress-strain or load-displacement behaviour of the test data collected in objectives (i) and (ii). Key input parameters for use with the developed models are also to be established.

(iv) To design a full-scale test rig for testing typical sheathed wall studs, as built in practice, under combined compression and bending. Bending should be enforced as a uniformly distributed load (or as an equivalent loading scheme) to represent wind loading.

(v) To test a series of full-scale sheathed stud columns under pure compression, pure bending and combination of compression and bending, and examine the effect of the sheathing board and of different spacings of sheathing-to-steel fixings on the capacity and behaviour of the stud columns.

(vi) To develop numerical (finite element) models which can simulate the behaviour of sheathed stud wall systems tested in the current study and other similar tests found in the literature.

(vii) To validate the finite element models against physical tests and establish suitable parameters (mainly from the results from objective (iii)) for use in parametric studies.

(viii) To carry out parametric studies to investigate the effect of the board, screw connector spacing and section depth on the ultimate capacity of cold-formed steel members under different loading schemes.

(ix) To assess current design rules against findings from the tests and numerical studies.

(x) To provide recommendations and improvements of current design rules, based on the results of the tests and numerical studies, which can be relatively easily adopted in the current design practice.

1.7 Methodology

To achieve the objectives stated in the previous section, a series of different methodologies were adopted:

1. Literature review

A literature review is conducted to report the state-of-the-art on cold-formed steel members, studies on sheathed wall studs and the technical background of different design approaches.

2. Experimental studies

A significant portion of the research presented herein was carried out in the Structures Laboratory of the Department of Civil and Environmental Engineering at Imperial College London. More than 100 material and component tests, and 17-full scale tests on sheathed stud columns were conducted.

The material and component tests were designed, built, prepared for testing, tested and data post-processed by the author. For recording strains either strain gauges were mounted on the specimens or digital image correlation (DIC) was used. Optical extensometers and linear variable displacement transducers (LVDTs) were used to measure larger displacements, mainly in the component tests. Calibration of measuring and testing equipment was also performed. Material specimens were tested in a 150 kN Instron 5984 testing machine, while more substantial component tests such as push-out tests were performed using a 750 kN Instron hydraulic testing machine. Recording and post-processing of the DIC images was performed using the DaVis (2019) software, while the load was recorded using the Bluehill (2019) and Datascan (2019) data acquisition systems.

For the full scale tests, the test rig was designed in Solidworks (2017) and built by the technicians of the Structures Laboratory, under supervision, using a 1000 kN Instron actuator for compression and a 500 kN Instron actuator for the lateral loading. 3D printed clamps were readily produced for mounting LVDTs, while strain gauges, LVDTs, inclinometers and stringpots were also used. The Bluehill (2019) and Datascan (2019) data acquisition systems were employed for data recording. The full scale tests were all designed, built and tested by the author.

As part of the study, an imperfection rig was also designed, built and calibrated for measuring geometric imperfections of specimens up to 2.4 m long. The rig was built out of cast aluminium rails and steel section parts, allowing reconfigurability and recalibration. It is now part of the testing equipment in the laboratory and has been used by other researchers as well.

3. Analytical modelling

Analysis of an assembled experimental database of more than 400 physical tests was performed. The mechanical behaviour determined by material and component tests was examined and a set of analytical expressions was developed to describe the nonlinear stress-strain and load-displacement profiles. The development of the analytical expressions was based on modifying and adapting existing formulations found in the literature, while predictive expressions for the ultimate capacities were devised and recommended values for the remaining model parameters were provided.

4. Numerical modelling

Numerical modelling was performed by means of finite element simulations using the ABAQUS (2016) software in an implicit analysis. The numerical analyses were conducted using input files and external scripts in *Matlab* and *Python*, where all finite element modelling parameters were defined explicitly. This was done to allow for automation and facilitate parametric studies.

Input files were created using *Matlab*, where geometries, material models, node mesh,

type and properties of elements and other properties of the analysis were defined. Through *Matlab*, an elastic buckling analysis was also carried out using the CUFSM software (Li & Schafer 2010), where elastic critical buckling half-wavelengths along with respective cross-sectional buckling shapes were extracted to be post-processed back in *Matlab* to create appropriate input files of imperfections for use along with the main input files in the finite element analyses. About 10,000 lines of code were written in *Matlab* to develop the engine for generating the input files for the main analysis and the imperfections. Extraction of data once the finite element analyses were completed, was performed using *Python* scripts, while *Visual Basic for Applications (VBA)* and the *Microsoft Excel* software were utilised for analysing and post-processing the data. The order of execution of these processes, is illustrated in the flow chart in Figure 1.5.

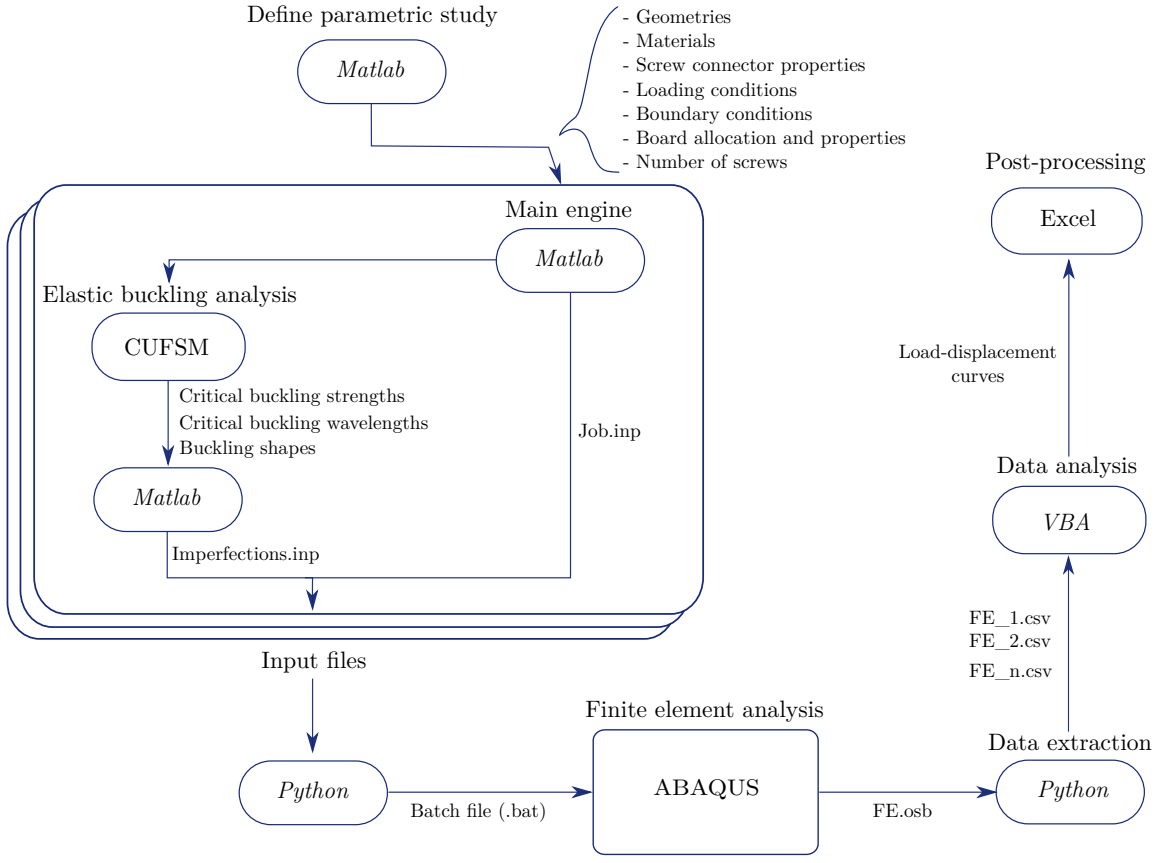


Figure 1.5: Order of executions for the finite element analyses

5. Design methodology

Existing design methodologies from the Eurocode (EN 1993-1-3 2006) and North American design guidance (AISI S100 2016) are assessed against the findings of the current study and recommendations for a more efficient design are provided. Note that the complex iterative process of the effective width method provided in EN 1993-1-3 (2006), for the calculation of the effective properties of cold-formed steel members, was coded in *Visual Basic for Applications* using the guidance given in EN 1993-1-3 (2006), EN 1993-1-5 (2006) and Way & Heywood (2012), to allow close examination of the method and generate properties as needed.

For the preparation of this thesis, the LaTeX text and document processor was used.

1.8 Thesis outline

The present chapter provides a general introduction relevant to this thesis and states the motivation, objectives and methodology for the research presented herein. In Chapter 2, a literature review is provided, aiming primarily to inform on the research precedent in cold-formed steel members and to provide a general background on sheathed wall stud studies and existing design methodologies.

In Chapter 3, an experimental study of more than 100 material and components from typical sheathed cold-formed steel stud walls is presented. At the end of Chapter 3, an assemblage of experiments, from the literature, relevant to those described at the earlier stages of the chapter is provided. A collection of more than 400 tests was compiled. This chapter deals with objectives (i) and (ii), as described in Section 1.6.

In Chapter 4, analytical models to describe the material and connection behaviour of the key components of sheathed cold-formed steel wall systems are developed and assessed. A review of key existing formulations is provided at the beginning of the chapter, while in the later parts of the chapter, the developed models are fitted to test data and are shown to accurately predict the stress-strain behaviour of materials and load-displacement curves of

sheathing-to-steel connectors in shear and pull-through. This chapter deals with objective (iii), as described in Section 1.6.

In Chapter 5, an experimental study of 17 full-scale sheathed wall studs subjected to compression, major axis bending and combined loading is described. Material tests on the tested cold-formed steel specimens are also reported, as well as stub column tests and measurements of geometric imperfections. Experimental results are reported in terms of axial load-displacement curves for pure compression specimens and in terms of mid-height horizontal load-displacement for pure bending and combined load cases. Finally, results from strain gauges are reported to demonstrate that the loading was as intended and a brief discussion is provided where comparisons are made with other relevant tests found in the literature. This chapter deals with objectives (iv) and (v), as described in Section 1.6.

In Chapter 6, the structural behaviour of sheathed wall studs is studied numerically by developing sophisticated finite element models. Details of the methodology adopted for the development of the finite element model are provided and its key features are described. Following validation of the developed finite element models against tests from four different studies, including the tests presented in Chapter 5, a set of parametric studies is presented. The influence of the board material, changing connector spacing in various configurations of loads and changing section depth is parametrically studied. This chapter deals with objectives (vi), (vii) and (viii), as described in Section 1.6.

In Chapter 7, a preliminary design method capturing the structural behaviour of sheathed cold-formed steel studs under axial and lateral loading is provided. Existing design methodologies are assessed against the test results from Chapter 5, while both test results and numerical findings presented in Chapter 6 are used to provide recommendations on the existing design guidance. This chapter deals with objectives (ix) and (x), as described in Section 1.6.

In Chapter 8, the conclusions of the current research are provided highlighting the key findings and the major contributions to cold-formed steel construction. Finally, suggestions and recommendations for future research are provided.

1.9 Publications

The research work undertaken as part of this study and presented in this thesis has contributed to the following publications, while at least one more journal article is anticipated to be submitted based on the work presented in this thesis.

Journal publications:

- Kyprianou, C., Kyvelou, P., Gardner, L. and Nethercot, D. A. (2021*c*) 'Experimental study of sheathed cold-formed steel beam-columns', *Thin-Walled Structures [Accepted].*
- Kyprianou, C., Kyvelou, P., Gardner, L. and Nethercot, D. A. (2021*b*) 'Characterisation of material and connection behaviour in sheathed cold-formed steel wall systems - Part 2: Analytical modelling', *Structures* **30**, 1184-1199.
- Kyprianou, C., Kyvelou, P., Gardner, L. and Nethercot, D. A. (2021*a*) 'Characterisation of material and connection behaviour in sheathed cold-formed steel wall systems - Part 1: Experimentation and data compilation', *Structures* **30**, 1161-1183.
- Kyvelou, P., Nethercot, D., Hadjipantelis, N., Kyprianou, C. and Gardner, L. (2020) 'The evolving basis for the design of light gauge steel systems', *International Journal of Structural Stability and Dynamics* **20**(13), 2041008.
- Kyvelou, P., Kyprianou, C., Gardner, L. and Nethercot, D. A. (2019) 'Challenges and solutions associated with the simulation and design of cold-formed steel structural systems' *Thin-Walled Structures* **141**, 526-539.

Conference publications:

- Kyprianou, C., Kyvelou, P., Gardner, L. and Nethercot, D. A. (2021*d*) Experiments on sheathed cold-formed steel beam-columns, *in* 'Eurosteel 2021', Sheffield, UK [Accepted].
- Kyprianou, C., Kyvelou, P., Gardner, L. and Nethercot, D. A. (2018) Numerical study of sheathed cold-formed steel columns, *in* 'Proceedings of the ninth international conference on Advances in Steel Structures (ICASS 2018)', Hong Kong, China.

Chapter 2

Literature review

2.1 Introduction

THE aim of this chapter is to present a review of the relevant research precedent to this thesis, although it should be noted that significant literature, where relevant, is referenced throughout the thesis. Firstly, an overview of studies on cold-formed steel, mainly relevant to the development of finite element simulations is presented. Secondly, an appraisal of previous studies, mainly experimental, on sheathed stud columns is provided. Finally, existing design methods for cold-formed steel members, historical background and the latest developments on the design of sheathed wall studs are presented.

2.2 Cold-formed steel members

Cold-formed steel sections are formed into shape at room temperature. Three main processes are used for their manufacture: rolling, folding and pressing. These processes induce plastic deformations affecting the overall shape of the stress-strain curve, the yield strength, the ductility and the development of residual stresses, as described in the following subsections.

2.2.1 Material behaviour

2.2.1.1 Stress-strain behaviour

The stress-strain curve is a key part of the description of the mechanical behaviour of steel. The stress-strain behaviour of steel sections manufactured by hot-rolling is characterised by a sharp-yielding point, as shown in Figure 2.1. For steels with a stress-strain behaviour as shown in Figure 2.1, the yield point or yield strength, f_y is defined at the level where the stress-strain curve becomes horizontal (i.e. yielding plateau). Steels that are cold-worked tend to exhibit a more rounded stress-strain behaviour, demonstrating gradual yielding, as shown in Figure 2.2. This rounded stress-strain profile has been exhibited by numerous tensile tests on cold-formed steel coupons, such as those studied by Sivakumaran (1987) and Rogers & Hancock (1997). Compression tests on channel sections by Young & Rasmussen (1998*c*) and Young & Hancock (2003) also showed the same rounded stress-strain behaviour. The ultimate stress f_u and the corresponding strain ε_u, as shown in Figure 2.1 and 2.2, are the limiting points of interest in design and when modelling the material behaviour of steel in finite element simulations.

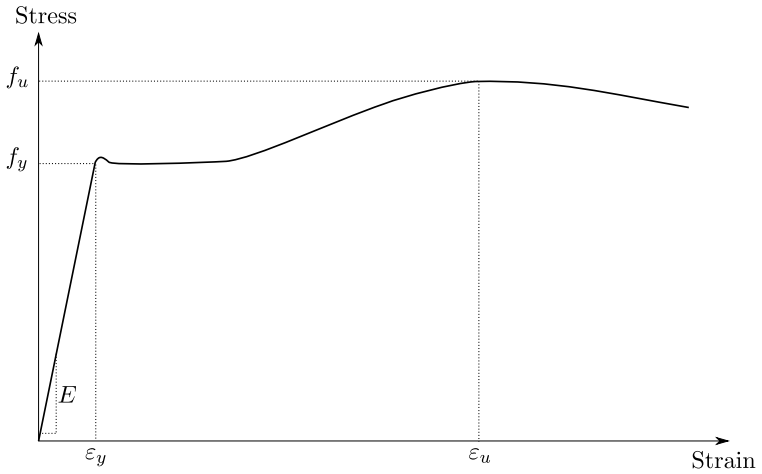


Figure 2.1: Stress-strain curve for structural steel with sharp yielding

The stress-strain behaviour is commonly determined by tensile coupon tests. The yield stress f_y for steels exhibiting gradual yielding, is usually determined by the offset method, according to which the yield stress is determined by intersecting the stress-strain curve with

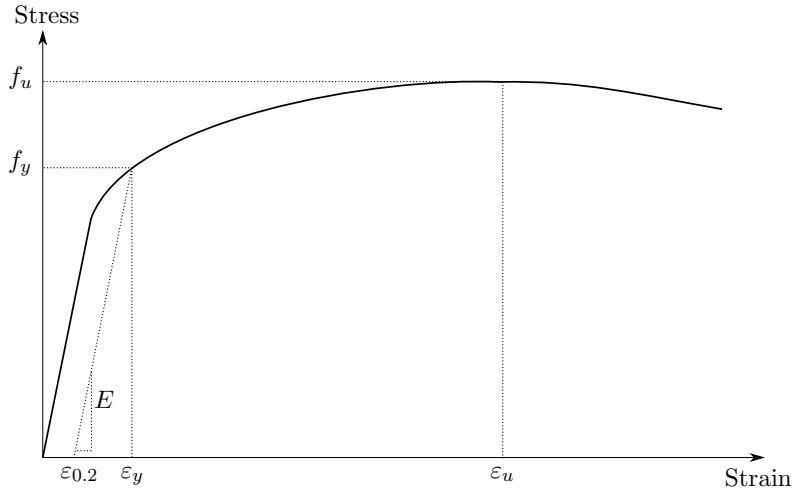


Figure 2.2: Stress-strain curve for structural steel with gradual yielding

a straight line of gradient equal to the Young's modulus E, usually at an offset specified at a strain of 0.2% $\varepsilon_{0.2}$, as shown in Figure 2.2.

Cold-formed steel has been shown to be anisotropic (Rogers & Hancock 1997). Tensile coupon tests on high strength ($f_y = 550$ N/mm^2) cold-rolled sheets by Rogers & Hancock (1997) were used to determine the degree of anisotropy and its effect on ductility. Coupons extracted in opposing directions of the steel sheet revealed disparities in ductility, elastic modulus E (stiffness) and ultimate stress f_u. Compression member tests using steel of similar strength by Ye & Rasmussen (2008) and tensile coupon tests from cold-formed stainless steel C-lipped channel members by Becque & Rasmussen (2009*a*) also confirmed these findings. Experimental findings and finite element analyses by Becque & Rasmussen (2009*b*) demonstrated that material anisotropy can be accounted using Hill's criterion (Hill 1950). However, numerical studies by Rasmussen et al. (2003) on cold-formed stainless steel plates have demonstrated that the effect of anisotropy is small and may be neglected in numerical simulations.

2.2.1.2 Material models for cold-formed steel

Various material models have been developed to capture the rounded stress-strain response of cold-formed steel. Although Moreyra & Peköz (1994) and Feng et al. (2003) proposed various tri-linear models for modelling cold-formed steel, the most commonly

used model for materials with a rounded stress-strain behaviour, initially developed for aluminium, is the one proposed by Ramberg & Osgood (1943) and later modified by Hill (1944):

$$\varepsilon = \frac{\sigma}{E} + 0.002 \left(\frac{\sigma}{\sigma_{0.2}} \right)^n \tag{2.1}$$

where ε and σ are the engineering strain and stress respectively, E is the elastic modulus of the material, $\sigma_{0.2}$ is the 0.2% proof stress and n is the strain hardening exponent describing the roundedness of the stress-strain curve.

Research by Mirambell & Real (2000) and Rasmussen (2003) led to extending the original Ramberg-Osgood model into a two-stage model, to more accurately capture the behaviour of stainless steel, which also exhibits a rounded stress-strain curve. While Equation (2.1) is still used to describe the stress-strain curve up to the 0.2% proof stress $\sigma_{0.2}$, Equation (2.2) is employed to capture the stress-strain profile beyond $\sigma_{0.2}$ and up to the ultimate engineering stress σ_u:

$$\varepsilon = \frac{\sigma - \sigma_{0.2}}{E_{0.2}} + \varepsilon_u \left(\frac{\sigma - \sigma_{0.2}}{\sigma_u - \sigma_{0.2}} \right)^m + \varepsilon_{0.2} \qquad \text{for} \qquad \sigma_{0.2} < \sigma \leqslant \sigma_u \tag{2.2}$$

where $E_{0.2}$ is the tangent modulus of the stress-strain curve at $\sigma_{0.2}$, $\varepsilon_{0.2}$ is the corresponding strain and ε_u is the ultimate strain at the ultimate engineering stress σ_u. A second strain hardening component is also introduced with the empirical parameter m.

Further work on the Ramberg-Osgood model by Gardner & Nethercot (2004*b*) demonstrated that the model's accuracy can be improved at low strains by utilising the 1.0% proof stress $\sigma_{1.0}$ rather than the ultimate stress σ_u in Equation (2.2). The final version of this model is presented by Gardner & Ashraf (2006). Similarly, as with the Mirambell & Real (2000) model, the first stage of the model, for stresses up to $\sigma_{0.2}$, utilises Equation (2.1), while the second stage is given by Equation (2.3) and is applicable up to the ultimate engineering stress σ_u:

$$\varepsilon = \frac{\sigma - \sigma_{0.2}}{E_{0.2}} + \left(\varepsilon_{1.0} - \varepsilon_{0.2} - \frac{\sigma_{1.0} - \sigma_{0.2}}{E_{0.2}} \right) \left(\frac{\sigma - \sigma_{0.2}}{\sigma_{1.0} - \sigma_{0.2}} \right)^{n'_{0.2,1.0}} + \varepsilon_{0.2} \quad \text{for} \quad \sigma_{0.2} < \sigma \leqslant \sigma_u \tag{2.3}$$

In Equation (2.3), $\sigma_{1.0}$ and $\varepsilon_{1.0}$ are the 1.0% proof stress and the corresponding strain

respectively, while $n'_{0.2,1.0}$ is the strain hardening exponent describing the curve between 0.2% and 1.0% proof stresses.

Arrayago et al. (2015) provide an expansive summary on the description of the above models, along with empirical recommendations for the values of the strain hardening exponents. Haidarali (2011) recommended the use of Equation (2.4) for calculating the 1.0% proof stress $\sigma_{1.0}$ in the absence of experimental data. This empirical determination was based on cold-formed steel tensile coupon testing by Yu & Schafer (2003) and Yu & Schafer (2006).

$$\frac{\sigma_{1.0}}{\sigma_{0.2}} = 1.8656\sigma_{0.2}^{-0.0948} \tag{2.4}$$

Gardner & Yun (2018) developed predictive models for the key input parameters of the two stage Ramberg-Osgood model for cold-formed steel.

2.2.1.3 Cold-forming effects and enhanced strength in corner regions

The effect of cold-working on the mechanical properties of steel was experimentally studied at Cornell University in the 1960s by Chajes et al. (1963), Karren (1967) and Karren & Winter (1967). The extent of the effects of cold-working depends on the type of steel and the amount of cold-work undertaken as well as on whether compressive or tensile stresses are induced and their direction with respect to the direction of cold-working. These studies concluded that, due to strain hardening effects, the mechanical properties of mild carbon steel are altered by cold-forming in the following ways: (i) strengths increased while ductility decreases, (ii) higher values of ultimate to yield strength ratio f_u/f_y correspond to higher strain hardening potential, (iii) higher values of the internal radius to thickness ratio r/t correspond to increasing amount of work required and, as a result, to more pronounced strain hardening, and (iv) material anisotropy increases with the amount of cold-work. These are the reasons why fabrication of sharper and thicker corners (i.e. smaller internal radius to thickness ratio) requires more cold-work and as a result a higher yield strength is induced (Hancock 2003, Rossi et al. 2013).

The work by Karren (1967) led to the development of semi-empirical equations for the

ratio of the yield stress in the corner regions over that in the flat regions. Later research by Abdel-Rahman & Sivakumaran (1997) debated that the initial equations by Karren (1967) should impose a 40% reduction. The findings of numerous other researchers have confirmed that corners, when compared to their neighbouring flat regions, have different mechanical properties, with the most significant difference being an overall increase in stresses, as reported by Zhao & Hancock (1992) following studies on cold-formed steel hollow sections. Based on studies on cold-formed square and rectangular hollow sections, Gardner et al. (2010), proposed modified equations to the ones originally recommended by Karren (1967). Studies by Hui (2014) and Kyvelou et al. (2017*b*) on purlin systems demonstrated an increase in yield strength of about 10% to 20% for 1.5 - 3.0 mm thick corner and stiffener regions when compared to flat surfaces.

Afshan et al. (2013) showed that full stress-strain curves can be used to describe the different material behaviour for flat and corner regions by using the modified Ramberg-Osgood curves as described in Section 2.2.1.2. In finite element simulations by Kyvelou et al. (2017*b*), a 17% increase in strength in the material model of the corner regions was adopted, in comparison to the one adopted for the flat regions, while in the finite element studies of Hui (2014), a 10% increase in strength for the corner regions was adopted. In finite element models of sheathed stud columns by Vieira & Schafer (2016) and Fratamico & Schafer (2014), no enhanced strength in the corner regions was considered. In the current research, although strength enhancements in the corner regions were considered in the finite element models presented in Chapter 6, their effect on the ultimate capacity of the sheathed stud columns was found to be negligible due to the small corner area compared to the total area of the section (less than 8% in terms of the total steel area), the presence of the sheathing boards and the small thickness of steel (less than 1.5 mm) corresponding to a moderate r/t ratio.

2.2.1.4 Residual stresses

Residual stresses are stresses that arise during the manufacture and fabrication of members. For hot-rolled steel structural sections, residual stresses are the result of uneven cooling

after hot-rolling or welding (Yu & LaBoube 2010), while for cold-formed steel sections, residual stresses are induced due to plastic deformations imposed during fabrication. The distribution of residual stresses and their effect on the load-carrying capacity of cold-formed steel members has been analytically and experimentally studied by a number of researchers, including Ingvarsson (1977), Moen et al. (2008) and Weng & Peköz (1990). Residual stresses can be split into membrane and flexural stresses. Membrane stresses are compression stresses idealised as constant through the plate thickness, while flexural ones vary linearly through the thickness of the plate.

Experimental studies by Schafer & Peköz (1998*a*) demonstrated that cold-formed steel sections are dominated by flexural residual stresses. Tests showed that although membrane stresses are small enough to be neglected, the magnitude of flexural stresses can be up to 40% of the yield strength. Moen et al. (2008) developed a mechanics-based method in predicting and modelling initial residual stresses which vary along the thickness of the steel plate. Such methods can be used in finite element modelling to predict the premature yielding caused by residual stresses. In accordance with the studies by Schafer & Peköz (1998*a*) and Schafer et al. (2010), the effects of residual stresses and enhanced corner strength on cold-formed steel members offset each other and should either be both included or both ignored in numerical simulations. However, research by Jandera et al. (2008) on cold-formed stainless steel sections showed that flexural stresses do not need to be defined in finite element simulations when the stress-strain curve used to describe the material behaviour is obtained from tensile coupon tests, since they are inherently included in the stress-strain curve; this is also supported by Dubina et al. (2012). Therefore, for the present study, the effect of residual stresses on cold-formed steel is assumed to be inherently included in the stress-strain curves used in the finite element simulations reported in Chapter 6, since these have been obtained by tensile tests.

2.2.2 Service hole openings in the web of the member

Structural cold-formed steel members often comprise service holes (see Figure 2.3) to accommodate cables and various pipes for electrical, plumbing and other services (Kulatunga

& Macdonald 2013). For lipped channel stud column members, these service holes are typically cut in the web of the member - see Chapter 5. The effect of the openings on the ultimate capacity of the member depends on the dimensions of the hole, the type of loading on the member, and the proximity of the hole to the edges of the member and to other holes along the length of the member. In accordance with the effective width theory discussed briefly in Section 2.4.1 and in greater detail, in terms of the EN 1993-1-3 (2006) implementation in Chapter 7, if the ratio of the width of the hole to the width of the member h_{hole}/h is small enough, the presence of the hole may be not detrimental to the local buckling capacity of a specimen under pure compression.

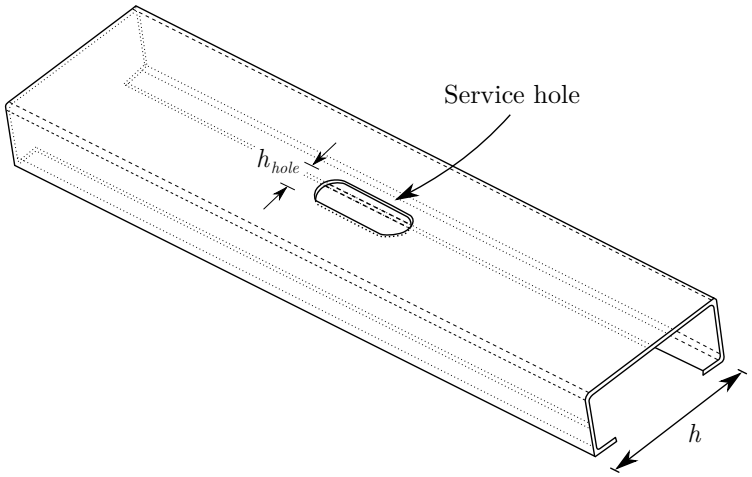


Figure 2.3: A typical lipped channel section with a service hole in the web

Various researchers employed numerical modelling for studying cold-formed steel members with holes. Finite element modelling of cold-formed steel studs with holes subjected to compression was undertaken by Kulatunga & Macdonald (2013) to investiagte the influence of the location and size of holes on the stud performance, while Chen et al. (2020) successfully modelled back-to-back cold-formed channel lipped sections with openings. These studies demonstrated accurate numerical predictions of physical test results, while studies by Kulatunga & Macdonald (2013) showed that the ultimate load capacity of lipped channels under compression vary depending on the position of the holes, with holes closer to the stud ends having a greater weakening effect. For members in bending, finite element models of cold-formed steel lipped channel members with holes were developed by Uzzaman et al. (2012*a*,*b*) and Lian et al. (2016), where the effect of web crippling was studied.

Simplified methods for approximating the critical buckling loads of cold-formed steel members with holes were developed by Moen & Schafer (2009), based on parametric studies conducted using finite element simulations. These studies led to the development of the CUFSM (Li & Schafer 2010) engine by Cai et al. (2017) to include a hole effect calculator in the finite strip eigenvalue buckling analysis.

In the finite element models presented in Chapter 6 of the current study, the service hole openings are modelled to allow direct comparison with the tests presented in Chapter 5 and with 'as built' wall stud frames. Although investigation of effects such as web crippling is not the scope of this study, it is nevertheless the desire to capture all the detrimental effects of holes on the behaviour of the modelled systems.

2.2.3 Buckling behaviour

Owing to the thin-walled nature of cold-formed steel members, their behaviour is complex since they are susceptible to local instability phenomena. Depending on their slenderness, cold-formed steel members suffer buckling at stress levels lower than their material yield stress. Slender cross-sections are susceptible to local and distortional buckling, while unrestrained slender members are prone to global buckling modes such as flexural, torsional or flexural-torsional buckling when in compression and lateral-torsional buckling in bending. The shapes of the individual buckling modes are illustrated in Figure 2.4. Details on how buckling is treated in accordance with the Eurocode 3 (EN 1993-1-1 2005) provisions and determination of the ultimate capacity are provided in Chapter 7.

2.2.3.1 Cross-sectional buckling

2.2.3.1.1 Local buckling

The effect of local buckling in thin-plate elements, has been the subject of many studies in the past (Bleich 1952, Timoshenko & Gere 1961, Bulson 1970, Trahair et al. 2008). Local buckling is the limiting state of buckling of a thin-plate element in compression. As such, for a cross-section, local buckling involves significant deformation of the flat parts between

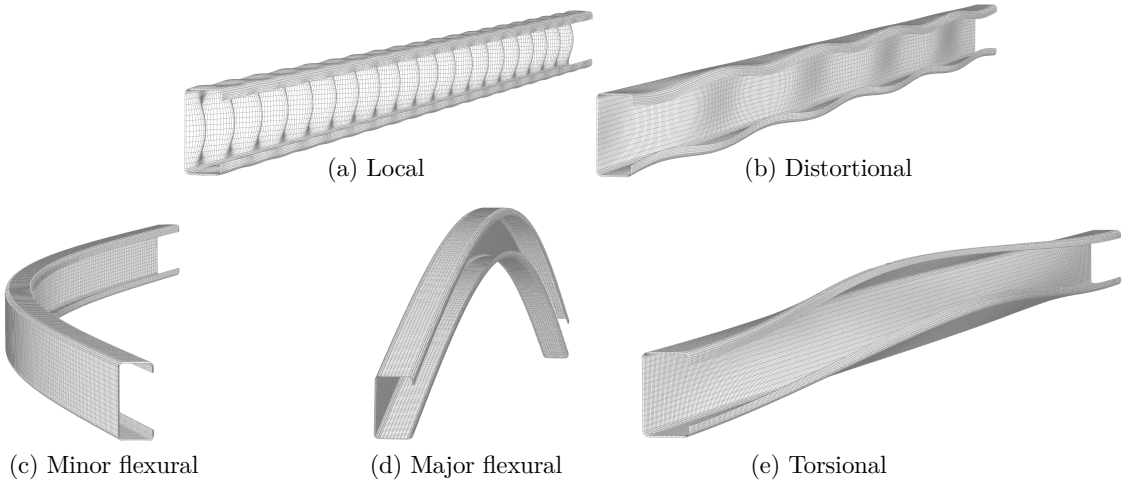


Figure 2.4: Longitudinal distribution of: (a,b) cross-sectional and (c-e) global buckling modes

the fold lines of a cross-section (i.e. the corners), since the flat parts are less stiff than the corner regions. As shown in Figure 2.5 by the demarcated dashed lines of the local buckling mode shape of a lipped channel section under compression, the corners are translationally fixed, but rotationally free, while the maximum deformation takes place at the greatest distance away from these points, i.e. at mid-web and at mid-flange. The buckle form is of a sinusoidal shape and its half-wavelength is typically shorter or equal in length to the largest unrestrained or unstiffened dimension of the cross-section subjected to compression - see Figure 2.4 (a). Hence, decreasing the effect of local buckling by restraining it, is not easy, since it requires introducing stiffeners (such as introducing bends in the geometry) at the flat regions, or alteration of the end boundary conditions of the individual flat elements making up the cross-section or increase of the overall thickness. The ultimate capacity of cold-formed steel members is typically attained with failure triggered by local buckling.

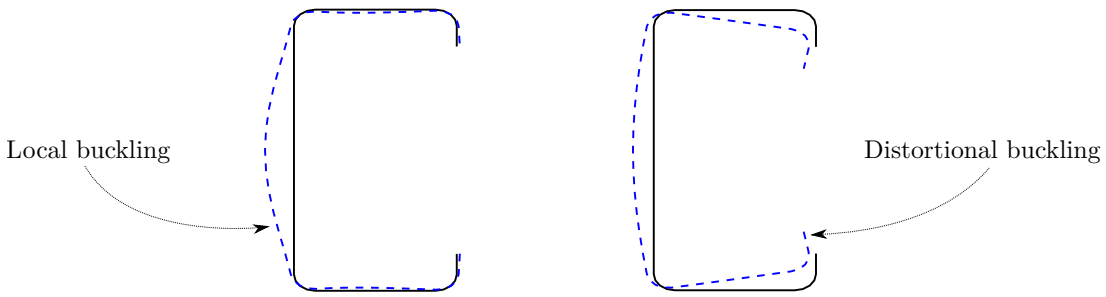


Figure 2.5: Local and distortional buckling

2.2.3.1.2 Distortional buckling

Unlike local buckling, where fold line regions remain fixed in position and deformation takes place within the length of the flat elements, in distortional buckling, instability can occur at both rigid regions and flat regions. For instance, as shown in Figure 2.5, the distortional buckling mode shape of a lipped channel section under compression has its web distorted as well as rotation of the rigid edge-stiffened flange-lip regions. In accordance with Dubina et al. (2012), for deeper channel sections, as the unstiffened web becomes longer, the influence of the rotational stiffness offered by the web-flange corners is reduced, hence the member is more prone to distortional buckling.

The half-wavelength of distortional buckling is typically several times larger than that of local buckling, as shown in Figure 2.4 (b), but smaller than the half-wavelength of global buckling modes, when the member is long enough. Since the critical wavelength of distortional buckling lies between that of local and global modes, bracing can be effective in retarding distortional buckling; therefore sheathing or sheeting connected at spacings shorter than the distortional half-wavelength of the member can result in strengthening (AISI S100 2016). The distortional half-wavelength is dependent on the geometry of the section and loading. For members with sufficiently stiff edge stiffeners subjected to compression, distortional buckling may be prevented (AISI S100 2016), whereas for members under bending, distortional buckling can be critical since it has been observed to result in lower postbuckling capacities than local buckling (Schafer & Peköz 1999). In fact, it is based on such observations and analytical work by Lau & Hancock (1987), that led to the development of the first design curves for cold-formed steel members undergoing distortional buckling to be proposed by Hancock et al. (1994), while later, served as the basis for the development of the direct strength method (Schafer 2008).

2.2.3.2 Global buckling

Global buckling is a mode of buckling developing along the length of the member, which involves translation and/or twist of the entire cross-section with no distortion of the individual plate elements of the cross-section. The principal mode shapes of global buckling

are illustrated in Figure 2.4 (c), (d) and (e), and correspond to flexural buckling about the minor and major axis, and to torsional buckling, respectively. For columns, the global buckling modes that need to be considered are flexural, torsional and flexural-torsional. Flexural buckling is a form of buckling, where a member in compression deflects laterally about its major or minor axis without twist or change in its cross-section. Torsional buckling is a form of buckling, where a member twists about its shear centre. Flexural-torsional buckling is a combination of flexural and torsional modes. For members in bending, global buckling in the form of lateral-torsional buckling needs to be considered, which can be visualised as a combination of the minor axis flexural and torsional buckling modes, since it involves flexural buckling with deflection out of the plane combined with twist about the shear centre of the cross-section.

Members can be restrained against global buckling by the use of bracing. In composite construction, floor sheeting such as trapezoidal or re-entrant decks attached to the main structural horizontal members, provide restraint against lateral-torsional buckling (Davison & Owens 2012). In wall stud frame construction, horizontal bracing members are employed in restraining the columns against flexural and flexural torsional buckling (Way & Heywood 2012). One of the main objectives of this study is to quantify the benefits of the bracing effect offered by the sheathing.

2.2.4 Geometric imperfections

Structural steel members inherently possess out-of-straightness deviations along their length, such as bowing and twisting (global imperfections), while their plate surfaces are also imperfect because of local deviations and undulations (cross-sectional imperfections). Imperfections can arise during manufacture, transportation, storing and construction. Due to the unpredictability of circumstances occurring during the latter three phases, only the imperfections that arise during manufacturing are accounted for in design.

Geometric imperfections are highly critical to the capacity and post-buckling behaviour of cold-formed steel structures; therefore it is necessary to consider the magnitude and distribution of these imperfections. It is generally accepted that imperfections are subdivided

into cross-sectional and global imperfections (Zeinoddini & Schafer 2012).

2.2.4.1 Initial studies

The adverse effect of taking into consideration an imperfect plate by assuming small initial curvatures was the focus of early studies such as those conducted by Yamaki (1960) and Timoshenko & Gere (1961). Yamaki (1960) investigated the postbuckling behaviour of plates with initial curvature and loaded along the edge in compression, while Timoshenko & Gere (1961) used classical solutions with double Fourier Series to approximate the deflected shapes and capacities of plates under various load cases. Since the 1970s several researchers attempted to measure geometric imperfections of cold-formed steel sections. These studies concentrated on determining the shapes and amplitudes of the various imperfections present, like Dawson & Walker (1972) who studied simply supported cold-formed steel plates and reported expressions of imperfection amplitudes in terms of the thickness of the plate, and Dat & Peköz (1980) who reported imperfection amplitudes and examined their influence on the ultimate strength of cold-formed steel columns.

2.2.4.2 Categorising imperfections and imperfection amplitudes

The magnitude of cross-sectional imperfections is most commonly described as a percentage of the thickness of the steel section, while their shape is typically described by the local and distortional buckling modes - see Section 2.2.3. Such characterisation of initial geometric cross-sectional imperfections has been adopted in studies by Chou et al. (2000), Gardner & Nethercot (2004*a*), Camotim et al. (2005), Ashraf et al. (2006), Dinis et al. (2007), Schafer et al. (2010) and Pham & Hancock (2010).

Schafer & Peköz (1998*a*), based on measurements of maximum geometric imperfections from previous research done by Ingvarsson (1977), Thomasson (1978), Dat & Peköz (1980), Mulligan & Peköz (1984), Lau (1988), Kwon & Hancock (1992) and Bernard (1993), established simple rules of thumb for quantifying cross-sectional imperfections. The measured imperfections were classified into two categories: (i) type 1, defined as the maximum local

imperfection (δ_L) in a stiffened element and (ii) type 2, defined as the maximum deviation (δ_D) from straightness of a flange (with or without a lip stiffener) susceptible to distortional buckling. Both types of imperfections are illustrated in Figures 2.6 and 2.7 for a typical C-lipped section under axial compression, when the flanges are buckled inwards and outwards respectively. According to the simple rules established by Schafer & Peköz (1998*a*), the maximum local imperfection is defined as $\delta_L \approx 6te^{-2t}$ and is applicable to stiffened elements with a width to thickness ratio less than 200 while the maximum distortional imperfection is defined as $\delta_D \approx t$ and is applicable to elements with a width to thickness ratio less than 100, where t is the thickness of the plate and is assumed to be always less than 3 mm thick.

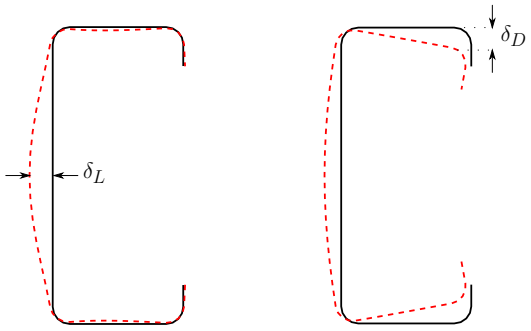


Figure 2.6: Local (δ_L) and distortional (δ_D) imperfections with flanges buckling inwards

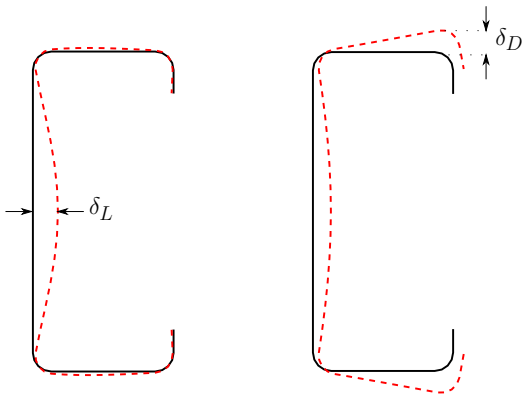


Figure 2.7: Local (δ_L) and distortional (δ_D) imperfections with flanges buckling outwards

A summary of reported measured amplitude imperfections is provided by Zeinoddini & Schafer (2012); the mean values of imperfections as well as the percentiles of probabilities of exceedance are reported in Table 2.1. The amplitudes for the local δ_L and distortional δ_D imperfections are given as a function of the plate thickness t, while the global amplitudes for

minor axis flexural $\delta_{G,min}$ and major axis flexural $\delta_{G,maj}$ buckling imperfections are given in terms of the length of the member L. Finally, the imperfection amplitudes corresponding to twist $\theta_{G,tor}$ are typically expressed in terms of degrees per metre. The summary of Zeinoddini & Schafer (2012) was compiled based on the collected dataset from the researchers previously mentioned in the studies by Schafer & Peköz (1998*a*) as well as measurements by Young (1997), Shifferaw et al. (2010), Zeinoddini & Schafer (2011) and Peterman (2012).

Table 2.1: Imperfection amplitudes provided by Zeinoddini & Schafer (2012)

	Local	Distortional	Flexural minor	Flexural major	Twist
	δ_L/t	δ_D/t	$L/\delta_{G,min}$	$L/\delta_{G,maj}$	$\theta_{G,tor}$ (deg/m)
Mean	0.47	1.03	2242	3477	0.36
COV	1.32	0.94	1.36	1.63	0.64
25%ile	0.17	0.43	4755	6295	0.20
50%ile	0.31	0.75	2909	4010	0.30
75%ile	0.54	1.14	1659	2887	0.49
95%ile	1.02	3.06	845	1472	0.85
99%ile	3.87	4.46	753	1215	0.95

A set of expressions for the prediction of imperfection magnitudes is provided in the studies by Selvaraj & Madhavan (2018*a*) where the results from Mulligan & Peköz (1984), Young (1997), Schafer & Peköz (1998*a*), Zeinoddini & Schafer (2011) and Peterman (2012) were analysed along with a set of new geometric imperfection measurements undertaken on lipped channel sections using a 3D non-contact laser scanner.

2.2.4.3 Simulating imperfections

It is recognised that the strength and post-buckling behaviour of cold-formed steel members is highly influenced by imperfections, typically having the shape of the most fundamental eigenmode determined by an elastic buckling analysis (Schafer & Peköz 1998*a*). Therefore, the most common way of replicating geometric imperfections prior to the start of a numerical simulation is to carry out an elastic buckling analysis for the determination of

the fundamental eigenmode shape, which is then introduced as initial imperfections of the modelled member (Moreyra & Peköz 1994). Modelling of imperfections by using the lowest eigenmode from an eigenvalue buckling analysis has been shown by Bonada et al. (2012) and Sadovskỳ et al. (2012) to be inadequate in capturing vigorously the local and distortional modes. The shapes of the lowest modes are often mixtures and not distinct shape forms of local and distortional modes, which, as a result, could lead to inappropriate shapes for initial imperfections and may provide conservative capacity estimates.

Isolating pure local and distortional buckling mode shapes can be made possible with the finite strip analysis CUFSM program (Li & Schafer 2010), offering an alternative way for modelling imperfections. Numerous researchers, such as Haidarali (2011), Hui (2014), Kyvelou (2017) and Hadjipantelis et al. (2019) have successfully used the CUFSM software to determine and impose imperfections to the member prior to a finite element analysis. Therefore, the simulation of imperfections for this study has been implemented using the CUFSM software, with post-processing of the results in MATLAB to create input files of imperfect geometries for use in the finite element analyses.

Signature curves, such as the one shown in Figure 2.8, can be readily produced using CUFSM (Li & Schafer 2010). In Figure 2.8, the critical load factors (plotted on the vertical axis as P_{cr}/P_y where P_{cr} is the critical load and P_y is the yield strength multiplied by the gross area of the cross-section) and corresponding half-wavelengths for the fundamental buckling modes, are identified by the minima points of the signature curve. Typical minima indications for local, distortional, torsional-flexural and minor axis flexural buckling of a C-lipped section under pure compression are provided in Figure 2.8.

In numerical simulations of elements with imperfections modelled as a combination of local and distortional modes, as demonstrated by Dinis et al. (2007), the collapse mechanism and load-bearing capacity is affected by the shape of the imperfections of the flange plates (i.e. inward or outward deformation) at the critical region of the member. Numerical sensitivity case studies on flexural cold-formed steel members performed by Hui (2014) demonstrated that the most critical scenario (i.e. lower ultimate capacity) arises when both local and distorional modes are superimposed, with both flange imperfections facing

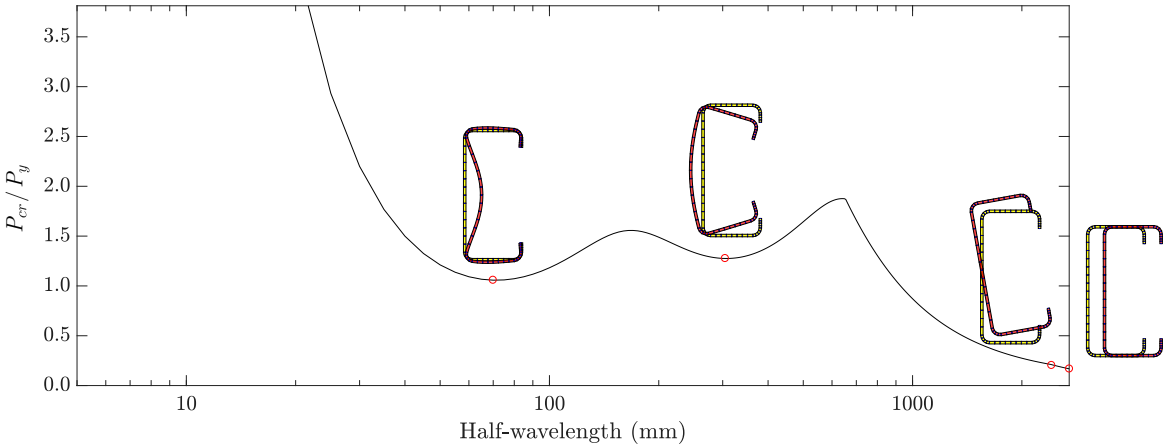


Figure 2.8: Signature curve and deformed shapes using CUFSM (Li & Schafer 2010)

inwards at mid-length of the member - see Figure 2.6. Global imperfections of flexural and torsional buckling modes are particularly influential to the mode of failure for members in compression. The global imperfection shapes are described using single half-sine for the flexural mode and full cosine functions for the torsional buckling mode, as recommended by Zhao (2016) and adopted by Vieira & Schafer (2016) and Kechidi et al. (2017).

2.3 Sheathed wall stud systems

Cold-formed steel lipped channel vertical members (studs) set in tracks and sheathed with wood-based boards or gypsum plasterboards are frequently employed in the construction industry, both as non-structural and load-bearing wall stud systems, offering practicality, economy and versatility. Load-bearing light-steel frames are becoming increasingly popular in buildings exceeding four storeys, with their use being further promoted by the recent emerging practice of lightweight modular construction (Lawson & Ogden 2008). When sheathed wall stud frames are used as load-bearing systems, additional cold-formed steel members are employed to provide lateral bracing, as illustrated in Figure 2.9 (a). Recognising the presence of sheathing is a practical way to increase the buckling resistance of the studs by taking into account the bracing effect arising as a result of the connection between the two components and the stabilising effect from the sheathing. Although several studies such as those by Vieira & Schafer (2013) and Peterman & Schafer (2014) have shown that

the attached sheathing (Figure 2.9 (b)) can provide sufficient bracing and result in improved axial and flexural capacities, current design guidances (EN 1993-1-3 2006, AISI S100 2016) remain conservative regarding the treatment of the attached sheathing. It should be noted that for buildings subjected to high repeated wind loads or dynamic effects the stabilising effect from sheathing should be justified by testing (Lawson et al. 2019), since the limitations from the interconnection between the cold-formed steel and the sheathing should be carefully considered for the bracing effect of the sheathing to be accounted for.

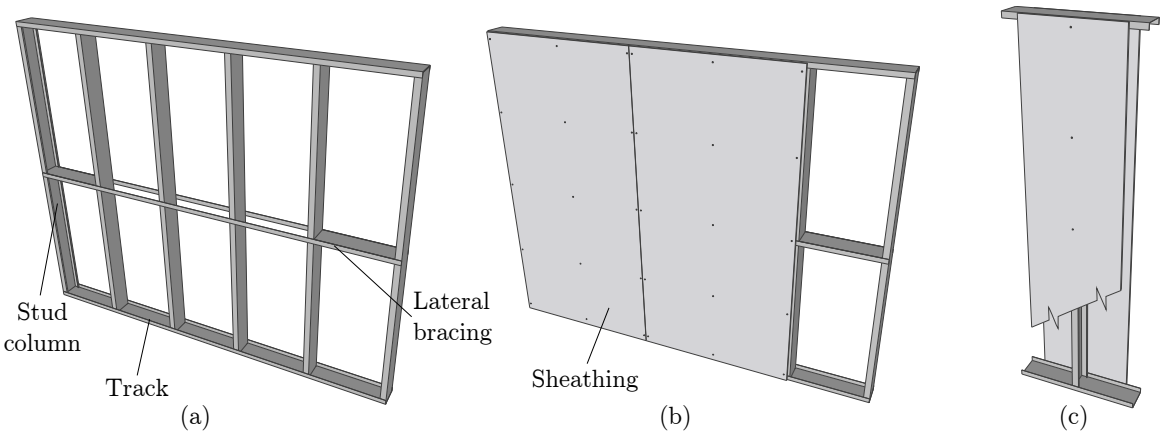


Figure 2.9: Illustrations of (a) stud wall with lateral bracing (b) stud wall with sheathing (c) single sheathed column

2.3.1 Sheathed studs under compression

It is well understood that column strength can be increased by bracing the member, and since sheathing is present in most load-bearing stud applications, it is logical to utilise its presence structurally (Green et al. 1947, Simaan & Peköz 1976, Miller & Peköz 1994, Lee & Miller 2001, Telue & Mahendran 2004, 2006, Tian et al. 2007, Vieira & Schafer 2013, Peterman & Schafer 2014, Fratamico & Schafer 2014, Kechidi et al. 2020, Lawson et al. 2019), and potentially eliminate the need for secondary steel bracing members. Although a series of investigations by Telue & Mahendran (2004, 2006), Tian et al. (2007), Miller & Peköz (1994), Lee & Miller (2001), Vieira & Schafer (2013), Fratamico & Schafer (2014) and Kechidi et al. (2020) have been conducted to examine the bracing effect of sheathing on the axial load-bearing capacity of cold-formed steel studs, research on the possibility of

achieving further performance gains by increasing the number of connectors between the columns and boards has been limited (Telue & Mahendran 2004, 2006, Tian et al. 2007).

Analytical work by Tian et al. (2007) on cold-formed steel studs under axial load, sheathed on one or both sides, indicated that no significant benefits can be achieved by decreasing the connector spacing from 600 mm to 300 mm or by using stronger sheathing material, while numerical investigations with plasterboard sheathing on one or both sides of the stud by Telue & Mahendran (2004) and Tian et al. (2007) indicated further enhancements in capacity could be achieved by decreasing the connector spacing to less than 300 mm.

It is well established, through theoretical and experimental work (Green et al. 1947, Simaan & Peköz 1976, Miller & Peköz 1994, Lee & Miller 2001, Tian et al. 2007), that the presence of sheathing can provide adequate restraint to an axially loaded cold-formed steel stud against minor axis flexural and flexural torsional buckling. It has been debated whether this restraining effect emerges from a local restraint at the point of connectors (Green et al. 1947, Miller & Peköz 1994) or due to global shear diaphragm behaviour (Simaan & Peköz 1976). Experimental and numerical studies by Miller & Peköz (1994), Lee & Miller (2001), Telue & Mahendran (2004) and Telue & Mahendran (2006) demonstrated that the load-bearing capacity of a stud wall system is insensitive to the spacing between the studs, contradicting the findings of Simaan & Peköz (1976), that the sheathing acts as a diaphragm. Furthermore, experimental studies on full stud-wall systems by Vieira et al. (2011) demonstrated that a single column experiment, as shown in Figure 2.9 (c), can accurately replicate the overall performance of a wall system comprising five studs. Through experimental and analytical work by Vieira & Schafer (2012) and Vieira et al. (2011), it was deduced that bracing from sheathing is derived from both local deformation and shear diaphragm effects and can be predicted using a model of springs in series with individual stiffness definitions for both phenomena. These stiffness definitions can be either determined from experiments (Peterman et al. 2014, Vieira 2011), using analytical models (Vieira & Schafer 2012, 2013) or numerical analysis (Vieira & Schafer 2016). In the studies by Lawson et al. (2019), a design formula for the effective minor axis slenderness of lipped channel

sections sheathed on one side was developed, based on experimental findings presented in the same study.

Reducing the connector spacing from 600 mm to 300 mm or having stronger sheathing material with one or both sides sheathed under axial load, was analytically shown to bring no significant benefits for cold-formed steel studs (Tian et al. 2007). Decreasing connector spacing on studs with plasterboard sheathing to less than 300 mm has been shown numerically (Telue & Mahendran 2004, 2006) to bring further enhancements in capacity. Nevertheless, previous numerical studies and analyses (Telue & Mahendran 2004, 2006, Tian et al. 2007) have been limited in scope, while provisions for considering the effect of sheathing with reduced effective length for flexural and torsional buckling were recommended. Numerical studies to date on sheathed wall studs (Telue & Mahendran 2004, 2006, Tian et al. 2007, Vieira & Schafer 2016) have utilised only elastic behaviour for the description of the sheathing material, while in studies by Kyvelou et al. (2018), flooring on steel joists was nonlinearly modelled with the results from the simulations accurately capturing the behaviour observed in physical experiments. Observed enhancements in load-bearing capacity with decreasing connector spacing between the sheathing and the steel (Telue & Mahendran 2004, Selvaraj & Madhavan 2018*b*, Peterman 2012) are believed to arise due to greater restraining effects and mobilisation of composite action between the two materials, when the system is primarily under bending.

2.3.2 Sheathed studs under combined compression and bending

Wall studs under combined compression and major axis bending, which can be the result of gravity and wind actions, have been the subject of a limited number of studies. Work on the beneficial influence of sheathing on stud columns under combined compression and major axis bending has been presented by Peterman & Schafer (2014), while studying sheathed specimens under pure bending was the focus of the research by Selvaraj & Madhavan (2019*a*, 2018*b*).

Experimental work on load-bearing cold-formed steel stud columns braced only by sheathing, under compression and out-of-plane mid-height load resulting in major axis bend-

ing was performed by Peterman (2012) and Peterman & Schafer (2014). The tested specimens were single-sided OSB sheathed studs and doubly-sided sheathed studs with OSB and gypsum boards under various combinations of compression and bending, loaded until failure; the capacities of the sheathed specimens were benchmarked against results from bare steel studs. Significant increases in load-carrying capacity were achieved when sheathing was added, as shown in Figure 2.10 (Peterman 2012, Peterman & Schafer 2014).

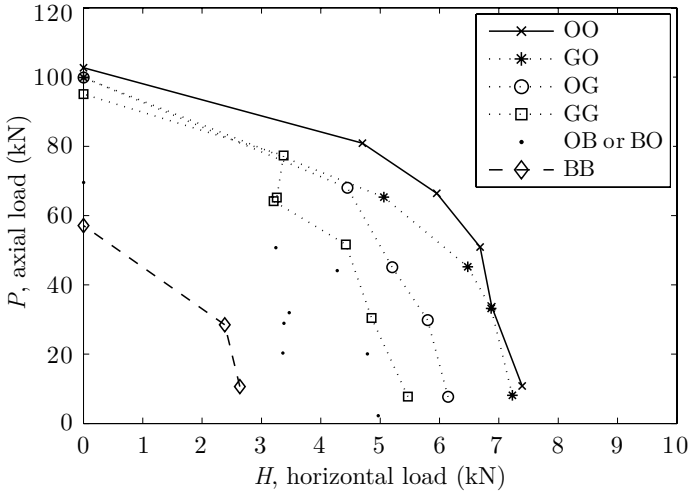


Figure 2.10: Observed axial and horizontal failure loads of the same size stud of length 2.4 m, set in track, with various sheathing configurations on the two stud flanges (B=bare, O=OSB, G=gypsum). From Peterman & Schafer (2014).

Building on the work of Vieira & Schafer (2013), design proposals for sheathed studs under compression and major axis bending were presented by Peterman & Schafer (2014), with the restraining effect of the sheathing being accounted for through the use of linear springs in an elastic buckling analysis, where the critical buckling loads are determined and subsequently used in the direct strength method (Schafer 2008). It is noted by Peterman (2012) that significant advancements are still possible, since many capacities determined by tests exceeded design predictions. It is worth noting that these design assumptions have only been based on a limited number of tests, considering only one size of member section, a standard connector spacing of 300 mm and no consideration of composite action.

When sheathed cold-formed steel members are subjected to compression, bending or a combination of the two, the forces that develop along the interface between the steel and the sheathing can cause excessive separation (pull-through failure) or slip (tilting-bearing

failure) between the two elements, if the strength and stiffness of the connection is not sufficient. Selvaraj & Madhavan (2019*a*, 2018*b*) tested plasterboard sheathed C shaped members (with no lip) under pure bending indicating pull-through and bearing connector failure for specimens screw connected at a spacing of 300 mm and 150 mm, while observing significant improvements in capacity, in excess of 80% when compared to the equivalent bare steel members. A combination of pull-through and bearing failures for connections in assemblies with plasterboard and cold-formed steel were reported by Selvaraj & Madhavan (2019*c*,*d*). Although screw and sheathing manufacturers tend to report characteristic pull-through capacities, experimental data on screws failing purely by pull-through are very limited.

2.3.3 Studies on components of wall stud systems

Experimental studies into the stress-strain response of cold-formed steel, which is typically more rounded than that of conventional hot-rolled steel due to the influence of the cold-forming process, have been widely reported in the literature (Gardner & Yun 2018, Kyvelou et al. 2017*b*, Vieira et al. 2011). Studies into the stress-strain response of sheathing material are, however, more scarce. A detailed experimental study into the mechanical properties of various types of plasterboard was reported by Petrone et al. (2016), while further test results were presented by Selvaraj & Madhavan (2019*b*). Similarly, results of tensile and compressive tests on OSB were presented by Chen & He (2017) and Plenzler et al. (2017), while Zhu et al. (2005) reported key properties from tests on OSB along with an empirical deduced material model for use in numerical simulations.

The nonlinear interaction between the board and the column in cold-formed steel wall systems, as well as the failure mode of the connectors, are dependent on the arrangement, type and material characteristics of the various system components. Past studies (Miller & Peköz 1994, Lange & Naujoks 2006, Serrette et al. 1997, Fülöp & Dubina 2004, Swensen et al. 2015) have focused primarily on the shear characteristics of the interface owing to its importance when the studied wall systems are designed to act as diaphragms. Individual shear connection tests, featuring OSB and plasterboard as the sheathing, and a range of

steel thicknesses and screw connector sizes, were reported by Serrette et al. (1997), Peterman et al. (2014), Fiorino et al. (2017, 2007), Vieira & Schafer (2009), Chen et al. (2016), Ye et al. (2016). Experimental studies into the shear response of sheathing-to-cold-formed steel connections have also been conducted for various other types of board material, including cement based boards (Fiorino et al. 2017, Abu-Hamd 2019), calcium silicate boards (Nithyadharan & Kalyanaraman 2011, Ye et al. 2016), fibre cement boards (Shahi et al. 2013) and Bolivian manganese boards (Ye et al. 2016).

The tests carried by Peterman et al. (2014) and Peterman & Schafer (2013) included both monotonic and cyclic loading schemes, with the aim to characterise the monotonic and hysteretic behaviour of the connection between cold-formed steel studs and sheathing when subjected to in-plane lateral shear demands, as part of an effort to advance seismic performance-based design of cold-formed steel frames. The specimens were composed of two channel lipped sections with their flanges facing each other and connected on both sides with sheathing. The studied parameters included three different thicknesses for the cold-formed steel members, and plasterboard and OSB sheathing connected to the steel members with 3.5 mm and 4.8 mm in diameter screws respectively. The backbone curves from the cyclic tests compared similarly with the respective monotonic load-slip curves, with slightly reduced strengths (about 10% - 20%) but higher initial stiffnesses observed (more than 20% increase). The specimens connected to the plasterboard failed primarily by tilting-bearing while the specimens connected to OSB failed by pull-through and bending of the screw. Higher scatter of results was also observed for the specimens connected to plasterboard.

In a set of experimental studies, the load-deformation characteristics of lapped connections between cold-formed steel members were examined by Ho & Chung (2006), where an empirical formula was developed describing the observed behaviour. Monotonic and cyclic shear tests on cold-formed steel plates connected with screws were performed by Moen et al. (2016, 2014) in order to investigate whether the effect of cyclic loading on the strength and stiffness of the connection is detrimental. The difference between the backbone profiles from the cyclic and monotonic tests was deemed not significant, with strength reduction found to be negligible, while some increased stiffness was demonstrated due to the screw threads

locking into the connected members.

2.4 Existing design methods

The two main methods, currently, formally available in designing cold-formed steel members are the effective width method (EWM) and the direct strength method (DSM). The effective width method is available, in some form, worldwide, including the European Eurocode 3 (EN 1993-1-3 2006) and the North American AISI (AISI S100 2016) standards, while the DSM has been adopted for use as a second designing option (Schafer 2008) in North America (AISI S100 2016) and Australia/New Zealand (AS/NZS 4600 2018).

2.4.1 Effective width method (EWM)

The effective width concept was originally conceived by Von Kármán (1932) and was later developed by Winter (1947). The main idea is that local buckling of slender plate elements under compression leads to a reduction of their effectiveness to carry load. When under compression, local instabilities are expected to be triggered in the central regions of slender plate elements with simply supported edges, away from corners and stiffeners, and as such, these central excess regions are ignored in the calculation of effective width properties - see Figure 2.11, where b is the actual width of the plate, b_{eff} is the effective width of the plate and f_y is the yield strength of the material. The effective width method conceptualises the entire cross-section as a collection of plated elements with simply supported edges and thus requires the determination of the effective width of each element, with a clear indication of where the cross-section is ineffective in carrying load due to local buckling. The resulting reduced cross-section properties are known as the effective local cross-sectional properties.

In design codes such as Eurocode 3 (EN 1993-1-3 2006), further reductions of the cross-sectional properties of a member may be realised due to distortional buckling, which is accounted for through an effective thickness approach. For C-shaped lipped sections, this thickness reduction is performed in the stiffener region, where distortional instabilities develop. Details of the effective width calculation approach for accounting for the effects from

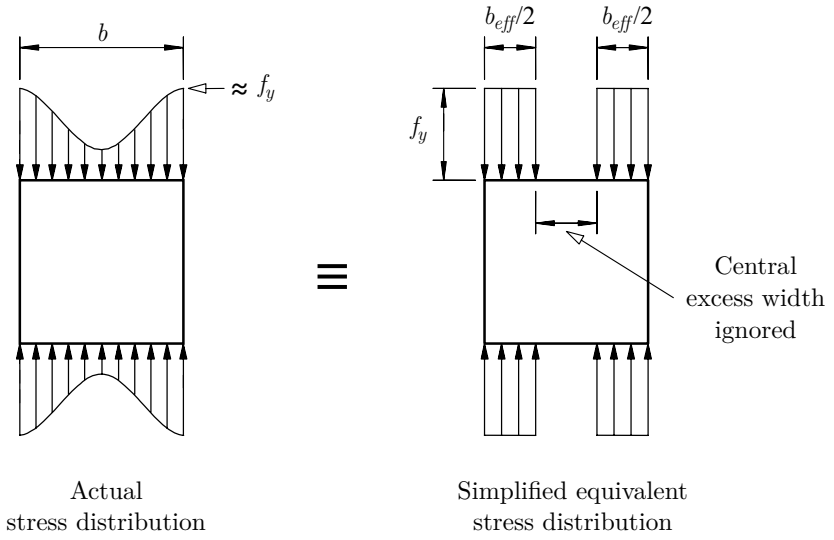


Figure 2.11: The effective width concept applied to a plate. Adapted from Trahair et al. (2008)

local and distortional buckling in accordance with the EN 1993-1-3 (2006) guidance are provided in Chapter 7.

2.4.2 Direct strength method (DSM)

North American design specifications in the 1990s for cold-formed steel columns (AISI 1996) failed to recognise the local-global buckling interaction and did not provide an explicit check for distortional buckling. To recognise the effects of distortional buckling on cold-formed steel cross-sections, Hancock et al. (1994) proposed a set of strength design curves for members experiencing distortional buckling. The concept of this 'direct' approach was later introduced by Schafer & Peköz (1998*b*) as a new method, where the strength curves were calibrated against a collection of test data, and the determination of the elastic buckling strength of cold-formed steel members can be predicted using computational elastic buckling analysis methods. In the work of Schafer (2002), a set of direct strength column curves, which had been calibrated against experimental data, were proposed for the prediction of local and distortional buckling of cold-formed steel columns members. In the studies by Yu & Schafer (2003) and Yu & Schafer (2006), a series of flexural tests were reported and distortional buckling was shown to be a predominant failure mode. This work led to the development of the method known as the Direct Strength method (Schafer 2008), which is

an alternative to the traditional effective width concept. The direct strength method has been incorporated in the North American Specifications as an Appendix I since 2004 and joined the main body as an equal alternative to the effective width method since 2016 (AISI S100 2016).

The direct strength method is fundamentally different from the effective width method. While the effective width method uses reduced effective cross-section properties along with the yield strength to calculate capacities, for the calculation of capacities with DSM, the gross cross-section properties are used in conjunction with a 'direct' reduced strength, based on the elastic stability of the gross cross-section (Schafer 2008). The elastic instabilities of the gross cross-section, under compression or bending may be identified using numerical elastic buckling solvers such as the finite strip method CUFSM (Li & Schafer 2010). Once these critical loads of local, distortional or global instabilities are determined through elastic buckling analysis, they are then fitted in empirical 'direct' expressions to predict the member strength. These expressions are collectively known as the Direct Strength method and are reported in detail by Schafer (2008) for members in pure compression and bending.

2.4.2.1 DSM calculation procedure

In accordance with the DSM, for members subjected to compression, the nominal strength P_n is determined by taking the minimum of the global buckling strength P_{ne}, local-global buckling interaction P_{nl} and distortional buckling P_{nd}, i.e. $P_n = \min(P_{ne}, P_{nl}, P_{nd})$. The expressions for P_{ne}, P_{nl} and P_{nd} are empirical formulas (Schafer 2008), with the input parameters being: the tensile yield capacity of the member P_y (calculated by multiplying the gross area of the cross-section with the yield strength) and the critical loads for global P_{cre}, local P_{crl} and distortional P_{crd} elastic buckling determined using a rational analysis. An elastic buckling analysis using a software such as CUFSM (Li & Schafer 2010) provides a signature curve where the relevant critical local P_{crl} and distortional P_{crd} loads are determined as the minima, points on the curve while the global critical load P_{cre} is taken as the value corresponding to a length equal to that of the member as shown in Figure 2.8. Note that for cases where the distortional mode does not correspond to a minimum point on

the signature curve, modal decomposition using the constrained finite method cFSM (Li & Schafer 2010) can be used for determining the critical wavelength and, as such, the critical distortional load on the signature curve.

Similarly, in accordance with the DSM, for members in bending the nominal bending strength M_n is determined using $M_n = \min(M_{ne}, M_{nl}, M_{nd})$. The respective global M_{ne}, local M_{nl} and distortional M_{nd} buckling strengths are calculated using the DSM expressions (Schafer 2008) with the input parameters being: the yield moment M_y (calculated by multiplying the elastic section modulus of the cross-section with the yield strength) and the critical elastic buckling moments for global M_{cre}, local M_{crl} and distortional M_{crd} buckling, determined by an elastic buckling analysis.

2.4.2.2 Beam-column interaction

For a member under a compression-moment ($P - M$) interaction, current design guidance in AISI S100 (2016) assumes a simple linear $P-M$ interaction as indicated by Equation (2.5), where P and M are the axial compression and bending moment in the member respectively.

$$\frac{P}{P_n} + \frac{M}{M_n} \leq 1 \tag{2.5}$$

In recent studies by Torabian & Schafer (2018) on members subjected to combined compression and bending, it has been observed that the current approach for the design of beam-column cold-formed steel members is overly conservative due to the assumption of a linear interaction relationship, since the stability of the member under the actual stress distribution arising due to combined actions is not considered directly. Numerical (Torabian & Schafer 2018) and experimental (Torabian et al. 2015) studies were performed to study the effects of combined loading on members of different cross-sections; this led to a proposed extension of the current DSM provisions (Torabian & Schafer 2018), which accounts for the potential gains in capacity when the actual stress distribution is considered.

The actual stress distributions arising from both compression and bending are utilised in a buckling analysis to determine the critical buckling parameters. The difference, and

potential gains from the new DSM method, between the nominal strengths achieved assuming a linear interaction and the actual stress distributions are illustrated in the dark grey areas of Figure 2.12 for a channel lipped cross-section. Note that the interaction obtained is cross-section specific and varies in the $P - M_1 - M_2$ space, where P is the axial load, while M_1 and M_2 are the bending moments about the major and minor axis respectively.

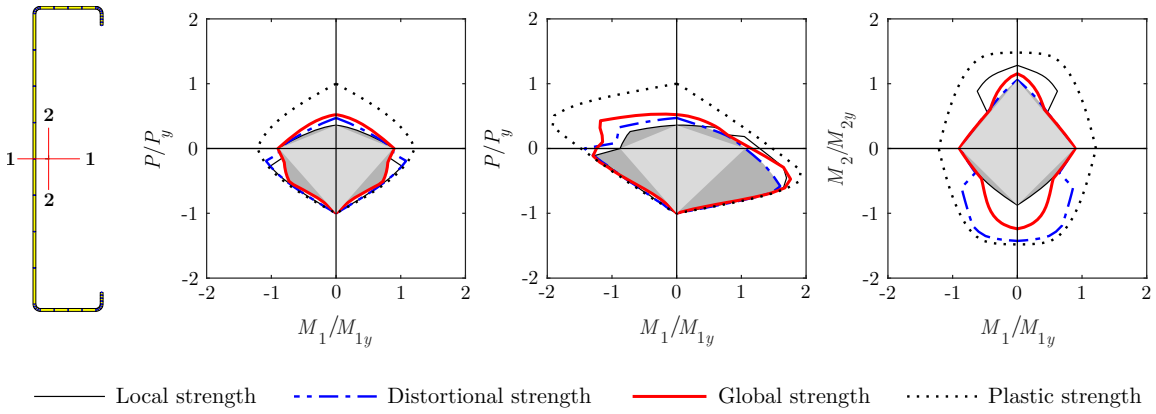


Figure 2.12: Comparison between the current DSM linear interaction equations (with light grey) and the difference with the proposed beam-column interaction DSM for a single symmetric channel lipped section which is indicated with dark grey; from Torabian & Schafer (2018)

As reported by Torabian & Schafer (2018), the new DSM provisions accounting for combined stress contributions in the buckling analysis provide more representative predictions of capacities and eliminate the conservatism of the linear interaction. It should be noted though that considering combined stress distributions and carrying elastic buckling analysis at several stages of the combined loading scheme to achieve a representative $P - M$ profile can be a complex process for use in design, compared to the simplicity of an interaction curve where only strengths at the two ends (under pure compression and pure bending) are required.

Note that the current EN 1993-1-3 (2006) guidance is even more conservative than a linear relationship between compression and bending, since a concave profile (achieved with 0.8 power coefficients) of the beam-column interaction is provided for the design of cold-formed steel members under combined loading. For members which are sheathed and adequate bracing is provided, a linear, but even more so a concave, $P-M$ interaction profile is overly conservative, as shown by the test results of Peterman & Schafer (2014), which

demonstrated a convex profile - see Figure 2.10. Further discussion and assessment of the current EN 1993-1-3 (2006) guidance is provided in Chapter 7.

2.4.3 Comparisons between the EWM and the DSM

The effective width method and direct strength method are fundamentally different and although both have their merits, it is sometimes more efficient to use one over the other. Because of the way the effective width method is conceptualised, there is a clear indication of where local buckling takes place (Trahair et al. 2008). It has been a long established method and reliable in predicting local buckling behaviour of members. For simple shaped members, such as C-shaped or Z-shaped members the process of calculating properties under pure compression or pure bending is relatively straightforward (Way & Heywood 2012). However, for cross-sections with stiffeners and of complex geometries, the method can be involved and cumbersome, as well as the interaction and compatibility between the elements not recognised. Stiffeners are usually accounted for in design using effective 'springs'. Also, calculating effective properties under combined stress distributions, although possible, can be very complicated. Treatment of distortional buckling through the concept of effective thickness is a lengthy and iterative process and is preferably performed through the use of a coded 'loop' solver.

The clear advantage of the direct strength method is that the cross-section is considered as a whole and any interaction between elements is ensured (Schafer 2008), while the required calculations are simple to perform for any cross-sectional shape, since the gross sectional properties are used and therefore no shift of the neutral axis occurs. However, advanced elastic buckling analysis through computational solvers is required for calculating the elastic buckling critical loads; engines such as CUFSM (Li & Schafer 2010) are readily available, although care should be taken when deciding on the mesh of the system and the input parameters, such as stresses and boundary conditions. The DSM, although relatively new in comparison with the effective width method, has been demonstrated to be reliable and as accurate, if not more, than the effective width method; comparisons between the two methods can be found in the works of Schafer (2008), Yu & LaBoube (2010) and Cam-

otim et al. (2016). The DSM has been calibrated against test data and allows for further extensions, as recent developments have been made to include members with holes in their cross-sections (Moen & Schafer 2009), built-up members (Kechidi et al. 2020, Fratamico et al. 2018), members at elevated temperatures, as well as other materials such as stainless steel, hot-rolled steel, aluminium and plastics (Camotim et al. 2016).

2.4.4 Considering sheathing into the design of wall studs

In 1947, Green et al. (1947) and Winter (1952, 1960) developed a method, which was later incorporated in the North American specifications (AISI 1962), that acknowledged that sheathing, through its restraining effect, can act as bracing to stud columns under compression. This method became known as the 'local stiffness' approach and features two key assumptions: (i) the fasteners connecting the sheathing to the stud provide a stabilising effect to the stud column in compression and can be simulated using a set of translational springs of stiffness k as shown in Figure 2.13, (ii) the stiffness k can be determined from small-scale sheathing-to-stud shear experiments. In accordance with this approach (AISI 1962), flexural buckling about the minor axis with the springs included had to be greater than or equal to the column squash load (failure in cross-sectional buckling), flexural buckling about the minor axis over an unbraced length (equal to twice that of connector spacing) had to be equal to or greater than the flexural strength about the main axis, and the connector fixings had to be designed for approximately 2% of the axial demand. No consideration was made for flexural-torsional buckling or distortional buckling, while some of the prerequisites were thought to be arbitrary (Vieira & Schafer 2013); as such the method was abandoned from the North American design guidance in 1980.

An alternative methodology to account for the bracing effect of sheathing on wall studs, developed by Simaan & Peköz (1976), was adopted in the North American design guidance in 1980 (AISI 1980) and was used until 2004. This method became known as the 'diaphragm stiffness' approach and it treated bracing provided by the sheathing and the connectors in a global manner. The local stiffnesses offered by the connectors were replaced with an experimental shear stiffness of a diaphragm in global behaviour. The buckling resistance

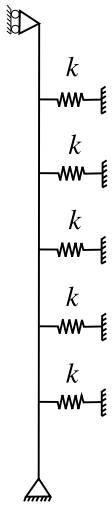


Figure 2.13: Local stiffness approach by Green et al. (1947), Winter (1952, 1960). Adapted from Vieira & Schafer (2013).

of the sheathed studs was calculated based on the energy dissipated as the studs deformed with in-plane shear deformation of the assumed diaphragm (Vieira & Schafer 2013). The method considered flexural-torsional buckling and theoretically could account for dissimilar sheathing, though this was not adopted by AISI (1980). The method also included a distinct check for the shear strain of the sheathing, although critical failures were known to be at the locations of connectors and did not correspond to material failure of the sheathing. As commented by Vieira & Schafer (2013), this method was complex, resulted to a non-efficient design of stud spacings for wall stud frames and test results by Miller & Peköz (1993) did not agree well with the method.

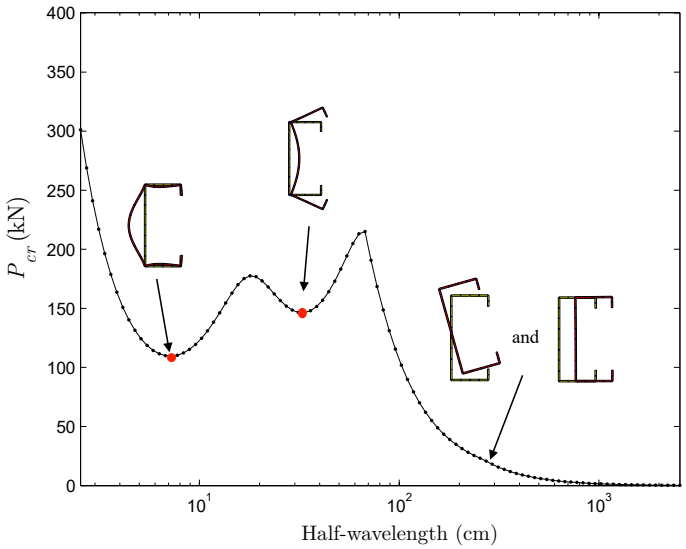
Current North American specifications AISI S100 (2016), since 2004, have adopted a method similar to the original 'local stiffness' approach, without the need to characterise bracing stiffness. The stud is required to be checked for all global buckling modes, including that of flexural-torsional buckling for an unbraced length equal to that of two times the spacing of the connectors, as well as checking the fastener capacities for 2% of the axial demand. As commented by Vieira & Schafer (2013), this method is extremely simple and ignores the effect of stiffness of the sheathing-to-steel connection on the stability of the member, as well as not distinguishing between different types of connector, sheathing and stud spacing.

Recent analytical (Vieira & Schafer 2013) and experimental (Vieira & Schafer 2012, Vieira et al. 2011) work on sheathed wall studs under pure compression, has demonstrated that restraint from sheathing is supplied to the stud from both local connector deformations and global shear diaphragm behaviour (which is dominated by the shear modulus of the sheathing material). Incorporation of these effects into an elastic buckling analysis and subsequent use of the direct strength method can result in accurate capacity predictions (Schafer 2013). Analytical formulae for determining appropriate stiffnesses for use in CUFSM (Li & Schafer 2010) have been developed by Vieira & Schafer (2013, 2012) while stiffnesses derived directly from tests were reported by Vieira (2011) and Peterman (2012). Implementation of this approach is illustrated in Figure 2.14, where significant improvements in capacity are observed for the global modes. An extension to this approach for wall studs under combined compression and bending was performed by Peterman & Schafer (2014). Assessment of these proposals is performed in Chapter 7, through comparisons against the full scale beam-column tests reported in Chapter 5.

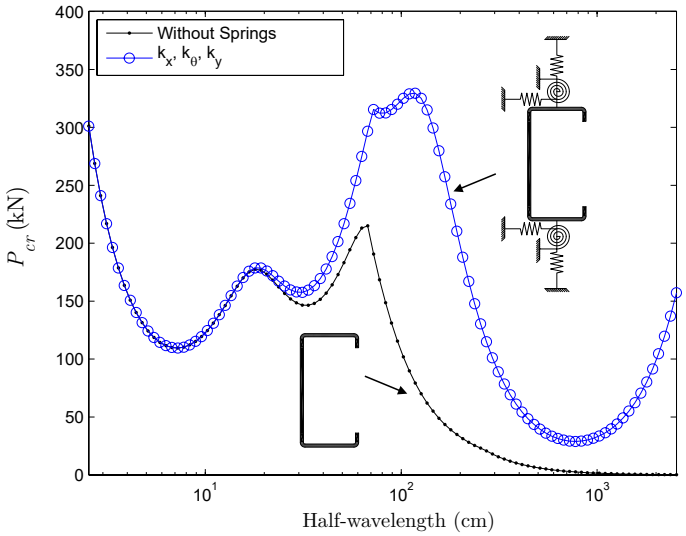
2.5 Concluding remarks

An overview of the relevant literature of the subjects that are investigated within this thesis has been provided in this chapter. The literature overview focused on three main areas, namely, research on cold-formed steel members, research on sheathed stud wall frames and, finally, technical background on the current design methodologies adopted for both cold-formed steel stud members and sheathed stud walls. Any further, appropriate literature is to be introduced and examined along with the relevant studies presented in each individual chapter.

In general, research on cold-formed steel is extensive and work on sheathed wall studs has mainly focused on specimens under pure compression. Although recommendations on ameliorating the design have been made by several researchers, it is evident that significant improvements can still be made, especially for sheathed members under combined loading. Therefore, it is the scope of the following chapters to explore the behaviour of sheathing-to-



(a) Buckling curve and modes of unrestrained members



(b) Comparison between restrained and unrestrained buckling curves

Figure 2.14: Illustrating the use of springs in elastic buckling analysis (CUFSM Li & Schafer (2010)) for determining enhanced capacities. From Vieira (2011).

column connections and the structural benefit of sheathing to stud wall systems experiencing combined compression and bending, and provide recommendations for a more efficient design approach than is currently available.

Chapter 3

Experimental study on components of sheathed cold-formed steel wall systems

3.1 Introduction

WALL systems built using cold-formed steel members and sheathed with boards such as plasterboard and orientated strand board (OSB), are commonplace in the construction industry and are being increasingly used as load bearing elements. Cold-formed steel frames have been employed successfully as an alternative to timber and masonry construction for low and medium rise buildings, principally due to their speed of construction, lightweight nature and sound structural performance. Whereas traditionally the contribution of the sheathing to the strength and stiffness of cold-formed steel columns and walls has been ignored, it has been shown by several researchers (Vieira & Schafer 2012, Peterman & Schafer 2014, Lawson et al. 2019) that sheathing can offer effective bracing to columns, provided a suitably strong and stiff inter-connection exists. Thus, it is recognised that a more efficient design can be achieved if the influence of the sheathing is taken into account. First though, a thorough understanding of the material behaviour of the individual components and of the interaction between them is required.

An experimental investigation into the material response of the different components used to form a typical sheathed cold-formed steel wall system, as well as the load-slip behaviour of the employed fasteners in pull-through and shear are presented herein. A total of 103 material and component tests was performed, including six cold-formed steel tensile coupon tests, nine tests on screws in tension, nine tests on screws in shear, 36 material tests on plasterboard and orientated strand board (OSB), 25 pull-through connection tests and 18 push-out (shear) connection tests. In Section 3.2, a description of the material and screw connector tests, along with the obtained results, is provided, while the results of the pull-through tests featuring various arrangements of plasterboards and OSB, are presented in Section 3.3. Push-out tests, examining the shear behaviour of cold-formed steel-to-sheathing connections are reported in Section 3.4. In Section 3.5, the results from corresponding material and connection tests reported in the literature are collected and compared to those obtained in the present study. In Chapter 4, the combined dataset is analysed and used to underpin the development of predictive models. The experimental studies on components of sheathed cold-formed steel wall systems presented in this chapter have been published by Kyprianou et al. (2021*a*).

3.2 Material and component testing

Material tests were carried out to determine the stress-strain behaviour of the cold-formed steel and sheathing material used in the pull-through and shear tests, while experiments to determine the ultimate load-carrying capacity of the employed screw connectors were also undertaken. Testing was carried out in the Structures Laboratory of Imperial College London under controlled temperature and humidity conditions, in the range of 20 - 24 °C and 30 - 50% respectively.

3.2.1 Cold-formed steel

Tensile coupon tests were conducted to determine the engineering stress-strain behaviour of the cold-formed steel material of grade S450 galvanised with Z275 zinc coating.

Four coupons were extracted longitudinally from the web of 150 mm deep lipped channel sections of 1.2 mm and 2.0 mm nominal thickness (two coupons for each thickness) while, for each thickness, one coupon was also extracted from the coil prior to section forming. The nominal dimensions of the tensile coupons are illustrated in Figure 3.1.

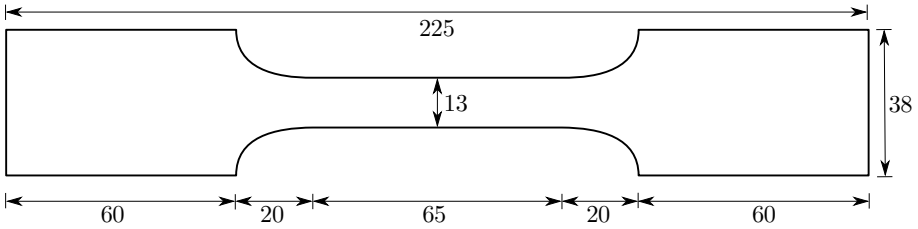


Figure 3.1: Nominal dimensions of steel tensile coupons (in mm)

3.2.1.1 Testing tensile cold-formed steel coupons

The tensile coupons were tested in accordance with EN ISO 6892 (2016) where an axial strain rate of 0.00007 s^{-1} was initially applied and gradually increased to 0.00025 s^{-1} after the 0.2% proof stress had been reached through three intermediate strain rate steps. A 150 kN Instron 5984 testing machine was used, along with the Bluehill data acquisition system, collecting data every second.

To capture the strains at the early stages of testing accurately, two strain gauges were mounted on each coupon (one per side). An optical video extensometer with a gauge length of 50 mm was also used as an additional method of capturing strain measurements. Illustrations of the strain gauges and the optical extensometer are shown in Figure 3.2.

3.2.1.2 Results of tensile cold-formed steel coupons

The key measured material properties of the tested coupons are presented in Table 3.1 while the full stress-strain curves are illustrated in Figure 3.3. The notation of the coupons begins with the letter C, followed by the nominal thickness of the material ($\times 10$) in mm and then, either the number of the test for the repeated tests or the word 'coil' for the samples taken from the coil. In Table 3.1, E is the Young's modulus, $\sigma_{0.2}$ is the 0.2% proof stress



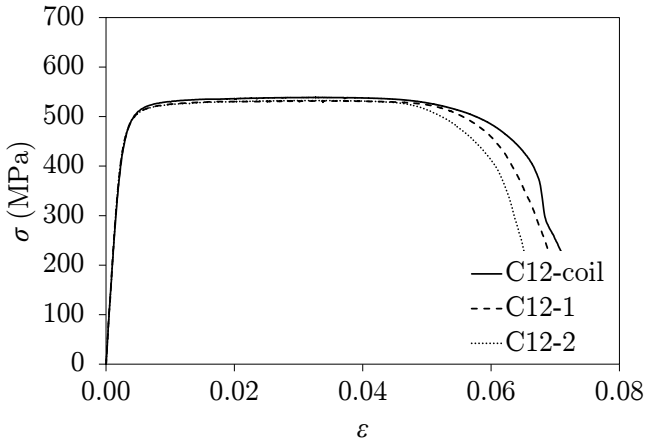
(a) Tensile coupon at point of failure (b) Optical extensometer reading during testing

Figure 3.2: Test setup for cold-formed steel tensile coupons

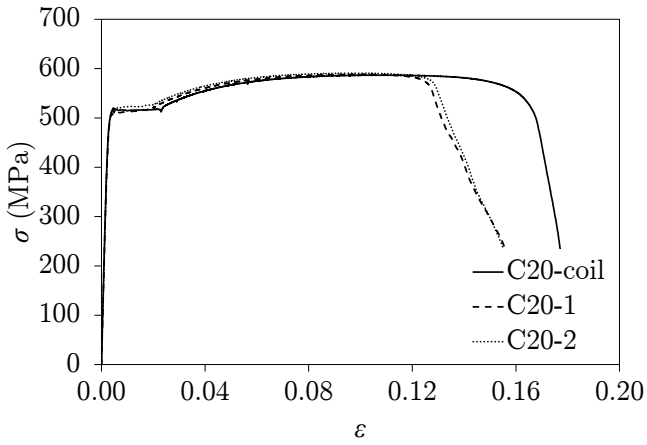
(considered as the yield strength), $\sigma_{1.0}$ is the 1% proof stress, σ_u is the ultimate strength, ε_{sh} is the strain at the end of the yield plateau, ε_u is the strain at σ_u, ε_f is the elongation at fracture measured over the standard gauge length (EN ISO 6892 2016). The average measured material properties and thickness t for the nominally 1.2 mm and 2.0 mm thick cold-formed steel coupons are presented in Table 3.2.

Table 3.1: Material properties obtained from tensile coupon tests on cold-formed steel

Coupon ID	E (GPa)	$\sigma_{0.2}$ (MPa)	$\sigma_{1.0}$ (MPa)	σ_u (MPa)	ε_{sh} (%)	ε_u (%)	ε_f (%)
C12-coil	207	502	533	539	-	3.25	7.31
C12-1	207	499	528	532	-	3.44	7.03
C12-2	205	500	527	532	-	3.28	6.56
C20-coil	210	519	516	589	2.05	10.5	17.9
C20-1	203	509	514	588	1.92	9.77	16.2
C20-2	205	518	523	591	1.71	9.75	16.0



(a) 1.2 mm thickness



(b) 2.0 mm thickness

Figure 3.3: Stress-strain curves of tensile coupons of (a) 1.2 mm and (b) 2.0 mm thickness

Table 3.2: Average material properties obtained from tensile coupon tests on cold-formed steel

t (mm)	E (GPa)	$\sigma_{0.2}$ (MPa)	$\sigma_{1.0}$ (MPa)	σ_u (MPa)	ε_{sh} (%)	ε_u (%)	ε_f (%)
1.19	206	500	529	534	-	3.32	6.97
1.99	206	515	518	589	1.89	10.0	16.7

3.2.2 Plasterboard

Material tests were performed on standard type gypsum-based plasterboard, designated as Type A in accordance with EN 520 (2009), of average measured thickness and density of 12.5 mm and 665 kg/m^3 respectively. A standard type A plasterboard is composed of a gypsum based core encased and bonded to durable paper on one face to which suitable

plastering and finishes may be applied, and to a much coarser and weaker paper lining on the other side which is not intended to carry any decoration. This type of board is typically used as sheathing for metal frame stud walls and ceilings.

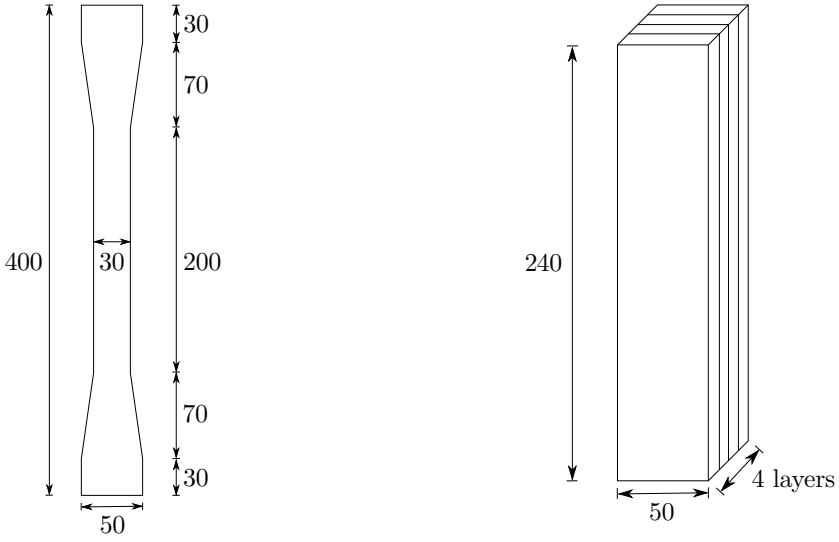
3.2.2.1 Tensile and compressive plasterboard tests

Tensile and compressive material tests were carried out to determine the stress-strain curves and key material properties of the examined plasterboard. The tests were performed in accordance with EN 789 (2005), which provides guidance on determining the mechanical properties of wood-based panels; this standard was used in preference to EN 520 (2009), which is a specification for gypsum plasterboard, since more extensive information on the determination of compressive and tensile properties is provided (Petrone et al. 2016). Tests were carried out on specimens loaded both longitudinally and transversely to the production direction of the board. Five tensile tests and four compressive tests were performed for each direction; 18 plasterboard material experiments were carried out in total.

The dimensions of the tensile and compressive coupons are shown in Figures 3.4 (a) and 3.4 (b) respectively. Each compressive coupon comprised four boards glued together using a spray adhesive which was non-absorbent and hence would not be expected to alter the mechanical properties of the plasterboard. For the tensile coupons, failure occurred within the parallel length - see Figure 3.5 (a). For the compressive coupons, load was introduced through a hemispherical bearing, seated on a steel plate, to achieve a uniform applied stress, as shown in Figure 3.5 (b). The coupons were tested under displacement control, at a rate of 0.25 mm/min, using a 150 kN Instron 5984 testing machine, while the Bluehill data acquisition system was used to record data every second.

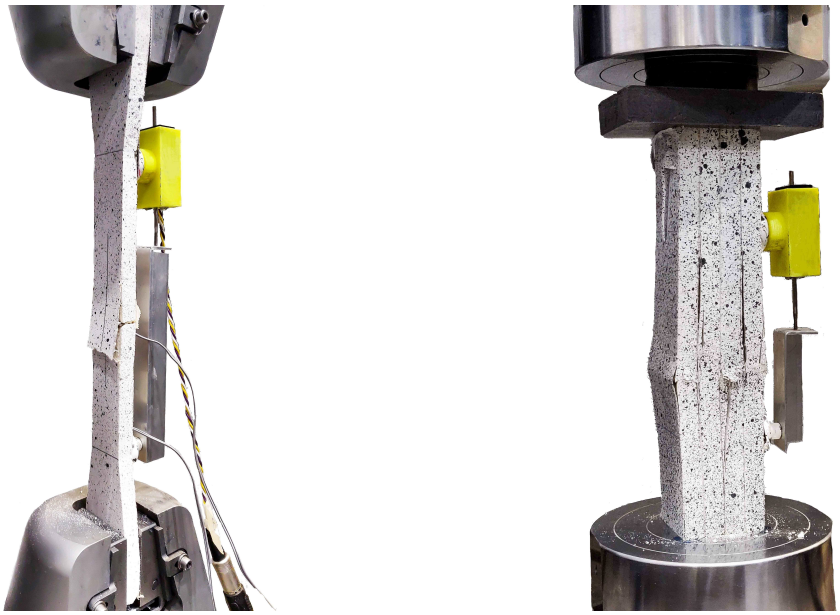
Although 50 mm long strain gauges, typically used for concrete samples, were initially considered, finally these were not used due to difficulties in attaching them to the plasterboard surface. Hence, for capturing accurately the overall strain field of the examined systems, digital image correlation (DIC) was employed. A speckle pattern was first applied to all specimens to allow the use of DIC. The non-contact optical DIC system was used with two cameras tracking the same speckled pattern from two different angles. The DaVis

(2019) software was employed to record and process the images captured at a frequency of 2 Hz. One linear variable displacement transducer (LVDT) was also mounted on the reverse side of each specimen, out of view of the DIC, as shown in Figure 3.5, providing a second method of measuring the overall deformation of the specimen. The LVDT measurements were recorded using the Bluehill data acquisition system at one second intervals.



(a) Dimensions of tensile coupons in mm (b) Dimensions of compressive coupons in mm

Figure 3.4: Dimensions of (a) tensile and (b) compressive plasterboard coupons



(a) Plasterboard tensile coupon test (b) Plasterboard compression coupon test

Figure 3.5: Test setup for (a) tensile and (b) compressive material tests on plasterboard

3.2.2.2 Results of material tests on plasterboard

Loading of all specimens was continued until failure could be clearly observed. The adopted notation for the tensile and compressive plasterboard coupons begins with PL, denoting plasterboard, following by the letter t for tension or c for compression, then the capital letter L or T to designate longitudinal or transverse respectively and, finally, the test number.

Failure of the tensile specimens was marked by a sharp decrease in load, together with the development of a distinct horizontal crack in both the internal gypsum and the outer paper surfaces, perpendicular to the direction of the applied load, as shown in Figures 3.5 (a) and 3.6 (b). The key measured properties of the plasterboard from the tensile tests - the Young's modulus in tension E, the ultimate tensile stress f_u and the corresponding strain ε_u are provided in Table 3.3. The stress-strain curves for the longitudinal and transverse tensile coupons, shown in Figure 3.7 (a) and (b) respectively, generally exhibit a rounded profile with no distinct yield point. Two transverse specimens, T1 and T3, displayed initial peaks before dropping to the rounded stress-strain responses exhibited by other specimens; this behaviour may relate to the weaker paper not failing until after the internal gypsum core had fractured or a delay in the fracture of the internal gypsum core. Note that these two sharp peaks were ignored when determining the ultimate tensile strength f_u, as indicated in Table 3.3.

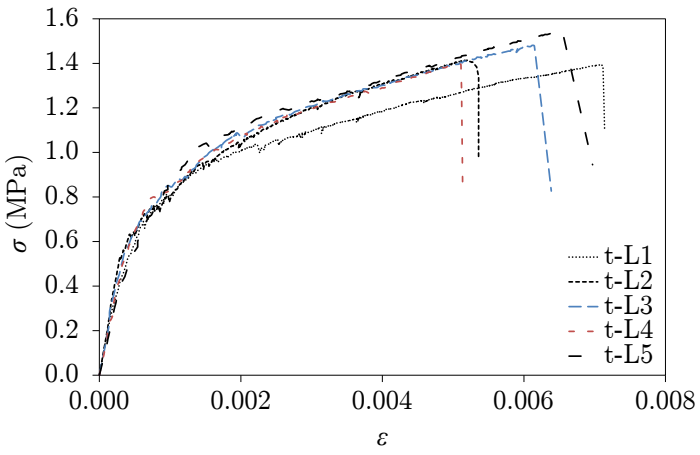


(a) Plasterboard tensile coupon before test

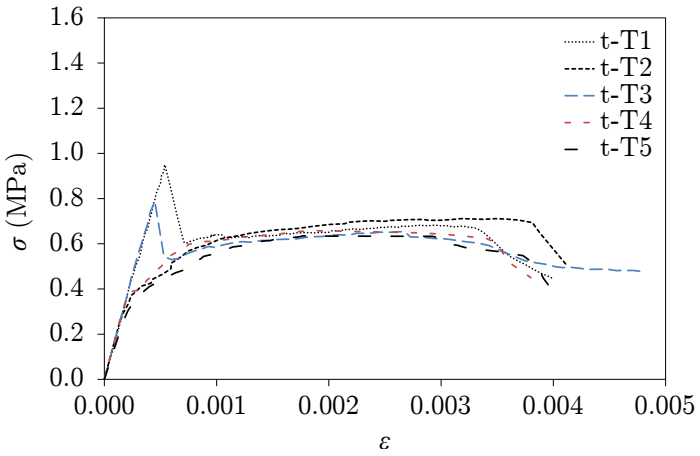


(b) Plasterboard tensile coupon after test

Figure 3.6: Typical plasterboard tensile coupon (a) before and (b) after test



(a) Longitudinal



(b) Transverse

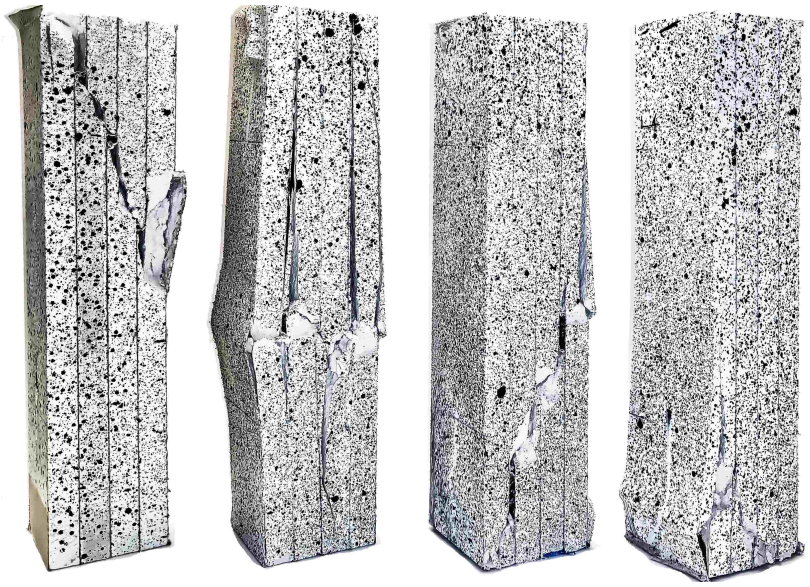
Figure 3.7: Stress-strain curves obtained from plasterboard tensile coupon tests in (a) the longitudinal and (b) the transverse directions

Table 3.3: Key tensile material properties from plasterboard coupon tests

Loading direction	Specimen	E (MPa)	f_u (MPa)	ε_u (%)
Longitudinal	PL-t-L1	1580	1.39	0.74
	PL-t-L2	1880	1.41	0.54
	PL-t-L3	1770	1.48	0.62
	PL-t-L4	1630	1.40	0.51
	PL-t-L5	1380	1.54	0.65
	Average	1650	1.45	0.61
	COV	0.10	0.05	0.15
Transverse	PL-t-T1	1780	0.68*	0.37
	PL-t-T2	1620	0.71	0.41
	PL-t-T3	1850	0.65*	0.37
	PL-t-T4	1720	0.66	0.36
	PL-t-T5	1390	0.63	0.38
	Average	1670	0.67	0.38
	COV	0.11	0.04	0.05

* Sharp peaks ignored in the determination of f_u

Two distinct modes of failure were observed for the compressive plasterboard specimens: (a) a diagonal shear plane across the four plasterboards and (b) crushing of the material, with the outer boards folding outwards and vertical cracks forming within the boards, both of which can be seen in Figure 3.8. Failure appeared to be essentially simultaneous across the four boards for both modes of failure. The profile of the stress-strain curves obtained from the compression tests was consistent for both the longitudinal and transverse specimens, featuring an elastic region, some loss of stiffness, attainment of the peak stress and then a gradual decrease in stress - see Figure 3.9.

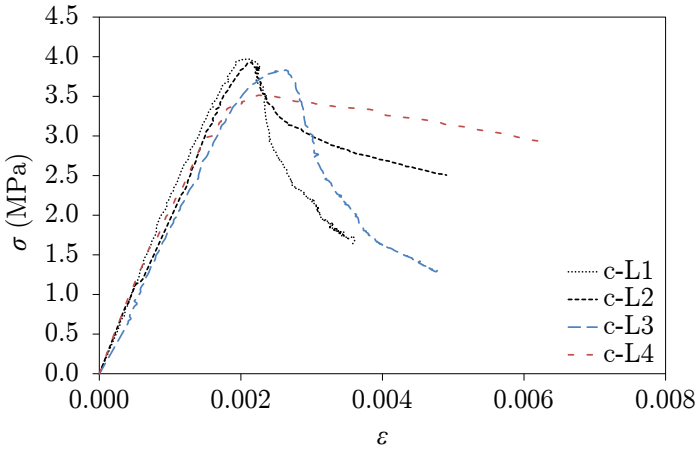


(a) Longitudinal

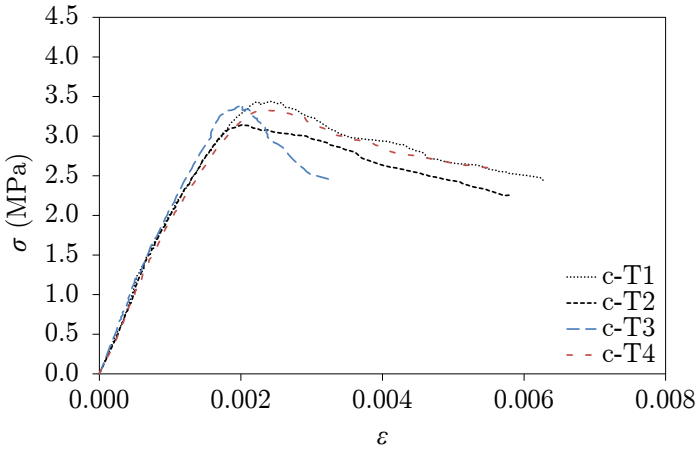


(b) Transverse

Figure 3.8: Failure modes observed in compressive coupon tests on plasterboard in (a) the longitudinal and (b) the transverse directions



(a) Longitudinal



(b) Transverse

Figure 3.9: Stress-strain curves obtained from compressive coupon tests on plasterboard in (a) the longitudinal and (b) the transverse directions

The key measured properties of the plasterboard from the compression tests - the Young's modulus in compression E, the ultimate compressive strength f_u, the corresponding strain ε_u and the strain $\varepsilon_{u,0.8}$ at which the post peak stress level had dropped to 80% of the ultimate strength, are reported in Table 3.4. The notation defining the key points on the material stress-strain is illustrated in Figure 3.10. While the difference between the stiffness of the longitudinal and transverse samples was small for both the tensile and compressive tests, a difference of 30% was observed between the values of stiffness in tension and compression. In terms of strength, the ultimate compressive stress was similar in the two loading directions (transverse and longitudinal), while the ultimate tensile stress showed far greater variation, with higher strengths in the longitudinal direction.

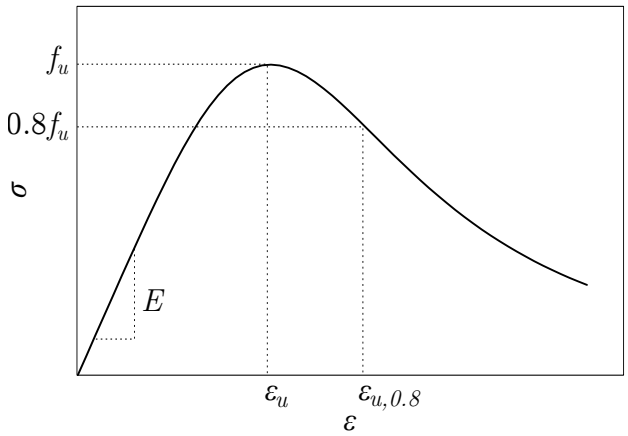


Figure 3.10: Notation defining key points on material stress-strain curves

Table 3.4: Key compressive material properties from plasterboard coupon tests

Loading direction	Specimen	E (MPa)	f_u (MPa)	ε_u (%)	$\varepsilon_{u,0.8}$ (%)
Longitudinal	PL-c-L1	2210	3.97	0.21	0.24
	PL-c-L2	2130	3.93	0.22	0.27
	PL-c-L3	1790	3.83	0.26	0.30
	PL-c-L4	2290	3.51	0.22	0.69
	Average	2110	3.81	0.23	0.37
	COV	0.10	0.05	0.11	0.57
Transverse	PL-c-T1	2120	3.44	0.25	0.46
	PL-c-T2	2130	3.14	0.21	0.46
	PL-c-T3	2170	3.39	0.20	0.28
	PL-c-T4	2080	3.33	0.26	0.50
	Average	2130	3.33	0.23	0.42
	COV	0.02	0.04	0.13	0.24

3.2.3 Oriented strand board (OSB)

Orientated strand boards are multi-layered boards made from strands of wood bonded together with adhesive. In the external layers, the strands are aligned while in the internal layers the strands tend to be either randomly orientated or perpendicular to the direction of the external layers. As part of the experimental programme presented herein, material

tests were carried out on type OSB/3 oriented strand boards, suitable for load-bearing use in humid conditions, as indicated in EN 300 EN 300 (2006) and EN 1995-1-1 EN 1995-1-1 (2004). The tested material had on average measured thickness of 11 mm and a density of 590 kg/m^3.

3.2.3.1 Tensile and compressive tests on OSB material

Determination of the tensile and compressive mechanical properties of the OSB was conducted in accordance with the provisions of EN 789 EN 789 (2005). Similarly to the approach followed for the plasterboard material testing, tests were carried out on specimens cut both longitudinally and transversely to the production direction of the board. In total, ten tensile and eight compressive OSB material tests were carried out.

The dimensions of both the tensile and compressive coupons were the same as those of the plasterboard coupons illustrated in Figure 3.4. The employed test setup (see Figure 3.11) and procedure were also the same. Digital image correlation with two cameras recording



(a) Tensile OSB coupon test (b) Compression OSB coupon test

Figure 3.11: Test setup for OSB coupons in (a) tension and (b) compression

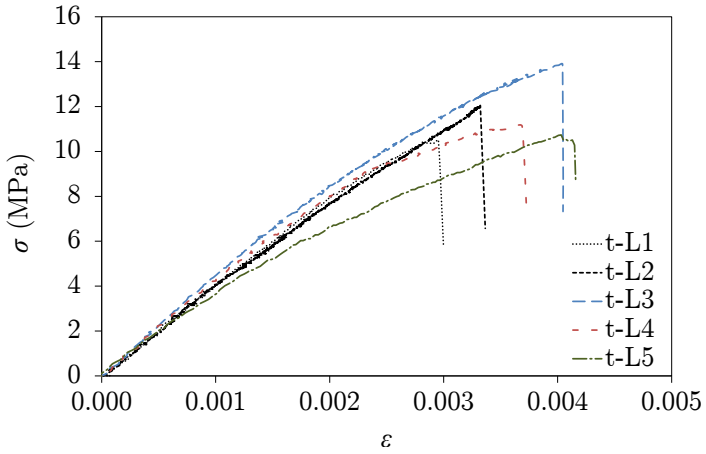
images at a frequency of 2 Hz was employed for measuring the strains, while the acquisition of load and strain measurements was carried out using the Bluehill data acquisition system

and DaVis (2019) respectively.

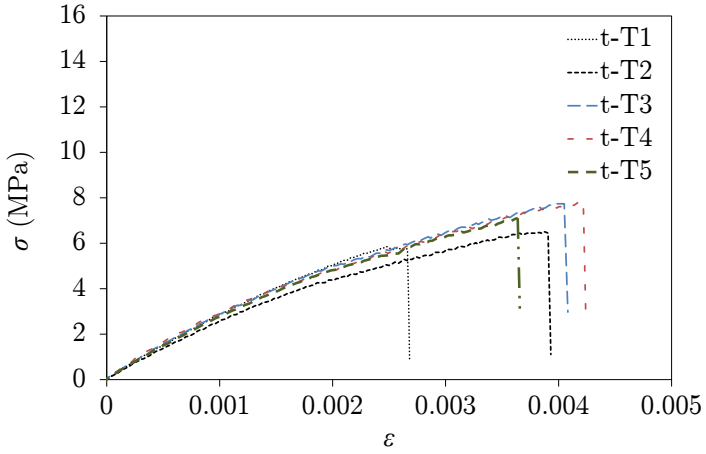
3.2.3.2 Results of OSB material tests

All tests were carried out until failure of the coupons could be observed. The notation of the OSB tensile and compressive coupons begins with the capital letters OSB; this is followed by the letter t for tension or c for compression, then the capital letter L or T to designate the coupons as either longitudinal or transverse and finally the number of the test.

Sudden failure without any significant plastic deformation was exhibited by all tensile coupons, as apparent in the stress-strain curves depicted in Figure 3.12. The failure mode



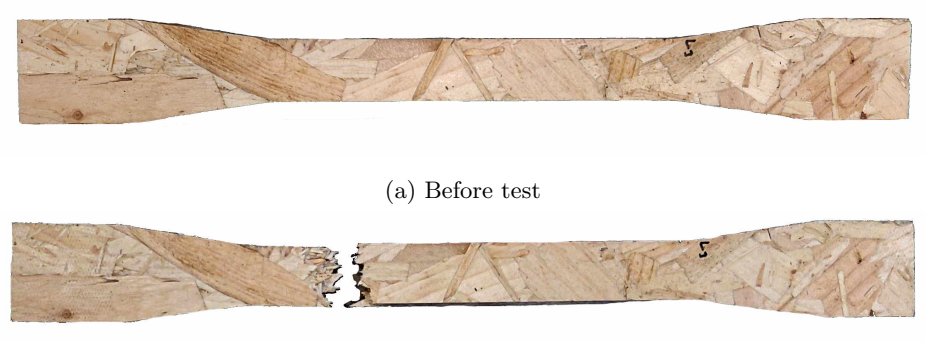
(a) Longitudinal



(b) Transverse

Figure 3.12: Stress-strain curves obtained from OSB tensile coupon tests in (a) the longitudinal and (b) the transverse directions

of a typical tensile coupon is shown in Figure 3.13. The key measured material properties are listed in Table 3.5. The values of the Young's modulus and tensile strength of the longitudinal coupons were found to be, on average, about 40% and 70% higher, respectively than those of the transverse coupons. This is attributed to the direction of production of the OSB panels, with the orientation of the strands parallel to the loading direction having a beneficial influence on the material response.



(a) Before test

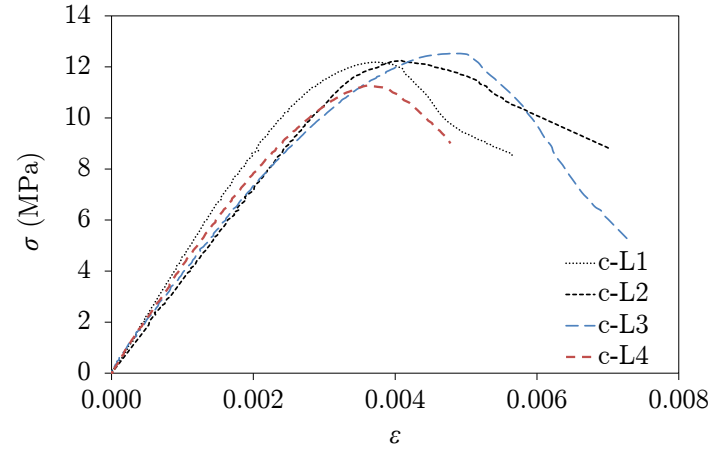
(b) After test

Figure 3.13: Typical OSB tensile coupon (a) before and (b) after test.

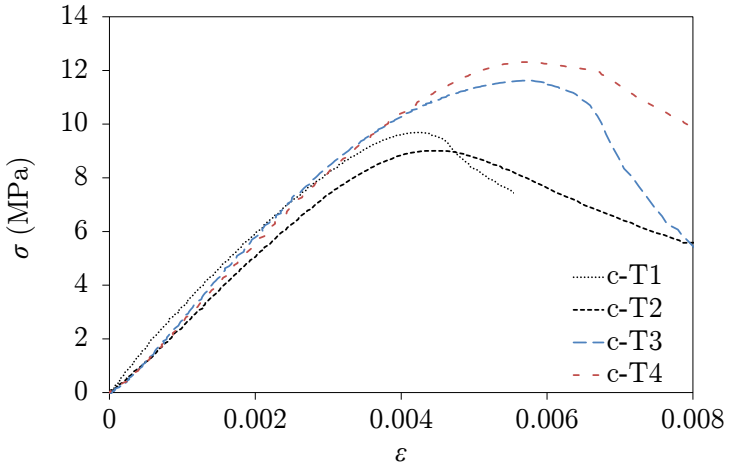
Table 3.5: Key measured tensile material properties from OSB tests

Loading direction	Specimen	E (MPa)	f_u (MPa)	ε_u (%)
Longitudinal	OSB-t-L1	4020	10.5	0.30
	OSB-t-L2	3960	12.1	0.33
	OSB-t-L3	4490	13.9	0.40
	OSB-t-L4	4330	11.2	0.37
	OSB-t-L5	3720	10.7	0.42
	Average	4100	11.7	0.37
	COV	0.07	0.12	0.13
Transverse	OSB-t-T1	2980	5.86	0.26
	OSB-t-T2	2650	6.51	0.39
	OSB-t-T3	3040	7.74	0.41
	OSB-t-T4	3200	7.85	0.42
	OSB-t-T5	1800	7.11	0.37
	Average	2940	7.01	0.37
	COV	0.07	0.12	0.17

The stress-strain curves of the coupons tested in compression were rounded, with a gradual decrease in stiffness prior to the peak strength and a gradual post peak softening response - see Figure 3.14. The two main failure modes that were observed for both sets



(a) Longitudinal



(b) Transverse

Figure 3.14: Stress-strain curves obtained from OSB compressive coupon tests in (a) the longitudinal and (b) the transverse directions

of coupons (i.e. longitudinal and transverse) were diagonal shear and folding out of the external surfaces resulting in horizontal cracks between the boards; these are shown in Figure 3.15. The key measured compressive material properties are reported in Table 3.6. Similarly to in tension, the Young's modulus in compression was about 40% higher in the longitudinal direction than in the transverse direction. However, the ultimate compressive strength f_u was only 13% higher in the longitudinal direction than in the transverse direction. The key material properties were generally similar in tension and compression, except for

ultimate strength in the transverse direction, which was about 50% higher in compression than tension.



(a) Longitudinal



(b) Transverse

Figure 3.15: Failure modes observed in the OSB compression tests in (a) the longitudinal and (b) the transverse directions

Table 3.6: Key measured compressive material properties from OSB tests

Loading direction	Specimen	E (MPa)	f_u (MPa)	ε_u (%)	$\varepsilon_{u,0.8}$ (%)
Longitudinal	OSB-c-L1	4510	12.2	0.37	0.48
	OSB-c-L2	3620	12.2	0.41	0.62
	OSB-c-L3	3810	12.5	0.48	0.60
	OSB-c-L4	4140	11.3	0.34	0.48
	Average	4020	12.1	0.40	0.54
	COV	0.10	0.05	0.15	0.14
Transverse	OSB-c-T1	3230	9.7	0.42	0.53
	OSB-c-T2	2490	9.0	0.44	0.63
	OSB-c-T3	2750	11.6	0.57	0.69
	OSB-c-T4	2630	12.3	0.57	0.80
	Average	2780	10.7	0.50	0.66
	COV	0.12	0.15	0.16	0.17

3.2.4 Screw connectors

Three different types of screw connectors of 3.5 mm, 4.8 mm and 5.5 mm diameter were examined in this study and tested in tension and shear. The three types of screws considered are illustrated in Figure 3.16 and the average measured geometric properties are reported in Table 3.7, where d is the nominal diameter of the screw, $d_{s,thr}$ is the diameter at the threads, $d_{s,sh}$ is the diameter of the shank excluding the threads, $d_{s,hd}$ is the diameter of the head of the screw, $s_{s,thr}$ is the pitch between the threads, $h_{s,hd}$ is the depth of the head and $s_{s,nonthr}$ is the non-threaded length of the shank below the head of the screw and before the start of the threads.

The 3.5 mm diameter screws had a bugle head and sharp tip and can be self-driven into up to 2.2 mm thick steel; these screws are typically used for attaching plasterboard to cold-formed steel sections. The 4.8 mm diameter screws are typically employed for attaching OSB sheathing to cold-formed steel sections while the 5.5 mm diameter screws were examined to investigate the effect of a larger screw diameter. Both of the 4.8 mm and 5.5 mm diameter screws had 'wings' just above the screw tip; these were manually removed to allow a direct comparison with the screws of 3.5 mm diameter.



Figure 3.16: Types of screws considered (a) 3.5 mm (b) 4.8 mm and (c) 5.5 mm in diameter and (d) notations of the dimensions

Table 3.7: Average measured dimensions of screw connectors

d (mm)	$d_{s,thr}$ (mm)	$d_{s,sh}$ (mm)	$d_{s,hd}$ (mm)	$s_{s,thr}$ (mm)	$h_{s,hd}$ (mm)	$s_{s,nonthr}$ (mm)
3.5	3.51	2.63	8.36	1.15	3.33	1.67
4.8	4.73	3.50	10.02	1.45	4.00	0.25
5.5	5.38	4.04	10.55	1.65	4.48	1.63

3.2.4.1 Tensile and shear tests on screws

Tensile screw tests were performed using an 150 kN Instron 5984 hydraulic testing machine; the screws were held in the specifically designed jig shown in Figure 3.17. Within the jig, the bugle head screw was free to rotate in part 1 and screwed into part 2 - see Figure 3.17. The force F was applied under displacement control at a constant rate of 0.25 mm/min, while data were collected using the Bluehill data acquisition system at one second intervals.

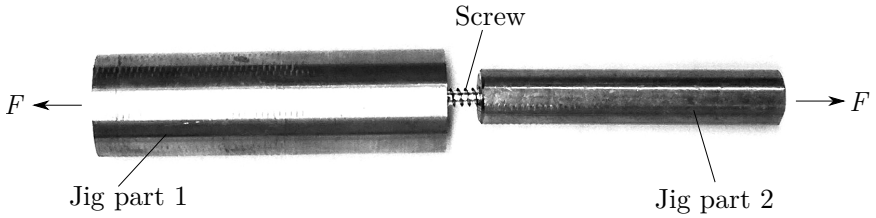


Figure 3.17: Jig for tensile testing of screw connectors

Double shear screw tests were performed using an 150 kN Instron 5984 testing machine by means of the setup shown in Figure 3.18, where tension was maintained throughout testing to avoid any movement/slippage of the screw during loading. The force F at each shear plane was applied using displacement control at a constant rate of 0.25 mm/min; the Bluehill data acquisition system was employed to collect data at one second intervals.

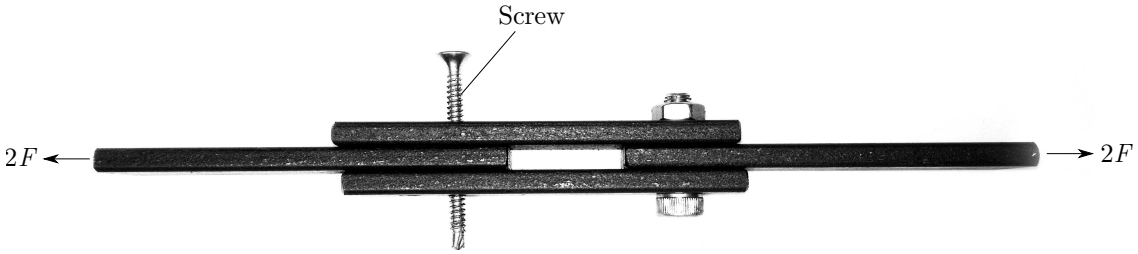


Figure 3.18: Test setup for double-shear tests on screw connectors, applying force F at each shear plane

3.2.4.2 Results of tensile and shear tests on screws

Three tensile tests and three double shear tests were performed for each of the three different screws; the results are summarised in Tables 3.8 and 3.9 respectively, where $F_{u,s}$ is the ultimate tensile resistance and $F_{u,v}$ is the ultimate shear resistance. The ultimate tensile stresses $f_{u,s}$ can be calculated using Equation 3.1.

$$f_{u,s} = \frac{F_{u,s}}{\pi({d_{s,sh}}^2/4)} \tag{3.1}$$

Table 3.8: Results of tensile tests on screws

	$F_{u,s}$ (kN) for three screw diameters:		
Test number	3.5 mm	4.8 mm	5.5 mm
Test 1	5.92	9.72	10.19
Test 2	6.36	8.90	11.09
Test 3	6.08	8.86	11.20
Average	6.12	9.16	10.83
COV	0.04	0.05	0.05

Table 3.9: Results of shear tests on screws

	$F_{u,v}$ (kN) for three screw diameters:		
Test number	3.5 mm	4.8 mm	5.5 mm
Test 1	3.64	5.12	6.45
Test 2	3.37	4.95	5.95
Test 3	3.49	5.38	5.99
Average	3.50	5.15	6.13
COV	0.04	0.04	0.05

The experimental ultimate shear resistances $F_{u,v}$ reported in Table 3.9 were found to be within 3% of the shear resistance values calculated from Equation 3.2 using the measured ultimate tensile stresses $f_{u,s}$ and screw shank diameters $d_{s,sh}$.

$$F_{u,v} = \pi \frac{{d_{s,sh}}^2}{4} \frac{f_{u,s}}{\sqrt{3}} \tag{3.2}$$

3.3 Pull-through behaviour of sheathing-to-steel screws

Although pull-through tests have featured in some studies (Peterman & Schafer 2014, Selvaraj & Madhavan 2019*d*), this failure mode in isolation has not been extensively investigated in the literature. Hence, a series of pull-through tests are presented herein. The resistance of the examined connectors depends on the combined effect of the connector head bearing into the surface of the board and the screw threads interacting with the board material.

In total, 25 pull-through tests, covering five different cases, were carried out; the relevant details are given in Table 3.10. The specimen identification system starts with the letters PT, followed by the nominal diameter of the screw connector (×10) in mm, then the number of layers of board and finally a letter corresponding to the board type (with P for plasterboard and O for OSB). It should be mentioned that the use of double layer plasterboards is common practice to provide increased fire resistance.

Table 3.10: Details of pull-through test specimens

Designation	Screw diameter (mm)	No. of boards	Individual layer thickness (mm)	Board material	No. of tests
PT-35-1P	3.5	1	12.5	Plasterboard	5
PT-35-2P	3.5	2	12.5	Plasterboard	5
PT-55-1P	5.5	1	12.5	Plasterboard	5
PT-55-2P	5.5	2	12.5	Plasterboard	5
PT-48-1O	4.8	1	11.0	OSB	5
				Total:	25

3.3.1 Pull-through tests

Pull-through testing specifications for timber based materials, such as OSB, and plasterboard, are provided in EN 1383 (2016) and EN 14566:2008+A1 (2009) respectively. Although both procedures are similar, for consistency, testing was performed in accordance with the provisions of EN 1383 (2016) for all tests, using the setup shown in Figures 3.19 and 3.20. The board specimens were cut in squares of 100×100 mm. Each screw was driven

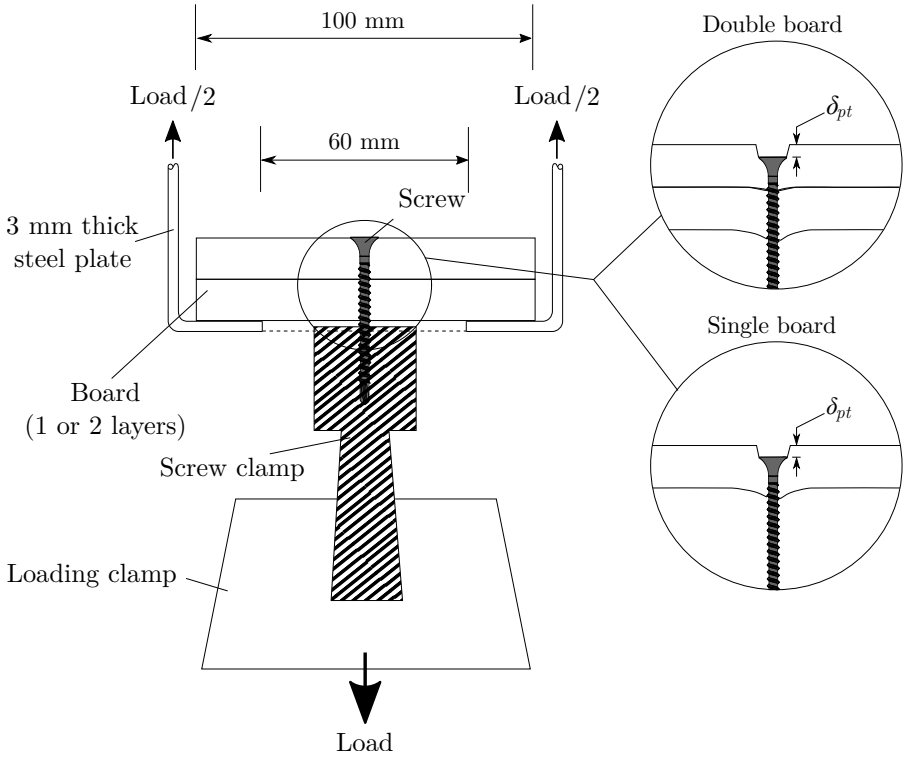
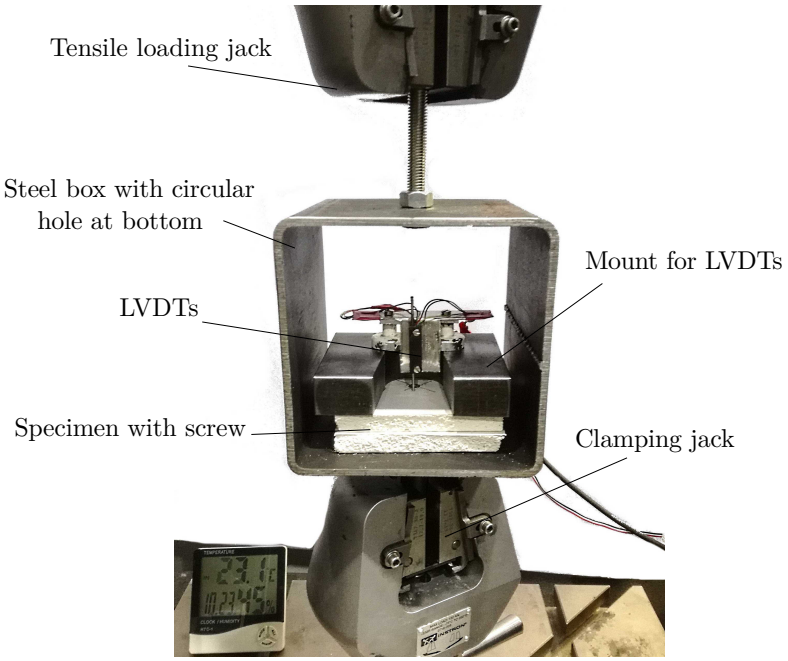
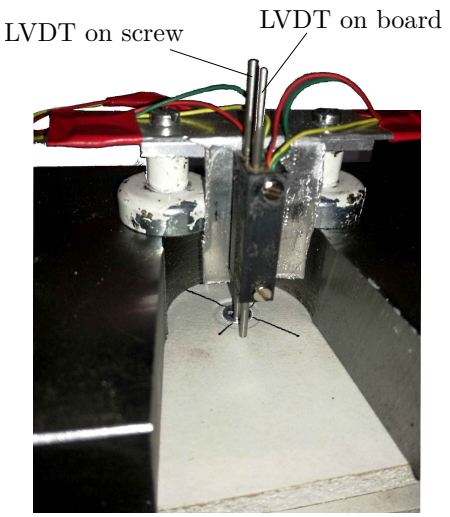


Figure 3.19: Schematic illustration of pull-through test arrangement

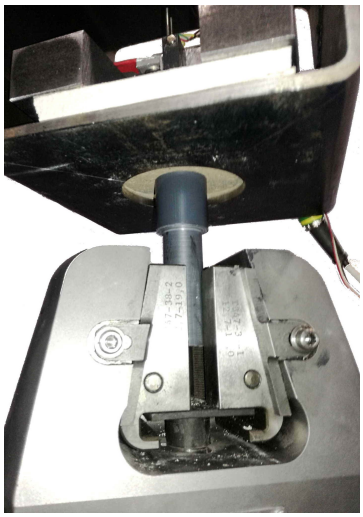
vertically through the middle of the board (or two boards) with its head finishing flush to the board surface - see Figure 3.19. The screws were then pulled through the board via a circular hole of 60 mm diameter at the base of a steel box by means of a screw clamp and loading clamp, as shown in Figure 3.20. Load was applied in displacement control at a constant rate of 0.25 mm/min using an 150 kN Instron 5984 testing machine. Data were acquired using the Bluehill software system at one second intervals.



(a)



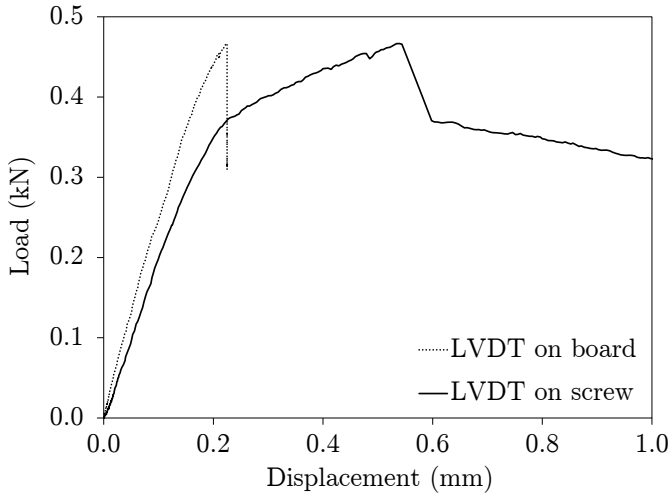
(b)



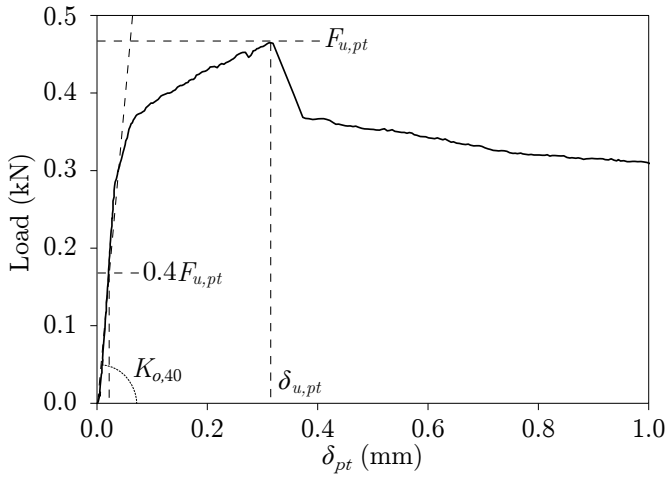
(c)

Figure 3.20: Pull-through test setup: (a) overall arrangement, (b) employed instrumentation and (c) bottom view

To capture the net embedment δ_{pt} of the screw into the board, two measurements of displacement were taken: the vertical deflection of the board adjacent to the screw and the vertical displacement of the screw itself - see Figure 3.20 (b). The net embedment of the screw δ_{pt}, as indicated in Figure 3.19, was determined by subtracting the deflection of the board from that of the screw. The load-displacement curves from the two LVDTs for a typical case are shown in Figure 3.21 (a), while the corresponding calculated embedment of the screw δ_{pt}, is shown in Figure 3.21 (b). The results for all tests are presented in the following section.



(a)



(b)

Figure 3.21: Load-displacement curves from pull-through tests (a) from two LVDTs (one on screw and one on adjacent board) and (b) showing the net embedment δ_{pt} and key properties, where $F_{u,pt}$ is the ultimate pull-through resistance, $\delta_{u,pt}$ is the corresponding displacement and $K_{o,40}$ is the secant stiffness at $0.4F_{u,pt}$

3.3.2 Results of pull-through tests

For all specimens, testing was continued until failure was clearly marked by a substantial drop in load. For the plasterboard specimens, failure occurred suddenly in the manner shown in Figure 3.22. The OSB specimens exhibited a more gradual decrease in load post peak; testing was ended after the load had decreased by at least 20% relative to the peak. Load–net embedment curves, where net embedment δ_{pt} is defined in Figure 3.21 (b), are given for the single board specimens in Figure 3.23 and for the double board specimens in Figure 3.24. Note that in Figure 3.23, for clarity, graphs are provided for each test on two separate horizontal scales. For the double layer test specimens, a third graph is also provided in Figure 3.24 up to a net embedment of 8 mm to include the second peak in the load-displacement curves, which was found to be a feature of the double board specimens.



(a) (b) (c)

Figure 3.22: Failure of plasterboard pull-through specimens: (a) top view, embedded screw (b) bottom view of board failing (c) rupture of the underside of plasterboard forming a conical surface

The load-displacement profile of the curves shown in Figure 3.23 for the 3.5 mm and the 5.5 mm diameter screw specimens are distinctively different in shape, with the 3.5 mm screw specimens exhibiting a more rounded and ductile response. This behaviour is attributed to the shape of the underside of the head of the screws, which is flatter in the case of the 3.5 mm diameter screws resulting in delayed cutting of the paper at the board surface and hence improved ductility.

A similar profile can be observed for the initial stage of the load-displacement curves of the double board specimens, shown in Figure 3.24, since the same screw types as those used in the respective single board arrangements were employed. Hence, doubling the board

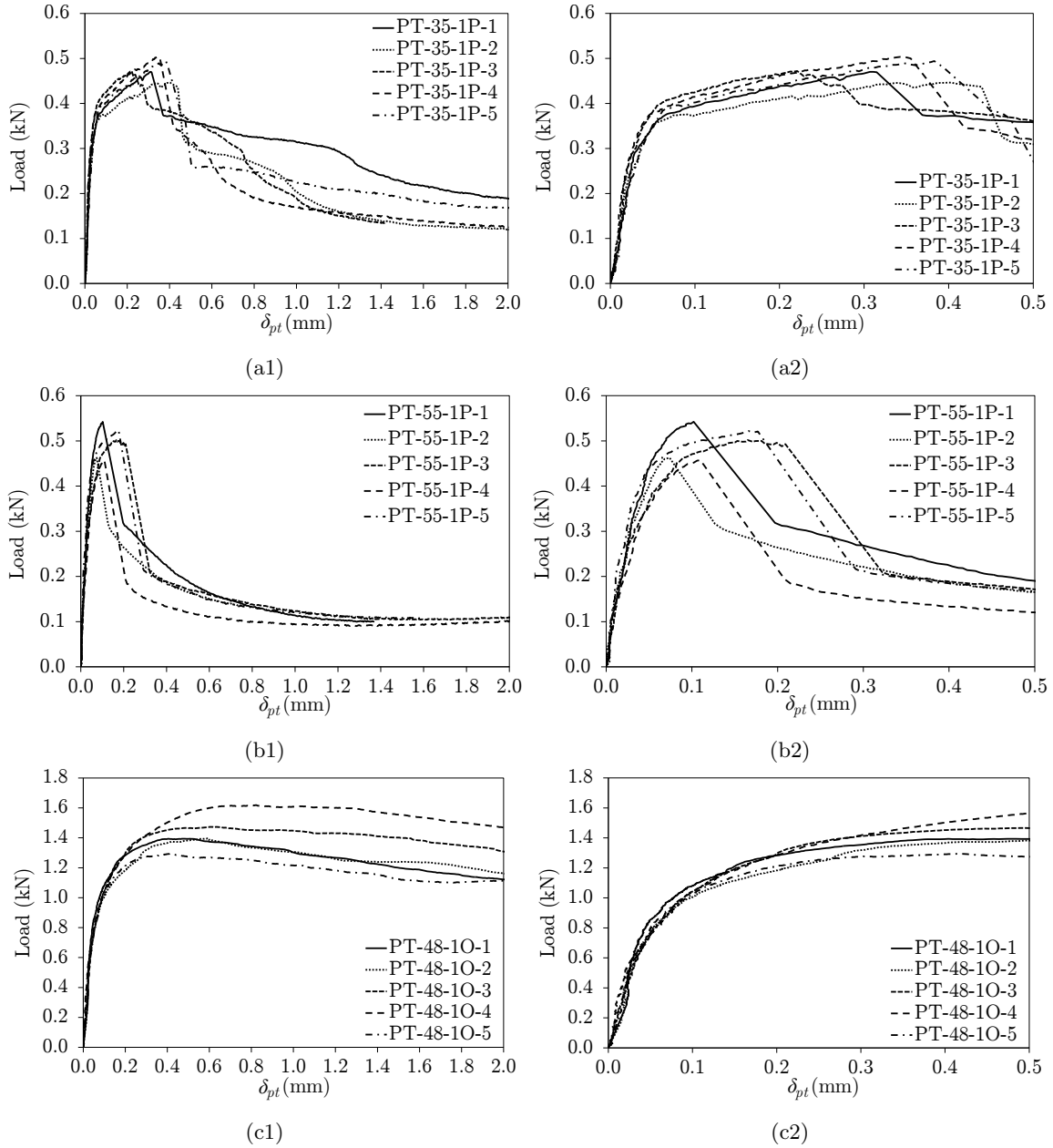


Figure 3.23: Single board pull-through load-displacement curves for (a) PT-35-1P, (b) PT-55-1P and (c) PT-48-1O on a horizontal scale up to 2 mm (a1, b1, c1) and up to 0.5 mm (a2, b2, c2)

layers does not significantly affect the initial behaviour because the dominant effect of the shape of the screw head in the early stages of loading remains the same. The first peak in capacity and the initial stiffness of the double board specimens, when compared to their single board equivalents, are shown to be 20-30% and 60-70% higher, respectively, due to the extra screw thread length engaged in the second layer of plasterboard. A characteristic of the two board specimens are the two peaks shown in Figure 3.24 (a1) and (a2). For

the 3.5 mm screws, the two peaks are more distinct with a decrease in load of about 20% between them, while for the 5.5 mm screws, the profile of the load-displacement is flatter. The displacement δ_{pt} at which the second peaks occurred is around 6 mm, which corresponds approximately to the mid-depth of the first board.

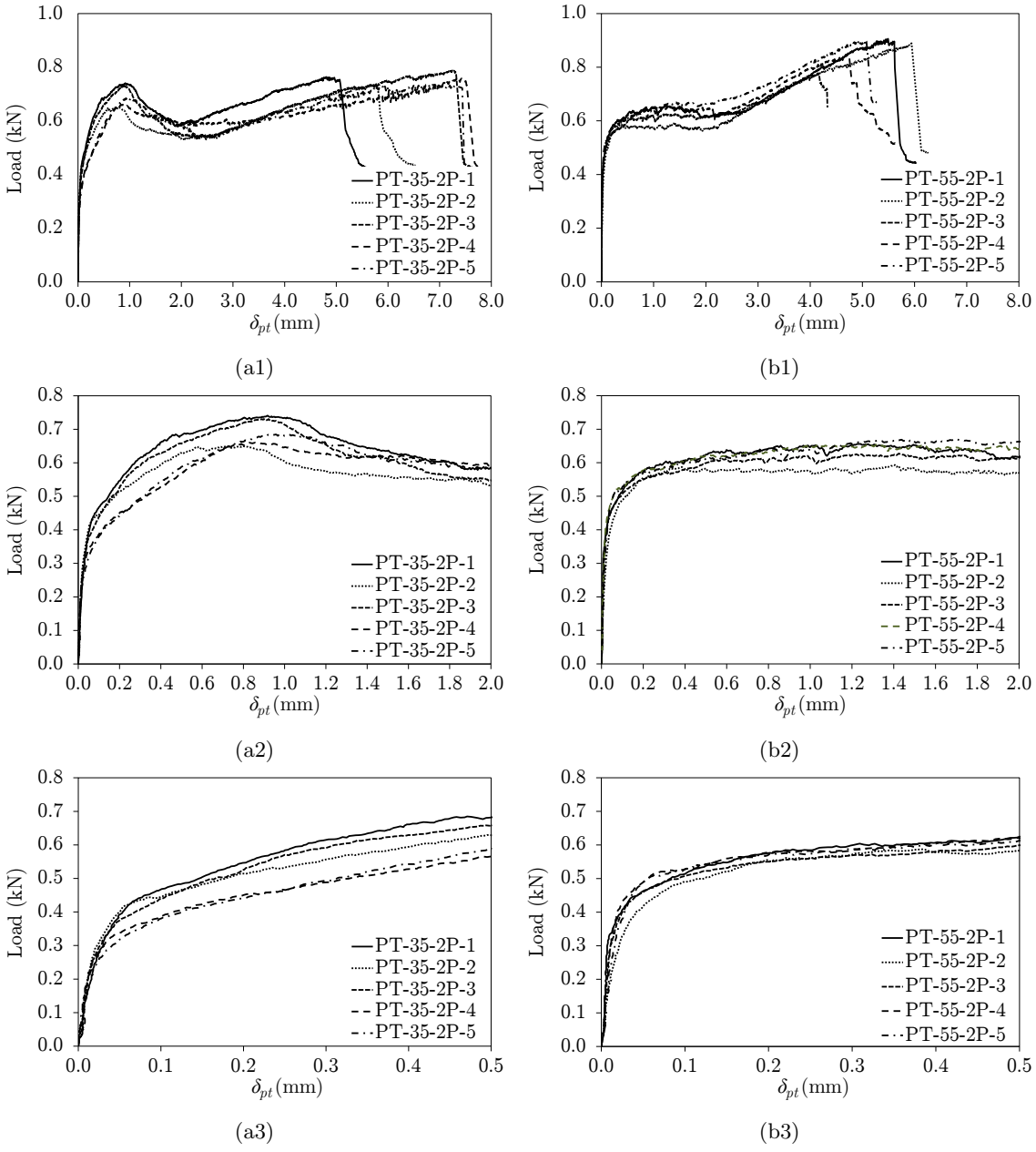


Figure 3.24: Two layer board pull-through load-displacement curves for (a) PT-35-2P and (b) PT-55-2P on a horizontal scale up to 8 mm (a1, b1), up to 2 mm (a2, b2) and up to 0.5 mm (a3, b3)

The OSB pull-through load displacements curves are shown in Figures 3.23 (c1) and

(c2), where a smooth profile can be observed both before and after the peak capacity. This is attributed to the screw being pulled through a relatively homogeneous timber-based material, unlike in the plasterboard arrangement where the gypsum core and outer surface paper layers have very different properties.

The key measured properties, as defined in Figure 3.21 (b), are tabulated for the single and double board specimens in Tables 3.11 and 3.12 respectively. These properties include

Table 3.11: Experimental results from pull-through tests with single boards

Designation	$K_{o,40}$ (kN/mm)	$F_{u,pt}$ (kN)	$\delta_{u,pt}$ (mm)	$F_{u,pt,0.8}$ (kN)	$\delta_{u,pt,0.8}$ (mm)
PT-35-1P-1	9.49	0.47	0.31	0.38	0.37
PT-35-1P-2	10.0	0.45	0.40	0.36	0.44
PT-35-1P-3	12.6	0.47	0.22	0.38	0.43
PT-35-1P-4	11.0	0.50	0.34	0.40	0.37
PT-35-1P-5	9.26	0.49	0.38	0.40	0.44
Average	10.5	0.48	0.33	0.38	0.41
COV	0.13	0.05	0.21	0.05	0.09
PT-55-1P-1	13.4	0.54	0.10	0.43	0.16
PT-55-1P-2	15.8	0.46	0.07	0.37	0.11
PT-55-1P-3	11.9	0.50	0.17	0.40	0.24
PT-55-1P-4	13.3	0.46	0.11	0.37	0.16
PT-55-1P-5	16.9	0.52	0.17	0.42	0.22
Average	14.2	0.50	0.12	0.40	0.18
COV	0.14	0.07	0.33	0.07	0.29
PT-48-1O-1	17.9	1.39	0.42	1.12	2.08
PT-48-1O-2	17.5	1.40	0.56	1.12	2.32
PT-48-1O-3	18.8	1.47	0.55	1.18	2.42
PT-48-1O-4	19.4	1.62	0.74	1.29	2.46
PT-48-1O-5	18.9	1.29	0.41	1.03	2.71
Average	18.5	1.44	0.54	1.15	2.40
COV	0.04	0.08	0.25	0.08	0.10

the peak capacity $F_{u,pt}$, the displacement at the peak capacity $\delta_{u,pt}$ and the secant stiffness

$K_{o,40}$, calculated by dividing the load at 40% of $F_{u,pt}$ by the corresponding displacement, as shown in Figure 3.21 (b). For the specimens comprising two boards, the peak capacity and corresponding displacement at the second peak are denoted by $F_{u,pt,2}$ and $\delta_{u,pt,2}$ respectively. Finally, the post peak properties $F_{u,pt,0.8}$ and $\delta_{u,pt,0.8}$ are also provided, where $F_{u,pt,0.8}$ is the load at 80% of $F_{u,pt}$ and $\delta_{u,pt,0.8}$ is the corresponding displacement. For the tests with the 5.5 mm screws and two boards, since the load did not decrease as low as $F_{u,pt,0.8}$ between $F_{u,pt}$ and $F_{u,pt,2}$, $F_{u,pt,0.8}$ was taken as the lowest point between the two peaks and $\delta_{u,pt,0.8}$ as the corresponding measured displacement. A summary of the average measured key properties is provided by Table 3.13.

Table 3.12: Experimental results from pull-through tests with two layers of board

Designation	$K_{o,40}$ (kN/mm)	$F_{u,pt}$ (kN)	$\delta_{u,pt}$ (mm)	$F_{u,pt,0.8}$ (kN)	$\delta_{u,pt,0.8}$ (mm)	$F_{u,pt,2}$ (kN)	$\delta_{u,pt,2}$ (mm)
PT-35-2P-1	14.0	0.74	0.92	0.59	1.83	0.76	4.81
PT-35-2P-2	17.7	0.65	0.80	0.52	2.05	0.74	5.77
PT-35-2P-3	15.6	0.73	0.90	0.58	1.65	0.79	7.24
PT-35-2P-4	17.1	0.66	0.86	0.53	2.30	0.76	7.42
PT-35-2P-5	17.9	0.69	0.98	0.55	2.29	0.74	6.90
Average	16.5	0.69	0.89	0.55	2.03	0.76	6.43
COV	0.10	0.06	0.08	0.06	0.14	0.03	0.17
PT-55-2P-1	31.1	0.66	1.24	0.61*	1.91*	0.91	5.43
PT-55-2P-2	18.4	0.59	1.42	0.56*	1.94*	0.89	5.63
PT-55-2P-3	27.6	0.63	1.42	0.61*	1.81*	0.78	3.90
PT-55-2P-4	29.5	0.65	1.28	0.60*	2.16*	0.85	5.09
PT-55-2P-5	21.4	0.67	1.70	0.65*	1.84*	0.90	4.75
Average	25.6	0.64	1.41	0.61	1.93	0.86	4.96
COV	0.21	0.05	0.13	0.05	0.07	0.06	0.14

*Load did not drop to 80% of $F_{u,pt}$; $F_{u,pt,0.8}$ taken as lowest point between the first and second peaks

Table 3.13: Average measured results from pull-through tests

Designation	$K_{o,40}$ (kN/mm)	$F_{u,pt}$ (kN)	$\delta_{u,pt}$ (mm)	$F_{u,pt,0.8}$ (kN)	$\delta_{u,pt,0.8}$ (mm)	$F_{u,pt,2}$ (kN)	$\delta_{u,pt,2}$ (mm)
PT-35-1P	10.5	0.48	0.33	0.38	0.41	-	-
PT-35-2P	16.5	0.69	0.89	0.55	2.03	0.76	6.43
PT-55-1P	14.2	0.50	0.12	0.40	0.18	-	-
PT-55-2P	25.6	0.64	1.41	0.61*	1.93*	0.86	4.96
PT-48-1O	18.5	1.44	0.54	1.15	2.40	-	-

*Load did not drop to 80% of $F_{u,pt}$; $F_{u,pt,0.8}$ taken as lowest point between the first and second peaks

3.4 Shear behaviour of sheathing-to-steel screw connectors

The principal action resisted by fixings connecting two elements and resisting relative slip between them is shear. Hence, the shear behaviour of an individual connection between two elements (the sheathing and the steel in the present context) is characterised by its load-slip response. A procedure to determine the shear behaviour and strength of a connection between plasterboard and timber is provided in EN 520 (2009) - see Figure 3.25 (a). This test procedure was adapted by Fiorino et al. (2017) where, instead of timber members, two cold-formed steel sections were used, with the plasterboard screwed to the opposite flanges of the cold-formed steel profiles. Similar test setups with plasterboard connected to both sides of cold-formed steel members were employed by Serrette et al. (1997), Peterman et al. (2014), Vieira & Schafer (2009) and Ye et al. (2016), while test arrangements with a single board and flat cold-formed steel plates were reported by Chen et al. (2016). According to EN 1994-1-1 (2004), push-out tests are the standard means for determining the shear behaviour and capacity of connectors in composite construction - see Figure 3.25 (b). Therefore, several researchers have adopted this approach to determine the shear behaviour of fasteners connecting cold-formed steel sections and various types of boards, including plasterboards (Stergiopoulos et al. 2019), timber based boards (Kyvelou et al. 2017*b*, Vella et al. 2020) and cement based boards (Abu-Hamd 2019). The latter approach is considered to be more

representative of how a typical stud column is loaded in practice, and is therefore employed herein.

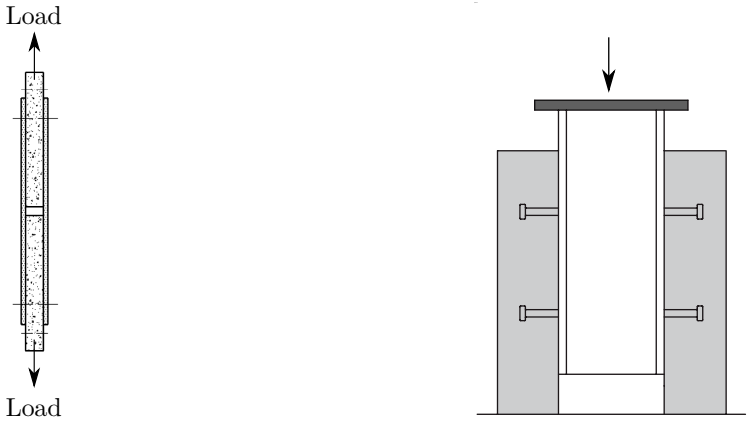


Figure 3.25: Standard tests for measuring the shear behaviour of a connector between two elements: (a) pull-test in EN 520 (2009) and (b) push-test in EN 1994-1-1 (2004)

In total, 18 push-out tests were performed with the varied parameters being the screw size, the number of plasterboard layers and the steel thickness in order to investigate their influence on the load-slip behaviour in shear. Details of the six investigated combinations of tests parameters are provided in Table 3.14; three repeat specimens were tested for each combination. The adopted labelling system for the test specimens begins with the letters PO

Table 3.14: Combinations of parameters investigated in push-out tests

Designation	Screw diameter (mm)	No. of boards	Steel thickness (mm)	No. of tests
PO-35-1P-12	3.5	1	1.2	3
PO-35-2P-12	3.5	2	1.2	3
PO-35-1P-20	3.5	1	2.0	3
PO-35-2P-20	3.5	2	2.0	3
PO-55-1P-12	5.5	1	1.2	3
PO-55-2P-20	5.5	2	2.0	3
			Total:	18

for push-out tests, followed by the nominal diameter of the screw in mm multiplied by ten, then by 1P or 2P for single or double plasterboard layers respectively and finally by the

nominal thickness of the steel section in mm multiplied by ten. The key characteristics of the steel, plasterboard and screws are as provided in Section 3.2.

3.4.1 Push-out tests

Schematic views of the employed push-out test setup are shown in Figure 3.26. The test specimens consisted of two back-to-back 400 mm long cold-formed steel lipped channel sections of 150 mm depth and 44 mm width, with square 400 × 400 mm boards connected to their flanges. Single or double layers of plasterboard were connected to the steel sections with four screws.

Loading was applied to the push-out specimens by a 750 kN Instron hydraulic testing machine in the arrangement shown in Figures 3.26 and 3.27. The specimens were loaded under displacement control at a constant displacement rate of 0.25 mm/min. The slip δ_{po} between the steel section and the boards, illustrated in Figure 3.26, was measured using four LVDTs, as shown in Figure 3.28 (b); the LVDTs were mounted on the steel section and recorded the slip between steel and the inside surface of the boards, as shown in Figure 3.27, to eliminate any additional displacement from the potential crushing of the plasterboard edges under the compression load.

Load and slip were recorded at one second intervals using the DATASCAN acquisition system. Load-slip measurements were reported after averaging the four LVDT displacement readings and after dividing the force recorded from the hydraulic actuator by eight to calculate the load per screw.

3.4.2 Results of push-out tests

All tests were carried out until failure or until the recorded slip exceeded three times the diameter of the screw fixing. Typical failure modes are shown in Figure 3.29. For the single board arrangements, the main failure mode observed was bearing of the screw into the board and tilting of the screw. For the double board arrangements, the failure modes also featured bearing and tilting, but this was accompanied in some cases by pull-through

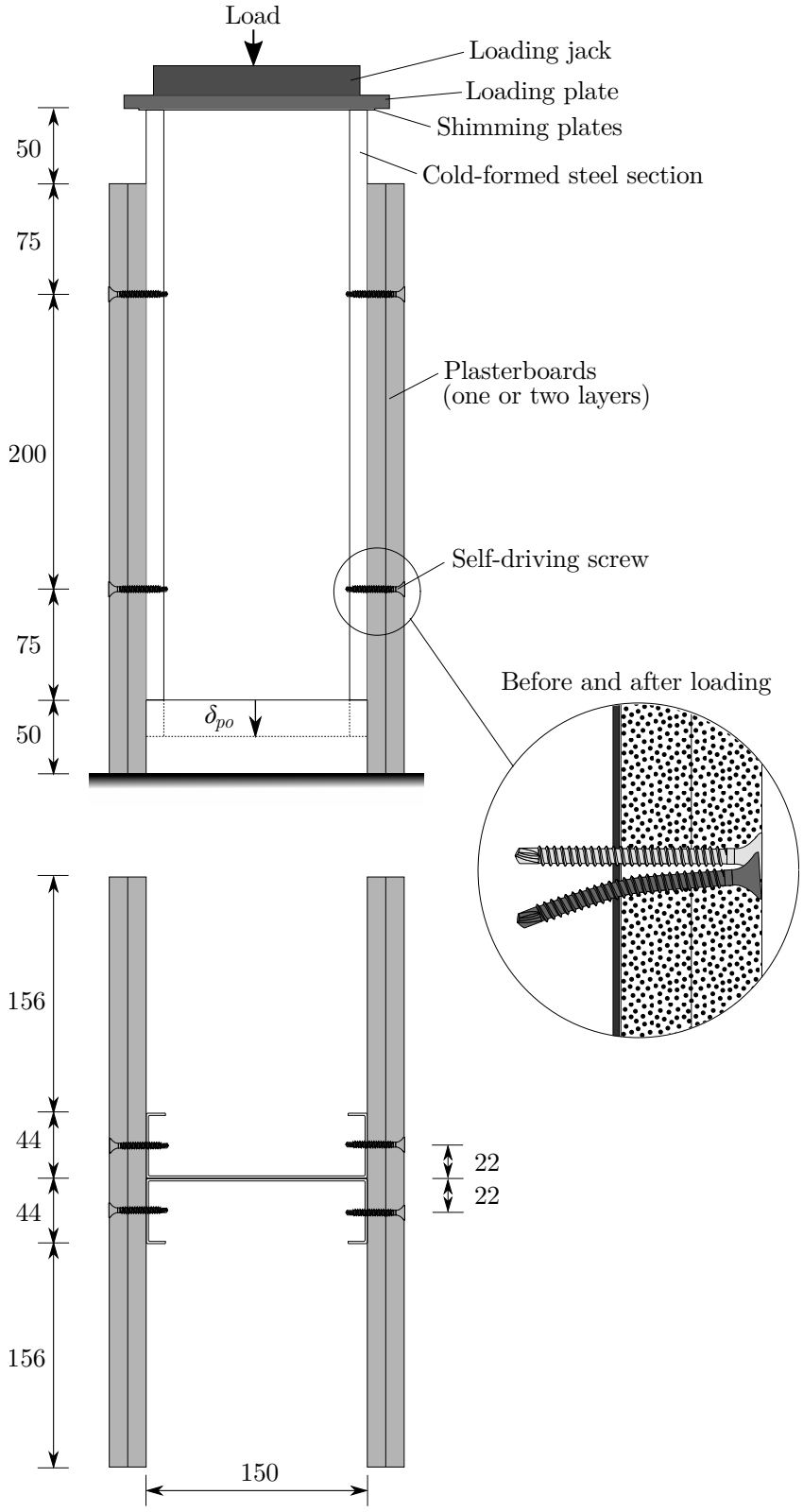


Figure 3.26: Schematic views of push-out test arrangement in elevation and from above. All dimensions are given in mm.

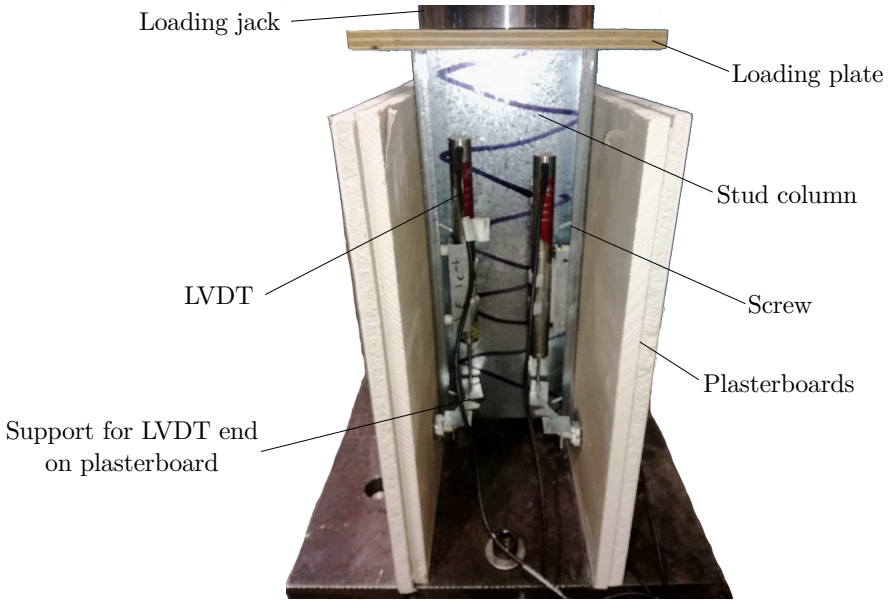


Figure 3.27: Experimental arrangement for push-out tests

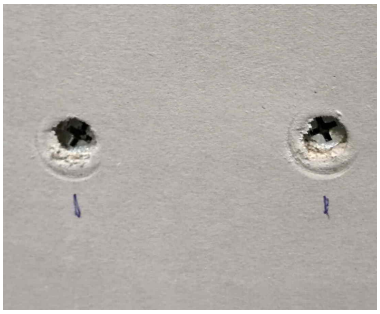


(a) (b)

Figure 3.28: (a) Overview and (b) top view of push-out test specimens

and screw bending; screw shear failure occurred for the specimens featuring the smaller diameter (3.5 mm) screws in the thicker steel section (2 mm). On the back surface of the plasterboards, the weaker paper was torn as the screw tilted downwards, as shown in Figure 3.29 (c).

The measured load-slip (δ_{po}) responses per connector are given in Figure 3.30 for the



(a)



(b)



(c)

Figure 3.29: Illustration of key aspects of failure modes (a) pull-through of screw for double board specimens, (b) bearing and tilting of screw for single board specimens and (c) typical failure surface on the back of the plasterboard

single board specimens and in Figure 3.31 for the double board specimens. For each set of tests, two graphs are given – one up to a slip of 16 mm, to show the overall response to the end of the test and a second up to a slip of 2 mm to enable the initial part of the load-slip profile to be seen more clearly. As expected, the shape of the load-slip response for all specimens with one layer of plasterboard is consistent since all the screws failed in a similar manner by tilting and bearing into the plasterboard. Higher capacities were achieved with the use of the 5.5 mm screws, compared to the conventional 3.5 mm ones, which is expected due to the larger contact area between the screw and the board.

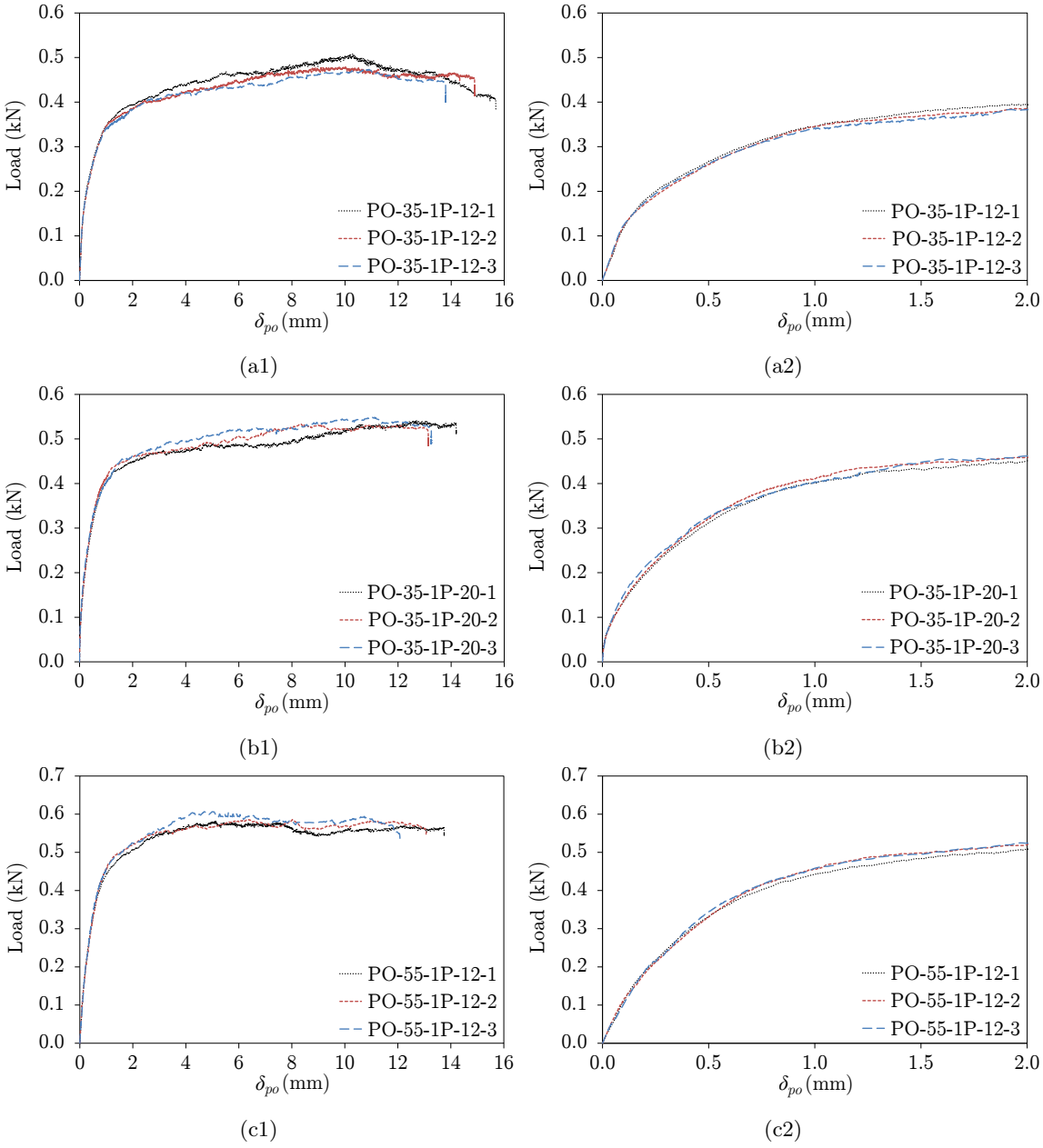


Figure 3.30: Single layer plasterboard push-out load-slip responses, averaged per screw, for (a) PO-35-1P-12, (b) PO-35-1P-20 and (c) PO-55-1P-12 over a horizontal scale up to 16 mm (a1, b1, c1) and up to 2.0 mm (a2, b2, c3)

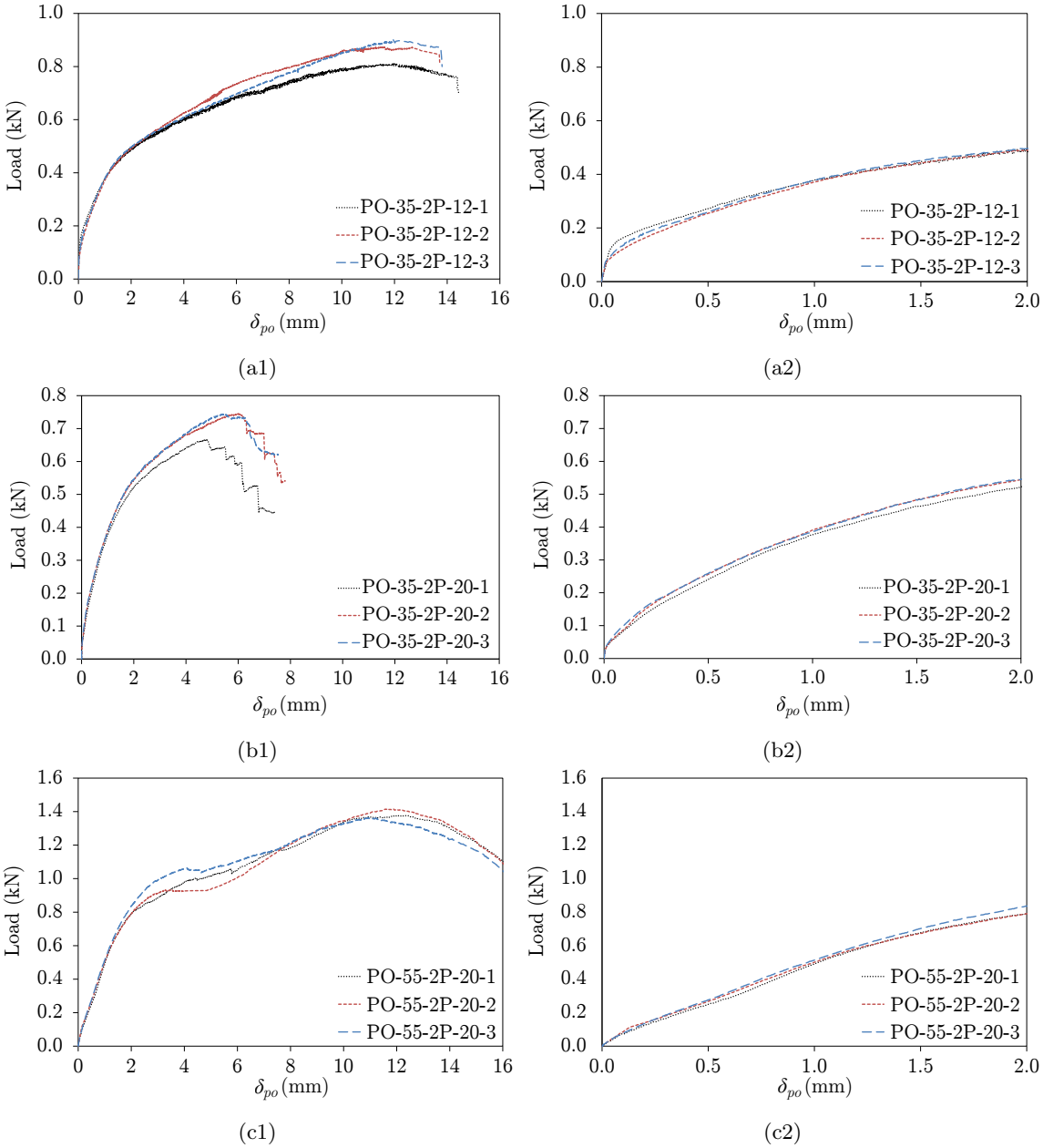


Figure 3.31: Double layer plasterboard push-out load-slip responses, averaged per screw, for (a) PO-35-2P-12, (b) PO-35-2P-20 and (c) PO-55-2P-20 over a horizontal scale up to 16 mm (a1, b1, c1) and up to 2.0 mm (a2, b2, c3)

The key measured properties from the push-out tests are tabulated for the single and double layer board specimens in Tables 3.15 and 3.16 respectively, where $F_{u,po}$ is the ultimate shear capacity per screw, $\delta_{u,po}$ is the displacement at the ultimate capacity, K_o is the initial stiffness calculated using Equation (3.3) and $K_{o,40}$ is the secant stiffness measured at 40%

of $F_{u,po}$.

$$K_o = \frac{1}{n}\left(\sum_{i=1}^{n} K_{o,i}\right) \qquad \text{while} \quad K_{o,n} \geq 0.75K_{o,1} \tag{3.3}$$

K_o is the the average value of the secant stiffnesses calculated between the points at $0.1F_{u,po}$ and either $0.4F_{u,po}$ or up to the point where the calculated stiffness is no less than 75% of the stiffness calculated at $0.1F_{u,po}$ (with $K_{o,i}$ being the secant stiffness corresponding to point i). The $K_{o,40}$ stiffness is typically reported in the literature (Peterman et al. 2014, Fiorino et al. 2017) and therefore represents a useful reference value, while K_o provides a more accurate representation of the initial stiffness, particularly when there is high degree of nonlinearity in the early stages of the load-slip response. Calculation of $F_{u,po}$, $\delta_{u,po}$ and K_o for typical load-slip curves per connector in shear are illustrated in Figure 3.32.

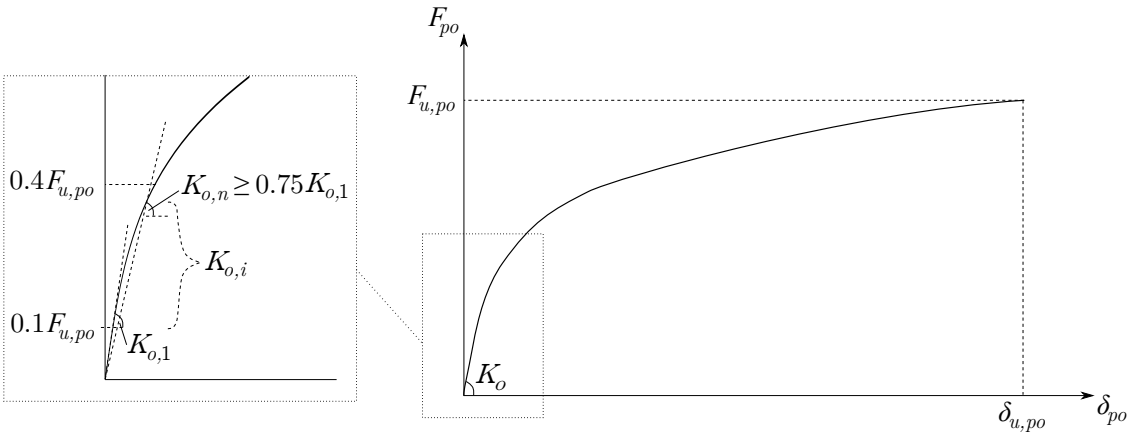


Figure 3.32: Typical load-slip curve per connector in shear and calculation detail for the initial stiffness K_o

A summary of the average measured properties from the push-out tests, along with the observed failure modes, is provided in Table 3.17. The failure modes are also illustrated in Figure 3.33. A combined failure mode is indicated by the + sign while progress to additional modes is indicated by the → sign. Higher capacities are observed when two boards are used, while thicker steel reduced tilting and increased bearing along the whole length of the screw in contact with board resulting in higher initial stiffness. A 180% increase in $F_{u,po}$ was achieved by increasing the diameter of the screw from 3.5 mm to 5.5 mm, increasing the number of layers of plasterboard from one to two and thickening the cold-formed steel section from 1.2 mm to 2.0 mm. It is important to note that the 5.5 mm screws are not designed

for use with plasterboards and therefore, their head shape is not ideal; a flatter head would have led to further improvements in performance, as demonstrated with the pull-through tests in Section 3.3.

Table 3.15: Measured results from push-out tests on single board specimens

Designation	K_o (kN/mm)	$K_{o,40}$ (kN/mm)	$F_{u,po}$ (kN)	$\delta_{u,po}$ (mm)
PO-35-1P-12-1	1.11	0.78	0.51	10.3
PO-35-1P-12-2	1.19	0.75	0.48	9.97
PO-35-1P-12-3	1.13	0.80	0.47	10.7
Average	1.14	0.77	0.49	10.3
COV	0.04	0.03	0.04	0.04
PO-35-1P-20-1	3.51	0.90	0.54	12.7
PO-35-1P-20-2	3.11	0.95	0.53	8.35
PO-35-1P-20-3	3.35	1.03	0.55	11.0
Average	3.32	0.96	0.54	10.7
COV	0.06	0.07	0.01	0.20
PO-55-1P-12-1	1.03	0.84	0.58	5.10
PO-55-1P-12-2	1.10	0.80	0.59	6.33
PO-55-1P-12-3	0.99	0.80	0.61	5.02
Average	1.04	0.81	0.59	5.48
COV	0.05	0.03	0.02	0.13

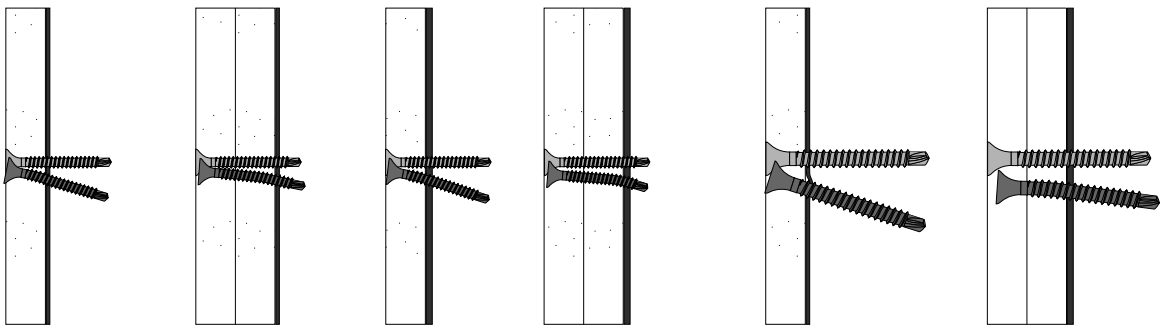


Figure 3.33: Illustrations of the observed failure modes for (a) PO-35-1P-12, (b) PO-35-2P-12, (c) PO-35-1P-20, (d) PO-35-2P-20, (e) PO-55-1P-12 and (f) PO-55-2P-20 specimens

Table 3.16: Measured results from push-out tests on double board specimens

Designation	K_o (kN/mm)	$K_{o,40}$ (kN/mm)	$F_{u,po}$ (kN)	$\delta_{u,po}$ (mm)
PO-35-2P-12-1	2.88	0.45	0.81	11.9
PO-35-2P-12-2	1.79	0.39	0.87	11.4
PO-35-2P-12-3	2.11	0.40	0.90	12.0
Average	2.26	0.41	0.86	11.8
COV	0.25	0.08	0.05	0.03
PO-35-2P-20-1	0.91	0.46	0.67	4.72
PO-35-2P-20-2	0.89	0.47	0.75	6.02
PO-35-2P-20-3	1.22	0.47	0.75	5.45
Average	1.00	0.47	0.72	5.40
COV	0.18	0.02	0.06	0.12
PO-55-2P-20-1	0.50	0.48	1.38	12.0
PO-55-2P-20-2	0.57	0.49	1.42	11.7
PO-55-2P-20-3	0.53	0.51	1.36	11.2
Average	0.54	0.49	1.38	11.6
COV	0.06	0.02	0.02	0.03

Table 3.17: Average measured results from push-out tests

Designation	K_o (kN/mm)	$K_{o,40}$ (kN/mm)	$F_{u,po}$ (kN)	$\delta_{u,po}$ (mm)	Failure mode
PO-35-1P-12	1.14	0.77	0.49	10.3	T + B
PO-35-2P-12	2.26	0.41	0.86	11.8	T + PT → M
PO-35-1P-20	3.32	0.96	0.54	10.7	T + B
PO-35-2P-20	1.34	0.47	0.72	5.40	T + PT → M → S
PO-55-1P-12	1.04	0.81	0.59	5.48	T + B
PO-55-2P-20	0.54	0.49	1.38	11.6	T + PT → M

T = tilting; B = bearing; PT = pull-through; M = bending of screw; S = shear failure of screw

3.5 Assemblage of experimental database

Experimental data from the literature, to complement those reported herein, have been collected. The combined dataset are utilised for the development and assessment of predictive models in Chapter 4. Data from material tests on cold-formed steel have not been collected since a detailed review and development of a predictive model for the description of stress-strain curves for cold-formed steels has been recently performed by Gardner & Yun (2018), where more than 700 experimental stress-strain curves were collected and analysed. Similarly, in the work by Yun & Gardner (2017), more than 500 stress-strain curves for hot-rolled steel were assessed and predictive models were developed. Also, no data were found in the literature for the individual mode of screw pull-through in plasterboard or OSB. Data collection was therefore focused on plasterboard and OSB material and the behaviour of screw connectors in shear.

3.5.1 Data on material behaviour

3.5.1.1 Plasterboard

A summary of the experimental data on the material properties of standard type plasterboard, both from the the current study and collected from the literature is presented in Table 3.18, along with the number of tests from each source. The average material properties are provided in the Table 3.18, while the individual stress-strain curves are examined in Chapter 4. The employed notation is as defined in Section 3.2.2.

In the experimental studies reported by Petrone et al. (2016), tests were performed on five different types of plasterboard, two of which are considered to be standard and have hence been included in Table 3.18. Three tensile coupons of 12.5 mm and 15.0 mm thick standard plasterboard tested in the longitudinal direction were reported by Selvaraj & Madhavan (2019*b*) as part of an experimental investigation on stud walls. For all the gathered experimental data, full stress-strains curves were provided and are examined in Chapter 4.

Table 3.18: Summary of key average material properties from the present study and the literature on standard plasterboard

Source	Thickness (mm)	Density (kg/m^3)	Tension				Compression				
			No. of tests	E (MPa)	f_u (MPa)	ε_u (%)	No. of tests	E (MPa)	f_u (MPa)	ε_u (%)	$\varepsilon_{u,0.8}$ (%)
Longitudinal											
Present study	12.5	665	5	1650	1.45	0.61	4	2110	3.81	0.23	0.37
Petrone et al. (2016)	12.5	720	15	1940	1.86	0.98	14	2470	3.28	0.19	0.36
Petrone et al. (2016)	18.0	862	16	4630	1.56	0.74	16	3310	5.48	0.22	0.28
Selvaraj & Madhavan (2019*b*)	12.5	NR	3	2100	1.29	0.96	-	-	-	-	-
Selvaraj & Madhavan (2019*b*)	15.0	NR	3	2270	1.40	0.90	-	-	-	-	-
Transverse											
Present study	12.5	665	5	1670	0.67	0.38	4	2130	3.33	0.23	0.42
Petrone et al. (2016)	12.5	720	16	1540	0.80	0.45	16	2130	3.02	0.30	0.65
Petrone et al. (2016)	18.0	862	15	3900	0.68	0.20	15	3080	4.94	0.22	0.31

NR = not reported

3.5.1.2 OSB

A summary of key material properties of OSB, gathered from the current study and the literature (Chen & He 2017, Plenzler et al. 2017, Zhu et al. 2005), are presented in Table 3.19. The number of tests and average properties from each source are reported along with the number (in brackets) of the available full stress-strain (σ-ε) curves, which are examined individually in Chapter 4. A database of 120 stress-strain curves for 9.5 mm thick OSB is reported by Chen & He (2017) for specimens tested both in tension and compression, cut at 0°, 45° and 90° to the direction of production of the board. Tests along these three directions were also performed in tension only by Plenzler et al. (2017) and in both compression and tension by Zhu et al. (2005). In the work by Plenzler et al. (2017), no stress-strain curves are provided, but the mean values of Young's modulus and strength are reported for the core and outer surfaces of an 18 mm thick type 3 OSB (OSB/3); the properties reported in Table 3.19 are those of the outer surfaces. Similarly, average properties are reported by Zhu et al. (2005), with only two stress-strain curves provided as typical examples in the longitudinal direction, both for tension and compression.

Characteristic values of key design properties such as density, Young's modulus and ultimate strengths in bending, compression and tension, both parallel and perpendicular to the direction of production of the board, for thicknesses of less than 25 mm are provided in EN 12369-1 (2001). In Table 3.19 the relevant properties for OSB/3, for thicknesses between 10 mm and 18 mm are provided for comparison with the the results of this study and the data gathered from the literature.

The results of the current study in tension are generally consistent with those reported in the literature, whereas in compression, the obtained values of strength are approximately 5-15% lower than the results from the literature. The tensile strength in the longitudinal direction given in EN 12369-1 (2001) is approximately 20% lower compared to the results from the current study and literature. On the other hand, the compressive strength reported in EN 12369-1 (2001) is approximately 10% higher compared to the data reported in the literature and 20-25% higher compared to the results of this study, both for the longitudinal and transverse load directions.

Table 3.19: Summary of key average material properties from the present study and the literature on OSB

Source	Thickness (mm)	Density (kg/m^3)	Tension No. of tests (σ-ε curves)	Tension E (MPa)	Tension f_u (MPa)	Tension ε_u (%)	Compression No. of tests (σ-ε curves)	Compression E (MPa)	Compression f_u (MPa)	Compression ε_u (%)	Compression $\varepsilon_{u,0.8}$ (%)
Longitudinal											
Present study	11	590	5 (5)	4100	11.7	0.37	4 (4)	4020	12.1	0.40	0.54
Chen & He (2017)	9.5	580	20 (20)	3160	12.1	0.38	20 (20)	3250	13.6	0.55	0.65
Plenzler et al. (2017)	18	594	5 (NR)	5150	11.2	NR	-	-	-	-	-
Zhu et al. (2005)	9	575	8 (1)	3770	11.9	0.39	5 (1)	3650	14.1	0.58	0.78
EN 12369-1 (2001)	10-18	550	NR	3800	9.4	NR	NR	3800	15.4	NR	NR
Transverse											
Present study	11	590	5 (5)	2940	7.01	0.37	4 (4)	2780	10.7	0.50	0.66
Chen & He (2017)	9.5	580	20 (20)	2330	9.7	0.42	20 (20)	2490	11.3	0.61	0.70
Plenzler et al. (2017)	18	594	5 (NR)	3720	6.15	NR	-	-	-	-	-
Zhu et al. (2005)	9	575	8 (NR)	2560	7.55	0.29	5 (NR)	2770	12.6	NR	NR
EN 12369-1 (2001)	10-18	550	NR	3000	7.0	NR	NR	3000	12.7	NR	NR
at 45°											
Chen & He (2017)	9.5	580	20 (20)	2760	10.9	0.39	20 (20)	2770	12.5	0.57	0.66
Plenzler et al. (2017)	18	594	5 (NR)	4850	5.84	NR	-	-	-	-	-
Zhu et al. (2005)	9	575	8 (NR)	3170	9.14	0.29	5 (NR)	3100	13.9	NR	NR

NR = not reported

3.5.2 Shear behaviour

Test data on the shear behaviour of screws connecting boards to cold-formed steel have been collected from the literature based on the following three conditions. Firstly, only standard plasterboard and OSB were considered. Secondly, tests in which the screws were located near to the edge or end of the board, leading to the board breaking away (Fiorino et al. 2017, Serrette et al. 1997, Swensen et al. 2015, Vieira & Schafer 2009, Chen et al. 2016, Ye et al. 2016), were ignored; all other failure modes were considered. Finally, data obtained from both push and pull tests were considered but only under monotonic loading.

A summary of the key details and average results from the shear behaviour tests featuring screwed connections between cold-formed steel and plasterboard or oriented strand board collected from the literature (Serrette et al. 1997, Peterman et al. 2014, Fiorino et al. 2007, Vieira & Schafer 2009, Chen et al. 2016, Ye et al. 2016, Stergiopoulos et al. 2019) is presented in Table 3.20, along with the results of the current study. The data from a total of 51 tests on plasterboard specimens from seven different sources and 42 tests on OSB specimens from five different sources were collected. Full load-displacement (F-δ) curves were available for 42 of the plasterboard tests and 24 of the OSB tests, which allowed calculation of properties such as the initial stiffness K_o (as described in Section 3.4.2) and the analysis of the form of the response, as examined in Chapter 4. For each group of tests, along with the number of test data from each source and the average measured properties ($F_{u,po}$, $\delta_{u,po}$, $K_{o,40}$ and K_o), key details for each group of tests are provided, such as the diameter of the screws and the thicknesses of the steel sections and boards. The observed failure modes are also provided.

Some comments on the data collection follow. The pull tests performed by Peterman et al. (2014) and Vieira & Schafer (2009) with connectors spaced at different distances apart were grouped together since the variation in spacing between the connectors did not have a strong effect on the results, while the tests performed by Vieira & Schafer (2009) with overdriven screws and those that examined the influence of the humidity content of the board were excluded. For the tests reported by Chen et al. (2016), only the room temperature

specimens, and not those subjected to elevated temperatures were considered.

Regarding the observed modes of failure, for tests comprising a single layer plasterboard, the main failure mode was tilting of the screws and subsequent bearing into the material. On the other hand, for the OSB test specimens, bending of the screws was shown to be the principal mode of failure after some initial tilting and bearing into the material. Tilting of the screws generally arises in specimens with weaker and thinner board material while screw bending occurs when the board is sufficiently strong or thick to restrict tilting and hence enforce flexure of the screws. The thickness of the steel also plays a role, with thicker material restricting tilting of the screws (Vella et al. 2020). For the groups of tests in the current study employing two layers of plasterboard, screw bending was dominant. Pull-through usually developed eventually in all cases, following the types of failure mentioned above, for both the plasterboard and OSB specimens.

As described in Section 3.4.2, the test specimens with two layers of plasterboard, 2.0 mm thick steel and 3.5 mm screws all featured failure of the screws in shear. Peterman et al. (2014) reported similar shear failures of the screws in specimens with 4.8 mm diameter screws connecting OSB material to 2.46 mm thick steel. In both studies (i.e. the present study and the one by Peterman et al. (2014)), when the same tests were repeated using thinner steel sections, the ultimate load was higher and shearing of the screw did not occur. Although further investigation is needed to support this, it appears that when the steel is thick enough (at least half the diameter of the screw connector) and the board is sufficiently strong (either through material strength or thickness), shearing of the screw can occur as a result of high shear, coupled with bending and axial tension in the screw.

From the collected data, it can be observed that the average stiffness calculated at 40% of the peak load $K_{o,40}$ varies between about 0.4 and 1.8 kN/mm for the plasterboard specimens and between about 0.6 and 1.9 kN/mm for the OSB specimens. The average initial stiffness K_o can be seen to be consistently higher than $K_{o,40}$ for all test specimens, indicating early nonlinearity of the load-displacement curves.

Table 3.20: Summary of key average results from shear behaviour tests from the present study and the literature

Source	No. of tests	Full F - δ curves	Screw diameter (mm)	Steel thickness (mm)	Board thickness (mm)	$F_{u,po}$ (kN)	$\delta_{u,po}$ (mm)	$K_{o,40}$ (kN/mm)	K_o (kN/mm)	Failure mode
Plasterboard										
Present study	3	3	3.5	1.2	12.5	0.49	10.3	0.77	1.14	T + B
	3	3	3.5	1.2	2 × 12.5	0.86	11.8	0.41	2.26	T + PT → M
	3	3	3.5	2.0	12.5	0.54	10.7	0.96	3.32	T + B
	3	3	3.5	2.0	2 × 12.5	0.72	5.40	0.47	1.00	T + PT → M → S
	3	3	5.5	1.2	12.5	0.59	5.48	0.81	1.04	T + B
	3	3	5.5	2.0	2 × 12.5	1.38	11.6	0.49	0.54	T + PT → M
Peterman et al. (2014)	4	4	3.5	0.84	12.7	0.51	7.49	0.61	0.63	T + B + PT
	4	4	3.5	1.37	12.7	0.56	6.48	0.61	0.70	T + B + PT
	4	4	3.5	2.46	12.7	0.48	4.19	0.74	1.03	T + B + PT
Fiorino et al. (2007)	6	2	3.5	1.0	12.5	0.60	4.28	1.77	2.49	T + PT
Ye et al. (2016)	6	4	4.8	0.9	12.5	0.75	3.77	0.69	0.82	T + B
	2	NR	4.8	1.2	12.5	0.79	3.5	NR	NR	T + B
Chen et al. (2016)	1	1	4.2	1.00	12.5	0.72	1.35	0.99	1.07	T + B
	1	1	4.2	1.00	2 × 12.5	1.04	1.87	1.17	1.20	T + B
Stergiopoulos et al. (2019)	1	NR	3.5	1.2	12.5	0.5	NR	0.54	NR	T + B + PT
OSB										
Peterman et al. (2014)	4	4	4.8	0.84	11.1	1.98	7.62	0.85	1.50	T + M + PT
	4	4	4.8	1.37	11.1	2.16	6.73	1.52	1.95	T + M + PT
	5	4	4.8	2.46	11.1	1.66	2.49	1.90	2.33	B + M + S
Fiorino et al. (2007)	16	4	4.2	1.0	9	1.69	5.60	1.05	2.26	T + M + PT
Vieira & Schafer (2009)	1	1	4.8	1.81	11.1	2.35	8.13	1.19	1.42	T + M
Ye et al. (2016)	6	4	4.8	0.9	18	1.98	9.27	0.50	0.62	T + B + M
Serrette et al. (1997)	3	NR	3.5	0.88	11.1	1.03	NR	NR	NR	T + B + M + PT
Total:	86	59								

T = tilting; B = bearing; PT = pull-through; M = bending of screw; S = shear failure of screw. NR = not reported.

The ultimate capacities of the specimens with a single board and 3.5 mm screws from the current study are generally similar to those reported in the literature by Peterman et al. (2014), Fiorino et al. (2007), Vieira & Schafer (2009) and Stergiopoulos et al. (2019). When two layers of plasterboard are used, increases in capacities of up to 75% over equivalent setups with a single layer of plasterboard were found in both the present study and in the work by Chen et al. (2016). The average ultimate capacities from the present study and the literature for the OSB specimens are about three to four times higher than the respective plasterboard specimens; this is attributed to the higher stiffness and strength of the OSB, which changes the main failure mode from tilting to bending of the screw. Displacements at the ultimate capacities $\delta_{u,po}$ can be seen to be rather variable from the collected data. For the plasterboard data, the shear push-out test specimens, examined in this study, exhibited $\delta_{u,po}$ values in excess of 10 mm, whereas the pull-out test specimens, the results of which were collected from the literature (Peterman et al. 2014, Fiorino et al. 2007, Ye et al. 2016, Chen et al. 2016), tend to exhibit lower $\delta_{u,po}$ values, ranging between 2 - 7 mm.

3.6 Conclusions

An experimental investigation into the material response of, and interaction between, the different components of a typical sheathed cold-formed steel wall system has been presented. A total of 103 material and component tests was performed, covering tensile tests on cold-formed steel coupons, compressive and tensile material tests on OSB and plasterboard coupons (extracted from both the longitudinal and transverse board directions), tensile and shear screw connector tests and, finally, pull-through and push-out (shear) tests to examine the behaviour of screwed steel-to-board connections.

The material tests conducted on plasterboard revealed that, although the values of Young's modulus and compressive strength were similar for the longitudinal and transverse directions, the ultimate tensile stress in the longitudinal direction was substantially higher than in the transverse direction. Also, the mechanical properties of the plasterboard material in compression were found to be higher than in tension.

The response of the OSB material was found to be influenced significantly by the direction of loading relative to the production direction of the board, with higher values of Young's modulus and strength measured in the longitudinal direction compared to the transverse direction. This anisotropy is related to the orientation of the strands in the OSB, which are generally parallel to the direction of production (i.e. the longitudinal direction).

Addressing a lack of relevant test data in the literature, a series of pull-through experiments was conducted, featuring different types of screws and sheathing boards – OSB and plasterboards, with the latter board type studied in both single and double layer arrangements. The shape of the underside of the screw head was found to have a significant influence on the pull-through response, with flatter heads resulting in delayed cutting of the paper at the board surface and hence in improved ductility. Using two layers of plasterboard led to average increases of 60% in stiffness and 30% in strength, when compared to a single plasterboard layer. The specimens with the OSB sheathing reached ultimate capacities of about three times those attained by the single layer plasterboard specimens.

To investigate the shear behaviour of screwed connections between cold-formed steel sections and sheathing boards, push-out tests were undertaken, with the varied parameters being the screw size, the number of board layers and the steel thickness. The shear strength of the connection was found to increase with increasing steel thickness, screw diameter and number of plasterboard layers. The main failure modes were screw tilting and screw bending, with the latter mode being more prominent in the specimens with the stronger and thicker boards.

Finally, experimental data from the literature, to complement those reported in the present chapter, have been collected and discussed. In Chapter 4, the combined dataset is employed for the development and assessment of analytical models to describe the observed mechanical responses of the material and components in sheathed cold-formed steel wall systems.

Chapter 4

Analytical modelling of components of sheathed cold-formed steel wall systems

4.1 Introduction

ANALYTICAL models to describe the material and connection behaviour of the key components of sheathed cold-formed steel wall systems are developed and assessed in the present chapter. The experimental data generated and collected in Chapter 3 are utilised for the calibration of the developed models. The assembled experimental database comprises the results of more than 400 physical tests, featuring material tests on plasterboard and oriented strand board (OSB), screw connector tests as well, such as pull-through and push-out tests. A review of key existing formulations by Ramberg & Osgood (1943) and by Mander et al. (1988) type models, which are the basis of the proposed models, is provided in Section 4.2. Material models for describing the behaviour of key components of sheathed wall studs, such as cold-formed steel, plasterboard and OSB are presented in Section 4.3. Predictive behavioural models, expressions of ultimate capacities and recommended values for the remaining model parameters for the interaction between screw connected steel and sheathing components in pull-through and shear are presented in Section 4.4. The develop-

ment of predictive models, presented in this chapter and summarised in Section 4.5, which have been based on the analysis of the collected dataset presented in Chapter 3, are suitable for use in numerical simulations and advanced design methods. The analytical modelling of components of sheathed cold-formed steel wall systems presented in this chapter has been published by Kyprianou et al. (2021*b*).

4.2 Review of key existing formulations

The general form of the stress-strain and load-deformation curves studied herein are characterised by an initial linear portion, followed by a rounded response up to a peak load and an unloading path. Although other expressions exist, the most widely adopted formulations to represent the above described behaviour are the Ramberg & Osgood (1943) and Mander et al. (1988) type models. The two models are introduced below.

4.2.1 Ramberg-Osgood model

As already discussed in Section 2.2.1.2 of Chapter 2, the Ramberg-Osgood model presented in Equation (4.1), was initially devised for the constitutive modelling of aluminium (Ramberg & Osgood 1943, Hill 1944), and has been widely used for describing the material behaviour of metals exhibiting a rounded stress-strain curve, with no distinct yield point. A two stage version (Rasmussen 2003, Mirambell & Real 2000) of the original model is now used to provide an accurate description of the stress-strain behaviour of several metals, including cold-formed steel (Gardner & Yun 2018), stainless steel at both room temperatures (Rasmussen 2003, Mirambell & Real 2000, Arrayago et al. 2015) and elevated temperatures (Liang et al. 2019) and aluminium alloys (Gardner & Ashraf 2006); the second stage was introduced to enable an accurate description of the stress-strain response of these materials over their full range, overcoming limitations in accuracy of the original expression.

The two-stage Ramberg-Osgood model, in its latest format as provided by Gardner & Yun (2018), is presented in Equations (4.1) and (4.2), comprises two parts: the first stage describes the stress-strain response from the origin to the 0.2% proof stress $\sigma_{0.2}$ while

the second stage describes the curve from the 0.2% proof stress to the ultimate stress σ_u; continuity in position and slope is ensured at the intersection between the two stages. In Equations (4.1) and (4.2), σ and ε are the engineering stress and strain respectively, E is the Young's modulus, $E_{0.2}$ is the tangent modulus at $\sigma_{0.2}$, ε_u and $\varepsilon_{0.2}$ are the total strains corresponding to the ultimate and 0.2% proof stresses respectively while n and m are strain hardening exponents determining the degree of roundedness of the stress-strain curve.

$$\varepsilon = \frac{\sigma}{E} + 0.002\left(\frac{\sigma}{\sigma_{0.2}}\right)^n, \qquad \text{for} \quad \sigma \leq \sigma_{0.2} \tag{4.1}$$

$$\varepsilon = \frac{\sigma - \sigma_{0.2}}{E_{0.2}} + \left(\varepsilon_u - \varepsilon_{0.2} - \frac{\sigma_u - \sigma_{0.2}}{E_{0.2}}\right)\left(\frac{\sigma - \sigma_{0.2}}{\sigma_u - \sigma_{0.2}}\right)^m + \varepsilon_{0.2}, \qquad \text{for} \quad \sigma_{0.2} < \sigma \leq \sigma_u \tag{4.2}$$

A generalised form of the single stage Ramberg-Osgood model is illustrated in Figure 4.1 and given by Equation (4.3) where σ_x and ε_x are the stress and strain of the point through which the curve is forced to pass.

$$\varepsilon = \frac{\sigma}{E} + \left(\varepsilon_x - \frac{\sigma_x}{E}\right)\left(\frac{\sigma}{\sigma_x}\right)^n \tag{4.3}$$

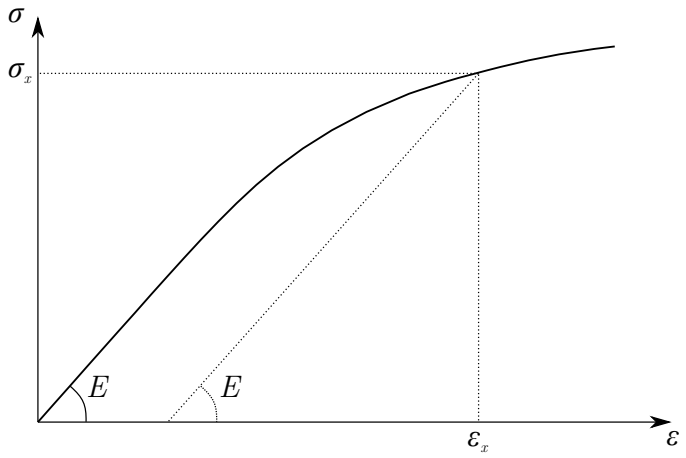


Figure 4.1: Generalised form of single stage Ramberg-Osgood model

4.2.2 Mander model

The Mander model (Mander et al. 1988), given by Equation (4.4) and illustrated in Figure 4.2, has been shown to be capable of accurately capturing the full stress-strain curve

of confined concrete for various arrangements of transverse reinforcement. It accounts for both the strength enhancement due to confinement and the slope of the descending part of the material curve.

$$\sigma = f_c \frac{\varepsilon}{\varepsilon_c} \frac{r}{r - 1 + \left(\frac{\varepsilon}{\varepsilon_c}\right)^r} \quad \text{for} \quad 0 < \varepsilon < \varepsilon_{c,u} \tag{4.4}$$

$$\text{with} \quad r = \frac{E}{E - \frac{f_c}{\varepsilon_c}} \tag{4.5}$$

In Equation (4.4), f_c and ε_c are the compressive strength and corresponding strain respectively, $\varepsilon_{c,u}$ is the final compressive strain while r is defined according to Equation (4.5), where E is the Young's modulus.

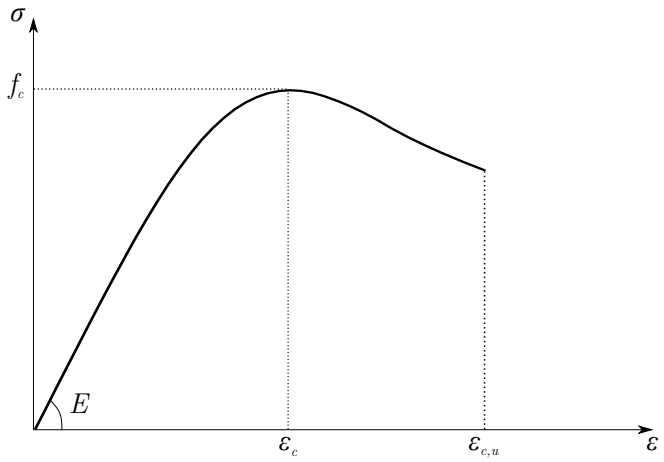


Figure 4.2: Mander et al. (1988) model

4.2.3 Discussion

The formulation of the Ramberg-Osgood model is such that it can only describe the ascending part of a curve, with strain expressed as a function of the stress. The Ramberg-Osgood expressions (Rasmussen 2003, Mirambell & Real 2000, Arrayago et al. 2015, Gardner & Ashraf 2006, Gardner & Yun 2018) usually provide a very accurate fit to experimental data obtained from material tests on metals with rounded stress-strain responses, since the degree of roundness can be directly captured through the strain hardening exponents n and m. On the other hand, the response observed during compression tests on materials

such as confined concrete can be more completely described by the Mander model since, with a single expression for stress in terms of strain, both the ascending and descending parts of the response can be captured, accounting for the post-peak capacity. Note that, in both models, three basic parameters need to be defined i.e. E, $\sigma_{0.2}$ and n for the single stage Ramberg-Osgood model and E, f_c and ε_c for the Mander model. The suitability of these two models, and adaptations thereof, for representing the nonlinear stress-strain and load-deformation responses studied herein, is examined throughout the present chapter.

4.3 Material modelling

Describing the material response of the key components (i.e. the steel and the sheathing) of sheathed cold-formed steel wall systems is the focus of the present section. The experimental data assembled in Chapter 3 are analysed and predictive models are developed and assessed.

4.3.1 Cold-formed steel

A model to describe the stress-strain response of cold-formed steel, based on the two-stage Ramberg-Osgood formulation, was developed by Gardner & Yun (2018). Predictive expressions for the key parameters were devised based on an extensive dataset of more than 700 experiments. Use of these expressions led to stress-strain curves that could accurately capture the rounded nature of the material response obtained from tensile testing of the 1.2 mm thick cold-formed steel coupons presented in Chapter 3. However for the steel coupons of 2.0 mm thickness, although some degree of roundness was exhibited up to the yield point $\sigma_{0.2}$, a plateau was observed thereafter, rendering the use of the 2-stage Ramberg-Osgood model inappropriate. This supports the previous observations (Gardner & Yun 2018) that thinner sheet material generally undergoes a higher level of cold-work and is therefore more likely to exhibit a shorter (or no) yield plateau and a more rounded stress-strain curve.

To achieve a good fit to the stress-strain data of the 2.0 mm thick coupons, a three step model is adopted; (i) Equation (4.1) up to $\varepsilon_{0.2}$, (ii) a flat plateau at $\sigma_{0.2}$ and (iii)

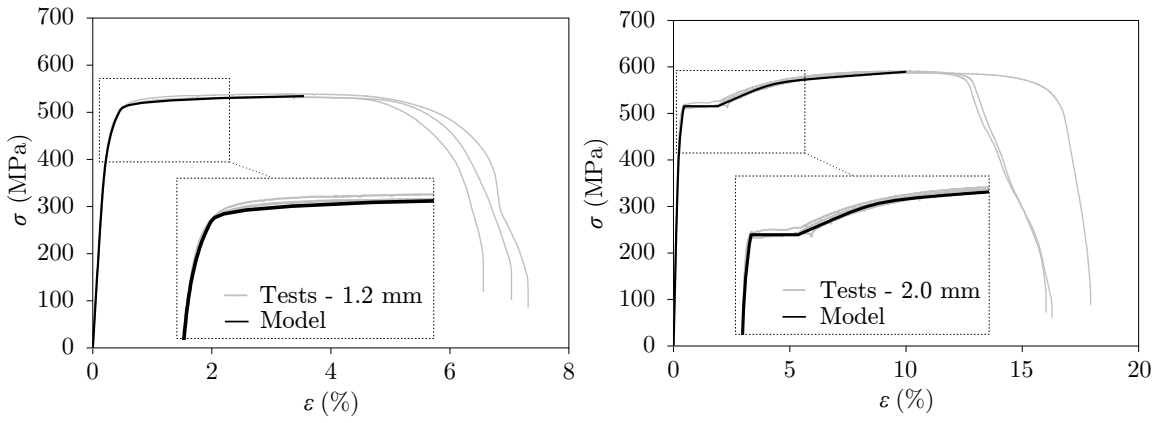
the nonlinear strain hardening model, established and used by Yun & Gardner (2017) for hot-rolled steel, fitted up to ε_u - see Equation (4.6), where ε_{sh} is the strain at the end of the $\sigma_{0.02}$ plateau and the start of the strain hardening expression.

$$\sigma = \begin{cases} \sigma_{0.2} & \text{for} \quad \varepsilon_{0.2} < \varepsilon \leq \varepsilon_{sh} \\ \sigma_{0.2} + (\sigma_u - \sigma_{0.2}) \left\{ 0.4 \left(\dfrac{\varepsilon - \varepsilon_{sh}}{\varepsilon_u - \varepsilon_{sh}} \right) + \dfrac{2 \left(\dfrac{\varepsilon - \varepsilon_{sh}}{\varepsilon_u - \varepsilon_{sh}} \right)}{\left[1 + 400 \left(\dfrac{\varepsilon - \varepsilon_{sh}}{\varepsilon_u - \varepsilon_{sh}} \right)^5 \right]^{1/5}} \right\} & \text{for} \quad \varepsilon_{sh} < \varepsilon \leq \varepsilon_u \end{cases} \tag{4.6}$$

A comparison between the predicted and experimental stress-strain curves reported in Chapter 3 is shown in Figure 4.3 while the average material properties of the tested steel coupons are presented in Table 4.1, where the employed notation is as determined in Section 4.2.1 and t is the average measured thickness. Both models provide a good fit to the respective sets of data and are therefore recommended for the material modelling of the respective cold-formed steel sections.

Table 4.1: Averaged material properties of cold-formed steel reported in Chapter 3 for use in models

t (mm)	E (GPa)	$\sigma_{0.2}$ (MPa)	$\varepsilon_{0.2}$ (%)	ε_{sh} (%)	σ_u (MPa)	ε_u (%)	n	m
1.19	206	500	0.443	-	534	3.323	8.7	4.0
1.99	206	515	0.450	1.894	589	10.007	8.7	-



(a) 1.2 mm thick coupons

(b) 2.0 mm thick coupons

Figure 4.3: Stress-strain curves predicted using (a) Equations (4.1) and (4.2) for the 1.2 mm thick coupons and (b) Equations (4.1) and (4.6) the 2.0 mm thick coupons

4.3.2 Sheathing material

4.3.2.1 Plasterboard

Plasterboard is the most commonly used sheathing material for stud wall systems. Physical tests have revealed orthotropic material behaviour, with the mechanical properties in the longitudinal direction of the panel being higher compared to those in the transverse direction. Numerous material test results have been reported in the literature, both in tension and compression. A summary of these is presented in Table 3.18 of Chapter 3.

Petrone et al. (2016) proposed the use of a bilinear stress-strain curve to describe the response of plasterboard material in tension while, when subjected to compression, use of the Mander et al. (1988) model was recommended. The data used for the model derivation by Petrone et al. (2016) were limited to the experimental results conducted by the authors themselves. A broader dataset of 147 material tests (Kyprianou et al. 2021*a*, Petrone et al. 2016, Selvaraj & Madhavan 2019*b*), has been assembled in Chapter 3 and is employed herein to assess the suitability of existing models presented in the literature, along with new predictive models proposed herein. Note that particular attention was given during the model derivation to maintaining a balance between accuracy and simplicity, such that all key aspects of the material behaviour are captured while limiting the required number of input parameters.

Following analysis of the experimental results, the model presented in Equation (4.7) has been established for modelling the material behaviour of plasterboard, both in tension and compression. The proposed model is based on the Ramberg-Osgood (R-O) formulation presented in Equation (4.3), appropriately adapted to fit the experimental curves. It should be mentioned that, when modelling the material response of plasterboard under compression, both the Mander et al. (1988) model presented in Equation (4.4) and the Ramberg-Osgood expression presented in Equation (4.7) were found capable of providing good fits to the experimental data, though the Ramberg-Osgood material was more accurate for individual specimens up to the peak stress owing to the ability to change the value of n to alter the degree of roundedness of the curve.

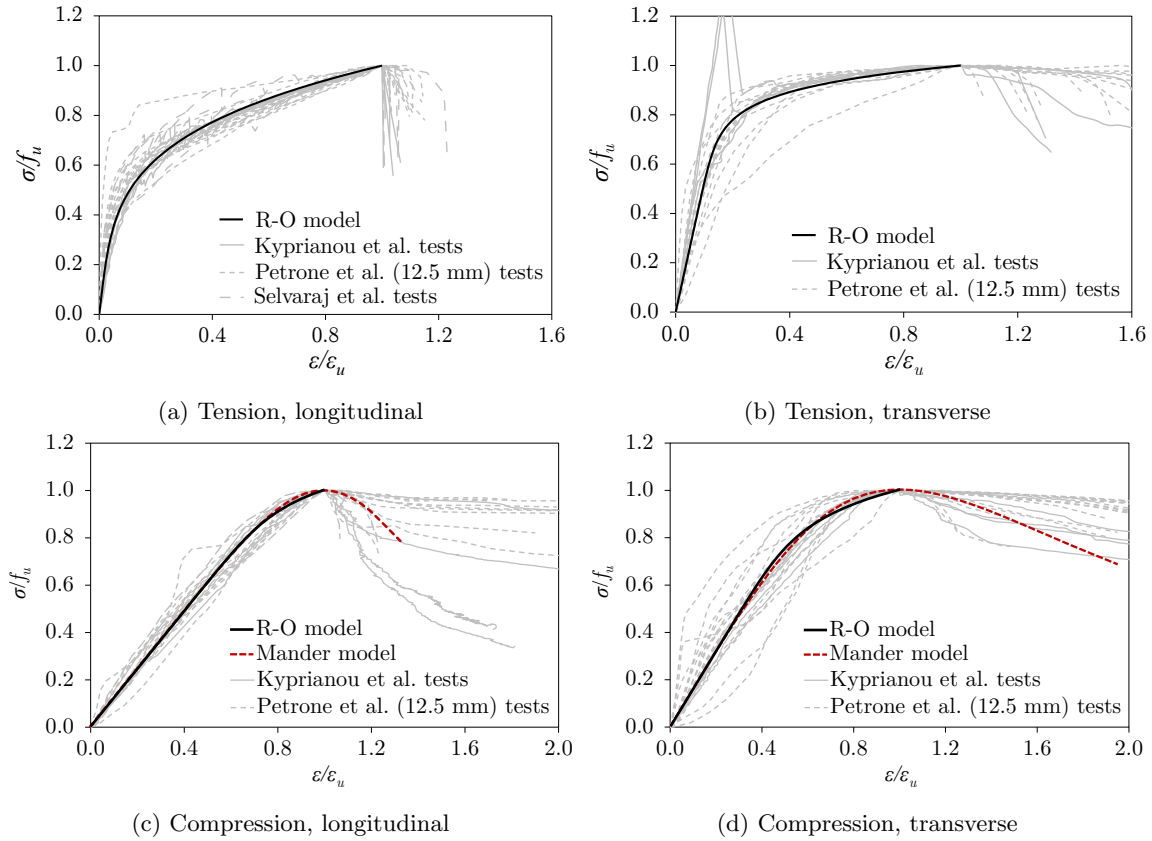
$$\varepsilon = \frac{\sigma}{E} + \left(\varepsilon_u - \frac{f_u}{E}\right)\left(\frac{\sigma}{f_u}\right)^n \tag{4.7}$$

The parameters employed in Equation (4.7) are the Young's modulus E (calculated as the slope of the curve between the points corresponding to 10% and 40% of the ultimate strength), the ultimate strength f_u, its corresponding strain ε_u and n, which is the exponent controlling the degree of roundness of the curve; these have been determined as the average values for the full examined dataset and are reported in Table 4.2. Note that the model can be used for describing the material behaviour of plasterboard both in tension and compression and in the longitudinal and transverse directions, by employing the corresponding values of E, f_u, ε_u and n.

Table 4.2: Averaged measured material properties of plasterboard

Thickness (mm)	Loading	Direction	E (MPa)		f_u (MPa)		ε_u (%)		n	
			Mean	COV	Mean	COV	Mean	COV	Mean	COV
12.5 – 15.0	Tension	Longitudinal	1940	0.30	1.66	0.17	0.90	0.31	4.0	0.18
		Transverse	1570	0.32	0.77	0.10	0.43	0.48	10.7	0.26
	Compression	Longitudinal	2390	0.23	3.40	0.09	0.20	0.16	10.2	0.16
		Transverse	2130	0.41	3.08	0.05	0.29	0.28	7.9	0.16
18.0	Tension	Longitudinal	4630	0.15	1.56	0.08	0.74	0.30	7.0	0.28
		Transverse	3900	0.16	0.68	0.10	0.20	0.32	5.0	0.30
	Compression	Longitudinal	3310	0.20	5.48	0.16	0.22	0.38	11.0	0.27
		Transverse	3080	0.25	4.94	0.20	0.22	0.36	11.0	0.27

Comparisons between the normalised experimental stress-strain curves on 12.5 mm and 15.0 mm thick plasterboard and the proposed model are shown in Figure 4.4, where the model can be seen to accurately capture the material response of the plasterboard in both directions (i.e. longitudinal and transverse) and loading configurations (i.e. tension and compression). Comparisons against the Mander et al. (1988) model (given by Equation (4.4) for which $f_c = f_u$ and $\varepsilon_c = \varepsilon_u$), employed as recommended by Petrone et al. (2016) for specimens in compression only and plotted up to 80% of f_u post-peak, are also shown in Figure 4.4 since this model has been also found to provide a good fit to the test curves. Note that the test results presented in Figure 4.4 are normalised against their respective



(a) Tension, longitudinal

(b) Tension, transverse

(c) Compression, longitudinal

(d) Compression, transverse

Figure 4.4: Comparison of the proposed model for plasterboard with normalised test curves for specimens of 12.5-15.0 mm thickness in (a-b) tension and (c-d) compression

values of f_u and ε_u to allow all curves to be shown together. Finally, the material models for plasterboard under compression and tension for both directions (i.e. longitudinal and transverse), presented for the average measured mechanical properties reported in Table 4.2, are shown in Figure 4.5.

4.3.2.2 Oriented Strand Board

Oriented strand boards (OSB) are frequently used as sheathing panels in wall systems due to their durability. Although several studies have been conducted (Zhu et al. 2005, Plenzler et al. 2017, Chen & He 2017) to determine the mechanical properties of OSB material, few models describing the observed stress-strain response have been devised. A parabolic stress-strain curve was proposed by Zhu et al. (2005) and Chen & He (2017) for OSB while the single Ramberg-Osgood formulation was adapted by Kyvelou et al. (2018) to describe

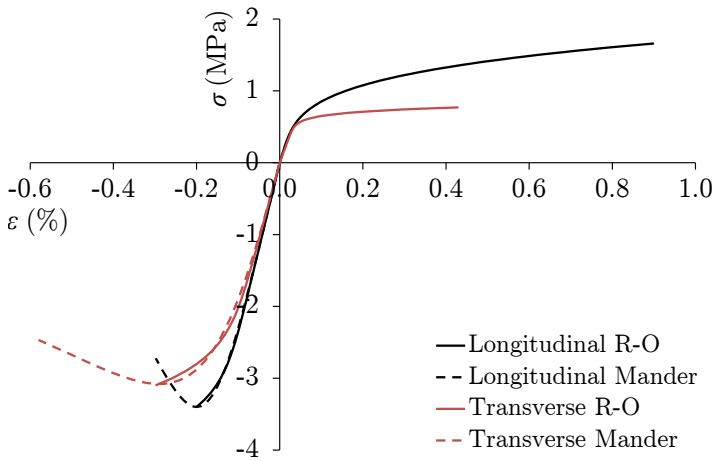


Figure 4.5: The Ramberg-Osgood (R-O) and Mander models using the average measured material properties of plasterboard, with positive values of stress and strain signifying tension (where only the R-O model is used) and negative values signifying compression (where both models are shown)

the stress-strain behaviour of wood-based particle boards. Aiming at the establishment of a material model for OSB derived on the basis of a wider experimental dataset, results from 195 material tests on OSB have been assembled in Chapter 3 and are employed herein; these are summarised in Table 3.19.

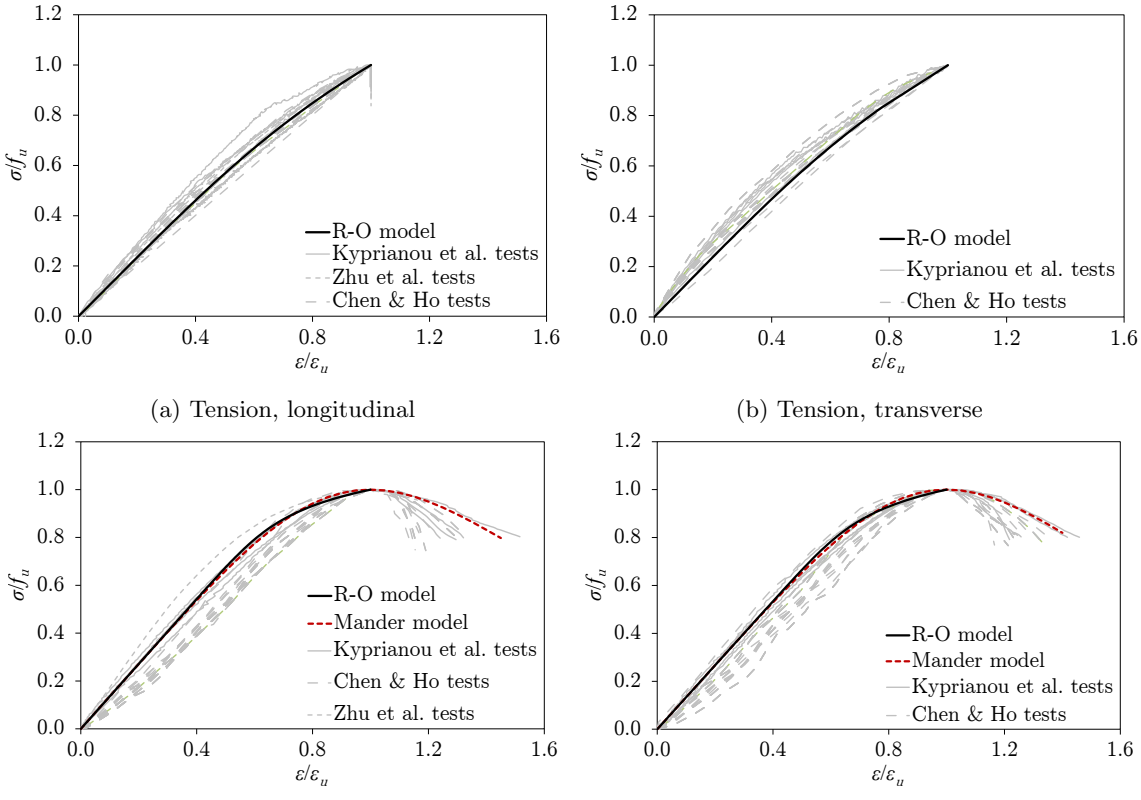
The Ramberg-Osgood formulation provided in Equation (4.7) has been adopted for the description of the material response of OSB; the definitions of the employed parameters are provided in Section 4.3.2.1. The proposed model can be used for both directions (i.e. longitudinal and transverse) and load configurations (i.e. tension and compression), using the respective mechanical properties. A summary of the average measured mechanical properties of the examined dataset is presented in Table 4.3.

The normalised experimental stress-strain curves and the proposed model given by Equation (4.7) are compared in Figure 4.6 where the model is shown to accurately capture the exhibited behaviour in both the longitudinal and transverse directions, both in tension and compression. Note that the presented curves are normalised against their respective ultimate strength f_u and corresponding strain ε_u. In a similar fashion to the plasterboard specimens tested under compression, the Mander et al. (1988) model, plotted up to 80% of f_u post-peak, was also fitted to the data from the OSB specimens tested under compression and was found to also provide a good fit. The material models for OSB under compression

and tension for both directions (i.e. longitudinal and transverse), presented based on the average measured mechanical properties reported in Table 4.3, are shown in Figure 4.7.

Table 4.3: Averaged measured material properties of OSB

Loading	Direction	E (MPa)		f_u (MPa)		ε_u (%)		n	
		Mean	COV	Mean	COV	Mean	COV	Mean	COV
Tension	Longitudinal	3670	0.19	11.9	0.08	0.38	0.08	4.2	0.06
	Transverse	2640	0.20	8.4	0.19	0.38	0.18	4.0	0.09
	A 45°	3180	0.15	9.7	0.10	0.36	0.12	4.0	0.10
Compression	Longitudinal	3430	0.10	13.4	0.07	0.53	0.15	11.5	0.11
	Transverse	2580	0.09	11.4	0.10	0.59	0.16	12.0	0.10
	At 45°	2840	0.08	12.8	0.06	0.57	0.10	12.0	0.10



(a) Tension, longitudinal

(b) Tension, transverse

(c) Compression, longitudinal

(d) Compression, transverse

Figure 4.6: Comparison of the proposed model for OSB with the obtained normalised test curves in both directions in (a-b) tension and (c-d) compression

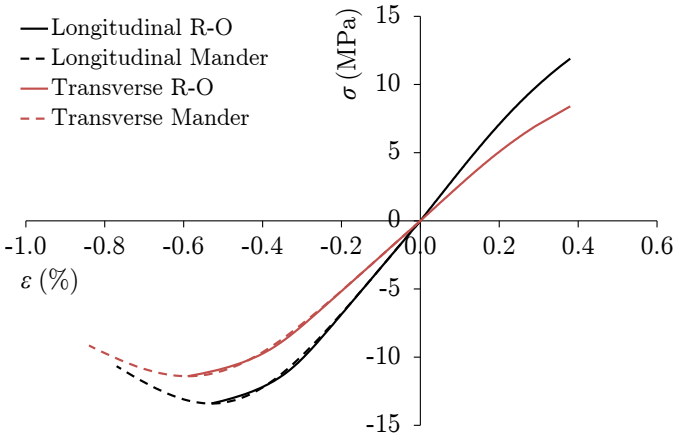


Figure 4.7: The Ramberg-Osgood (R-O) and Mander models using the average measured material properties of OSB, with positive values of stress and strain signifying tension (where only the R-O model is used) and negative values signifying compression (where both models are shown)

4.4 Modelling of interaction between components

The characteristics of the connectors employed within a stud wall system have been shown to play a significant role in the exhibited structural response, since, depending on their arrangement, they can allow effective bracing and mobilise composite action (Peterman & Schafer 2014, Vieira & Schafer 2013, 2016, Kyvelou et al. 2015, Selvaraj & Madhavan 2019*a*, Stergiopoulos et al. 2019). Self-drilling screws, which are the most frequently employed type of connector for stud wall systems, are the focus of the present study; their interaction with the steel studs and sheathing panels is examined in this section.

4.4.1 Pull-through load-deformation response

Although pull-through failures of steel stud-to-sheathing connectors have been reported by several researchers (Peterman & Schafer 2014, Selvaraj & Madhavan 2018*b*, 2019*c*), experiments focusing solely on this type of failure are very limited. In Chapter 3, a series of 25 pull-through tests was conducted and presented in detail; the obtained results are used herein as the basis for the derivation of a predictive model to describe the load-deformation response. Note that the pull-through deformation reported in the examined test results is the net embedment of the screw δ_{pt}, as indicated in Figures 3.19 and 3.21 of Chapter 3.

4.4.1.1 Pull-through load-deformation model

A generalised form of the Ramberg-Osgood expression, which has been used thus far for modelling the examined material responses, was also found to be capable of accurately capturing the shape of the pull-through load-deformation curves presented in Chapter 3 up to the ultimate capacity $F_{u,pt}$. The post-peak response can be described by a straight line passing from the peak point to a point corresponding to 80% of $F_{u,pt}$ post-peak (i.e. point ($\delta_{u,pt,0.8}$, $F_{u,pt,0.8}$)). Note that for the specimens comprising two boards, which were found to exhibit a second peak (i.e. $F_{u,pt,2}$ at a displacement $\delta_{u,pt,2}$), use of an additional linear part can be used for modelling the response between $F_{u,pt,0.8}$ and $F_{u,pt,2}$ - see Figure 4.8. The modified Ramberg-Osgood expression and the bilinear expression post $F_{u,pt}$ proposed herein for the modelling of the pull-through load-deformation characteristics of screw connectors, is provided by Equation (4.8) and illustrated in Figure 4.8.

$$\delta_{pt} = \begin{cases} \dfrac{F_{pt}}{K_{o,40}} + \left(\delta_{u,pt} - \dfrac{F_{u,pt}}{K_{o,40}}\right)\left(\dfrac{F_{pt}}{F_{u,pt}}\right)^{n} & \text{for} \quad \delta_{pt} \leq \delta_{u,pt} \\ \delta_{u,pt} + (F_{pt} - F_{u,pt})\left(\dfrac{\delta_{u,pt,0.8} - \delta_{u,pt}}{F_{u,pt,0.8} - F_{u,pt}}\right) & \text{for} \quad \delta_{u,pt} < \delta_{pt} \leq \delta_{u,pt,0.8} \\ \delta_{u,pt,0.8} + (F_{pt} - F_{u,pt,0.8})\left(\dfrac{\delta_{u,pt,2} - \delta_{u,pt,0.8}}{F_{u,pt,2} - F_{u,pt,0.8}}\right) & \text{for} \quad \delta_{u,pt,0.8} < \delta_{pt} \leq \delta_{u,pt,2} \end{cases} \tag{4.8}$$

In Equation (4.8), δ_{pt} is the pull-through deformation, F_{pt} is the load, $\delta_{u,pt}$ is the deformation at $F_{u,pt}$, $K_{o,40}$ is the secant stiffness calculated at $0.4F_{u,pt}$ and n is the exponent controlling the roundedness of the curve.

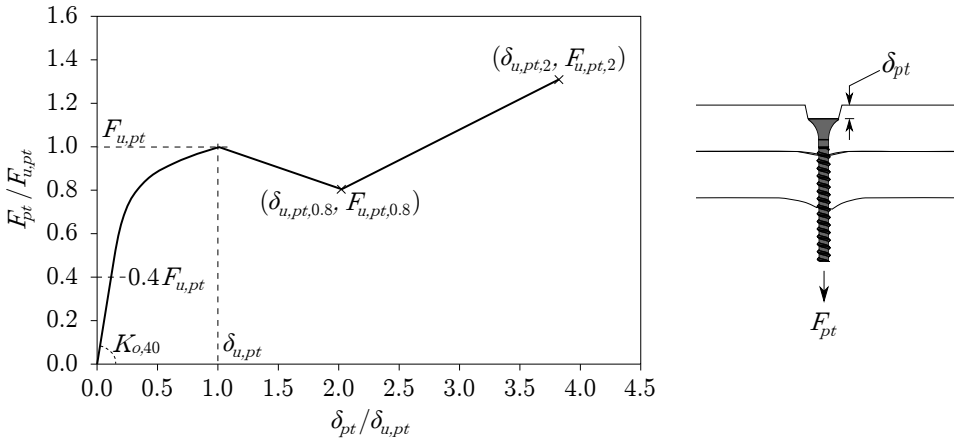


Figure 4.8: Pull-through load-deformation model

4.4.1.2 Calculation of key parameters for pull-through load-deformation model

Analysis of the test results revealed that the resistance of the examined connectors in pull-through depends on the combined effect of the connector head bearing into the surface of the board and the screw threads interacting with the board material. Based on these observations, Equation (4.9) has been devised for the calculation of $F_{u,pt}$, where A_{pt} is the total bearing area during pull-through and f_u is the compressive strength of the board material, taken herein as the average of measured values for the longitudinal and transverse directions. The average value of f_u for each group of tests is provided in Table 4.4 where the designations for the groups of tests start with the letters PT, followed by the screw diameter in mm $\times 10$, then the number of board layers and finally the type of material (with P for plasterboard and O for OSB).

$$F_{u,pt} = A_{pt} f_u \tag{4.9}$$

The bearing area A_{pt} consists of three components, as described by Equation (4.10):

$$A_{pt} = A_{s,thr} + A_{s,hd} + A_{s,eff} \tag{4.10}$$

where $A_{s,thr}$ is the contribution by the threads given by Equations (4.11) and (4.12):

$$A_{s,thr} = A_{s,thr,1}(t_b - h_{s,hd} - s_{s,nonthr})/s_{s,thr} \tag{4.11}$$

$$\text{in which} \quad A_{s,thr,1} = \pi \left[(d_{s,thr}/2)^2 - (d_{s,sh}/2)^2\right] \tag{4.12}$$

$A_{s,hd}$ is the area directly below the head of the screw given by Equation (4.13):

$$A_{s,hd} = \pi \left[(d_{s,hd}/2)^2 - (d_{s,thr}/2)^2\right] \tag{4.13}$$

$A_{s,eff}$ is an effective area around $A_{s,hd}$, defined by means of the angle $\theta_{s,eff}$ shown in Figure 4.9, as given by Equation (4.14):

$$A_{s,eff} = \pi \left[(d_{s,hd}/2 + l_{s,eff})^2 - (d_{s,hd}/2)^2\right] \tag{4.14}$$

$$\text{where} \quad l_{s,eff} = h_{s,hd} \tan \theta_{s,eff} \tag{4.15}$$

It should be mentioned that the area $A_{s,eff}$ has been established to account for the conical failure surfaces observed in the pull-through tests presented in Chapter 3 (see Figure 3.22), while the angle $\theta_{s,eff}$ was found to be dependent on the shape of the screw head, with the screws of 3.5 mm diameter having flatter heads (compared to the screws of 4.8 mm and 5.5 mm diameter) and thus higher values of $\theta_{s,eff}$. The recommended values of $\theta_{s,eff}$ for the different screw types have been determined based on the dataset presented in Chapter 3 and are reported in Table 4.4. The aforementioned areas can be determined using Equations (4.11) to (4.15) while their graphical illustration, along with the employed screw geometry notation, are provided in Figure 4.9.

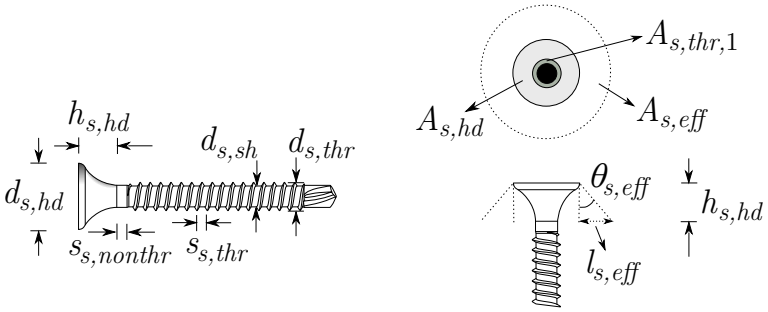


Figure 4.9: Screw connector geometry and bearing pull-through areas

The calculated $F_{u,pt}$ values, for the screws tested in Section 3.3 of Chapter 3, together with the contributing areas determined using Equations (4.11) to (4.15) are summarised in Table 4.4. Good agreement between the calculated and test values of $F_{u,pt}$ is demonstrated in Figure 4.10, with the average ratio of the test to calculated $F_{u,pt}$ values being 0.99 with a COV of 0.10.

Table 4.4: Pull-through screw properties and comparison between calculated and test capacity $F_{u,pt}$

Designation	Average f_u (N/mm^2)	$\theta_{s,eff}$ (°)	$A_{s,thr}$ (mm^2)	$A_{s,hd}$ (mm^2)	$A_{s,eff}$ (mm^2)	Calc. $F_{u,pt}$ (kN)	Test $F_{u,pt}$ (kN)	Test/Calc. $F_{u,pt}$
PT-35-1P	3.57	30	27.3	45.3	62.1	0.48	0.48	1.00
PT-35-2P	3.57	30	72.9	45.3	62.1	0.64	0.69	1.08
PT-55-1P	3.57	10	42.4	63.7	28.1	0.48	0.50	1.04
PT-55-2P	3.57	10	125.2	63.7	28.1	0.78	0.64	0.82
PT-48-1O	11.4	10	39.5	60.8	23.8	1.41	1.44	1.02

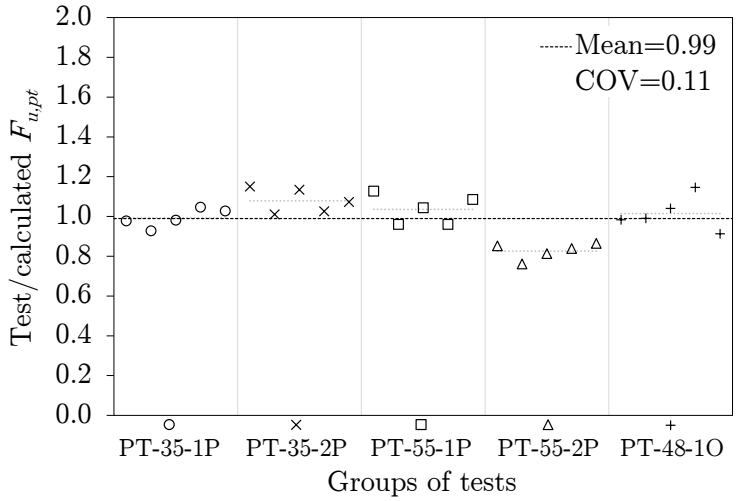


Figure 4.10: Comparison between experimental and calculated values of $F_{u,pt}$

Regarding the other input parameters required for the proposed pull-through load-deformation model given by Equation (4.8), namely the stiffness $K_{o,40}$ and ultimate displacement $\delta_{u,pt}$, recommended average values, expressed as a function of the nominal screw diameter d and overall board thickness t_b are provided in Table 4.5. The average measured

Table 4.5: Average measured properties for tested screws expressed in terms of screw diameter d, overall board thickness t_b and $F_{u,pt}$; recommended representative values for the key model parameters are also provided.

Designation	d (mm)	t_b (mm)		$K_{o,40}/d^2$ (kN/mm^3)	$\delta_{u,pt}/t_b$	$F_{u,pt,0.8}/F_{u,pt}$	$\delta_{u,pt,0.8}/t_b$	$F_{u,pt,2}/F_{u,pt}$	$\delta_{u,pt,2}/t_b$
PT-35-1P	3.5	12.5	Mean	0.85	0.026	0.80	0.033	-	-
			COV	0.13	0.214	0.00	0.090	-	-
PT-55-1P	5.5	12.5	Mean	0.47	0.010	0.80	0.014	-	-
			COV	0.14	0.330	0.00	0.293	-	-
PT-48-1O	4.8	11.0	Mean	0.80	0.049	0.80	0.218	-	-
			COV	0.04	0.250	0.00	0.095	-	-
PT-35-2P	3.5	25.0	Mean	1.34	0.036	0.80	0.081	1.09	0.26
			COV	0.10	0.075	0.00	0.141	0.05	0.17
PT-55-2P	5.5	25.0	Mean	0.85	0.056	0.95	0.077	1.36	0.20
			COV	0.21	0.128	0.02	0.071	0.07	0.14
Recommended representative values				0.80	0.035	0.80	0.075	1.20	0.20

post-peak displacement $\delta_{u,pt,0.8}$, as well as the second-peak displacement $\delta_{u,pt,2}$ for the two

layer specimens, are also provided in terms of t_b, while the loads $F_{u,pt,0.8}$ and $F_{u,pt,2}$ are expressed in terms of the experimental pull-through load $F_{u,pt}$. Note that for the specimens with 5.5 mm diameter screws and two board layers (PT-55-2P), since no more than 5% decreases in $F_{u,pt}$ were observed, $F_{u,pt,0.8}$ was taken as $0.95F_{u,pt}$ (rather than $0.8F_{u,pt}$). In the absence of experimental data, representative values for the key parameters are also provided in Table 4.5.

4.4.1.3 Assessment of proposed pull-through model against experimental data

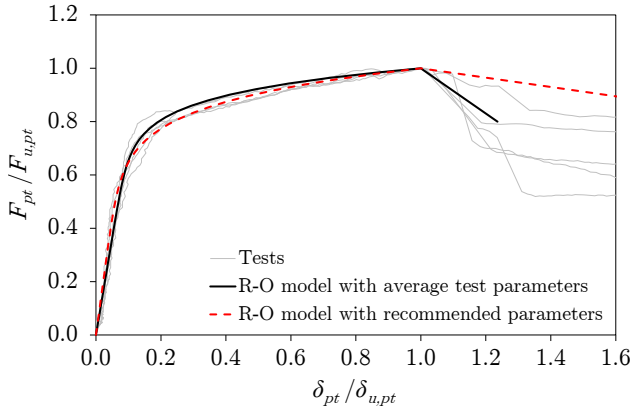
The proposed pull-through model was validated against the test curves reported in Section 3.3 of Chapter 3; typical comparisons between the model predictions and test curves for single- and double-layer specimens are presented in Figures 4.11 and 4.12 respectively, where the load F_{pt}, normalised by $F_{u,pt}$, is plotted against the pull-through deformation δ_{pt}, normalised by $\delta_{u,pt}$. It can be observed that the devised expression using average measured values for the model parameters (summarised in Table 4.6) provides a very good fit to the experimental curves and is therefore suitable for use in numerical simulations and advanced

Table 4.6: Average measured values of model parameters, as determined from pull-through tests

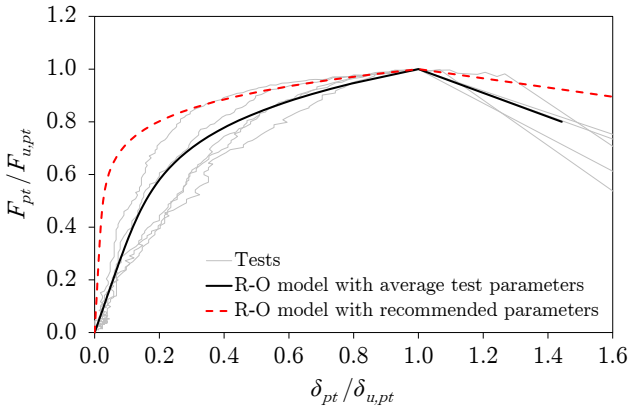
Designation	$K_{o,40}$ (kN/mm)	$F_{u,pt}$ (kN)	$\delta_{u,pt}$ (mm)	$F_{u,pt,0.8}$ (kN)	$\delta_{u,pt,0.8}$ (mm)	$F_{u,pt,2}$ (kN)	$\delta_{u,pt,2}$ (mm)	n
PT-35-1P	10.5	0.48	0.33	0.38	0.41	-	-	10.5
PT-55-1P	14.2	0.50	0.12	0.40	0.18	-	-	5.5
PT-48-1O	18.5	1.44	0.54	1.15	2.40	-	-	7.5
PT-35-2P	16.5	0.69	0.89	0.55	2.03	0.76	6.43	5.0
PT-55-2P	25.6	0.64	1.41	0.61	1.93	0.86	4.96	12.0

design models. Pull-through load-deformation curves based on calculated values of $F_{u,pt}$ and the recommended values for the key model parameters given in Table 4.5, along with a value of $n = 8$ for all curves, are also plotted in Figures 4.11 and 4.12 for comparison. The normalised load-deformation curves obtained using the recommended representative values for the parameters generally provide a good match with the experimental results, particularly up to the ultimate load $F_{u,pt}$, with the exception of the PT-55-1P case shown in Figure 4.11 (b), where the test ultimate displacement is somewhat lower than the recommended representative value; in the presented normalised format, this creates the impression of a

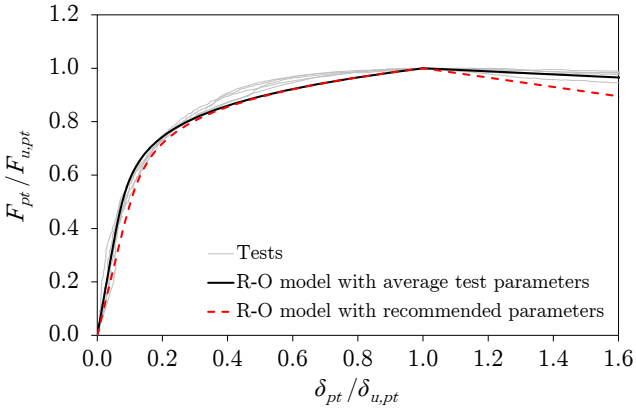
substantial deviation in initial stiffness, though this is not in fact the case when the curves are compared in their unnormalised form.



(a) PT-35-1P



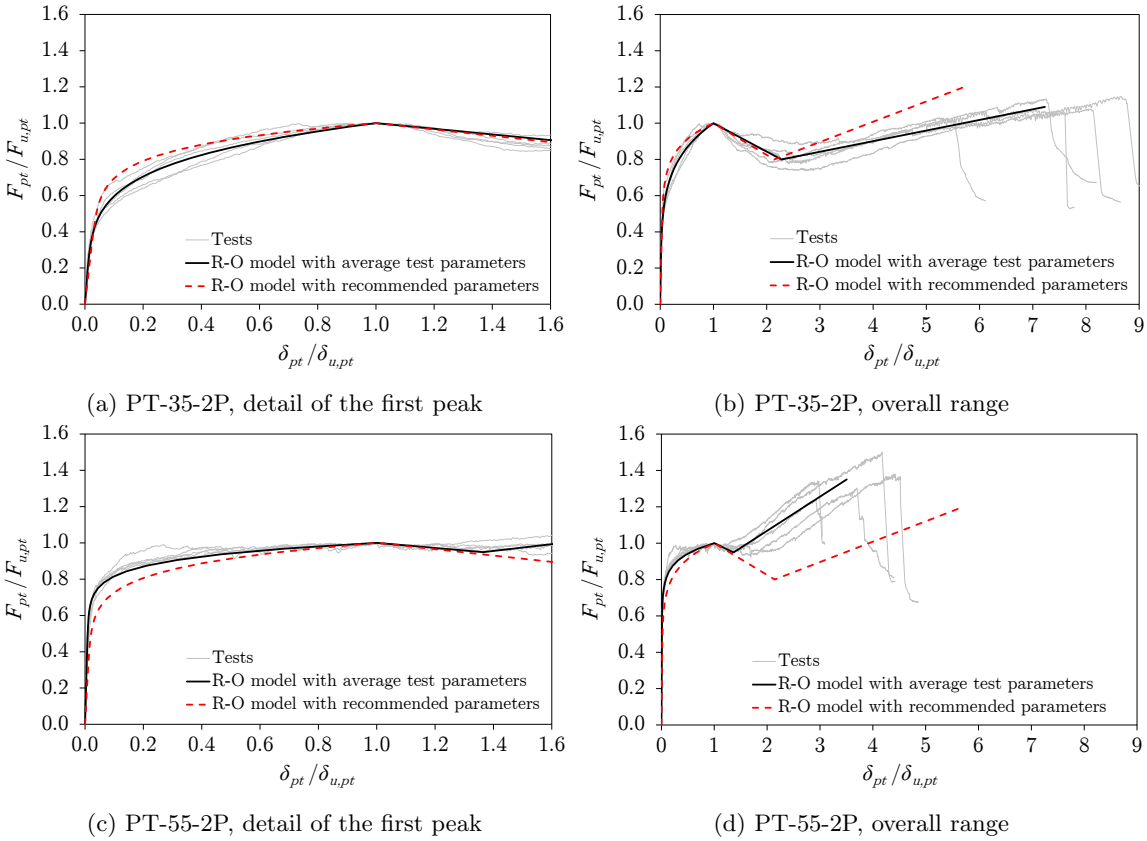
(b) PT-55-1P



(c) PT-48-1O

Figure 4.11: Comparisons of the proposed model using test and recommended predicted input parameters with test curves for single board specimens

The derived model curves for all five test groups using the average measured values of the key input parameters provided in Table 4.6 are plotted together in Figure 4.13 for



(a) PT-35-2P, detail of the first peak

(b) PT-35-2P, overall range

(c) PT-55-2P, detail of the first peak

(d) PT-55-2P, overall range

Figure 4.12: Comparisons of the proposed model using test and recommended predicted input parameters with test curves for double-board specimens

comparison. The curves emphasize the superior performance of the steel-to-OSB screwed connections in pull-through, with up to three times the capacity of their plasterboard counterparts. Substantially improved ductility can also be observed when two layers of plasterboard are used in place of a single layer.

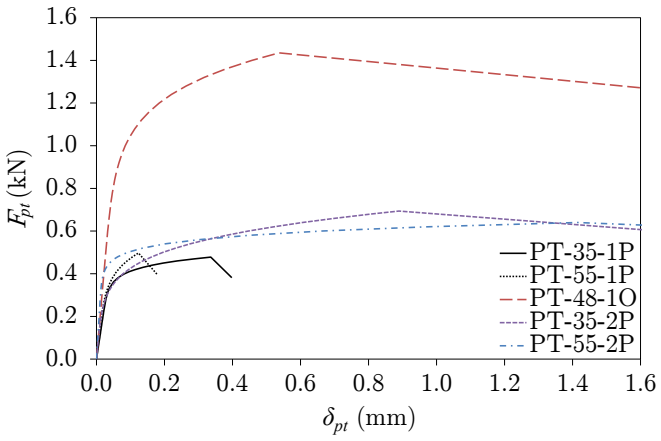


Figure 4.13: Pull-through load-deformation curves from proposed model for different test groups

4.4.2 Shear load-slip response

The shear load-slip response at the stud-to-sheathing interface, which is controlled by the characteristics of the employed shear connection, can have a significant influence on the structural behaviour of the examined systems; its thorough description is therefore essential. An empirical quad-linear model was devised by Peterman et al. (2014) and Ye et al. (2016) to capture the load-slip response at the interface between cold-formed steel and sheathing boards while, in the studies by Kyvelou et al. (2017*b*), a load-slip relationship for self-drilling screws connecting cold-formed steel beams and wood-based particle boards was proposed, utilising a generalised Ramberg-Osgood curve.

To facilitate the development of a predictive model for the shear load-slip response of screwed connections between cold-formed steel studs and sheathing boards (i.e. plasterboards and OSBs), more than 80 shear tests (including push-out and pull-out tests), from different sources, have been collected and analysed. A summary of the collected dataset is presented in Table 3.20 of Chapter 3. Note that only tests with plasterboard or OSB sheathing under monotonic loading were collected, while tests with board failure due to the connectors being close to the board edge were ignored. The examined connections failed mainly by tilting of the screw and bearing into the sheathing, while bending or shearing of the screws along with some pull-through was observed when more substantial components (i.e. stronger boards and thicker steel) were connected.

4.4.2.1 Shear load-slip model

Use of a generalised version of the Ramberg-Osgood formulation given by Equation (4.3), which has been used thus far for modelling the examined responses, was not found to be capable of accurately capturing the shape of some of the test curves over their full range using a single value for the strain hardening exponent n. Hence, a generalised Ramberg-Osgood model with two different exponents n_i (where $i = 1$ or 2) for describing the degree of roundedness of the early part and later part of the shear load-slip behaviour is recommended, as given by Equation (4.16) and illustrated in Figure 4.14:

$$\delta_{po} = \frac{F_{po}}{K_o} + \left(\delta_{x,po} - \frac{F_{x,po}}{K_o}\right)\left(\frac{F_{po}}{F_{x,po}}\right)^{n_i} \tag{4.16}$$

where F_{po} is the load, δ_{po} is the slip, K_o is the initial stiffness defined in Equation (3.3) in Section 3.4.2 of Chapter 3, $F_{x,po}$ is the load at a slip of $\delta_{x,po}$ and $F_{u,po}$ is the ultimate load at the corresponding ultimate displacement $\delta_{u,po}$.

For the initial part of the curve, when $F_{po} \leq F_{x,po}$, the first exponent is used i.e. $n_i = n_1$, while for the later part of the curve when $F_{x,po} < F_{po} \leq F_{u,po}$ the second exponent is used i.e. $n_i = n_2$. Based on the experimental results, a suitable point for the transition between the two curves was found to be at a slip of 1 mm i.e. $\delta_{x,po} = 1$ mm (denoted $\delta_{1,po}$), with the corresponding load denoted $F_{1,po}$. Values of n_1 are explored in Section 4.4.2.3 with reference to the experimental data, while n_2 can be expressed by Equation (4.17), by forcing the curve to pass through the ultimate point ($\delta_{u,po}$,$F_{u,po}$).

$$n_2 = \frac{ln\left(\delta_{u,po} - \frac{F_{u,po}}{K_o}\right) - ln\left(\delta_{x,po} - \frac{F_{x,po}}{K_o}\right)}{ln\left(\frac{F_{u,po}}{F_{x,po}}\right)} \tag{4.17}$$

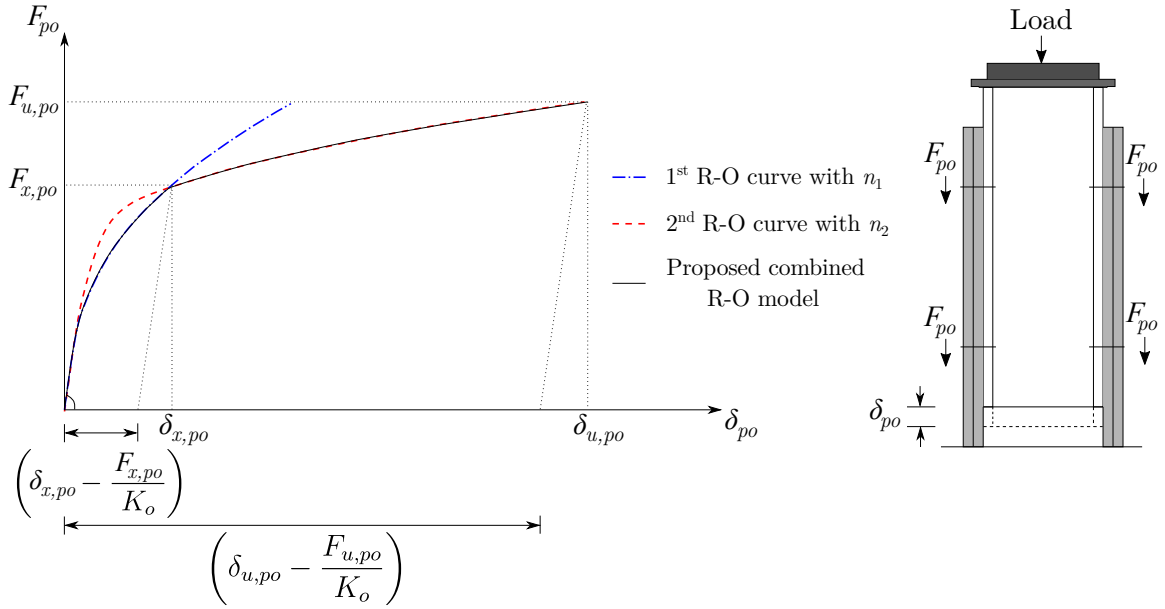


Figure 4.14: Proposed combined Ramberg-Osgood (R-O) model consisting of 2 single R-O curves for describing the shear load-slip behaviour of screw connections between cold-formed steel and sheathing

4.4.2.2 Calculation of key parameters for shear load-slip model

Expressions for the prediction of the load carrying capacity per shear plane of a screw connector in a steel-to-timber connection, as provided by EN 1995-1-1 (2004), are presented and assessed herein for the prediction of $F_{u,po}$ - see Equations (4.18) and (4.20). In accordance with EN 1995-1-1 (2004), the failure mode of a connector is dependent on the thickness of the steel section to which the sheathing is attached. A steel section with thickness less than half the nominal diameter of the screw (i.e. $t < 0.5d$) is classified as thin and the associated modes of failure are tilting and bending of the screw in the board; these failure modes are illustrated in Figures 4.15 (a) and (b) respectively, while the corresponding predictions of $F_{u,po}$ are given by Equation (4.18).

$$F_{u,po} = \min \begin{cases} 0.4 f_{h,k} t_b d & \text{(for Mode a)} \\ 1.15\sqrt{2 M_{y,screw} f_{h,k} d} + \dfrac{F_{u,pt}}{4} & \text{(for Mode b)} \end{cases} \tag{4.18}$$

where $f_{h,k}$ is the embedment strength in N/mm^2 of the board material, t_b is the thickness of the board, d is the diameter of the screw, $F_{u,pt}$ is the pull-through (withdrawal) capacity of the fastener, which can be calculated using Equation (4.9) in the absence of experimental data and $M_{y,screw}$ is the yield moment of the screw given by Equation (4.19).

$$M_{y,screw} = f_y d_{s,sh}^3 / 6 \tag{4.19}$$

where f_y is the yield strength of the screw and $d_{s,sh}$ - the diameter of the shank of the screw, which is approximately 0.75 times the nominal screw diameter d.

A steel plate is classified as thick when its thickness is greater than or equal to the diameter d of the screw; the associated modes of failure, shown in Figures 4.15 (c), (d) and (e), are bearing and single and double bending of the screw, respectively, while the corresponding predictions of $F_{u,po}$ are given by Equation (4.20).

$$F_{u,po} = \min \begin{cases} f_{h,k} t_b d & \text{(for Mode c)} \\ f_{h,k} t_b d \left(\sqrt{2 + \dfrac{4 M_{y,screw}}{f_{h,k} d t_b^2}} - 1 \right) + \dfrac{F_{u,pt}}{4} & \text{(for Mode d)} \\ 2.3 \sqrt{M_{y,screw} f_{h,k} d} + \dfrac{F_{u,pt}}{4} & \text{(for Mode e)} \end{cases} \tag{4.20}$$

In accordance with EN 1995-1-1 (2004), for the capacity of connections $F_{u,po}$ with steel plates between a thin and a thick steel plate, linear interpolation between the limiting thin and thick plate values may be carried out.

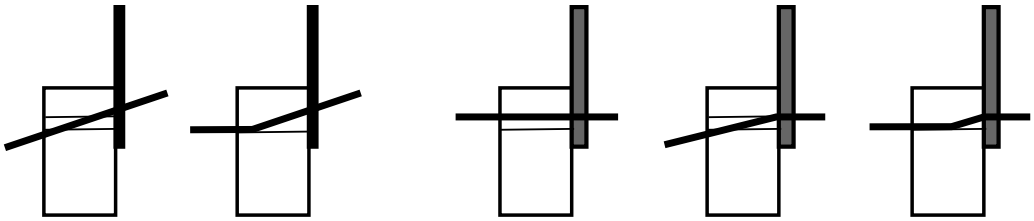


Figure 4.15: Failure modes for steel-to-timber connections in accordance with EN 1995-1-1 (2004): (a) tilting, (b) bending in board, (c) bearing, (d) bending at steel plate and (e) double bending

Use of Equation (4.21) is recommended by EN 1995-1-1 (2004) for the calculation of the embedment strength of timber $f_{h,k,gen}$, expressed as a function of the board density ρ_k, while, specifically for OSB, use of Equation (4.22) is recommended for the calculation of embedment strength $f_{h,k,OSB}$ (EN 1995-1-1 2004). Note that, although Equations (4.21) and (4.22) were initially developed for nails, they can be also employed for screws by taking their effective diameter d_{eff} equal to the shank diameter $d_{s,sh}$ (EN 1995-1-1 2004).

$$f_{h,k,gen} = 0.082 \rho_k d_{eff}^{-0.3} \tag{4.21}$$

$$f_{h,k,OSB} = 65 d_{eff}^{-0.7} t_b^{0.1} \tag{4.22}$$

Since there is no expression for the embedment strength of plasterboard in EN 520 (2009), Equation (4.23), which is analogous to Equation (4.22), was devised based on the collected dataset (of 47 tests) summarised in Table 3.20 in Chapter 3. Equation (4.23) was

defined in terms of the effective diameter d_{eff} (i.e. the screw shank diameter $d_{s,sh}$), board thickness t_b and steel thickness t with the coefficients determined by means of least squares regression analysis.

$$f_{h,k,gyp} = 83 d_{eff}^{-0.2} t_b^{-0.3} t^{-0.2} \tag{4.23}$$

In accordance with EN 1995-1-1 (2004), none of the specimens from within the examined dataset (summarised in Table 3.20 in Chapter 3) is classified as having thick steel plates and hence the predominant failure modes, corroborated by the conducted experiments, are screw tilting and bending. Note though that some of the specimens fall in the range between $0.5d$ and d (i.e. between thin and thick steel plate); this is considered to be the reason for multiple failure modes taking place at different stages during these tests, i.e. both tilting (thin plate) and bearing (thick plate) and bending of the screw (thin and thick plate) - or a combination of these - as reported in Table 3.17 in Chapter 3. All five failure modes illustrated in Figure 4.15 were therefore represented in the test data. In assessing the accuracy of the predictive equations for $F_{u,po}$ (i.e. Equations (4.18) and (4.20)), the measured values of the screw yield strength f_y were used for the tests performed in Chapter 3 ($f_y = 1020$ MPa for the 3.5 mm screws and $f_y = 730$ MPa for the 5.5 mm screws), while for the other tests reported in literature, which had nominal screw diameters ranging from 3.5 mm to 4.8 mm, an estimated value of $f_y = 800$ MPa was adopted, based on an analysis of the observed failure modes. The density of plasterboard was taken as 665 kg/m^3 in accordance with measurements reported in Chapter 3. Note though that plasterboard densities vary among manufacturers and with humidity (Kyprianou et al. 2021*a*, Vieira & Schafer 2009, Petrone et al. 2016).

4.4.2.2.1 Shear capacity predictions $F_{u,po}$ for screwed connections in plasterboard

For the 47 tests on screwed connections in plasterboard (collected in Table 3.20), comparisons between the test shear capacity values $F_{u,po,test}$ and the predicted values using Equations (4.18) and (4.20) with the generic embedment strength of Equation (4.21) (EN 1995-1-1 2004), are presented in Figure 4.16. The critical failure mode for all cases where $t/d \leq 0.5$ was Mode a (screw tilting) according to Equation (4.18). For the ten cases falling into the intermediate thickness range of $0.5 < t/d \leq 1.0$, the capacity prediction $F_{u,po}$ re-

quired interpolation between the critical results for thin plates (Equation (4.18)) and thick plates (Equation (4.20)), which were for Mode a and Mode d (i.e. screw bending in thick plates with pull-through) respectively. The predominant mode of failure from the tests was screw tilting and therefore largely in agreement with the predictions of EN 1995-1-1 (2004). Despite plasterboard not being explicitly covered by EN 1995-1-1 (2004), Equation (4.18) provides good predictions of the test results, though further improvements remain possible.

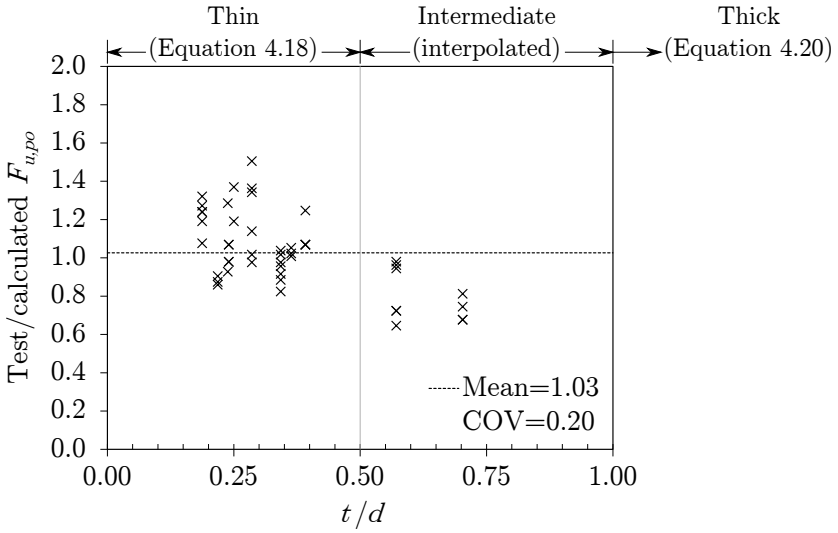
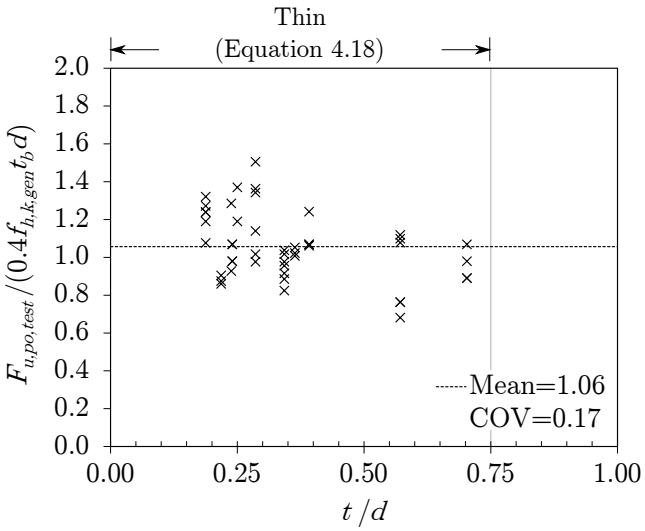
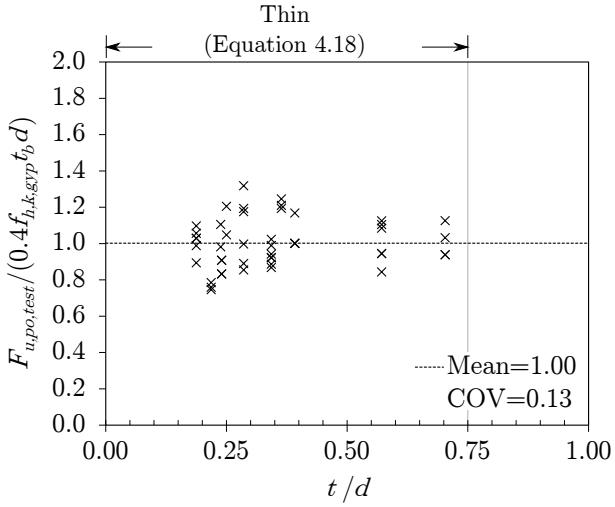


Figure 4.16: Comparisons between test and predicted $F_{u,po}$ values for all screwed connections in plasterboard, calculated using EN 1995-1-1 (2004), with Equation (4.21) for embedment strength and interpolation between critical values from Equations (4.18) and (4.20) for cases when $0.5 < t/d \leq 1.0$

In Figure 4.17, a comparison between the $F_{u,po,test}$ values and $F_{u,po}$ predictions obtained using Equation (4.18) up to an extended limit for the thin plates of $t/d \leq 0.75$, with the embedment strength calculated using Equation (4.21) and the newly proposed Equation (4.23), is provided. As apparent from the results, including the mean values and coefficients of variation shown in Figures 4.17 (a) and (b) and Table 4.7, use of Equation (4.23) for the calculation of the embedment strength, when plasterboard is used, provides a more accurate estimation of $F_{u,po}$ with reduced scatter. Hence, use of Equation (4.18) up to an extended limit for thin plates of $t/d \leq 0.75$, along with Equation (4.23), is recommended for screwed connections in plasterboard within the range of properties examined herein.



(a) Tilting with $f_{h,k,gen}$



(b) Tilting with $f_{h,k,gyp}$

Figure 4.17: Comparisons between test and predicted $F_{u,po}$ values calculated using Equation (4.18) Mode a (screw tilting) with embedment strength (a) $f_{h,k,gen}$ (Equation (4.21)) and (b) $f_{h,k,gyp}$ (Equation (4.23)) for all screwed connections in plasterboard with the thin plate limit extended to $t/d \leq 0.75$

Table 4.7: Comparisons between predictions of $F_{u,po}$ for shear tests with plasterboard using Equation (4.18) for Mode a (tilting) with embedment strength calculated using Equations (4.21) and (4.23)

Sheathing	t_b (mm)	t (mm)	d (mm)	No. of tests	$\frac{F_{u,po,test}}{0.4 f_{h,k,gen} t_b d}$		$\frac{F_{u,po,test}}{0.4 f_{h,k,gyp} t_b d}$	
					Mean	COV	Mean	COV
Plasterboard	12.5	0.8 - 2.0	3.5	21	1.10	0.13	1.00	0.14
	12.5	2.5	3.5	4	0.96	0.09	1.01	0.09
	12.5	1.0	4.2	1	1.29	-	1.11	-
	12.5	0.9 - 1.2	4.8	8	1.24	0.07	1.04	0.08
	12.5	1.2	5.5	3	0.88	0.03	0.76	0.03
	2×12.5	1.2	3.5	3	0.87	0.05	0.98	0.05
	2×12.5	1.0	4.2	1	0.93	-	0.98	-
	2×12.5	2.0	3.5	3	0.74	0.06	0.91	0.06
	2×12.5	2.0	5.5	3	1.03	0.02	1.22	0.02
				Overall	1.06	0.17	1.00	0.13

4.4.2.2.2 Shear capacity predictions $F_{u,po}$ for screwed connections in OSB

For the 39 tests on screwed connections in OSB (collected in Table 3.20), comparisons between the test shear capacity values and the predicted values $F_{u,po}$ using Equations (4.18) and (4.20) with the OSB embedment strength given by Equation (4.22), are presented in Figure 4.18. According to Equation (4.18), the critical failure mode for specimens with $t/d \leq 0.5$ was Mode a (tilting) in all cases, but the resulting resistance predictions can be seen from Figure 4.18 to be poor. Moreover, the predicted failure mode did not accord well with those observed in the physical experiments, where bending (Ye et al. 2016) and pull-through (Peterman & Schafer 2013, Fiorino et al. 2007, Serrette et al. 1997) failures were reported. Therefore, in Figure 4.19 and Table 4.8 comparisons are made between the $F_{u,po}$ test values and the $F_{u,po}$ predictions considering Mode b (i.e. bending and pull-through) in Equation (4.18) for the cases when $t/d \leq 0.5$. For the five specimens that fall marginally beyond the thin plate category, into the intermediate category, linear interpolation between Mode b in Equation (4.18) and the Mode d in Equation (4.20) was performed. The comparisons reveal that good predictions of the test results (both in terms of capacity and failure mode) are achieved using the Mode b resistance equation; use of Equation (4.24) is therefore

recommended for screwed connections in OSB and not the minimum between the resistances for Modes a and b from Equation (4.18), as recommended by EN 1995-1-1 (2004)), for cases when $t/d \leq 0.5$. For cases when $0.5 < t/d \leq 1.0$, interpolation between Equation (4.24) and the critical value from Equation (4.20) is recommended.

$$F_{u,po} = 1.15\sqrt{2M_{y,screw}f_{h,k,OSB}d} + F_{u,pt}/4 \tag{4.24}$$

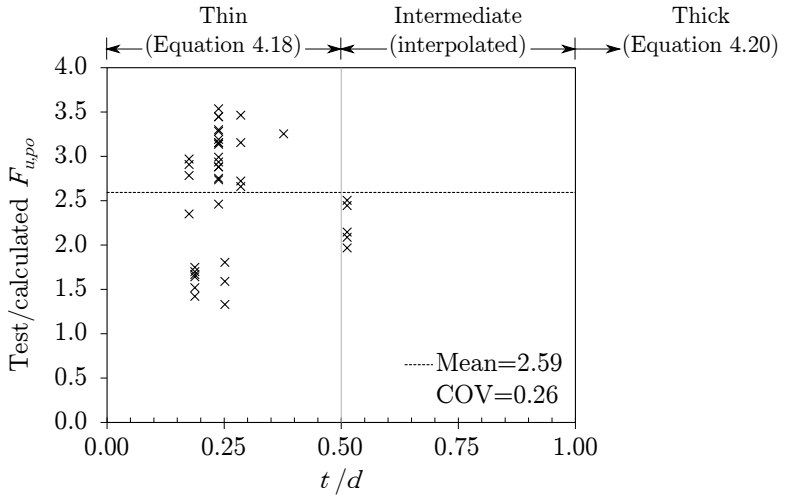


Figure 4.18: Comparisons between test and predicted $F_{u,po}$ values for all screwed connections in OSB, calculated using EN 1995-1-1 (2004), with Equation (4.22) for embedment strength and interpolation between the critical values from Equations (4.18) and (4.20) for cases when $0.5 < t/d \leq 1.0$

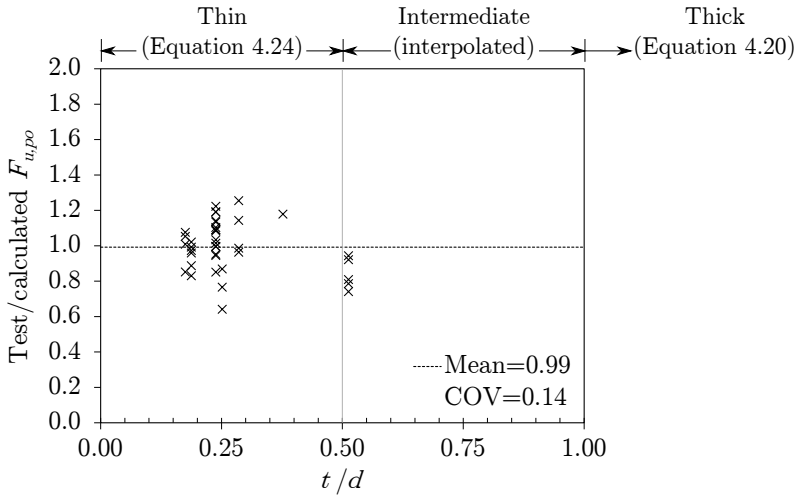


Figure 4.19: Comparisons between test and predicted $F_{u,po}$ values for all screwed connections in OSB, calculated using Equation (4.24) for cases $t/d \leq 0.5$ and interpolation between Equation (4.24) and the critical value from Equation (4.20) for cases when $0.5 < t/d \leq 1.0$

Table 4.8: Comparisons between test and predicted $F_{u,po}$ values for groups of screwed connections in OSB with similar characteristics, calculated using Equation (4.24) for cases $t/d \leq 0.5$ and interpolation between Equation (4.24) and the critical value of Equation (4.20) for cases when $0.5 < t/d \leq 1.0$

Sheathing	t_b (mm)	t (mm)	d (mm)	No. of tests	$\frac{F_{u,po,test}}{F_{u,po}}$		$F_{u,po}$ calculated using
					Mean	COV	
OSB	11.1	0.9	3.5	3	0.76	0.15	Equation (4.24)
	9.0	1.0	4.2	16	1.06	0.10	Equation (4.24)
	18	0.9	4.8	6	0.94	0.08	Equation (4.24)
	11.1	0.8 - 1.4	4.8	9	1.06	0.12	Equation (4.24)
	11.1	2.5	4.8	5	0.84	0.10	Interpolation between Eqs. (4.24) and (4.20)
				Overall	0.99	0.14	

4.4.2.2.3 K_o, $\delta_{u,po}$ and $F_{1,po}$ estimations

Recommended values for the remainder of the input parameters for the proposed model of Equations (4.16) and (4.17), namely the initial stiffness K_o and the ultimate displacement $\delta_{u,po}$ are provided in Table 4.9; these have been determined as the average values from groups

Table 4.9: Average measured values for key properties derived from full load-slip $F_{po} - \delta_{po}$ curves obtained from shear tests, grouped by common arrangement properties

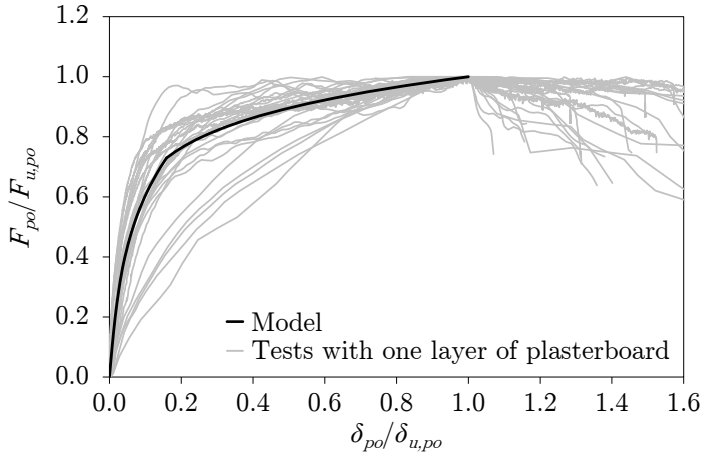
Sheathing	t_b (mm)	t (mm)	d (mm)	Full $F-\delta$	$\frac{K_o}{f_{h,k}d}$		$\delta_{u,po}/d$		$F_{1,po}/F_{u,po}$	
				curves	Mean	COV	Mean	COV	Mean	COV
Plasterboard	12.5	0.8 - 2.0	3.5	16	14.08	0.81	2.06	0.39	0.71	0.09
	12.5	2.5	3.5	4	11.01	0.19	1.20	0.68	0.96	0.07
	12.5	0.9 - 1.2	4.8	4	5.57	0.13	0.77	0.26	0.56	0.09
	12.5	1.2	5.5	3	6.69	0.05	1.00	0.13	0.76	0.01
	2×12.5	1.2	3.5	3	25.7	0.25	3.36	0.03	0.44	0.06
	2×12.5	2.0	3.5	3	12.68	0.18	1.54	0.12	0.53	0.05
	2×12.5	2.0	5.5	3	4.68	0.07	2.12	0.03	0.36	0.04
				Overall	12.25	0.77	1.67	0.56	0.67	0.26
OSB	9.0	1.0	4.2	4	14.84	0.16	1.33	0.23	0.55	0.20
	18	0.9	4.8	4	3.69	0.29	1.73	0.24	0.28	0.22
	11.1	0.8 - 1.4	4.8	9	10.45	0.19	1.52	0.15	0.51	0.17
	11.1	2.5	4.8	4	14.39	0.08	0.52	0.23	0.86	0.09
				Overall	10.75	0.40	1.33	0.34	0.54	0.38

of data with similar characteristics in terms of the embedment strength $f_{h,k}$ and screw diameter d. Embedment strength was calculated using Equation (4.21) for screw connections in plasterboard and using Equation (4.22) for screw connections in OSB. The force $F_{1,po}$ at 1 mm slip is also provided, expressed as a proportion of the ultimate test capacity $F_{u,po}$.

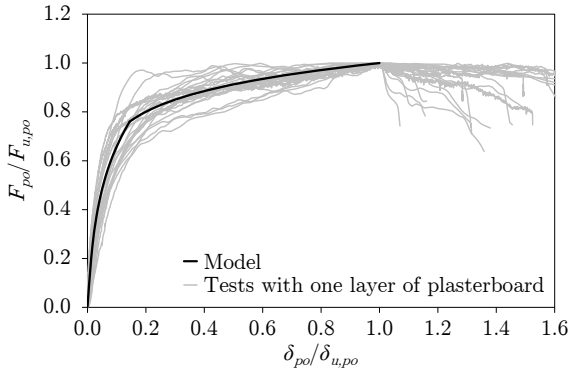
From Table 4.9, it can be seen that the properties are somewhat variable, but the average $K_o/(f_{h,k}d)$ values are approximately 10 for both plasterboard and OSB. For ultimate displacement $\delta_{u,po}$, the values typically range between $0.75d$ and $3.0d$ for the plasterboard specimens and between $0.5d$ and $1.75d$ for the OSB specimens.

4.4.2.3 Assessment of proposed shear model against experimental data

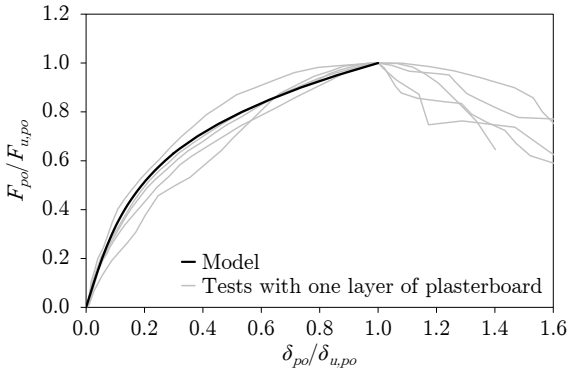
Typical comparisons between the proposed load-slip model and the respective experimental curves for the single- and double-layer plasterboard specimens, as well as for the OSB specimens, are presented in Figures 4.20, 4.21 and 4.22 respectively, where the load F_{po} normalised by the ultimate load $F_{u,po}$ is plotted against the slip at the shear interface δ_{po} normalised by the ultimate slip $\delta_{u,po}$. It can be observed that the devised expression provides a good fit to the experimental data and is therefore suitable for use in numerical simulations and advanced design methods. The average values of the key parameters used as input for the curves presented in Figures 4.20, 4.21 and 4.22 are provided in Table 4.10. Note that, the exponent n_1 used to define the degree of roundedness of the initial part of the curves (i.e. below a slip of 1 mm) was found to be within the range of 3.4 - 3.6 when the board connected was a single layer of either plasterboard or OSB, while for specimens with two layers of plasterboard, a value of $n_1 = 2$ was shown to provide a better fit to the respective test curves.



(a) All single layer plasterboard tests



(b) Tests with $d = 3.5$ and 5.5 mm



(c) Tests with $d = 4.2$ - 4.8 mm

Figure 4.20: Comparison between the proposed load-slip model and normalised test curves for specimens with one layer of plasterboard for (a) all collected tests, (b) tests with $d = 3.5$ or 5.5 mm and (c) tests with $d = 4.2 - 4.8$ mm

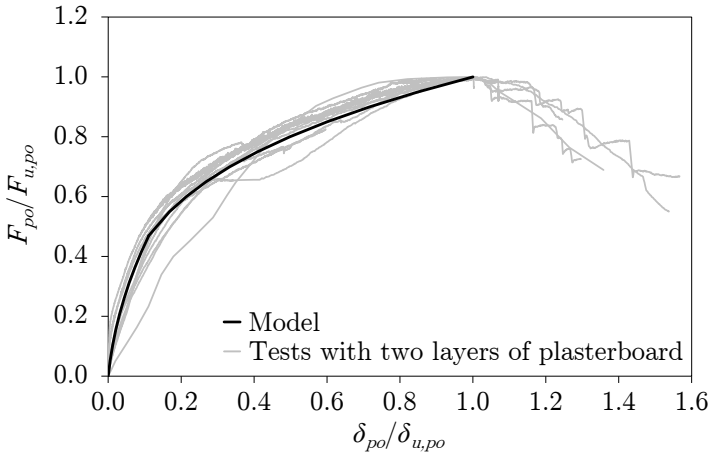


Figure 4.21: Comparison between the proposed load-slip model and normalised test curves for specimens with two layers of plasterboard

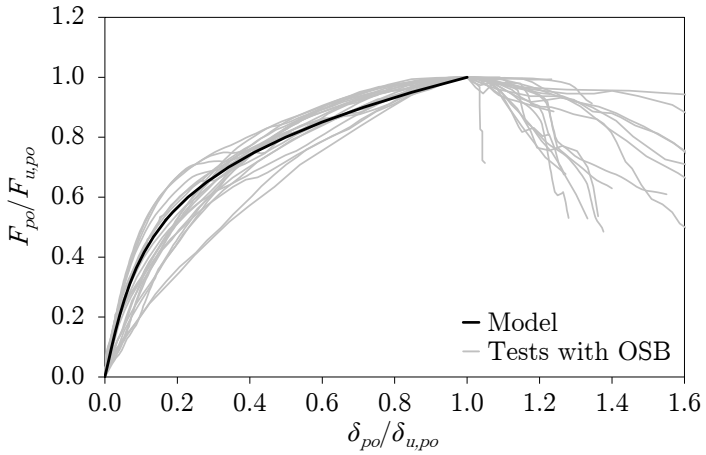


Figure 4.22: Comparison between the proposed load-slip model and normalised test curves for specimens with OSB

Table 4.10: Average values of the parameters required as input for the proposed models (t_b - board thickness, t - steel thickness, d - screw diameter)

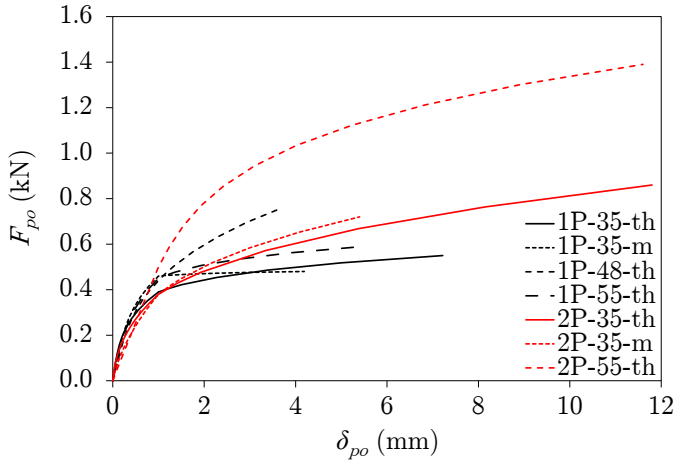
Sheathing	t_b (mm)	t (mm)	d (mm)	Full $F-\delta$ curves		K_o (kN/mm)	$F_{u,po}$ (kN)	$\delta_{u,po}$ (mm)	$F_{1,po}$ (kN)	n_1
Plasterboard	12.5	0.8 - 2.5	3.5 - 5.5	28	Mean	1.26	0.58	6.29	0.42	3.4
					COV	0.70	0.19	0.48	0.20	0.09
	12.5	0.8 - 2.5	3.5, 5.5	23	Mean	1.34	0.54	6.93	0.41	3.4
					COV	0.71	0.13	0.42	0.19	0.10
	12.5	0.9 - 1.0	4.2 - 4.8	5	Mean	0.87	0.77	3.35	0.48	3.5
					COV	0.70	0.19	0.48	0.20	0.09
	2 × 12.5	1.0 - 2.0	3.5 - 5.5	10	Mean	1.26	0.99	8.98	0.47	2.0
					COV	0.62	0.29	0.45	0.34	0.19
OSB	9 - 18	0.8 - 2.5	4.2 - 4.8	21	Mean	1.72	1.90	5.94	1.00	3.6
					COV	0.39	0.15	0.43	0.31	0.06

The average measured values of the key properties of screw connectors per shear plane for different steel-to-sheathing connections is provided in Table 4.11, while the associated two-part Ramberg-Osgood model curves for each type of connection are presented in Figure 4.23. The designation system employed for the specimens with plasterboard starts with 1P or 2P to indicate one or two layers of plasterboard (with the thickness of each layer ranging between 12.5 and 12.7 mm), while for the OSB specimens, the designation starts with O and is followed by the board thickness in mm. For all specimens, the designation

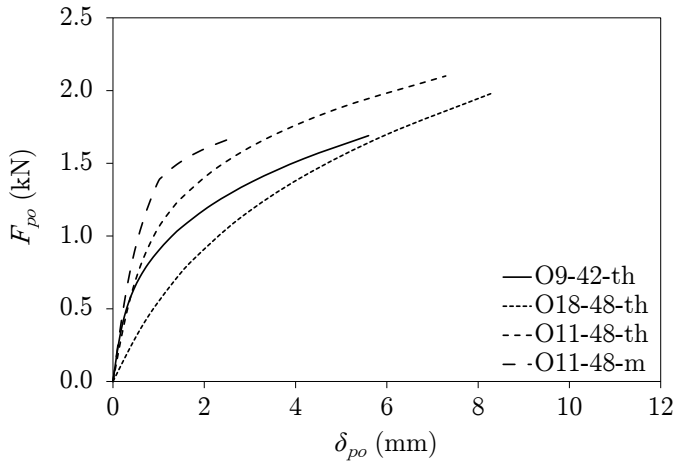
name is completed by the nominal diameter of the screw in mm multiplied by 10 and finally by the thickness of the steel section to which the fixing is connected, with 'th' denoting a thin plate (of thickness less than half of the screw diameter) and 'm' a medium thickness plate (in the range of $d/2 - d$). The curves shown in Figure 4.23, emphasize the greater ductility obtained when using two layers of plasterboard compared to a single layer and the higher shear resistances achieved by the OSB specimens in comparison to the plasterboard specimens.

Table 4.11: Average measured values of key properties of screw connectors per shear plane for different steel-to-sheathing connections (t_b - board thickness, t - steel thickness, d - screw diameter)

Designation	Sheathing	t_b (mm)	t (mm)	d (mm)	$F_{u,po}$ (kN)	K_o (kN/mm)	$\delta_{u,po}$ (mm)	$F_{1,po}$ (kN)	n_1
1P-35-th	Plasterboard	12.5	0.8 - 2.0	3.5	0.55	1.47	7.22	0.39	3.3
1P-35-m		12.5	2.5	3.5	0.48	1.03	4.19	0.46	3.6
1P-48-th		12.5	0.9 - 1.2	4.8	0.76	0.82	3.71	0.44	3.5
1P-55-th		12.5	1.2	5.5	0.59	1.04	5.48	0.45	3.2
2P-35-th		2×12.5	1.2	3.5	0.86	2.26	11.8	0.38	2.3
2P-35-m		2×12.5	2.0	3.5	0.72	1.01	5.40	0.38	1.9
2P-55-m		2×12.5	2.0	5.5	1.39	0.53	11.6	0.50	1.5
O9-42-th	OSB	9.0	1.0	4.2	1.69	2.26	5.60	0.90	3.5
O18-48-th		18	0.9	4.8	1.98	0.63	8.29	0.55	3.5
O11-48-th		11.1	0.8 - 1.4	4.8	2.10	1.69	7.29	1.06	3.6
O11-48-m		11.1	2.5	4.8	1.66	2.33	2.49	1.38	3.5



(a) Specimens with plasterboard



(b) Specimens with OSB

Figure 4.23: Model fitting of the average key properties presented in Table 4.11 and comparisons between the load-slip behaviour of a screw connector per shear plane when connected to (a) plasterboard and (b) OSB

4.5 Summary of proposals

Based on the conducted analyses, the proposed expressions to describe the response of the components of cold-formed steel stud wall systems, both at the material and connection levels, are summarised in Table 4.12. The key input parameters and references are also highlighted.

Table 4.12: Summary of models and associated parameters for each material and system interaction system

Level	Type	Load	Model formulation		Model parameters	
			Description	Reference	Parameters	Reference
Material	Cold-formed steel (rounded $\sigma-\varepsilon$ curve)	Tension/compression	2-stage R-O model	Eqs. (4.1) and (4.2) See Gardner & Yun (2018)	E, $\sigma_{0.2}$, σ_u, ε_u, n, m	Table 4.1 and Gardner & Yun (2018)
	Cold-formed steel ($\sigma-\varepsilon$ curve with plateau)	Tension/compression	Quadlinear or bilinear + nonlinear model	Eq. (4.1) and (4.6) See Yun & Gardner (2017)	E, $\sigma_{0.2}$, ε_{sh}, σ_u, ε_u	Table 4.1 and Yun & Gardner (2017)
	Plasterboard	Tension	R-O	Eq. (4.7)	E, f_u, ε_u, n	Table 4.2
		Compression	R-O	Eq. (4.7)	E, f_u, ε_u, n	Table 4.2
			Mander	Eqs. (4.4) and (4.5)	E, f_u, ε_u	Table 4.2
	OSB	Tension	R-O	Eq. (4.7)	E, f_u, ε_u, n	Table 4.3
		Compression	R-O	Eq. (4.7)	E, f_u, ε_u, n	Table 4.3
			Mander	Eqs. (4.4) and (4.5)	E, f_u, ε_u	Table 4.3
Component interaction	Pull-through (single layer board)		R-O + linear	Eq. (4.8)	$K_{o,40}$, $F_{u,pt}$, $\delta_{u,pt}$, n, $F_{u,pt,0.8}$, $\delta_{u,pt,0.8}$	Eqs. (4.9) - (4.15), Table 4.4, 4.5, 4.6
	Pull-through (two layer board)		R-O + bilinear	Eq. (4.8)	$K_{o,40}$, $F_{u,pt}$, $\delta_{u,pt}$, n, $F_{u,pt,0.8}$, $\delta_{u,pt,0.8}$, $F_{u,pt,2}$, $\delta_{u,pt,2}$	Eqs. (4.9) - (4.15), Table 4.4, 4.5, 4.6
	Shear with plasterboard for $t \leq 0.75d$		2 single R-O model	Eqs. (4.16) and (4.17)	K_o, $F_{u,po}$, $\delta_{u,po}$, n_1, $F_{1,po}$	Eq. (4.18) Eq. (4.23), Table 4.9
	Shear with OSB for $t \leq 0.5d$		2 single R-O model	Eqs. (4.16) and (4.17)	K_o, $F_{u,po}$, $\delta_{u,po}$, n_1, $F_{1,po}$	Eq. (4.24) - bending (Mode b) Eqs. (4.19), (4.22), Table 4.9

4.6 Conclusions

A comprehensive study into the material modelling of the different components forming a typical sheathed cold-formed steel wall system, as well as into the behaviour of the employed connectors in pull-through and shear has been presented. An experimental dataset comprising the results of more than 400 physical tests, assembled in Chapter 3, has been used as the basis for underpinning the development of predictive analytical expressions.

The stress-strain behaviour of the steel was shown to be well predicted by existing models (Gardner & Yun 2018, Yun & Gardner 2017). The material behaviour of both plasterboard and OSB was shown to be accurately described using the single stage of the Ramberg-Osgood expression up to the ultimate material stress f_u, both in the longitudinal and transverse direction and both under tension and compression. The Mander et al. (1988) model was also found to be capable of accurately capturing the response of plasterboard and OSB in compression while also accounting for the post peak decreasing capacity.

A modified version of the Ramberg-Osgood expression has been employed for modelling the pull-through behaviour of screwed connections both in plasterboard and OSB, up to the ultimate capacity. Linear functions were proposed to account for the observed post-peak behaviour. An expression based on the geometries of the screw and of the board, as well as on the board strength, has been devised for the calculation of the ultimate capacity in pull-through while the stiffness and ultimate displacement at peak capacity have been expressed as a function of the screw diameter and board thickness.

Regarding the shear behaviour of screwed connections between steel and either plasterboard or OSB, a model consisting of two single Ramberg-Osgood expressions has been adopted to accurately capture the load-slip behaviour up to the ultimate capacity. An extensive investigation into the failure modes of steel-to-board connections revealed that the expressions of EN 1995-1-1 (2004) for tilting can accurately predict the ultimate capacity of plasterboard while, for OSB, the expressions corresponding to failure due to screw bending for thin plates combined with pull-through yield consistent and accurate capacity predictions. A new empirical expression for the calculation of the embedment strength

of plasterboard has been developed while the stiffness and ultimate displacement can be expressed in terms of the embedment strength and screw diameter.

All devised models were found capable of accurately capturing the exhibited responses for different sheathing and fastening arrangements and are suitable for use in design by advanced computational analysis, as well as in numerical parametric studies. The devised models, along with the key input test parameters, are provided in a summary table.

Chapter 5

Sheathed cold-formed steel beam-columns experiments

5.1 Introduction

EXPERIMENTAL studies on sheathed cold-formed steel lipped channel wall studs, set in tracks, with service holes, subjected to compression and major axis bending are presented in this chapter. A total of 17 experiments were performed with both oriented strand board (OSB) and plasterboard used as sheathing and with varying connector spacing employed between the sheathing panels and the tested members. The tested specimens comprised a single 2.4 m long column sheathed on both sides and secured at the ends to top and bottom tracks. The member tests were complemented by material tests, stub column tests and initial geometric imperfection measurements.

The focus of the experimental study presented herein is to extend the existing experimental data and demonstrate that using closer-spaced connectors between the column and the sheathing can further enhance the capacity of stud-wall systems under both compression and bending, as well as preventing sudden failure of the sheathing-to-steel connectors. Sheathed stud columns, representative of a single vertical element in a stud wall system (Vieira & Schafer 2013, Peterman & Schafer 2014), are tested under combined compression and bending. Note, that the experiments presented herein are the only ones, known to the

author other than those by Peterman & Schafer (2014), where combined loading is used in tests with sheathed studs and the first to examine combined loading with equivalent uniform distributed loads instead of single mid-height horizontal point load as used by Peterman & Schafer (2014). The tested stud members, in bare steel conditions, are shown in Figure 5.1, with the geometry and placement of the featured service holes indicated. The material and geometric properties of all system components are provided in Section 5.2, while imperfection measurements, along with a detailed description of the specimens and of the test rig are reported in Section 5.3. The obtained results are presented in Section 5.4 with a discussion following in Section 5.5. The experimental studies presented in this chapter have been published by Kyprianou et al. (2021*c*,*d*)

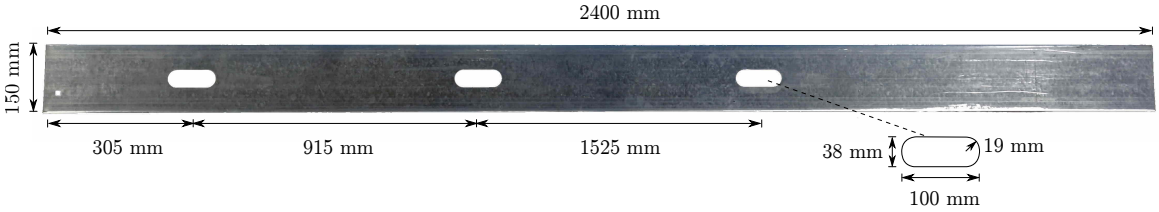


Figure 5.1: Stud column test specimen showing arrangement of service openings

5.2 Material tests

The stress-strain behaviour and key materials properties of the main components of the examined sheathed stud columns, shown in Figure 2.9 (c), were determined by coupon testing, as described in this section.

5.2.1 Cold-formed steel

For the determination of the material properties of the steel stud and track of steel grade S450GD (galvanised with zinc coat Z275) (BS EN 10346 2015, BS EN 10143 2006), three coupons were extracted along the length of the web of both members. The notation of the coupons begins with the letters CS, followed by the nominal thickness in mm multiplied by 10 (i.e. CS15 for the studs and CS12 for the track) and then the test number. The tensile coupons were tested in accordance with EN ISO 6892 (2016) at an initial axial strain rate

of 0.00007 s^{-1} which was gradually increased to 0.00025 s^{-1} via three intermediate steps. A 150 kN Instron 5984 testing machine was used to perform the tests, along with the Bluehill data acquisition system, collecting data every second. Accurate measurements of strains at the early stages of loading was ensured through the use of two strain gauges, mounted at mid-height on either side of the coupons, while an optical extensometer with a gauge length of 50 mm was used as an additional strain measurement method to capture the later parts of the stress-strain curves.

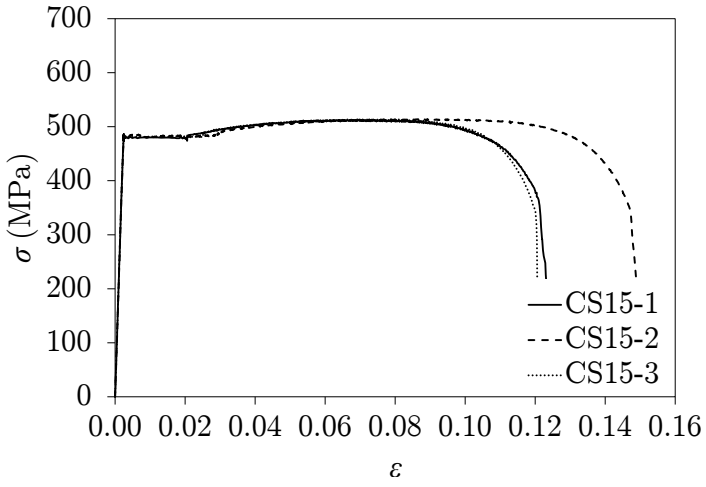
The key measured properties are presented in Tables 5.1 and 5.2 while the full stress-strain curves are illustrated in Figures 5.2 (a) and (b) for the stud and track respectively. In Tables 5.1 and 5.2, E is the Young's modulus, $\sigma_{0.2}$ is the 0.2% proof stress (considered as the yield strength), $\sigma_{1.0}$ is the 1% proof stress, σ_u is the ultimate strength, ε_u is the strain at σ_u and ε_f is the elongation at fracture measured over the standard gauge length (EN ISO 6892 2016).

Table 5.1: Material properties of cold-formed steel coupons extracted from columns (CS15)

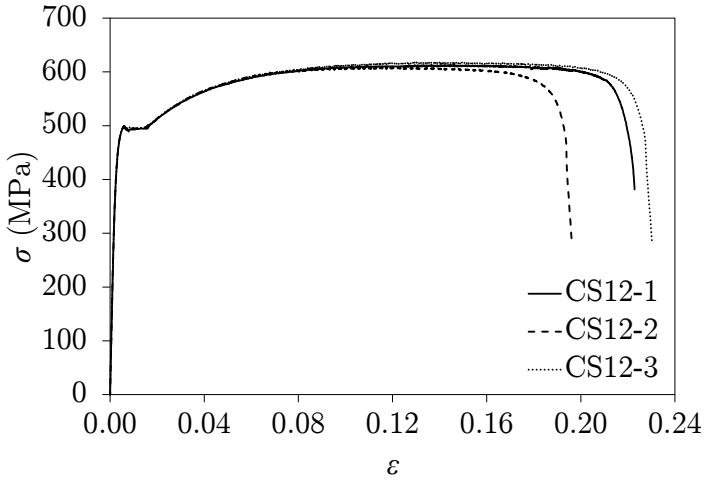
Designation	E (GPa)	$\sigma_{0.2}$ (MPa)	$\sigma_{1.0}$ (MPa)	σ_u (MPa)	ε_u	ε_f
CS15-1	203	481	481	514	0.069	0.121
CS15-2	203	484	484	514	0.089	0.148
CS15-3	205	481	482	514	0.079	0.120
Average	204	482	482	514	0.079	0.130

Table 5.2: Material properties of cold-formed steel coupons extracted from tracks (CS12)

Designation	E (GPa)	$\sigma_{0.2}$ (MPa)	$\sigma_{1.0}$ (MPa)	σ_u (MPa)	ε_u	ε_f
CS12-1	201	483	494	613	0.137	0.222
CS12-2	201	483	495	609	0.124	0.195
CS12-3	201	484	496	618	0.140	0.229
Average	201	483	495	613	0.134	0.215



(a) CS15 - column



(b) CS12 - track

Figure 5.2: Stress-strain curves of tensile coupons extracted from (a) stud and (b) track

5.2.2 Sheathing material tests

Two types of sheathing board were used: standard gypsum-based plasterboards and orientated strand board. The employed plasterboard was type A board in accordance with EN 520 (2009), was of 12.5 mm measured thickness and 665 kg/m^3 density. The employed oriented strand board was type 3 (OSB/3) as specified by EN 300 (2006), had a measured thickness of 11.0 mm and had a density of 590 kg/m^3. Material tests for both types of board were carried out in both compression and tension, as well as longitudinally and transversely to their direction of production in accordance with EN 789 (2005). A detailed description

of these tests is provided by Kyprianou et al. (2021*a*) and presented in Chapter 3 while a summary of the key material properties is provided in Table 5.3, where E is the Young's modulus, f_u is the ultimate strength, ε_u is the corresponding strain and $\varepsilon_{u,0.8}$ (only for compression) is the strain at 80% of f_u, post f_u.

Table 5.3: Average measured material properties of sheathing

Type	Longitudinal				Transverse			
	E (GPa)	f_u (MPa)	ε_u (%)	$\varepsilon_{u,0.8}$ (%)	E (GPa)	f_u (MPa)	ε_u (%)	$\varepsilon_{u,0.8}$ (%)
OSB, tension	4.10	11.7	0.37	-	2.94	7.01	0.37	-
OSB, compression	4.02	12.1	0.40	0.54	2.78	10.7	0.50	0.66
Plasterboard, tension	1.65	1.45	0.61	-	1.67	0.67	0.38	-
Plasterboard, compression	2.11	3.81	0.23	0.37	2.13	3.33	0.23	0.42

5.3 Member tests

5.3.1 Geometric properties

The cross-sectional shape of the stud columns, which are the main structural members of the examined system, is illustrated in Figure 5.3 along with the notation used for the cross-sectional dimensions. The average measured dimensions of the stud columns and tracks (which do not feature a lip) are provided in Table 5.4, where t is the thickness, h is the depth of the section, b is the flange width, c is the length of the lip and r is the internal corner radius of the section.

All stud columns were 2.4 m long and positioned in the centre of 800 mm long tracks. The columns came with 100×38 mm pre-cut holes for the installation of services, which is typical for columns deeper than 150 mm. The shape of the oval service holes, which had 19 mm radii at the ends, as well as their position along the column length are illustrated in Figure 5.1.

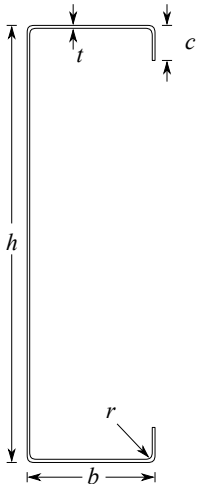


Figure 5.3: Notation for cross-sectional geometry of stud

Table 5.4: Average measured cross-sectional dimensions

Member	t (mm)	h (mm)	b (mm)	c (mm)	r (mm)
Column	1.44	149.15	43.92	11.95	2.50
Track	1.18	155.30	31.18	-	2.25

5.3.2 Stub column tests

A pair of stub columns was tested – one with and one without service hole openings in the web – to investigate the effect of the hole on the ultimate compression capacity of the section. Both columns were 450 mm long with the position of the hole for the respective member being at mid-length. The tests were carried out in accordance with EN 1993-1-3 (2006), with the axial load introduced using a 750 kN Instron hydraulic testing machine at a constant displacement rate of 0.25 mm/min. Both tests were continued beyond the ultimate capacities to observe the post-peak behaviour and the development of the failure mechanism.

The obtained axial load-displacement curves along with images of the deformed test specimens are provided in Figure 5.4 (a) and (b) respectively. For both stub columns, failure was triggered by a combination of local and distortional buckling, with the specimen comprising a service hole exhibiting 5% reduced capacity compared to the one without a

hole.

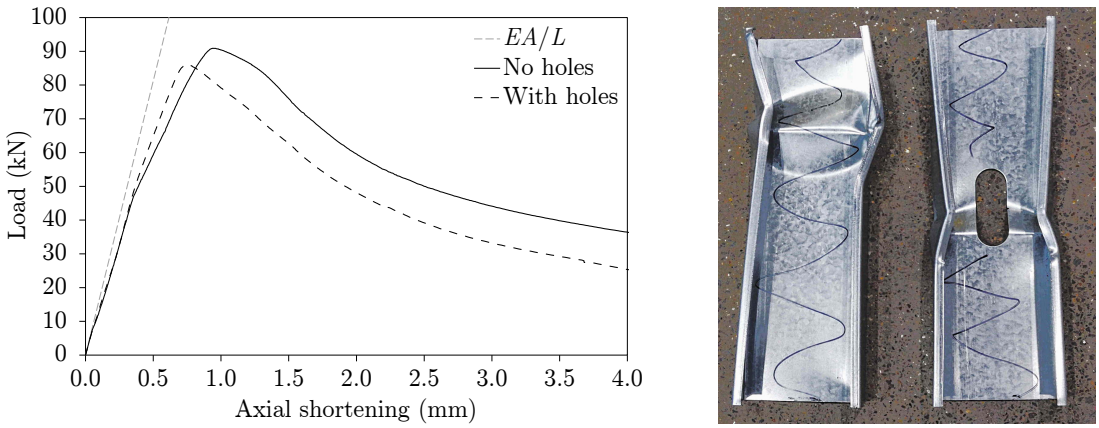


Figure 5.4: Stub column test results: (a) load-displacement curves and (b) failure modes

5.3.3 Imperfections

Initial geometric imperfections, including both cross-sectional (δ_L for local, δ_D for distortional) and global ($\delta_{G,maj}$ and $\delta_{G,min}$ for flexural about the major and minor axis respectively and $\theta_{G,t}$ for torsional) modes along the length of the member, were measured for ten specimens with service holes (- see Figure 5.1) and ten without service holes. The five modes of imperfection (the associated buckling modes of which are observed in Section 5.4), illustrated in Figure 5.5, were determined using an imperfection rig with seven LVDTs – see Figure 5.6 – which allowed the measurement of the variation of the cross-sectional shape along the length of the specimens. The method used to determine the imperfection magnitudes was similar to that described by Vieira et al. (2011). The seven LVDT mount ran on rails, as shown in Figure 5.7, with an attached string pot allowing determination of the position of the measurements along the length of the column and with the rails calibrated to remove their inherent imperfection. Data were recorded using the acquisition system DATASCAN every second.

The imperfections along the length of the columns were calculated using the following equations, where δ_L, δ_D, $\delta_{G,maj}$, $\delta_{G,min}$ and $\theta_{G,t}$ are as defined in Figure 5.5 and $\delta_1 - \delta_7$ are

the measurements of the LVDTs shown in Figure 5.6.

$$\delta_L = \text{mean}\left[(\delta_4 - \delta_3), (\delta_4 - \delta_5)\right] \tag{5.1}$$

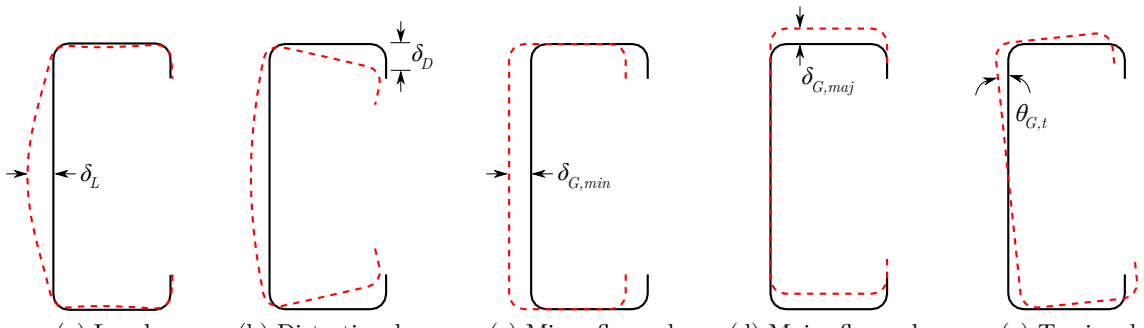
$$\delta_D = \text{mean}\left[(\delta_1 - \delta_2), (\delta_7 - \delta_6)\right] \tag{5.2}$$

$$\delta_{G,maj} = \text{mean}\left[\delta_2, \delta_6\right] \tag{5.3}$$

$$\delta_{G,min} = \text{mean}\left[\delta_3, \delta_5\right] \tag{5.4}$$

$$\theta_{G,t} = (\delta_3 - \delta_5)/h \tag{5.5}$$

The average imperfection amplitudes of the specimens with and without service holes are provided in Table 5.5, relative to the thickness for the cross-sectional modes and relative to the column length L for the global modes. Typical distributions of the imperfections along the member length are presented in Figures 5.8 and 5.9 for the cross-sectional and global imperfections respectively. In Figure 5.8, all data have been post-processed such that the measurements are plotted relative to a best fit line through the overall imperfection profile. The imperfection amplitude for the cross-section modes is then taken as the maximum deviation from this line. This measure of imperfection is deemed to be appropriate because it is the deviation from flatness that is the key trigger and influential factor for local and distortional buckling. For the global imperfections, a half-sine wave was fitted to the measured curves using least squares regression to allow determination of the maximum amplitude at mid-length, as shown in Figure 5.9.



(a) Local (b) Distortional (c) Minor flexural (d) Major flexural (e) Torsional

Figure 5.5: Illustrations of amplitudes of imperfection shapes for (a) local, (b) distortional, (c) flexural about the minor axis, (d) flexural about the major axis and (e) torsional modes

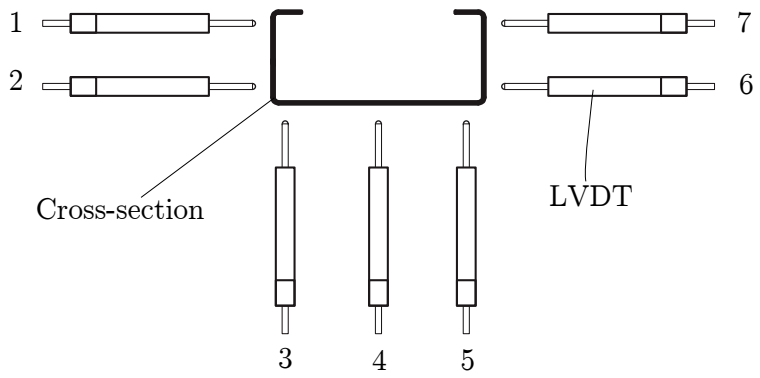


Figure 5.6: Positions of LVDTs mounted on the imperfection rig



(a) (b) (c)

Figure 5.7: Imperfection rig (a) elevation view (b) schematic and (c) detail of the rails and the LVDTs around the cross-section

Table 5.5: Summary of initial geometric imperfection amplitude measurements

Member	No.	δ_L/t	δ_D/t	$L/\delta_{G,min}$	$L/\delta_{G,maj}$	$\theta_{G,t}$ (deg/m)
No holes	1	0.19	0.47	-1700	18300	0.27
	2	0.18	0.57	-2370	8970	0.21
	3	0.27	0.39	-1970	12300	0.19
	4	0.19	0.42	-2020	12500	0.17
	5	0.22	0.62	-2100	16900	0.21
	6	0.20	0.29	-2000	14700	0.10
	7	0.31	0.39	-1460	6540	0.23
	8	0.26	0.42	-1180	15200	0.16
	9	0.27	0.50	-1680	5720	0.21
	10	0.25	0.39	-1180	19300	0.17
	Mean	0.23	0.44	-1770	13000	0.19
	COV	0.19	0.22	0.23	0.36	0.24
With holes	1	0.18	0.46	4680	10000	0.18
	2	0.18	0.59	3280	10100	0.18
	3	0.24	0.41	4060	28500	0.16
	4	0.18	0.47	5300	14100	0.15
	5	0.27	0.63	2200	27500	0.12
	6	0.20	0.62	2700	12200	0.11
	7	0.25	0.62	5620	11000	0.16
	8	0.20	0.33	7420	18400	0.18
	9	0.20	0.57	4290	14000	0.14
	10	0.18	0.53	4260	31000	0.10
	Mean	0.21	0.52	4380	17700	0.15
	COV	0.16	0.19	0.35	0.47	0.20

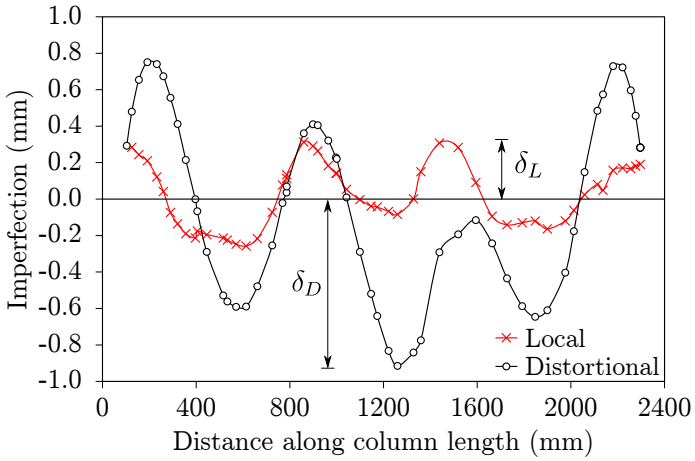


Figure 5.8: Cross-sectional imperfections along column length

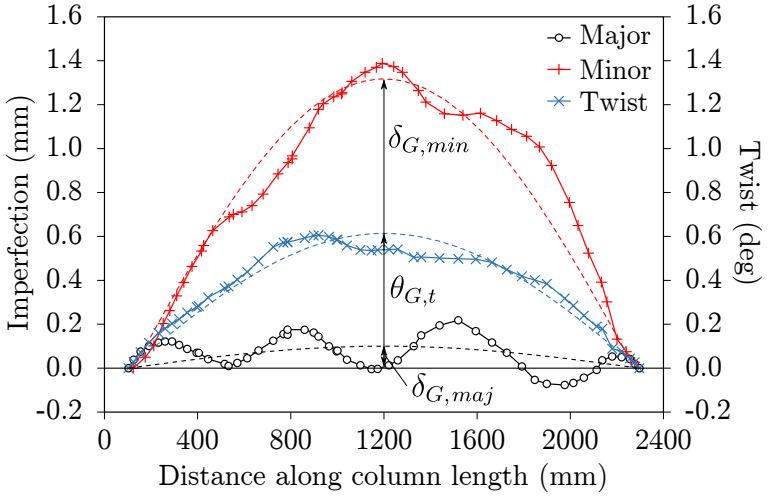


Figure 5.9: Global imperfections along the column length, with dashed lines marking the half-sine curves of best fit

The measured imperfection amplitudes for the members with and without holes show no significant discrepancies for the local, distortional, torsional and global major axis flexural modes, with the latter being around L/10000. Conversely, both the magnitude and direction of the minor axis bow imperfections were affected by the presence of the holes; this is attributed to the influence of the hole punching process. Note that the positive imperfection values denote that the imperfection direction is as per the illustration in Figure 5.5 (c), while negative values indicate that the imperfection direction is of the opposite sense.

5.3.4 Screws types and arrangements

The types of connector used for securing the sheathing panels to the steel studs were screws of 3.5 mm diameter for the plasterboard and 4.8 mm diameter for the OSB. Illustrations of the two screws are provided in Figure 5.10 (a) and (b) respectively, while further details of the properties of these screws and on their behaviour in shear and pull-through can be found in Chapter 3 and in the work presented by Kyprianou et al. (2021*a*). The connection between the flanges of the track and stud at both column ends were made using screws of 4.8 mm diameter - see Figure 5.10 (c). Finally, the webs of both tracks were secured onto square hollow sections, using bolts of 6 mm diameter (see Figure 5.10 (d)).



Figure 5.10: Types of connector used: (a) 3.5 mm diameter screw for plasterboard to steel (b) 4.8 mm diameter screw for OSB-to-steel (c) 4.8 mm diameter screw for steel-to-steel and (d) 6 mm diameter anchor bolt

The sheathed column specimens were tested with four different screw spacings: 600 mm, 300 mm, 150 mm and 75 mm, as shown in Figure 5.11. Note that a distance of 50 mm was kept between the edge connector and the column end, in order for the screw to not be driven into the track. For the specimens with a spacing of 600 mm, five screws were used on each side of the column, with the two outer screw spacings reduced to 550 mm. Similarly, for the other arrangements, the outer spacings were reduced to allow for a uniform spacing of connectors along the rest of the column length. For the 300 mm spacing, nine screws were used, while for the 150 mm and the 75 mm spacings, 17 and 33 screws were employed respectively. No connection between the track and the sheathing was implemented since the focus of this study was to investigate the column-to-sheathing connection.

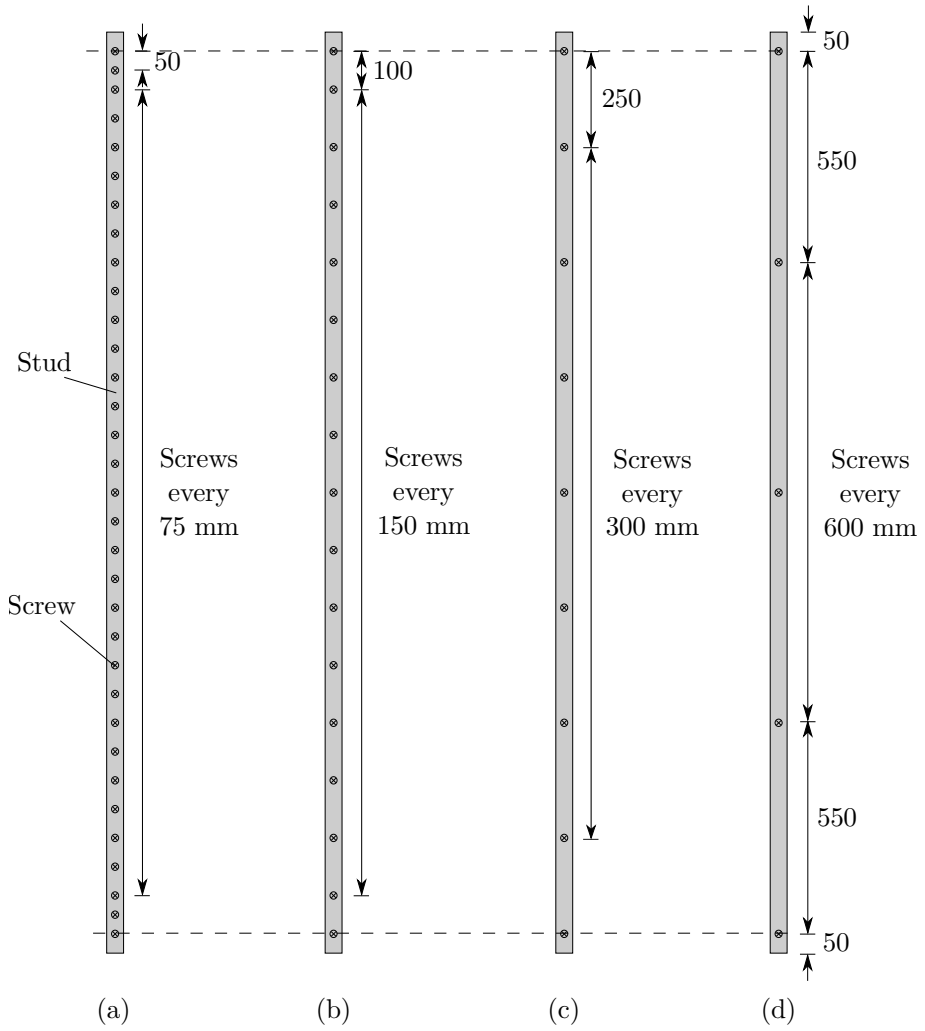


Figure 5.11: Connector arrangements for spacings of (a) 75 mm, (b) 150 mm, (c) 300 mm and (d) 600mm (dimensions in mm)

5.3.5 Test rig

The specimens were tested in a dual-actuator rig. Axial compression was applied to the overhead track by a vertical 1000 kN Instron actuator while bending was applied by laterally loading the sheathing using a four-line two-tier whiffletree system connected to an horizontal 500 kN Instron actuator in order to approximate a uniformly distributed load - see Figure 5.12. The top actuator was connected to a hot-rolled steel square hollow section, through which load was applied to the top track of the test specimens. Note that special attention was given to avoid contact between the square hollow section and the sheathing

such that axial load would be applied directly to the steel stud only. Rotation of the hollow section was prevented by the use of brackets at either end (see Figure 5.12), while Teflon was placed between the brackets and the hollow section to minimise friction. The bottom track was also secured to a hollow section fixed to the concrete lab floor. The whiffletree connected to the horizontal actuator was free to rotate, with pinned connections between its legs. Prior to each test, the whiffletree was laser-aligned to be parallel to the column length.

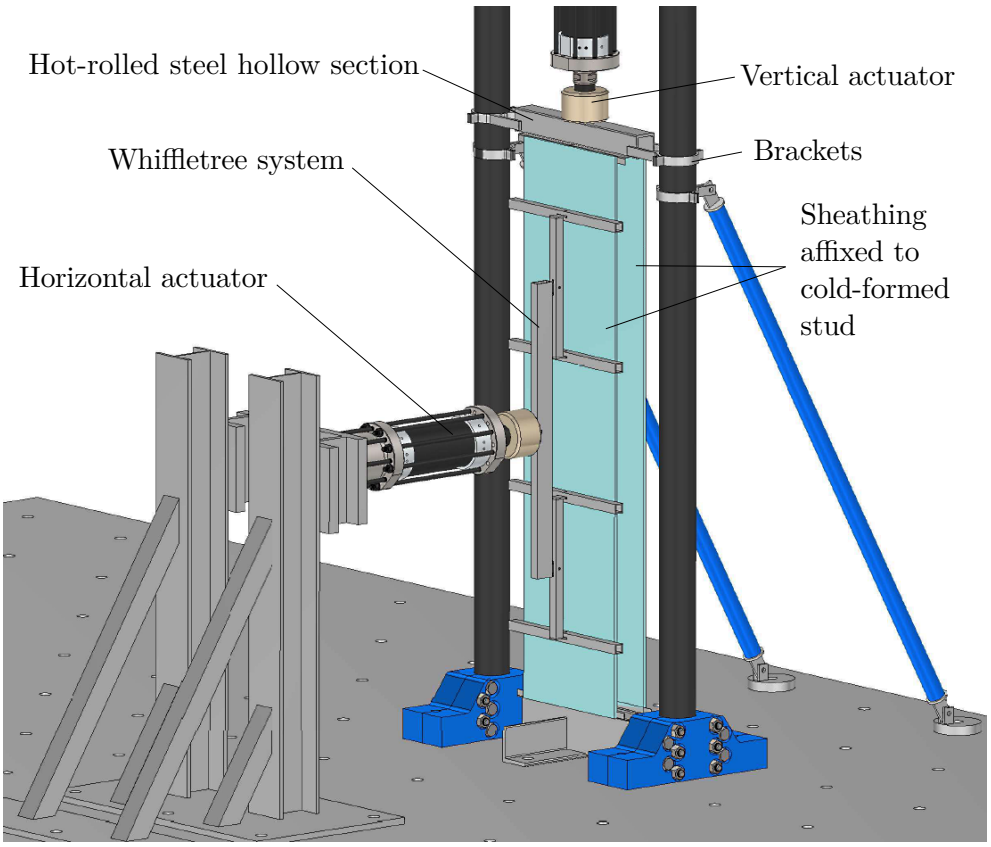


Figure 5.12: Illustration of rig for beam-column tests

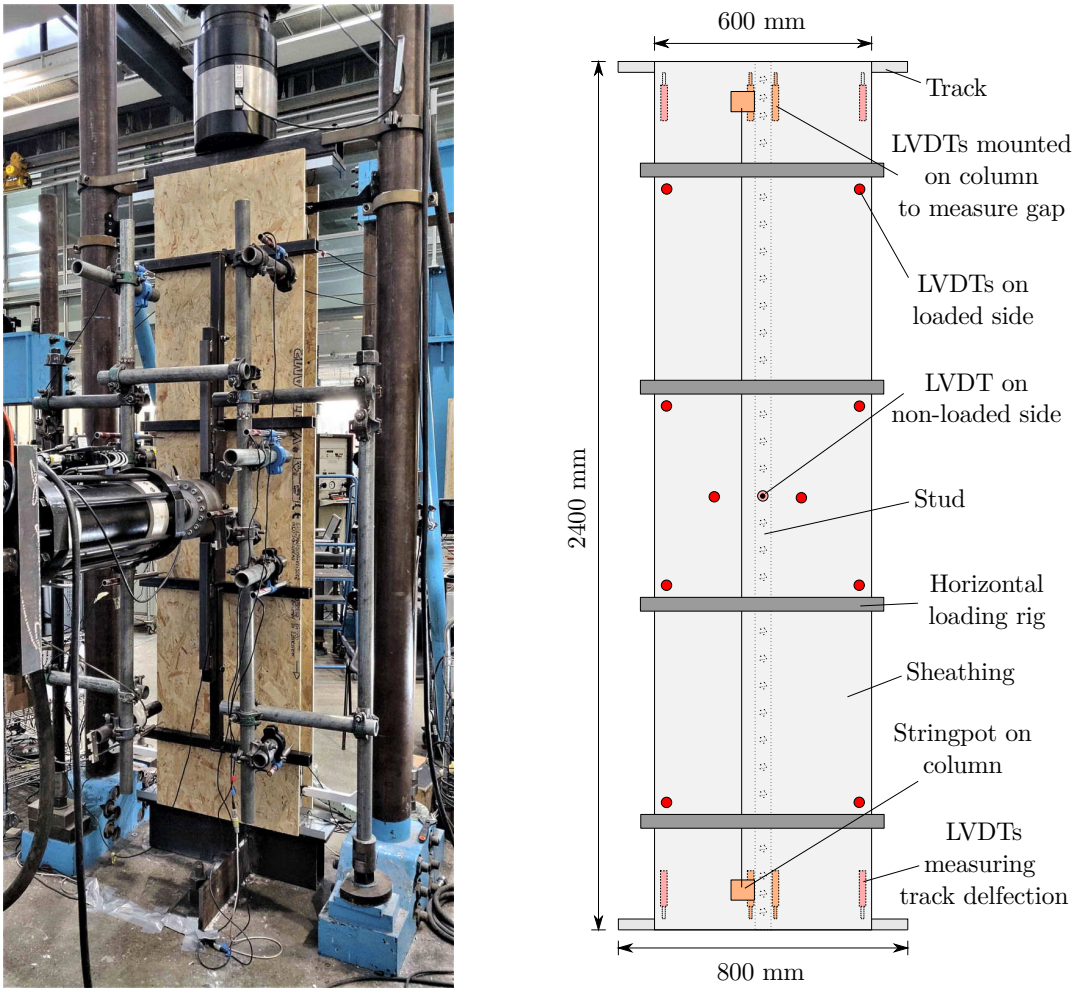


Figure 5.13: (a) Photo and (b) schematic illustration of test rig with employed instrumentation

In total 19 LVDTs and one string potentiometer were used to measure displacements. Eight LVDTs, along with the string-pot attached to the column, were used to measure the shortening of the column. At each column end, two LVDTs were used to measure the deflection of the track, while two LVDTs mounted on either side of the column measured the closing gap between the column and the track during loading. The net axial shortening of the column was calculated as the difference between the gap closure and track deflection. The axial shortening of the column was also measured using the string potentiometer spanning between the ends of the column, as shown in Figure 5.13. Ten LVDTs on the laterally loaded side and one in the centre of the non-loaded side were used to measure lateral displacements. The LVDTs on the loaded side were positioned in the middle of the sheathing and as close

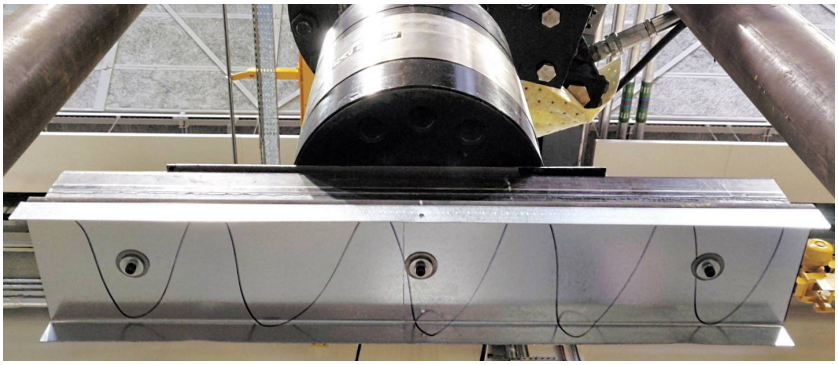
as possible to the loading arms of the whiffletree to record the maximum displacement due to bending, as shown in Figure 5.13. The loads and displacement measurements from the actuators, the LVDTs and the string potentiometer were captured using the DATASCAN acquisition system, recording at a frequency of 1 Hz.

5.3.6 Boundary and loading conditions

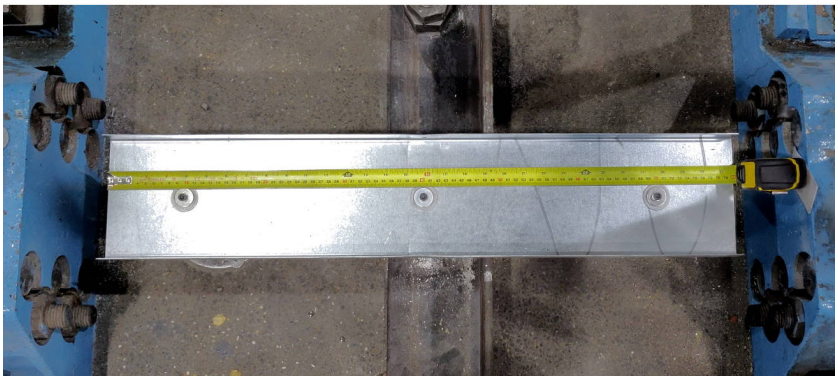
The length of the tracks of the tested specimens was 800 mm, as shown in Figure 5.13 (b). Detailed views of the top and bottom tracks connected to the test rig are shown in Figure 5.14, where the 6 mm in diameter anchor bolts with washers are also shown; these were used to secure the tracks to the hot-rolled steel sections. The connection between the column and the track is shown in Figure 5.15.

The boundary conditions at the member ends derived from the direct contact between the column ends and the web of the tracks. As such, the ability for the column ends to rotate depended on the applied axial load level. For low axial load levels, the boundary conditions were approximately pinned, while for higher axial load levels, increased end fixity arose. The bending moment diagram under the four-point loads and under an equivalent uniformly distributed load assuming pinned end conditions is shown in Figure 5.16 (a), while, in Figure 5.16 (b), the corresponding bending moment diagrams assuming fixed boundaries are shown. The total length of the column is designated by L and the horizontal load by H.

The axial load was applied using displacement control at a rate of 0.25 mm/min while the horizontal load was applied at a rate of 2.00 mm/min also under displacement control. The specimens subjected to pure compression or pure bending were loaded beyond the ultimate load, until a load decrease could be clearly observed. For the combined load cases, the specimens were first axially loaded to a pre-determined load level; the axial load was then held constant under load control, while the horizontal load was increased until failure occurred.



(a)



(b)

Figure 5.14: (a) Top and (b) bottom tracks connected to the test rig

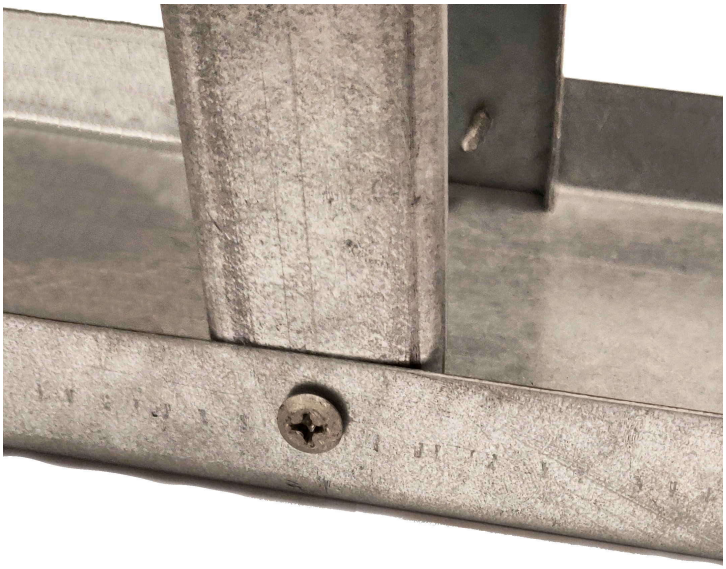


Figure 5.15: Column-to-track connection

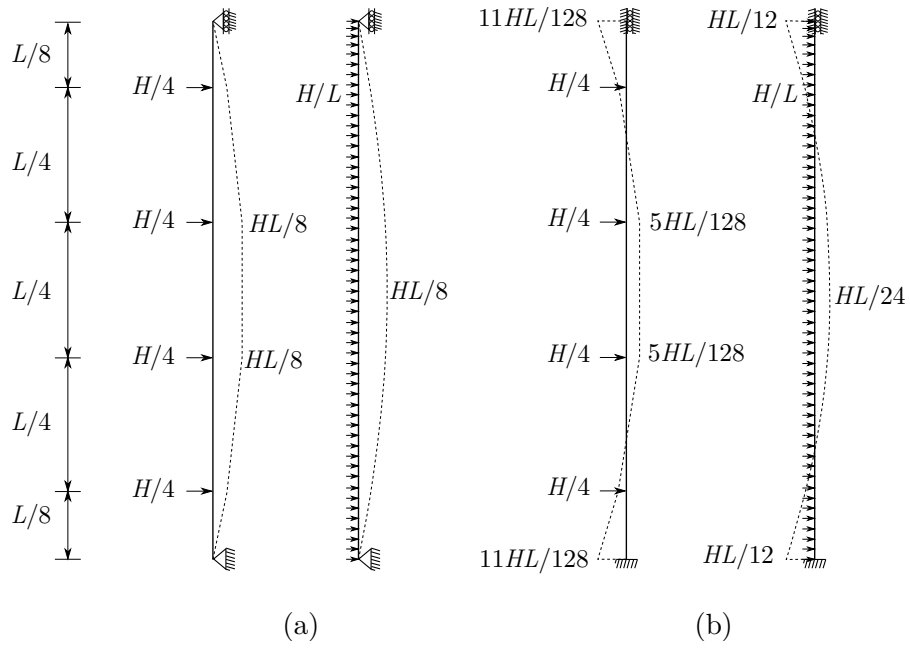


Figure 5.16: Bending moment diagrams under 4-point loads and the equivalent uniformly distributed load for (a) pinned and (b) fixed boundary conditions

5.4 Experimental results

A total of 17 member tests were conducted, with eight specimens subjected to pure compression, six to combined compression and bending and three to pure bending. The tested members were sheathed with the same type of board and using the same number of screws on both sides. A summary of the test details and results, including the type of sheathing used, the spacing between the screws, the axial load P_u and horizontal load H_u at failure and the mode(s) of failure, is provided in Table 5.6. The notation used for each test in Table 5.6 begins with the letter G for plasterboard (gypsum) or O for OSB, then with the level of the applied compressive load (expressed as a percentage of the compressive strength of the stud, as determined through the testing performed herein), followed by the letter S and finally by the spacing between the screws in mm. For repeat specimens, 1 or 2 was added at the end of their notation to differentiate between them.

Table 5.6: Summary of details of the tested specimens and observed failure loads

#	Designation	Sheathing type	Screw spacing (mm)	P_u		H_u	Failure mode *
				%	(kN)	(kN)	
1	G-100-S600-1	Gypsum	600	100	69.0	0.0	D → CF → FT
2	G-100-S600-2	Gypsum	600	100	77.7	0.0	D → CF → FT
3	G-100-S300-1	Gypsum	300	100	76.5	0.0	(L + D (hole)) → CF
4	G-100-S300-2	Gypsum	300	100	82.1	0.0	(D → CF) + $L_{(end)}$
5	G-100-S150	Gypsum	150	100	85.5	0.0	(L (end) + D) → CF
6	G-100-S75	Gypsum	75	100	90.5	0.0	L (end)
7	O-100-S600	OSB	600	100	79.5	0.0	L (end) + D
8	O-100-S75	OSB	75	100	90.7	0.0	L (end)
9	O-75-S600	OSB	600	75	60.0	14.0	L (hole)
10	O-75-S75	OSB	75	75	67.5	15.5	L (hole)
11	O-50-S600	OSB	600	50	40.0	17.4	L (hole)
12	O-50-S75	OSB	75	50	45.0	21.3	L (end) + L (hole)
13	O-25-S600	OSB	600	25	20.0	20.8	L (hole)
14	O-25-S75	OSB	75	25	22.5	23.5	L (end) + L (hole)
15	O-0-S600	OSB	600	0	0.0	20.8	L + L (end)
16	O-0-S75-1	OSB	75	0	0.0	22.3	L (end) + CF (column-to-track)
17	O-0-S75-2	OSB	75	0	0.0	20.8	L (end) + CF(column-to-track)

* CF: connector failure, L: local buckling, D: distortional buckling, FT: flexural torsional buckling

Six of the specimens under pure compression were sheathed with plasterboard and two with OSB. For the specimens sheathed with plasterboard, all four connector spacings were examined, i.e. 600 mm, 300 mm, 150 mm and 75 mm - as illustrated in Figure 5.11 while, for the specimens sheathed with OSB, only the two extreme spacings of 600 mm and 75 mm were studied.

Following testing of the plasterboard specimens under pure compression, and since pull-through failure was prominent, it was decided that the specimens to be tested under combined loading and pure bending would be sheathed with OSB only, with connectors spaced either at every 600 mm or 75 mm. Six tests were conducted under combined load, where the axial compression level was set to 75%, 50% and 25% of the stud compression resistance, which had been determined based on the two tests with OSB sheathing under pure compression.

5.4.1 Pure compression test results

A summary of the results of the pure compression tests is shown in Figure 5.17, where the failure load P_u is plotted against the employed spacing of connectors. Substantial increases in capacity can be observed with decreasing connector spacing (from 600 mm to 75 mm), with a 14% increase attained for the OSB sheathed specimens and 23% increase, on average, for the plasterboard sheathed specimens. Note that, in addition to the individual experimental results, an average line between the repeat tests has also been plotted for the plasterboard specimens to highlight the trend in the data. For all the specimens connected

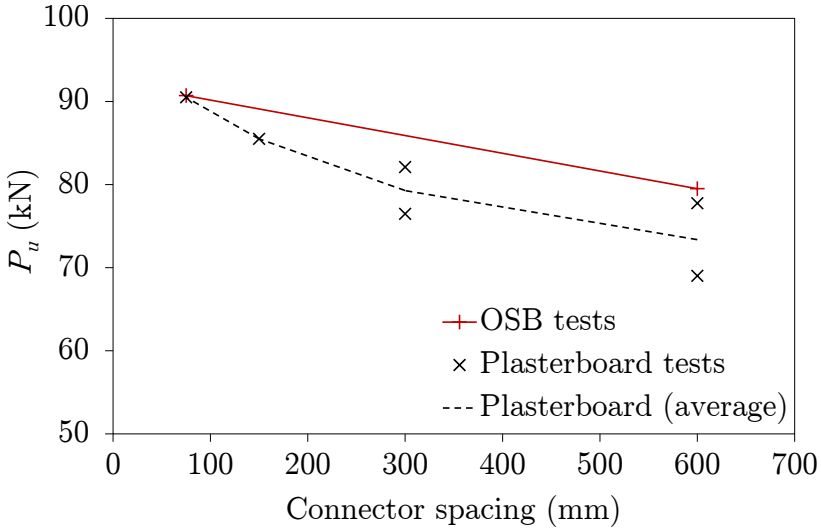


Figure 5.17: Ultimate load plotted against connector spacing for specimens under pure compression

at 300 mm and 600 mm intervals, pull-through failure of the connectors, exacerbated by distortional buckling of the flanges (see Figure 5.18 (a)), was observed; this was followed by sudden flexural torsional buckling of the column once the connection to the sheathing was lost. For the member sheathed with plasterboard and connected at 150 mm intervals, screw pull-through failure initiated at the top end of the specimen; this then led to the further development of local and distortional buckling and eventually to overall member failure. For the specimens with a connector spacing of 75 mm, pull-through of the screws was prevented and failure was triggered by local buckling near the bottom end of the columns. For the specimens sheathed with OSB, failure was due to a combination of distortional and local buckling; the specimen connected at 75 mm intervals reached a higher capacity due to the

greater restraint provided by the screw connectors.



(a) (b)

Figure 5.18: Typical failure modes: (a) distortional buckling (and pull-through failure of connectors) for a member under compression and (b) local buckling at a service hole for a member under bending

5.4.1.1 Boundary conditions under pure compression

The boundary conditions at the ends of the specimens under pure compression, set in tracks and connected at the flanges through screws, are effectively clamped due to the presence of the applied axial force – upon rotation of the end cross-section about either edge, a restoring moment $M_R = Ph/2$ is generated about that edge by the centroidally-acting axial force, leading to fixed boundary conditions – see Figure 5.19. This is particularly clear, and supported by the observed experimental results in this study and reported findings in the literature by Vieira et al. (2011) and Yun & Gardner (2018), for deeper members (larger h), but may diminish for shallower (smaller h) members.

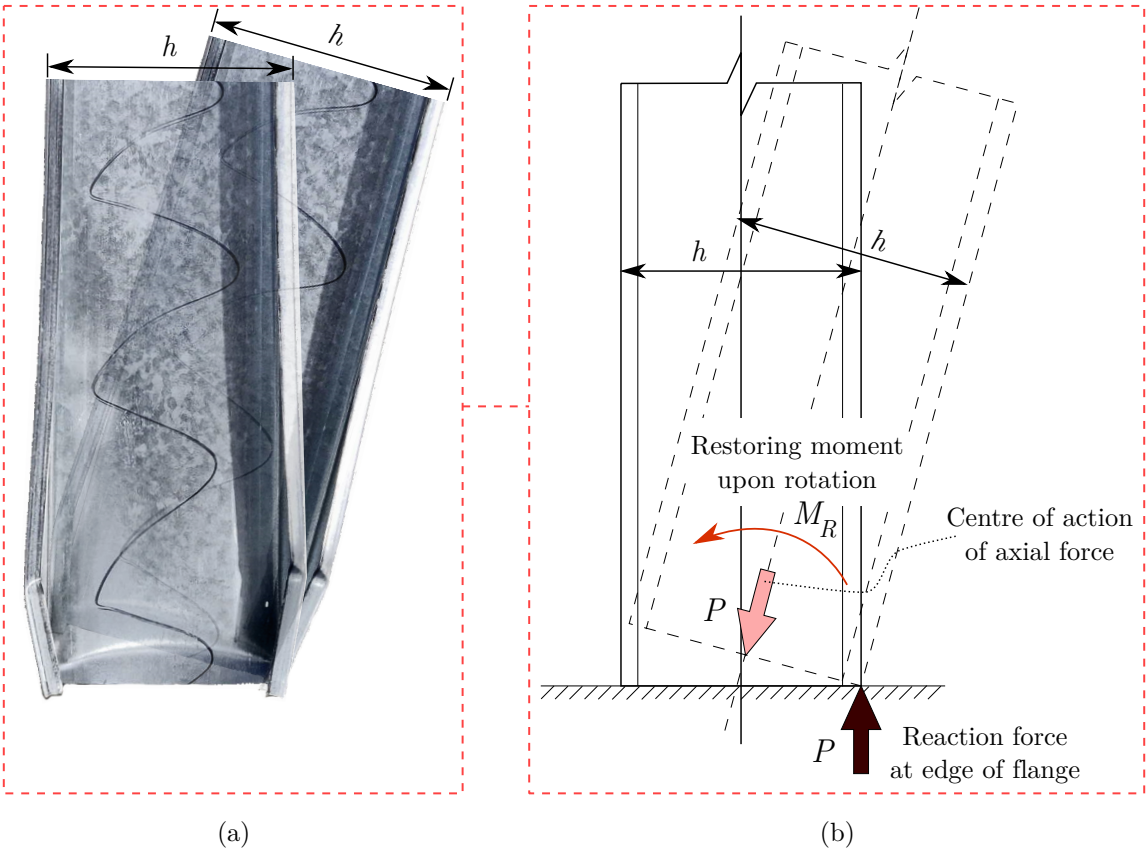


Figure 5.19: (a) Typical end failure mode for specimens under pure compression and (b) schematic illustration of end fixity arising due to the restoring moment from axial force. Note that the overall end rotation illustrated in (b) is prevented in the real system, as seen in (a), due to the action of the restoring moment.

5.4.1.2 Load-displacement curves under pure compression

Load-displacement curves derived from different measurement devices – the vertical actuator, the string potentiometer attached to the column and the difference between the measurements of the LVDTs positioned on the tracks and on the column measuring the gap between them – of a typical specimen under compression (G-100-S75) are shown in Figure 5.20. As shown in the figure, the load-displacement response based on the displacements recorded by the actuator exhibited a substantially lower stiffness than the theoretical axial stiffness of the column EA/L (where E is the Young's modulus of the steel, A is the cross sectional area of the column and L is the length of the column), with the gradual increase of stiffness at the beginning of the curve corresponding to the gradual closure of the gap

between the track and the column. Since the string potentiometer was not measuring across the gap, the resulting initial stiffness of the member closely matches the theoretical axial stiffness. Deviations at higher loads relate to the asymmetric nature of the measurements, which were taken on one side of the specimens only. Finally, the curve calculated based on the difference of the LVDT readings measuring the deflection of the tracks and the gap closure between the track and column (see Figure 5.13 (b)) closely matches the general response of the column.

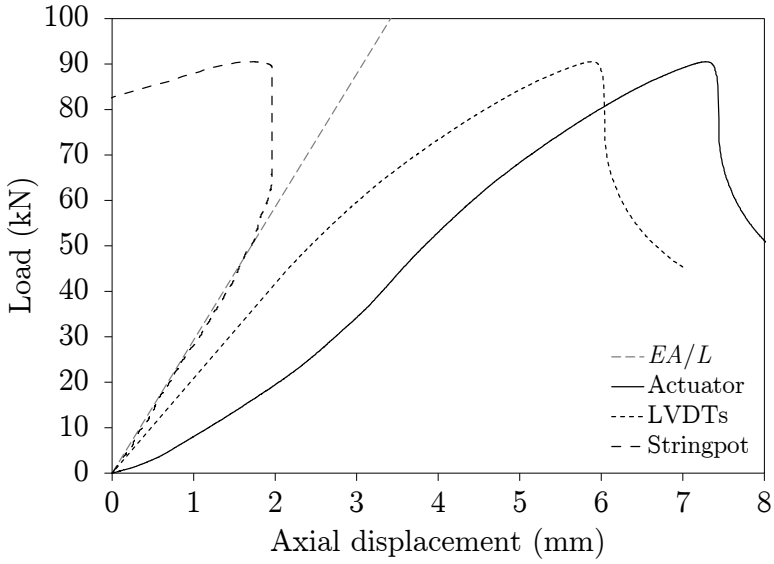


Figure 5.20: Axial load-displacement curves of a typical specimen under pure compression

For all specimens under pure compression, the reported load-displacement curves are based on the LVDT measurements, after correction of the full curves, using Equation (5.6), based on the 'true' initial stiffness captured from the stringpot, which closely matches the axial stiffness EA/L, as described below.

$$\delta_{true} = \delta_{LVDT} - \left(\frac{P}{k_{LVDT}} - \frac{P}{k_{stringpot}} \right) \tag{5.6}$$

In Equation (5.6), δ_{true} is the adjusted axial displacement, δ_{LVDT} is the axial displacement based on the LVDT measurements, P is the axial load, $k_{stringpot}$ is the initial stiffness from the stringpot curve and k_{LVDT} is the initial stiffness from the LVDT curve; the initial stiffnesses were determined based on measurements up to about 40% of the peak load where

the response remained approximately linear. Adjustment of a full axial load-displacement curve using Equation (5.6) for a typical specimen (G-100-S75) is demonstrated in Figure 5.21.

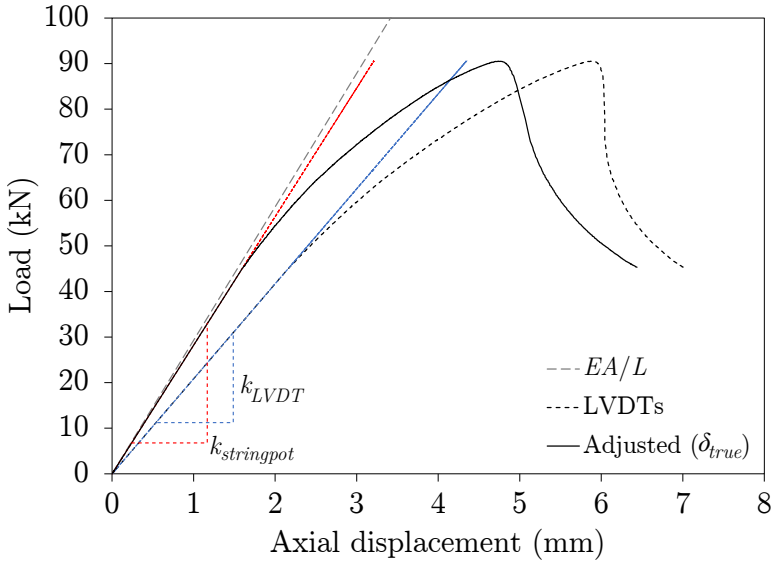


Figure 5.21: Adjustment of gradient for the results of axial load-displacement curves

The axial load-displacement curves for the OSB sheathed specimens are presented in Figure 5.22, while the corresponding curves for the specimens sheathed with plasterboard are shown in Figure 5.23. The discontinuities that can be seen in the specimens sheathed

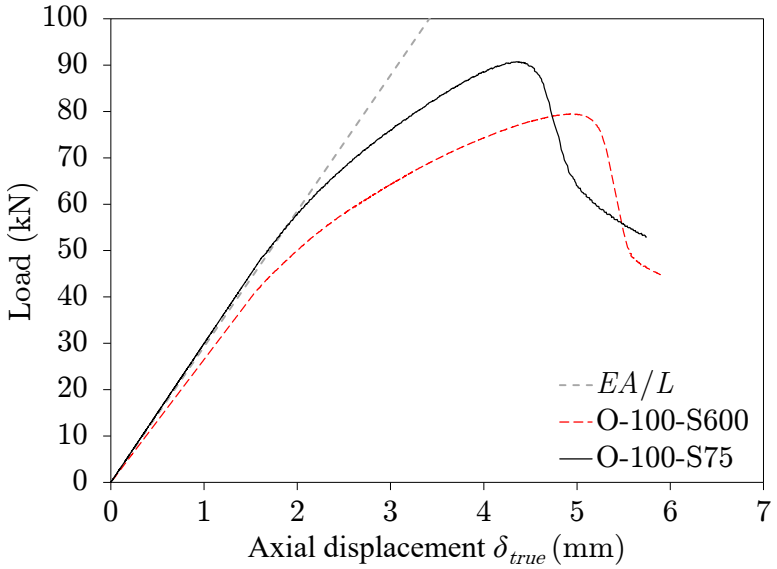


Figure 5.22: Axial load-displacement curves of specimens sheathed with OSB under compression

with plasterboard (Figure 5.23) and connected at 150 mm, 300 mm and 600 mm intervals correspond to failure of individual connectors.

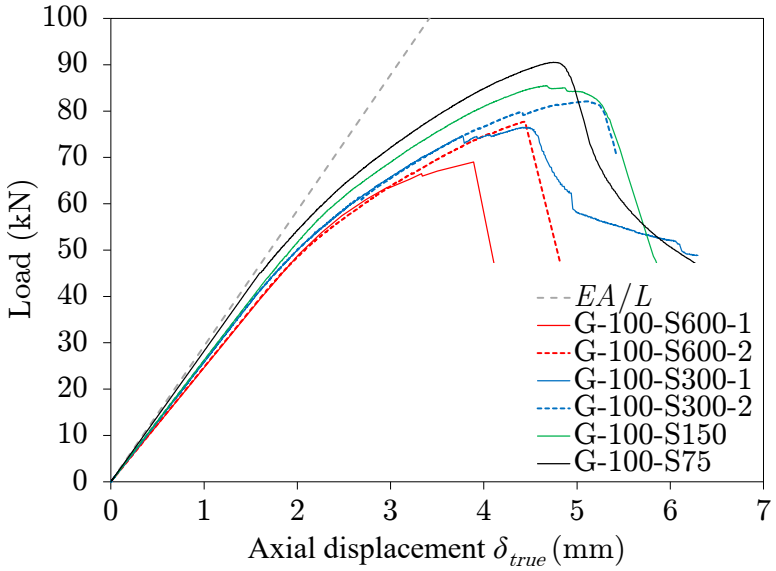


Figure 5.23: Axial load-displacement curves of specimens sheathed with plasterboard under compression

A comparison between the specimens sheathed with OSB and plasterboard and subjected to pure compression is presented in Figure 5.24. As expected, it can be observed that

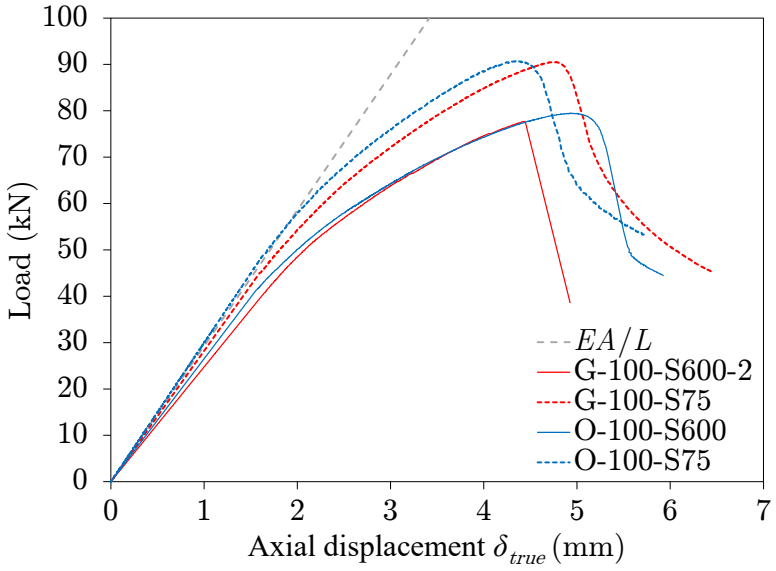


Figure 5.24: Comparison between the axial load-displacement curves of specimens sheathed with plasterboard and OSB under compression

the stiffness and capacity of the specimens increases with increasing numbers of connectors

due to the additional restraint to both the global and cross-sectional buckling modes. The specimens with the connectors spaced at 75 mm intervals exhibited similar peak capacities, although a slightly higher stiffness was observed for the specimens sheathed with OSB.

The failure modes of the columns sheathed with plasterboard are shown in Figure 5.25. For the specimens that were connected at 600 mm and 300 mm intervals, distortional buckling developed between the connectors, while the specimens connected every 150 mm and 75 mm suffered local buckling failure near the column ends.



(a) (b)

Figure 5.25: (a) Failure modes of columns sheathed with plasterboard and tested under compression (from left to right – connectors spaced at 600 mm, 300 mm (2 repeated), 150 mm and 75 mm), (b) test specimen with 600 mm connector spacings, post failure (with the sheathing removed to observe the failure mode)

5.4.2 Compression and bending test results

The results from the combined compression and bending tests are presented in Figure 5.26, where the ultimate compression loads P_u are plotted against the ultimate horizontal loads H_u; a distinction is made between the OSB-sheathed specimens with connectors spaced at 600 mm and 75 mm intervals. Increased capacities in both compression and bending (between 15 – 20%) were attained when closer-spaced connectors were employed. It should be mentioned that the capacity of the specimens tested under pure bending was limited by the strength of the connection between the track and the column.

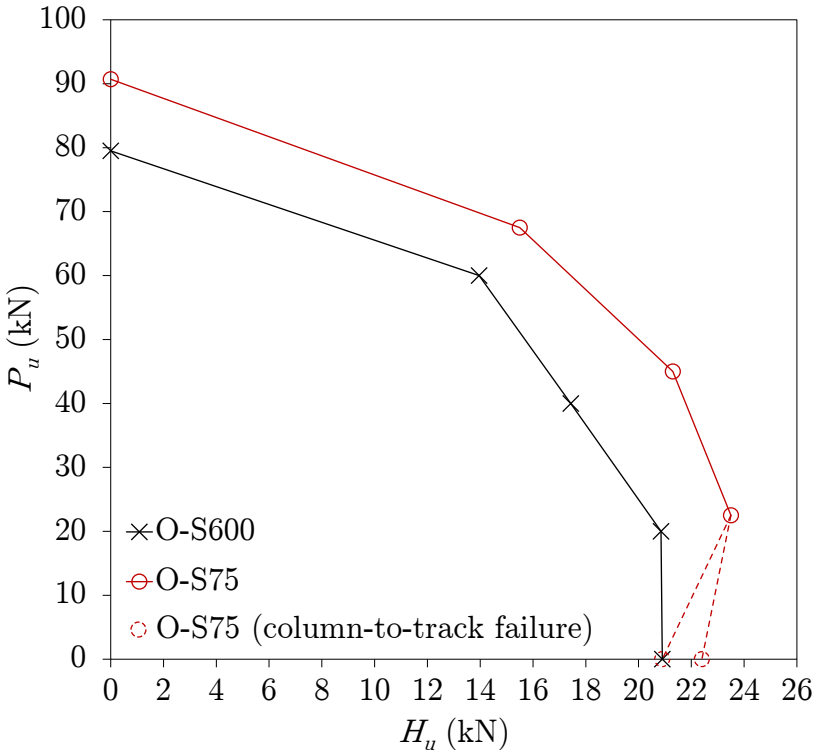
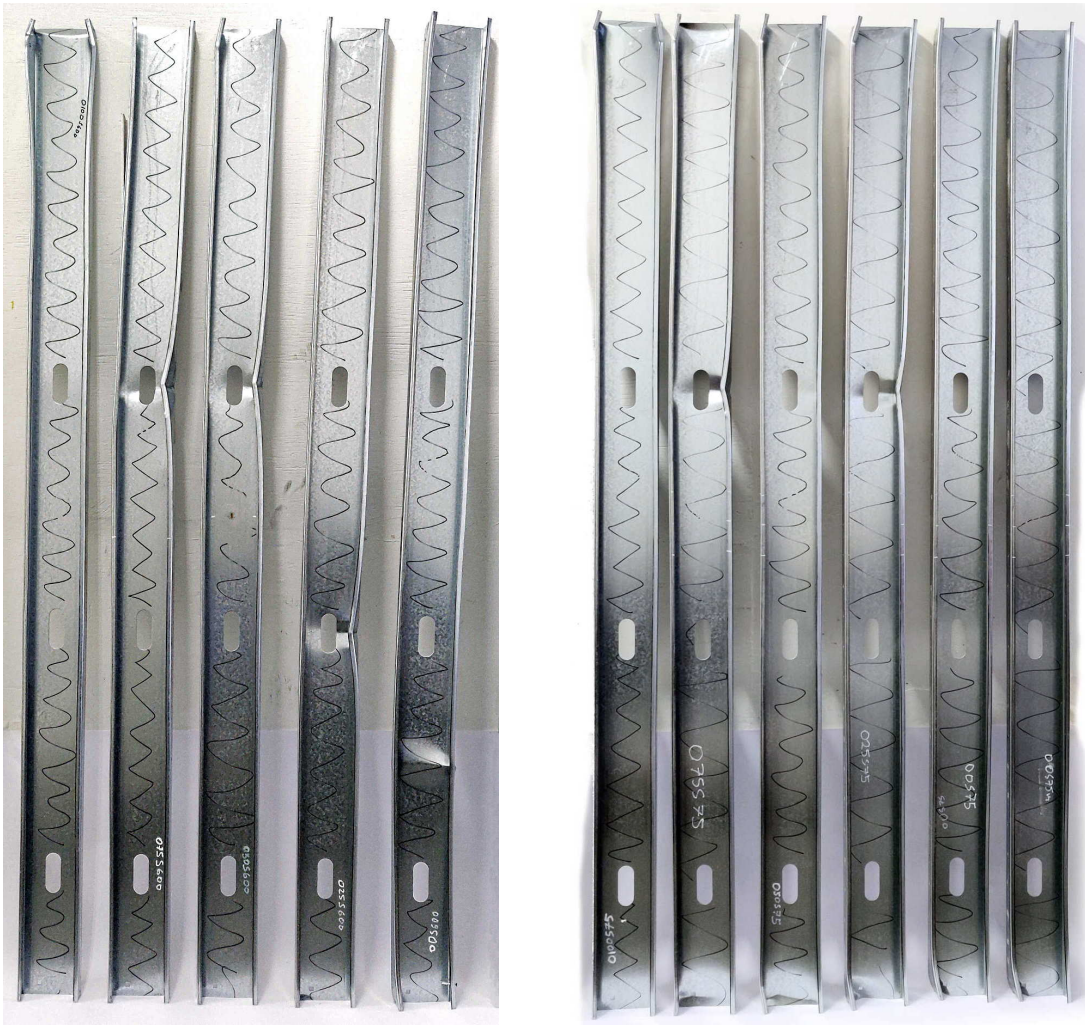


Figure 5.26: Ultimate compression (P_u) and horizontal (H_u) loads for beam-column specimens sheathed with OSB and connected at 600 mm and 75 mm intervals

The dominant failure mode of the OSB-sheathed beam-column specimens was local failure at the service openings and at the ends of the members, as shown in Figure 5.27. For the specimens under pure bending with the connectors spaced at 75 mm, shear failure of the screws between the main member and track occurred – see Figure 5.27 (b), without which, higher load-bearing capacities were anticipated.



(a) (b)

Figure 5.27: Failure modes of all the tests specimens (from left to right – 100% compression to 100% bending) with OSB sheathing connected at (a) 600 mm spacings and (b) 75 mm spacings

5.4.2.1 Load-displacement curves

The horizontal load versus mid-height displacement curves for the OSB sheathed beam-columns are shown in Figures 5.28 and 5.29 for the specimens connected at 75 mm and 600 mm spacings respectively; all tested specimens are plotted together in Figure 5.30. Note that the horizontal mid-height displacement was calculated by averaging the three LVDT measurements at mid-height (from the two LVDTs on the loaded side and the third on the non-loaded side – see Figure 5.13 (b)). The full load-deflection curves are shown in Figure

5.30 (a) while their initial part is presented in Figure 5.30 (b), where lines corresponding to the theoretical linear response in the case of pinned and fixed boundary conditions are also plotted. The theoretical responses were calculated assuming linear, elastic behaviour for the 4-point load configuration illustrated in Figure 5.16; the calculated mid-height deflections (δ_p and δ_f) and stiffnesses (k_p for pinned and k_f for fixed) were determined using Equations (5.7) and (5.8), where H is the total horizontal load, L is the length of the member and EI is the sum of the flexural rigidities of the steel member and the two sheathing boards. The calculated k_p and k_f values were 1.29 kN/mm and 6.60 kN/mm respectively.

$$\delta_p = \frac{41HL^3}{3072EI} \quad ; \quad k_p = H/\delta_p = \frac{3072EI}{41L^3} \tag{5.7}$$

$$\delta_f = \frac{HL^3}{384EI} \quad ; \quad k_f = H/\delta_f = \frac{384EI}{L^3} \tag{5.8}$$

It was found that the flexural stiffnesses of the specimens with the connectors spaced at 75 mm intervals that were subjected to axial loads corresponding to 75% and 50% of their compressive resistance were approximately 30% and 20% respectively higher than the theoretical flexural stiffness corresponding to a member with pinned-end conditions. For the specimens with connectors spaced at 600 mm intervals under axial loads equal to 75% and 50% of their compressive resistance, the flexural stiffnesses were about 20% and 10% respectively higher than the theoretical value for a pin-ended member. The relative degree of fixity can be expressed as $\beta = (k - k_p)/(k_f - k_p)$, where k is the initial stiffness determined from the horizontal load–mid-displacement curves (where $\beta = 0$ and $\beta = 1$ correspond to pinned and fixed end conditions and all intermediate values i.e. $0 \leq \beta \leq 1$ correspond to the partially restrained end conditions achieved in the tests.

In Figure 5.31, the relative degree of fixity β is plotted against the percentage of compression for all beam-column specimens. It can be observed that the relative degree of fixity increases with increasing compression and with decreasing connector spacing. This can be explained with reference to Section 5.4.1.1 and Figure 5.19, where, as described for the case of pure compression, the applied axial load generates a restoring moment as the member rotates about the outer edge of the cross-section. This effect weakens (or remains active up

to lower lateral load levels) as the level of applied compression reduces and as the overturning moment (i.e. the applied bending moment) becomes more dominant Yun & Gardner (2018).

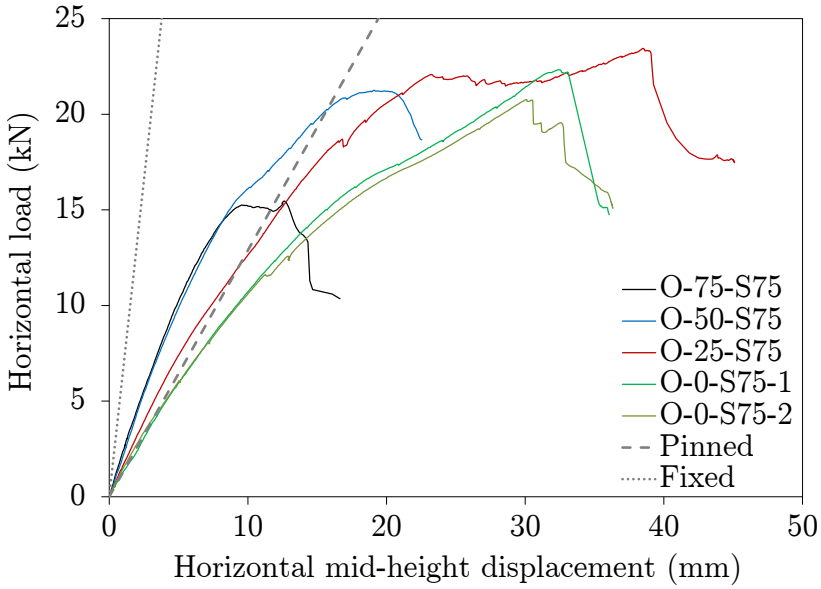


Figure 5.28: Horizontal load versus mid-height displacement curves for beam-column specimens connected at 75 mm intervals

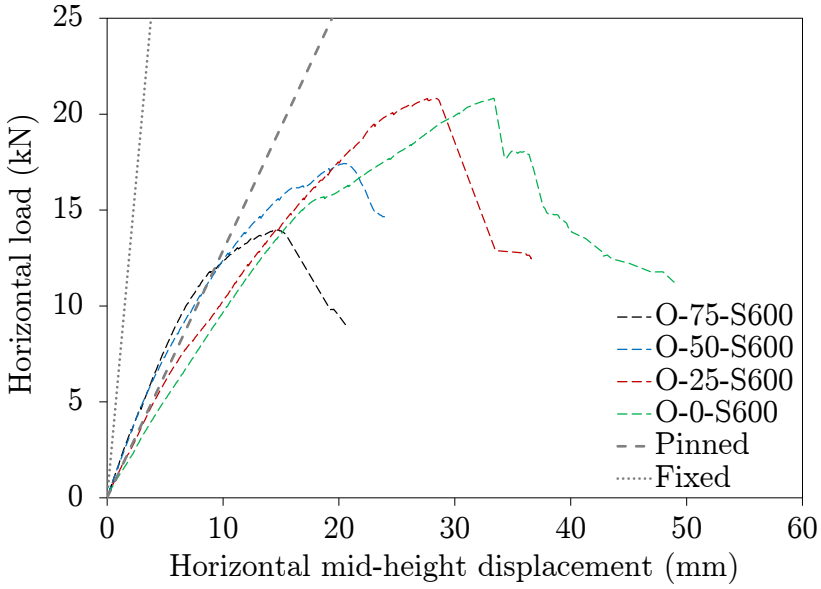


Figure 5.29: Horizontal load versus mid-height displacement curves for beam-column specimens connected at 600 mm intervals

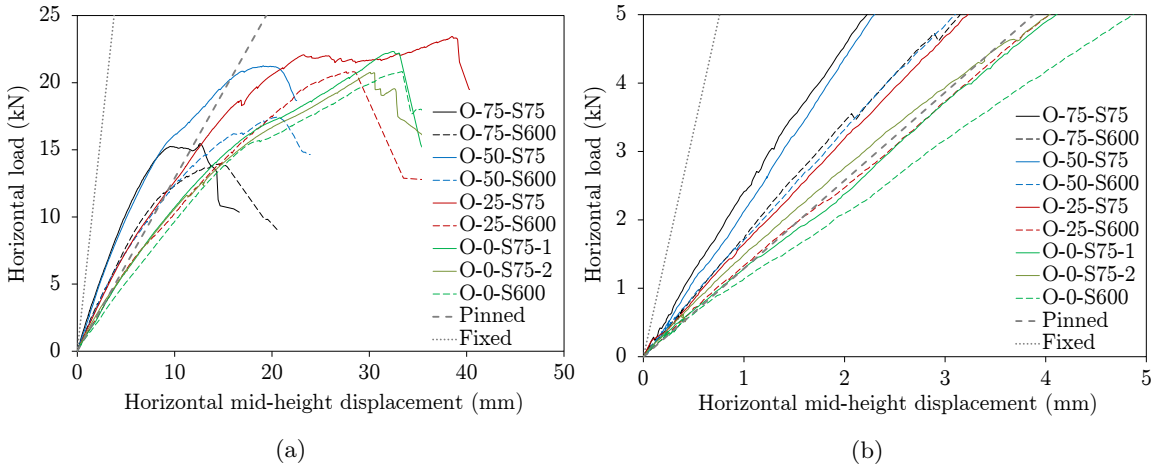


Figure 5.30: Horizontal load versus mid-height displacement curves for all specimens over (a) full range and (b) initial stages of loading for comparison with the theoretical stiffness for fixed and pinned boundary conditions

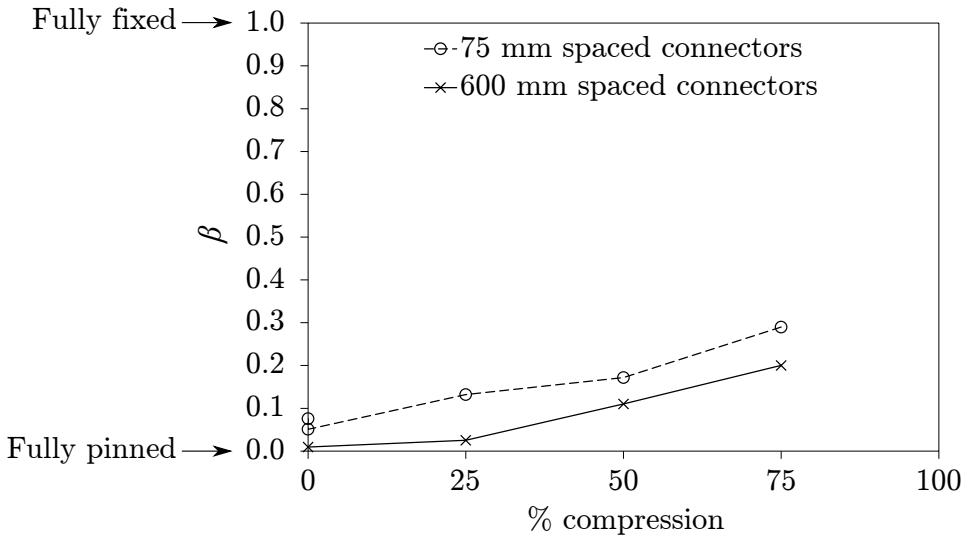


Figure 5.31: Relative degree of fixity β with increase in compression level for beam-columns based on slope of horizontal load-mid-span deflection curves

5.4.2.2 Load-rotation curves

Two inclinometers, mounted on the webs of the beam-column specimens at a distance of $L/10$ from each end, were used for determining the near-end rotations of the members during loading. The load-rotation curves, based on the average readings from the two inclinometers (which were close to symmetrical), are presented for the specimens with connector spacings

of 75 mm and 600 mm in Figures 5.32 and 5.33 respectively. The theoretical rotations, θ_p and θ_f, at $L/10$ and the rotational stiffnesses, $k_{\theta,p} = H/\theta_p$ and $k_{\theta,f} = H/\theta_f$, corresponding to the member response with pinned and fixed end conditions, calculated according to Equations (5.9) and (5.10) respectively, are also plotted. The calculated $k_{\theta,p}$ and $k_{\theta,f}$ values were 17.80 kN/deg and 118.20 kN/deg respectively.

$$\theta_p = \frac{259HL^2}{6400EI}\frac{180}{\pi} \quad ; \quad k_{\theta,p} = H/\theta_p = \frac{320\pi EI}{2331L^2} \tag{5.9}$$

$$\theta_f = \frac{39HL^2}{6400EI}\frac{180}{\pi} \quad ; \quad k_{\theta,f} = H/\theta_f = \frac{320\pi EI}{351L^2} \tag{5.10}$$

Similarly to the load-displacement results, the load-rotation results indicate increasing end fixity (or retention of fixity to higher lateral load values) with increasing compression levels and reducing connector spacing. This is shown in Figure 5.34, where the relative degree of fixity is now expressed in terms of the rotations i.e. $\beta_\theta = (k_\theta - k_{\theta,p})/(k_{\theta,f} - k_{\theta,p})$. The relative degrees of fixity derived from the load-rotation and the load-mid-span displacement curves are very similar (within 5%).

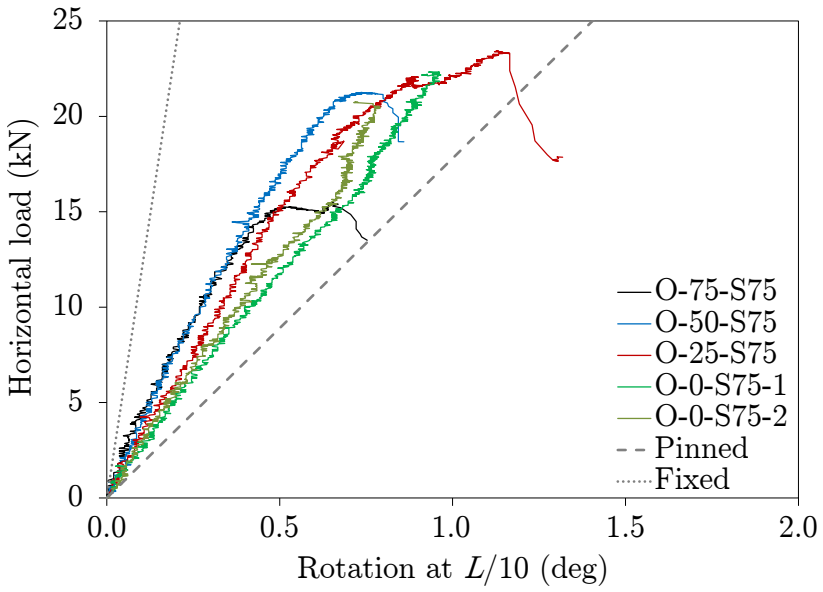


Figure 5.32: Horizontal load versus rotation at $L/10$ curves for beam-column specimens connected at 75 mm spacings

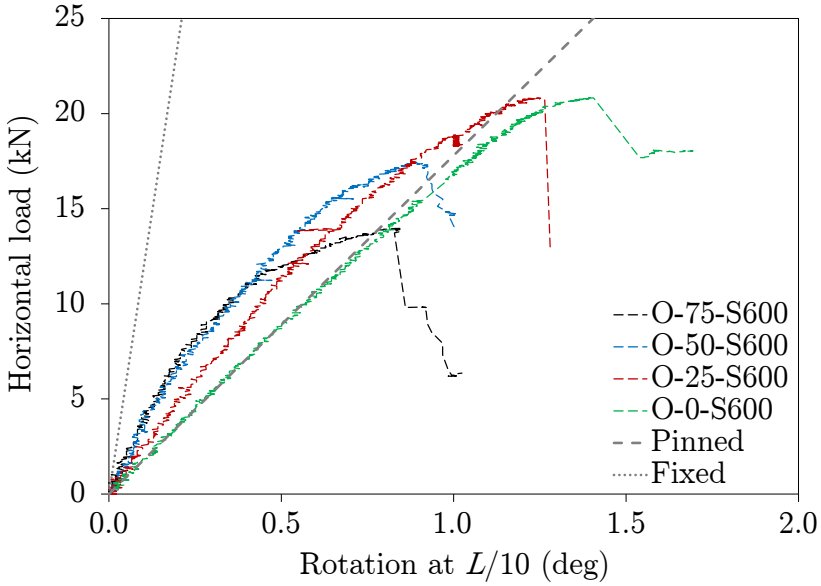


Figure 5.33: Horizontal load versus rotation at $L/10$ curves for beam-column specimens connected at 600 mm spacings

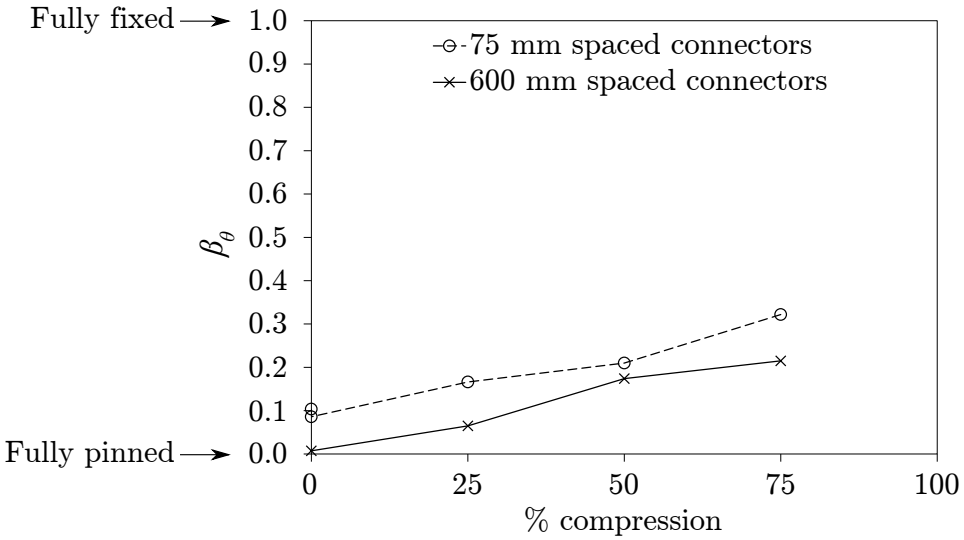


Figure 5.34: Relative degree of fixity β_θ with increase in compression level for beam-columns based on the slope of horizontal load versus rotation at $L/10$

5.4.2.3 Strain distributions

For the combined compression-bending specimens and the bending specimens, strain gauges were mounted at the mid-height of the members in the middle of the flanges, as shown in Figure 5.35 (b). The strain gauges were used to monitor the progression of strain

at key locations on the specimens during testing and to verify that the loading was applied as intended. The two strain gauges mounted on the members are designated as SGT for the one on the tension (or lower compression) flange and SGC for the one on the compression flange. A graph showing the development of strain for the typical case of the O-75-S600 specimen during the compression P and then horizontal H loading stages is illustrated in Figure 5.35 (a). Three key points are highlighted in Figure 5.35: (1) at the pre-determined compression load P_u (75% of the pure compressive resistance for the case illustrated) prior to the application of any horizontal load, (2) at P_u and 50% of ultimate horizontal load H_u and (3) at P_u and 100% of H_u. The similarity of compressive strains in the compression stage and symmetry (i.e. approximately equal and opposite strains) in the bending stage confirm that the test setup and specimens performed as intended.

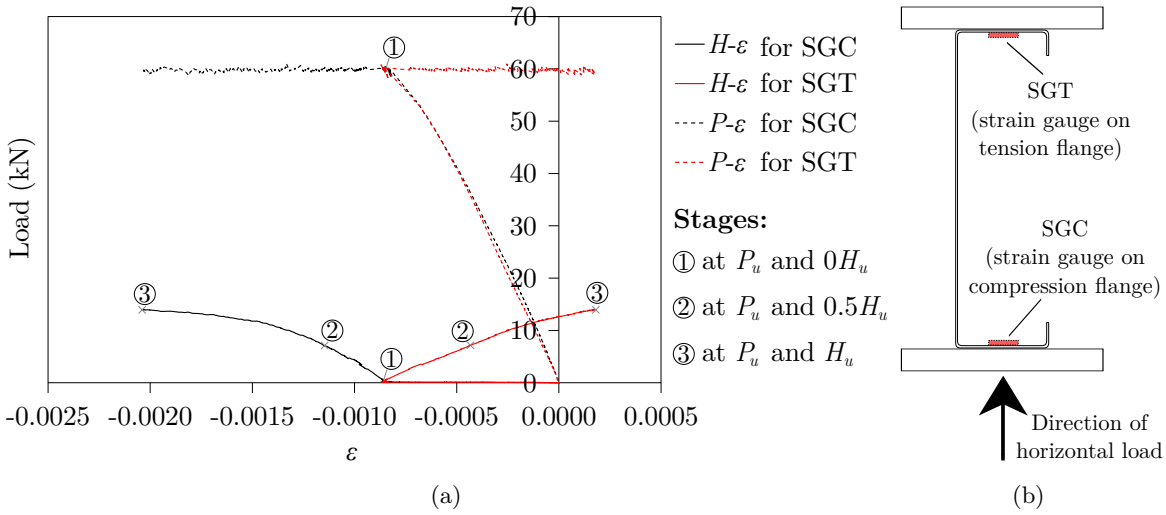


Figure 5.35: Strain gauge results from beam-column tests showing (a) development of strain for specimen O-75-S600 and (b) position of strain gauges at mid-height of member

5.5 Comparison with existing findings and code provisions

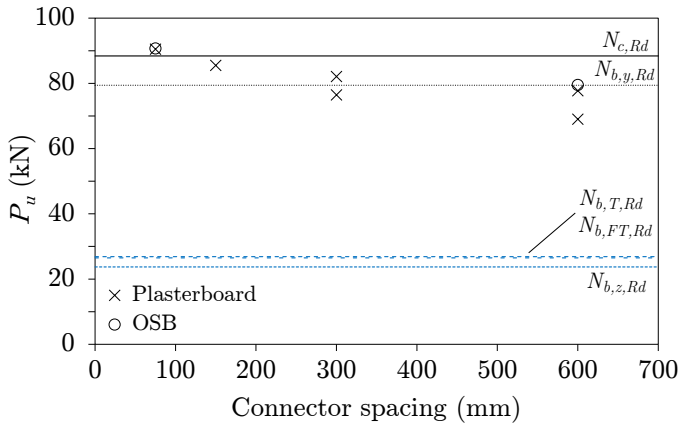
5.5.1 Comparison with previous experimental findings in the literature

The findings of Vieira et al. (2011), in which the screw connectors in sheathed cold-formed steel members were shown to provide effective restraint against global buckling modes, have been supported by the research presented herein. Full restraint to the global

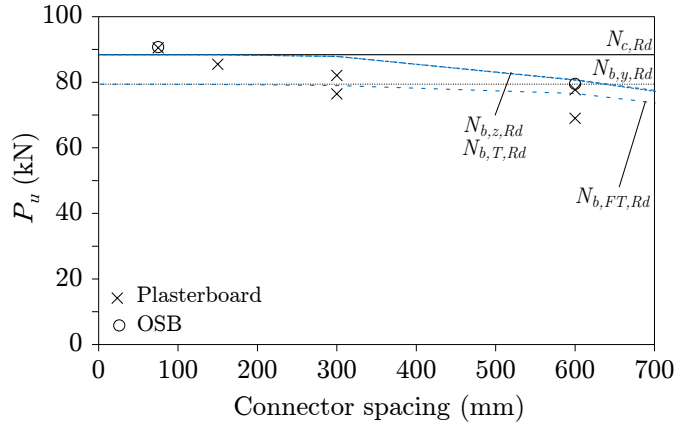
modes, such that local/distortional buckling only became the controlling failure modes, was achieved in the present study for specimens with the more substantial interconnection, as also found by Vieira et al. (2011). With regards, to the end fixity achieved in cold-formed steel wall systems, as also indicated by Peterman & Schafer (2014) and Peterman (2012) under pure bending, the end conditions are close to pinned, but as the level of axial load and the degree of interconnectivity increases, there is a transition towards fixed ended boundary conditions.

5.5.2 Comparison with Eurocode 3 design provisions

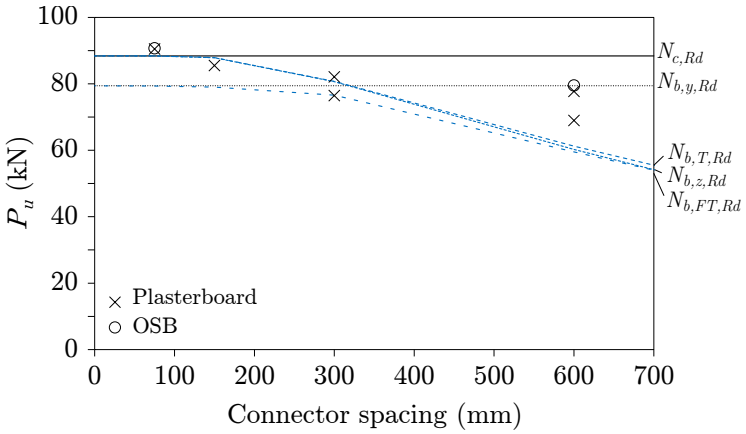
The compression capacities of the sheathed specimens, even for the widest connector spacing, were found to be significantly higher than those predicted using EN 1993-1-1 (2005) and EN 1993-1-3 (2006) with typical design assumptions, including that of pinned boundary conditions at the member ends. Comparisons between the Eurocode 3 axial resistance predictions and the obtained test results are provided in Figure 5.36. Note that the calculation of the cross-sectional compression resistance $N_{c,Rd}$, loss of effectiveness due to local and distortional buckling was accounted for in line with the EN 1993-1-3 (2006) provisions. The member resistances (i.e. the flexural buckling resistances about the major $N_{b,y,Rd}$ and minor $N_{b,z,Rd}$ axis, the torsional buckling resistance $N_{b,T,Rd}$ and the flexural-torsional buckling resistance $N_{b,FT,Rd}$) were initially calculated with the effective lengths for buckling about the major $L_{cr,y}$ and minor $L_{cr,z}$ axes taken as the full member length (2.4 m). This typical design assumption (Way & Heywood 2012) presupposes that no restraint is provided by the sheathing; the results are shown in Figure 5.36 (a). Equivalent comparisons are presented in Figure 5.36 (b), but with the effective length for buckling about the minor axis $L_{cr,z}$ taken equal to the spacing of the connectors. As shown in Figure 5.36 (a), without any restraint assumed from the sheathing, the test results are underestimated by about three to four times, with $N_{b,z,Rd}$ being the critical resistance. On the other hand, as shown in Figure 5.36 (b), taking $L_{cr,z}$ equal to the connector spacing leads to unsafe predictions for the plasterboard sheathed specimens connected at 300 mm and 600 mm intervals which suffered connector failure, but safe-sided predictions for the OSB-sheathed specimens where



(a) $L_{cr,y}$ = 2400 mm, $L_{cr,z}$ = 2400 mm



(b) $L_{cr,y}$ = 2400 mm, $L_{cr,z}$ = connector spacing



(c) $L_{cr,y}$ = 2400 mm, $L_{cr,z}$ = 2 × connector spacing

Figure 5.36: Comparisons between compression test results and EN 1993-1-3 (2006) resistance predictions with different assumptions made for $L_{cr,z}$ equal to (a) the full column length of 2400 mm (b) the connector spacing and (c) two times the connector spacing. $L_{cr,y}$ was taken as the full member length in all cases.

connector failure did not occur. An intermediate condition with $L_{cr,z}$ taken as twice the connector spacing, effectively assuming that every other connector has failed and does not contribute any restraint, is presented in Figure 5.36 (c) yielding safe-sided predictions for the specimens suffering connector failure.

The beam-column test results are compared with the EN 1993-1-3 (2006) interaction curve, given by Equation (5.11), in Figure 5.37. The design assumptions that have been considered are: (i) no restraint from the sheathing (ii) $L_{cr,z} = 600$ mm and (iii) $L_{cr,z} = 75$ mm. Note that the effective length about the major axis $L_{cr,y}$ was taken as the full length of the member in all cases.

$$\left(\frac{P_u}{N_{b,Rd}}\right)^{0.8} + \left(\frac{M_u}{M_{b,Rd}}\right)^{0.8} \leq 1.0 \tag{5.11}$$

In Equation (5.11) $N_{b,Rd}$ is taken as the minimum of $N_{c,Rd}$, $N_{b,y,Rd}$, $N_{b,z,Rd}$, $N_{b,T,Rd}$ and $N_{b,FT,Rd}$, while $M_{b,Rd}$ is the lateral torsional buckling resistance. Design moment resistances are converted to equivalent horizontal forces (H), for comparison with the horizontal test loads, using $H = M_{b,Rd} \times 8/L$ as shown in Figure 5.16 (a) assuming pinned boundary conditions and $L = 2.4$ m. Note, that calculation of the effective section properties for both compression and bending (i.e. the effective area and section modulus) was carried out by including iteration of the effective thickness for the effects of distortional buckling, while the influence of rounded corners was taken into account by using the mid-line design provisions by EN 1993-1-3 (2006); more details on the method are provided in Chapter 7.

As shown in Figure 5.37, assuming that the members have pinned end conditions and that no restraint is offered by the sheathing (i.e. $L_{cr,y} = L_{cr,z} =$ full member length) yields very conservative resistance predictions, while recognising the restraint from the connectors leads to considerably more accurate predictions, provided the connectors possess sufficient capacity (Kyprianou et al. 2021*a*,*b*, Peterman & Schafer 2014). The accuracy of the resistance predictions is however limited by the shape of the interaction curve set out in EN 1993-1-3 (2006). In particular, the concave nature of the curve, arising from the value of the powers in Equation (5.11) being 0.8 does not match the convex trend of the test data

points.

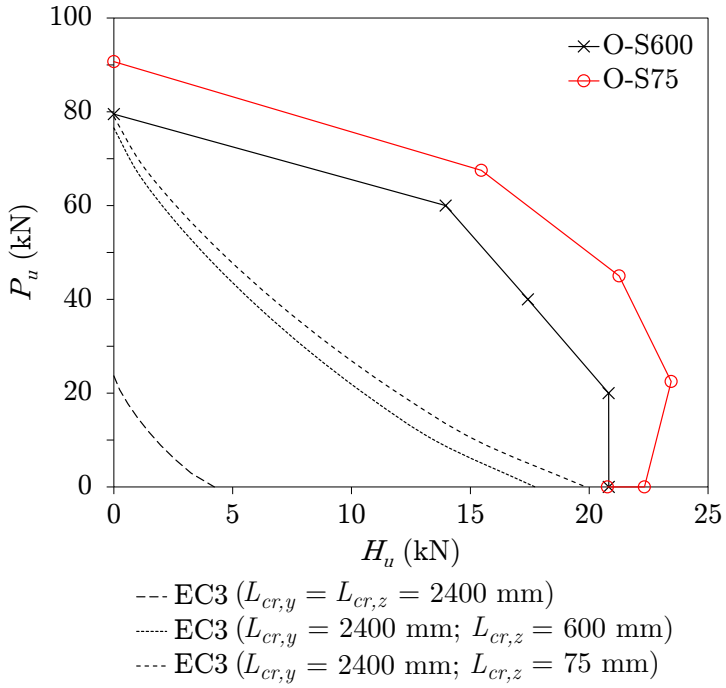


Figure 5.37: Comparison between tests results and EN 1993-1-3 (2006) resistance predictions assuming various effective lengths

5.6 Conclusions

An experimental study into the structural performance of sheathed cold-formed steel members has been presented in this chapter. Seventeen full-scale tests, comprising eight specimens under pure compression, six specimens under combined loading and three under pure bending, were carried out, along with supporting material tests and imperfection measurements. The tested specimens were sheathed with either plasterboard or OSB, on both sides, with various stud-to-sheathing connector spacings ranging from 600 mm to 75 mm.

When subjected to pure compression, the controlling failure mode exhibited by the studs connected to plasterboards at the wider spacings (i.e. 600 mm and 300 mm) was pull-through of the connectors, while for the studs sheathed with OSB and plasterboard at the denser connector spacings of 150 mm and 75 mm, local buckling was the dominant

failure mode. For the OSB-sheathed beam-column specimens local failure at the service openings was observed, while for the specimens subjected to pure bending, local buckling and stud-to-track connector failure occurred.

Reducing the spacing of the connectors from 600 mm to 75 mm resulted in up to 20% increases in the capacity of the specimens sheathed with OSB under both compression and bending. For the specimens sheathed with plasterboards and subjected to pure compression, reducing the connector spacing from 600 mm to 75 mm resulted in up to 30% increases in capacity while pull-through connector failure was also prevented.

Initial comparisons with existing design guidance revealed that if the effect of the sheathing is not considered, very conservative resistance predictions are obtained. Further investigations on the effect of the board and decreasing connector spacing are carried in the next chapter with the use of numerical simulations, validated against the results presented in this chapter.

Chapter 6

Finite element study on sheathed cold-formed steel beam-columns

6.1 Introduction

THE structural behaviour of sheathed cold-formed steel lipped channel section columns (studs) subjected to combined compression and major axis bending is investigated herein by means of numerical simulations. Finite element (FE) models of single studs, set in tracks and connected to oriented strand board (OSB) and gypsum plasterboard sheathing under varying combinations of axial compression and horizontal load were developed in ABAQUS (2016). The developed numerical models incorporated cross-sectional and global initial geometrical imperfections, while geometrical and material nonlinearities for both the steel and the sheathing were considered in the analyses. Particular emphasis was given to replicating the 'as-built' boundary conditions at the ends of the columns, controlled by the screws connecting the column to the track and by the column-track contact interaction. The interaction between the sheathing and the column as well as the behaviour of the fasteners connecting the two components were also explicitly modelled.

Finite element models of single sheathed studs or wall systems under compression have been presented by Telue & Mahendran (2004), Lawson et al. (2019), Vieira & Schafer (2016) and Kechidi et al. (2020), while no such sophisticated simulations have been presented for

combined axial and horizontal loading. Numerical studies to date (Telue & Mahendran 2004, Lawson et al. 2019, Vieira & Schafer 2016, Kechidi et al. 2020) have adopted a linear elastic material model for the sheathing. In the study by Vieira & Schafer (2016), the focus has been on the assessment of the shear demand on the screw connectors between the sheathing and the steel, while in the work by Kechidi et al. (2020), modelling of user-defined elements to describe the nonlinear, strength and stiffness deteriorating response of these screws under monotonic and cyclic loading was presented and evaluated against experimental results.

A detailed methodology of the finite element modelling is provided in Section 6.3, while the employed models of the screw connection behaviour in pull-through and shear, developed and presented in Chapter 4 (Kyprianou et al. 2021*b*) based on experimental studies presented in Chapter 3 (Kyprianou et al. 2021*a*), were employed to capture the connector limits and failures. After successful validation (see Section 6.4) against experimental data reported by Young (1997), Young & Rasmussen (1998*a*,*b*), Vieira et al. (2011), Vieira (2011), Peterman & Schafer (2014), Peterman (2012) and the tests described in Chapter 5 (Kyprianou et al. 2021*c*), the developed finite element model was employed for parametric studies. The parametric studies presented in Section 6.5 investigated the influence of the board on pure compression specimens and examined the effect of variable connector spacing and section depth under various combinations of load. Parts of the methodology and validation of the finite element modelling approach presented in this chapter have been published by Kyprianou et al. (2018).

6.2 Beam-column wall system

The examined structural system, illustrated in Figure 6.1, is made up of a single stud column connected to sheathing and tracks of appropriate width, reflecting the boundary and loading conditions experienced by stud columns in sheathed wall systems under compression and bending about the major axis. A single stud column was modelled for computational efficiency since based on experimental studies on single studs set in tracks and connected with sheathing were shown to have the same axial capacities as studs tested within stud

wall systems consisting of five studs (Vieira & Schafer 2013). Note that the conducted finite element simulations were based on the configurations presented in the experimental studies of Peterman & Schafer (2014), and those described in Chapter 5 and in Kyprianou et al. (2021*c*), where bending was introduced using a mid-height load and four point loads (simulating uniform distributed loading) respectively.

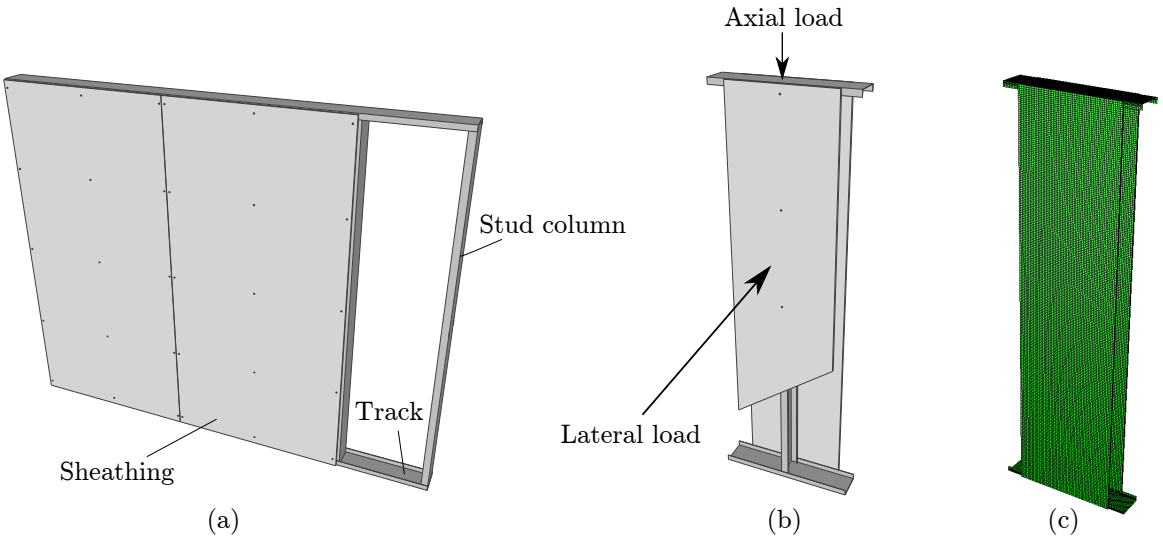


Figure 6.1: Illustrations of (a) stud wall with sheathing (b) single sheathed stud column under compression and bending about the major axis (c) finite element model

6.3 Finite element modelling

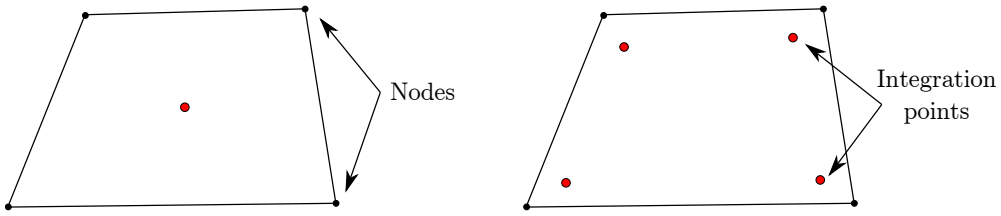
The finite element software ABAQUS (2016), which has been extensively used in the past for simulating cold-formed steel members (Young & Yan 2000, Dinis et al. 2007, Yu & Schafer 2007, Vieira & Schafer 2016, Hadjipantelis et al. 2019, Kyvelou et al. 2019, Kechidi et al. 2020, Kyvelou et al. 2020) as well as composite structural systems (Kyvelou et al. 2018), was employed for the numerical investigation presented herein. In the developed finite element model, shown in Figure 6.1, the C-lipped cold-formed steel columns (studs), the sheathing boards and the U-shaped tracks were explicitly replicated. The configurations considered involve OSB or plasterboard fastened to the cold-formed steel columns by means of screws, which are simulated with the use of spring elements. The key features of the developed finite element models as well as the relevant modelling assumptions are presented

in the following sections.

6.3.1 Element type

Shell elements are commonly used for the modelling of thin-walled structural members, whose thickness is significantly smaller than their two other dimensions, since they can accurately capture cross-sectional instability phenomena such as local and distortional buckling (Kyvelou et al. 2018, Hadjipantelis et al. 2019, Dinis et al. 2007, Schafer et al. 2010). Hence, the steel components of the examined system, namely the columns and tracks, were modelled with the commonly used (Kyvelou et al. 2018, Hadjipantelis et al. 2019) general purpose quadrilateral four-noded S4R (ABAQUS 2016) shell elements with reduced integration and hourglass control, while the default ABAQUS (2016) value, of five, for the number of section integration points through the element thickness was used.

The linear four-noded shell element with reduced integration S4R, shown in Figure 6.2 (a), is computationally more efficient than its counterpart S4 element with a full integration scheme, shown in Figure 6.2 (b), since the number of integration point locations per element is reduced from four to one. Although S4R elements are computationally less expensive, they tend to suffer from 'hourglassing', where zero strains can arise at the single integration point when the element is distorted, leading to mesh instability and problems of numerical convergence. Therefore, S4R elements are used with hourglass control, while a fine mesh and distributed loading is recommended to avoid excess stresses (ABAQUS 2016).

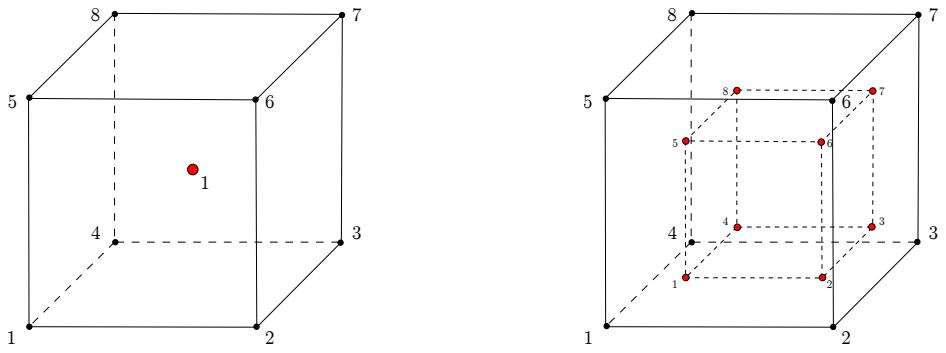


(a) S4R element (b) S4 element

Figure 6.2: Four-noded shell elements with (a) a reduced single integration point scheme and (b) a full 2×2 integration point scheme. Adapted from ABAQUS (2016).

Continuum 3D elements, also known as solid or brick elements, are frequently used for modelling the thicker members in composite structural systems, such as concrete slabs in

concrete-steel (Ellobody 2014) and boards in board-steel (Kyvelou et al. 2018) structural members. In the present study, the sheathing boards were modelled using eight-noded C3D8R (ABAQUS 2016) solid elements with reduced integration and hourglass control, with an aspect ratio approximately equal to one. The geometry of solid elements, shown in Figure 6.3, allows for an accurate and realistic replication of the connection between the board and the steel stud, since spring elements, which are used to simulate screwed connectors as explained below, can be attached to the top or bottom surface of the board, depending on the characteristics of the modelled response - see Section 6.3.4. As shown in Figure 6.3, the C3D8R elements with reduced integration are computationally less expensive than their counterpart fully integrated C3D8 elements, since the integration points are reduced from eight to one.



(a) C3D8R element (b) C3D8 element

Figure 6.3: Eight-noded brick (hexahedral) elements with (a) a reduced single integration point scheme and (b) a full $2 \times 2 \times 2$ integration point scheme. Adapted from ABAQUS (2016).

Spring elements were used to model the screwed connectors between steel-to-steel and steel-to-board elements in shear and pull-through, as well as to replicate physical restraints in certain directions that prevent rigid-body motion, such as contact with the loading surfaces or the presence of the foundation. SPRING1, SPRING2 and SPRINGA elements are available in the ABAQUS (2016) software and their behaviour can be modelled by assigning them a force-displacement or rotation-moment profile; in the current study, only force-displacement profiles have been assigned to all three aforementioned types of springs. SPRING1 elements are used for the implementation of connections between nodes and the ground, while SPRING2 elements, shown in Figure 6.4 (a), are used to connect two nodes;

both types of spring can act only in a fixed direction. SPRINGA elements act between two nodes, with their line of action being the line joining the two nodes, and with this line being able to rotate in large-displacement analysis. The springs can be defined either as linear, where a stiffness is used to describe them, or as nonlinear, where a series of load-displacement data points, as shown in Figure 6.4 (b), are used to define their response. The positive and negative spring profiles, shown in Figure 6.4 (b), describe the behaviour of the spring in compression and tension. Whether the positive profile corresponds to tension or compression depends on the spring element type, the order definition of the nodes and the global coordinate system of the finite element model.

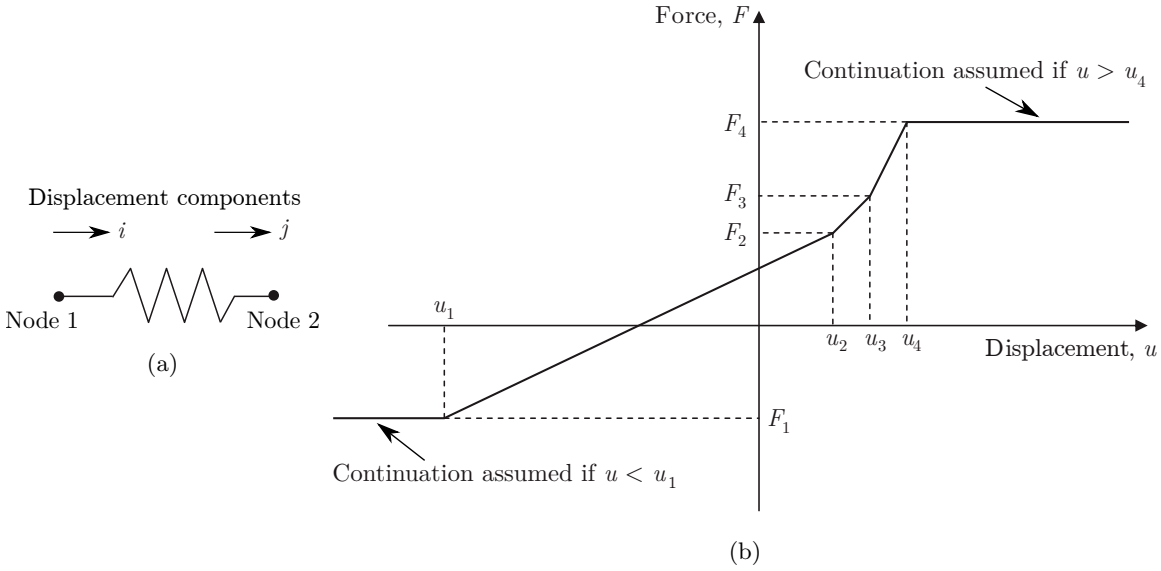


Figure 6.4: (a) Spring element notation and (b) nonlinear spring force-displacement relationship (ABAQUS 2016). Adapted from Ellobody (2014).

When describing the shear behaviour of a screw, typically modelled using a SPRING2 element between a node on the board and a node on the steel column, a symmetric profile in the positive and negative domains is employed since the shear behaviour is the same for both directions. Conversely, when using spring elements for modelling the pull-through behaviour of screws or for replicating restraints in certain directions, the spring response is defined only in its direction of action (i.e. for pull-through the springs are modelled with a profile that activates them only when in tension - see Section 6.3.4.1 for details on implementation).

6.3.2 Meshing scheme

Following a sensitivity study, a refined mesh, aiming at an aspect ratio of 1:1 for the flat regions of the cross-section and never exceeding 4:1 for the corners, was employed for the modelling of the cold-formed steel columns and tracks. The chosen mesh ensured that the arising local and distortional buckling modes could be accurately captured. The longitudinal element sizes for the columns and tracks were 5 mm and 10 mm, respectively. Typical cross-sectional mesh discretisations for various depths of cross-sections for the stud column are illustrated in Figure 6.5, where the number of nodes increases from 53 to 79 for sections increasing in depth from 68 to 252 mm.

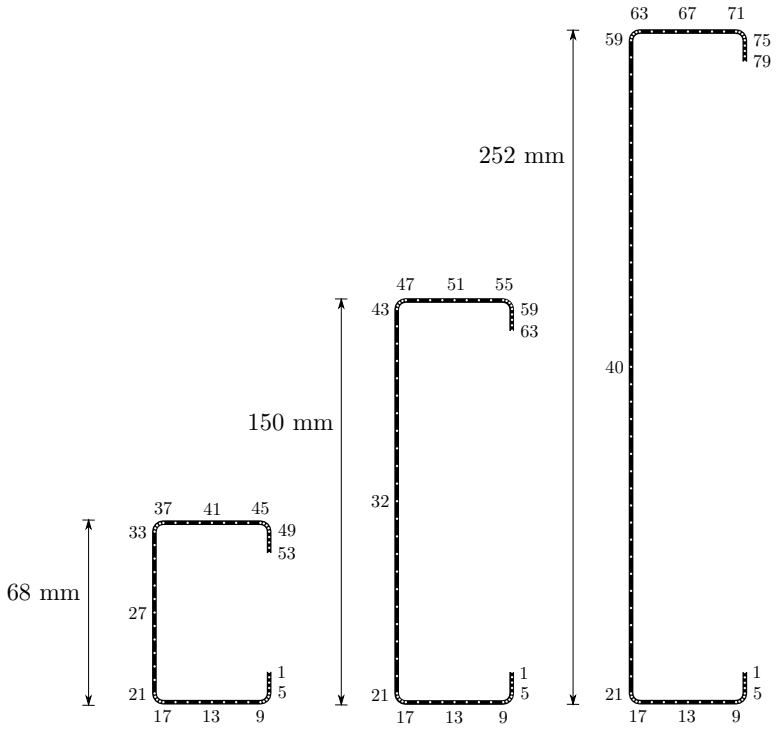


Figure 6.5: Stud column cross-sectional discretisation and node numbers for various section depths

For the board, a mesh size of 10 mm along its width and length was employed to ensure alignment with the nodes of the cold-formed steel columns at every other node. Following a sensitivity study, two layers of elements were employed through the board thickness since no significant improvements in accuracy were achieved by the use of three elements. The employed mesh was able to accurately capture the global bow deformation of the board during loading, while also being relatively computationally inexpensive. The cross-sectional

mesh discretisation of the sheathing and cross-sectional notation for both the stud column and the sheathing are illustrated in Figure 6.6, where h is the depth of the stud, b is the flange width, c is the lip length, r is the internal corner radius of the stud, t is the thickness of the stud and t_b is the thickness of the sheathing.

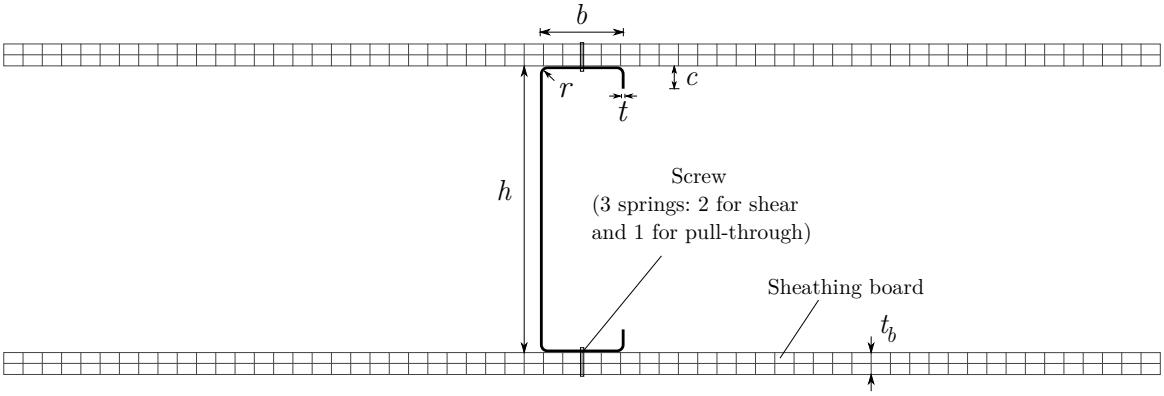


Figure 6.6: Cross-sectional notation of stud column and finite-element discretisation of sheathing

Since in practice service openings are cut in the web of stud members which are deeper than 150 mm, and to allow direct comparison of the finite element model with experiments on stud columns with service hole openings, explicit modelling of these openings was performed - see Figure 6.7. The nodal mesh was manually defined to capture the oval shape of the

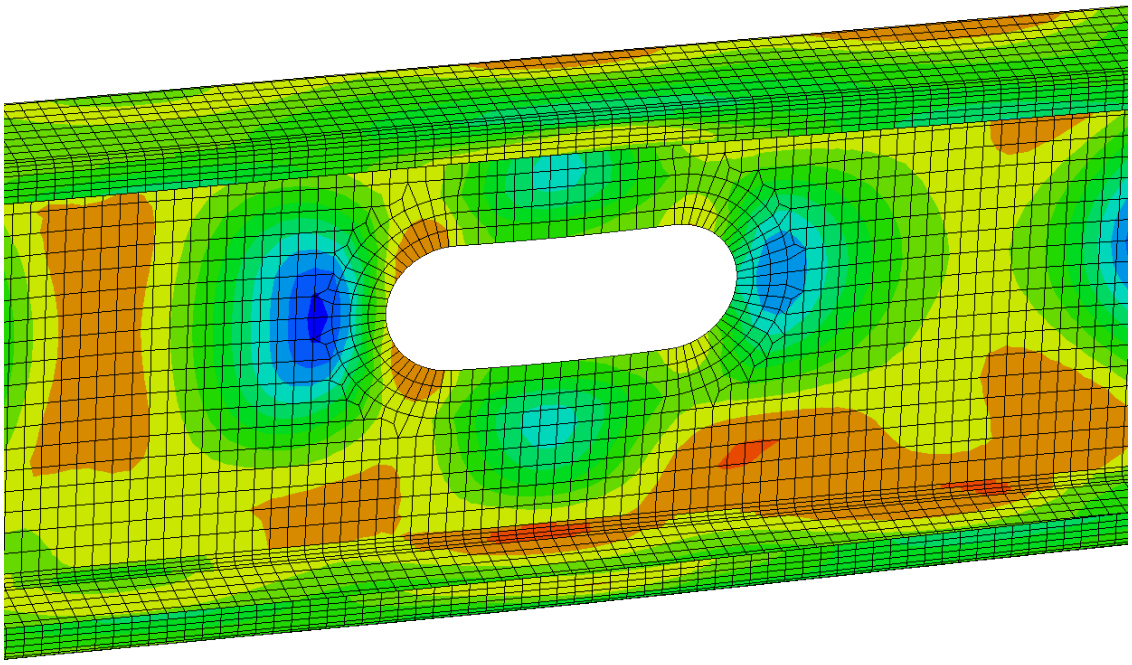


Figure 6.7: Adopted finite element mesh of the column with detail of the service hole mesh

openings, which was 100 × 38 mm with 19 mm radii at the ends as described in Chapter 5 and the tests presented by Kyprianou et al. (2021*c*). Note that the mesh was carefully designed to be symmetric along the length and width of the oval opening, to allow for four nodes for each element so that S4R elements could still be used and the shape of all the elements to be as square as possible.

6.3.3 Material modelling

6.3.3.1 Cold-formed steel

The stress-strain behaviour of cold-formed steels featuring a continuous nonlinear rounded stress-strain response can be modelled using the provisions set out by Gardner & Yun (2018), while for stress-strain responses featuring a yield plateau, use of the material model by Yun & Gardner (2017) is appropriate. The material response assigned to the cold-formed steel components of the systems examined herein and used in the validation of the finite element models was obtained from the respective stress-strain curves reported by Vieira & Schafer (2016), Young & Yan (2000), Peterman (2012) and Kyprianou et al. (2021*c*), which were derived by means of tensile coupon testing. For the tests reported in Chapter 5, which served as the basis for the validation (reported in Section 6.4.4) and parametric studies (reported in Section 6.5.2), the stress-strain response for the stud and track was modelled using Equation (6.1) (Yun & Gardner 2017), since the relevant experimental stress-strain curves featured a plateau at yield. The adopted material properties are provided in Table 6.1, where t is the thickness of the steel section, while a Poison's ratio of 0.3 was employed.

$$\sigma = \begin{cases} E\varepsilon & \text{for} \quad \varepsilon \leq \varepsilon_y \\ f_y & \text{for} \quad \varepsilon_y < \varepsilon \leq \varepsilon_{sh} \\ f_y + (f_u - f_y)\left\{ 0.4\left(\dfrac{\varepsilon - \varepsilon_{sh}}{\varepsilon_u - \varepsilon_{sh}}\right) + \dfrac{2\left(\dfrac{\varepsilon - \varepsilon_{sh}}{\varepsilon_u - \varepsilon_{sh}}\right)}{\left[1 + 400\left(\dfrac{\varepsilon - \varepsilon_{sh}}{\varepsilon_u - \varepsilon_{sh}}\right)^5\right]^{1/5}} \right\} & \text{for} \quad \varepsilon_{sh} < \varepsilon \leq \varepsilon_u \end{cases} \tag{6.1}$$

In Equation 6.1, σ is the stress, ε is the strain, E is the Young's modulus, f_y is the yield

strength, ε_y is the strain at f_y, ε_{sh} is the strain at the end of the yield plateau, f_u is the ultimate stress and ε_u is the ultimate strain.

Note that for the thinner sections which demonstrated a rounded stress-strain profile prior to yield (Kyprianou et al. 2021*c*), instead of using the linear expression of Equation 6.1 up to the yield point, Equation (6.2) was used, where n is a roundedness exponent.

$$\varepsilon = \frac{\sigma}{E} + 0.002\left(\frac{\sigma}{f_y}\right)^n \qquad \text{for} \quad \sigma \leq f_y \tag{6.2}$$

Table 6.1: Averaged material properties of stud and track reported by Kyprianou et al. (2021*c*) and used in the FE model

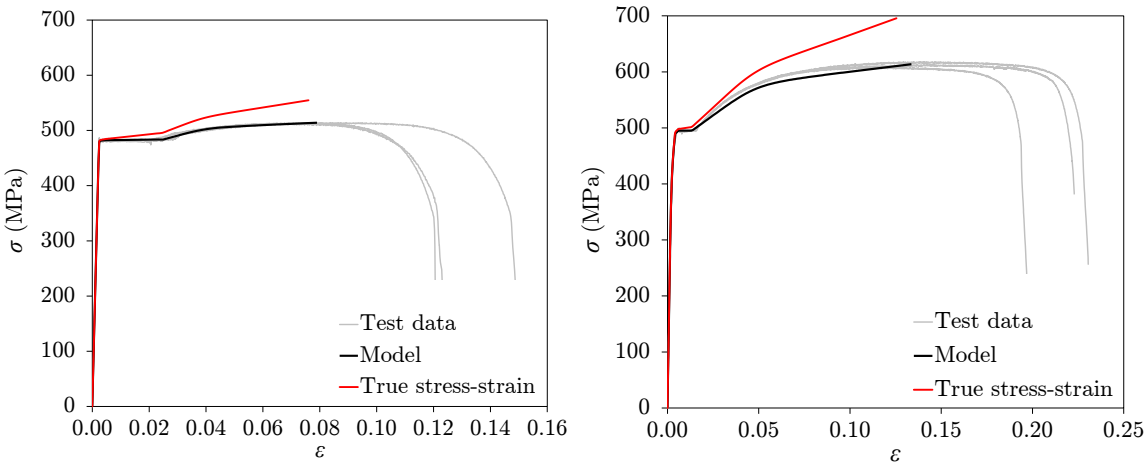
Member	t (mm)	E (GPa)	f_y (MPa)	ε_{sh} (%)	f_u (MPa)	ε_u (%)	n
Stud	1.44	204	482	2.38	514	7.90	-
Track	1.18	201	495	1.34	613	13.4	9

The stress-strain responses, corresponding to engineering stresses σ and strains ε, were then converted into true stresses σ_{true} and true plastic strains ε^{pl}_{true} for input into the ABAQUS (2016) software using Equations (6.3) and (6.4) respectively, to account for changes in the cross-sectional area due to inelastic straining in the plastic material definition.

$$\sigma_{true} = \sigma(1+\varepsilon) \tag{6.3}$$

$$\varepsilon^{pl}_{true} = \ln(1+\varepsilon) - \sigma_{true}/E \tag{6.4}$$

In Figure 6.8, the stress-strain responses of the tensile coupon test data reported in Chapter 5 (for the stud and track sections), along with the fitted models (Equations (6.1) and (6.2)) and the conversion to true stresses and strains, is presented. No strength enhancements in the corner regions were considered since their influence was deemed to be negligible due to the small thickness t and corner radius r of the modelled cold-formed steel cross-sections.



(a) Stud column

(b) Track

Figure 6.8: Stress-strain curves for use in FE modelling: (a) stud and (b) track

6.3.3.2 Plasterboard

Plasterboard displays different stress-strain responses in tension and compression, with the ultimate strength in compression f_u being higher by about two to four times compared with that in tension, and with the ultimate strain ε_u at f_u being significantly higher in tension due to increased ductility (Kyprianou et al. 2021*b*). Also, plasterboard displays a degree of anisotropy due to its production process, with the mechanical properties in the longitudinal direction being higher than these in the transverse direction (Kyprianou et al. 2021*b*, Petrone et al. 2016).

Material models established by Kyprianou et al. (2021*b*) and presented in Chapter 4 were employed for replicating the stress-strain behaviour of normal plasterboard under uniaxial loading, in both compression and tension. The adopted stress-strain behaviour is illustrated in Figure 6.9, with the positive values of stress and strain corresponding to tension and the negative values signifying compression. The nonlinear material behaviour in compression was extended beyond the ultimate capacity f_u, and up to 20% drop after f_u, using the Mander et al. (1988) model as demonstrated by Kyprianou et al. (2021*b*), Petrone et al. (2016) and Kyprianou et al. (2018). Note that the material response was assumed to be elastic up to $0.33f_u$ in tension and $0.7f_u$ in compression - see Figure 6.9.

A sensitivity study was conducted to investigate the influence of the degree of anisotropy

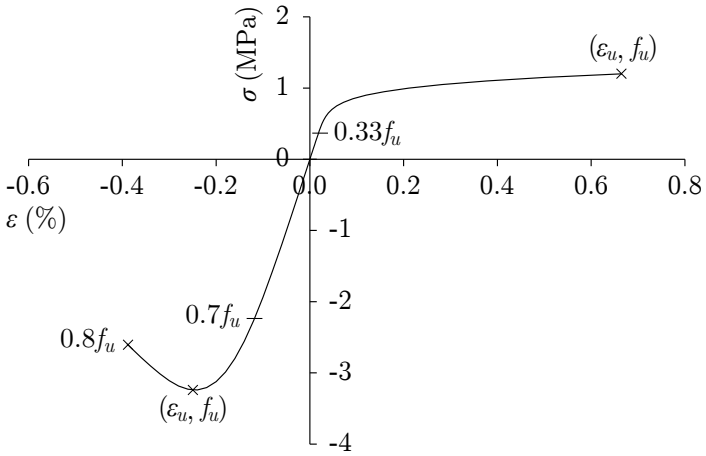


Figure 6.9: Uniaxial stress-strain behaviour of plasterboard adopted in finite element material model, with positive values signifying tension

of plasterboard on the overall structural behaviour of the examined systems. The observed degree of anisotropy reported by Kyprianou et al. (2021*b*) for 12.5 mm thick gypsum plasterboard (i.e. 12% difference in elastic modulus and 10% difference in compressive strength) was found to have a negligible impact (less than 2%) on the ultimate compression capacities of the studied systems, where plasterboard was modelled as isotropic with either the longitudinal or the transverse properties. Therefore, in order to achieve computational efficiency and since the degree of anisotropy exhibited by plasterboard was deemed to not have a significant influence on the structural response, the material behaviour was assumed to be isotropic. The employed material properties were therefore based on the mean values of the longitudinal and transverse properties reported in Chapter 4; these are summarised in Table 6.2, where E is the Young's modulus, v is the Poisson's ratio, ε_u is the ultimate strain and n is the roundedness exponent used with the Ramberg-Osgood formulation.

Table 6.2: Material properties of plasterboard adopted in FE models

		Tension			Compression	
E (MPa)	v	f_u (MPa)	ε_u (%)	n	f_u (MPa)	ε_u (%)
2010	0.2	1.20	0.665	7.25	3.24	0.245

The evolution of the yield surface, reflecting compressive crushing and tensile cracking of the gypsum, was simulated using the concrete damaged plasticity model in the (ABAQUS

2016) software. The concrete damaged plasticity parameters (i.e. the dilation angle ψ, the flow potential eccentricity ϵ, the ratio of the initial biaxial compressive strength to initial uniaxial compressive strength $\sigma_{bc}/f_{u,c}$, the ratio of the second stress invariant on the tensile meridian to that on the compressive meridian K_c and the viscosity parameter μ) were all taken as the default ABAQUS (2016) values (i.e. $\epsilon = 0.1$, $\sigma_{bc}/f_{u,c} = 1.16$, $K_c = 2/3$ and $\mu = 0$) apart from the dilation angle which was taken as $\psi = 11.0$ following sensitivity studies to ensure numerical convergence and good agreement with the experimental results. In compression, the post-elastic stress-strain behaviour was described using the *CONCRETE COMPRESSION HARDENING (ABAQUS 2016) function, while in tension the model was adapted to account for the ductile tensile behaviour of the gypsum, by defining explicitly the stresses and strains up to the ultimate tensile strain ε_u and stress f_u using the *CONCRETE TENSION STIFFENING (ABAQUS 2016) function.

6.3.3.3 OSB

Since OSB also displays anisotropy, the material properties employed for its modelling were taken as the mean values of the properties in the longitudinal and transverse directions reported in Chapter 4. The Ramberg-Osgood formulation provided in Chapter 4 was adopted to describe the stress-strain behaviour of the OSB material, which is illustrated in Figure 6.10. A summary of the material properties is presented in Table 6.3. Note that for all the conducted finite element analyses, the stress-strain response was defined using the compression parameters, while the stresses in the OSB were monitored to ensure that the tensile strength f_u of the material was not exceeded.

Table 6.3: OSB material model characteristics

		Tension	Compression		
E (MPa)	v	f_u (MPa)	f_u (MPa)	ε_u (%)	n
3080	0.2	10.2	12.4	0.56	12

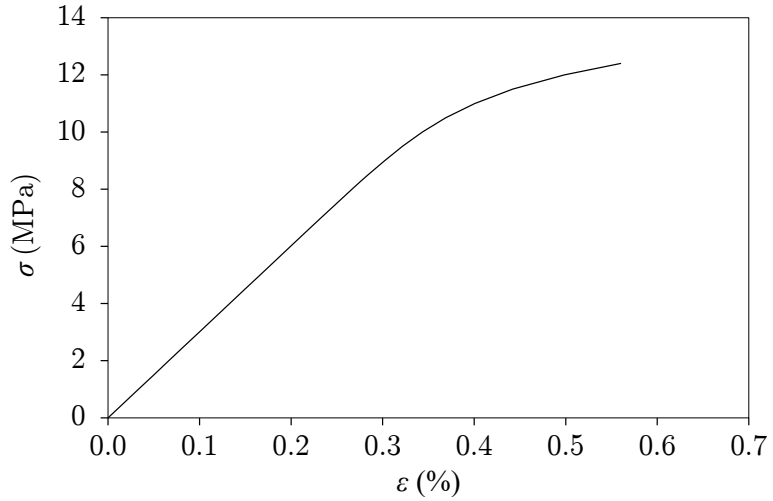


Figure 6.10: Stress-strain behaviour of OSB adopted in finite element material model

6.3.4 Modelling of screwed connections

6.3.4.1 Sheathing-to-steel connection

The self-drilling screws used for the connection between the sheathing boards and the flanges of the steel C-lipped columns were modelled using three 2-noded nonlinear translational springs (SPRING2 (ABAQUS 2016)) acting in the x, y and z directions, as illustrated in Figure 6.11. The spring in the y direction was defined between a node on the steel flange and a node on the outer surface of the sheathing, while the springs in the x and z directions were defined between the respective nodes on the inside surface of the sheathing and the steel flange.

The characteristics of the springs acting along the length and width of the stud-board interface (in z and x direction respectively as per Figure 6.11) were defined using the load-slip behaviour of the screwed connection in shear, while the separation of the two surfaces at the screw (spring) locations (i.e. along y direction) was defined using the pull-through behaviour of the screwed connection. The load-slip responses corresponding to the shear and pull-through behaviour of the connection at the sheathing-steel interface were determined in accordance with the models established in Chapter 4. Similarly, the properties that were used within the models for the specimens examined herein were calculated based on the recommendations in Chapter 4, which are summarised in Table 6.4 and 6.5; the derived

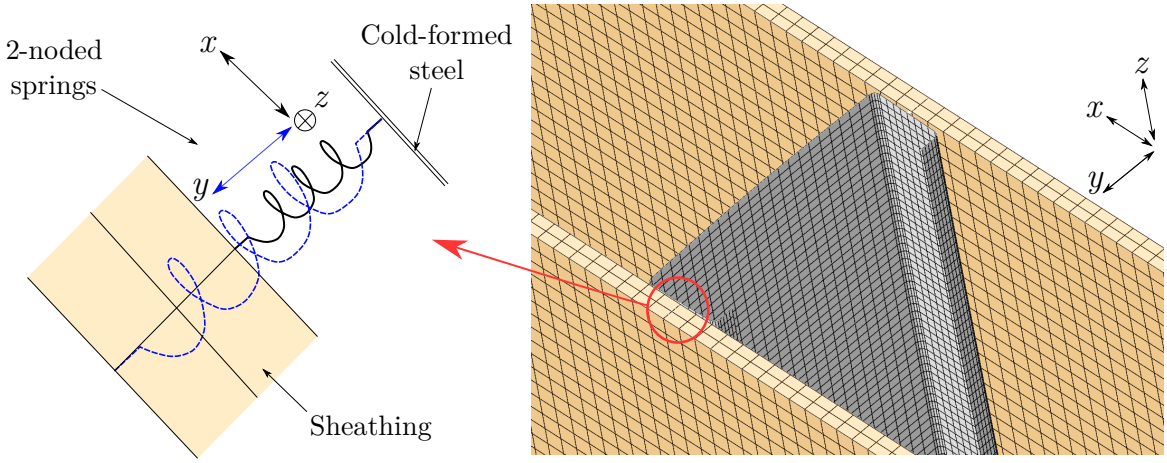


Figure 6.11: Simulation of screwed connection between sheathing and cold-formed steel using three 2-noded nonlinear springs in opposite directions

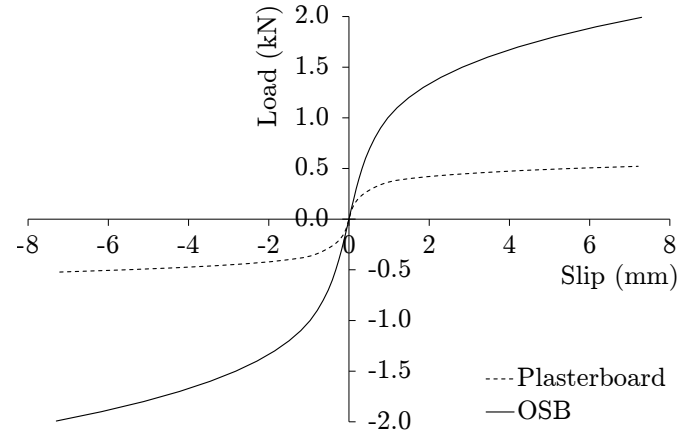
responses in shear and pull-through are illustrated in Figure 6.12 (a) and 6.12 (b) respectively. Designation names of properties given in Tables 6.4 and 6.5 are the same as the ones provided in Chapter 4. As shown in Figure 6.12 (a), for the springs describing the shear behaviour of the connection, the same load-slip response was assigned in both directions (to designate identical behaviour of the spring in tension and compression), while for the springs describing the pull-through behaviour, load-slip values were defined only in one direction, to activate the springs only when in tension.

Table 6.4: Properties adopted to describe the load-slip response model by Kyprianou et al. (2021*b*) for the shear behaviour of the springs for the given type of board and screw diameter

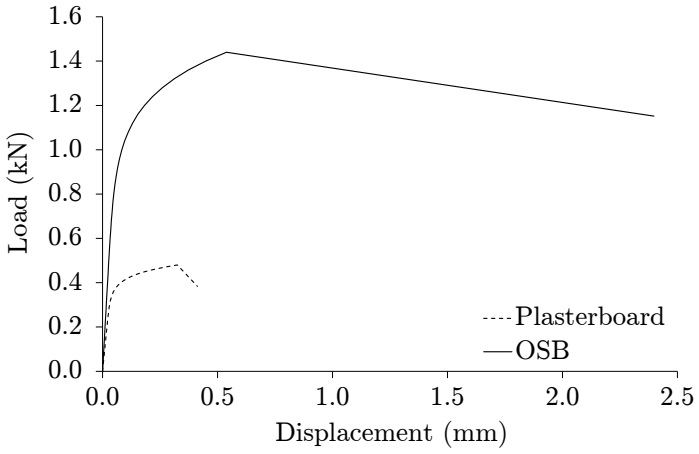
Board type, thickness (mm)	Screw diameter (mm)	Steel thickness (mm)	K_o (kN/mm)	$F_{1,po}$ (kN)	$F_{u,po}$ (kN)	$\delta_{u,po}$ (mm)	n_1
Plasterboard, 12.5	3.5	1.44	1.47	0.37	0.52	7.21	3.4
OSB, 11	4.8	1.44	1.69	1.02	1.99	7.30	3.6

Table 6.5: Properties adopted to describe the load-displacement response model by Kyprianou et al. (2021*b*) for the pull-through behaviour of the springs for the given type of board and screw diameter

Board type, thickness (mm)	Screw diameter (mm)	$K_{o,40}$ (kN/mm)	$F_{u,pt}$ (kN)	$\delta_{u,pt}$ (mm)	$F_{u,pt,0.8}$ (kN)	$\delta_{u,pt,0.8}$ (mm)	n
Plasterboard, 12.5	3.5	10.5	0.48	0.33	0.38	0.41	10.5
OSB, 11	4.8	18.5	1.44	0.54	1.15	2.40	7.5



(a) Shear



(b) Pull-through

Figure 6.12: Adopted load-slip response for springs in the FE model for simulating sheathing-to-steel (a) shear and (b) pull-through screwed connection behaviour

6.3.4.2 Steel-to-steel connection

The self-driving screws used in practice for the column-to-track connection were modelled using 2-noded nonlinear translational springs (SPRING2) along the longitudinal and transverse column-to-track interfaces. The load-slip response assigned to the springs was derived using a nonlinear bearing deformation curve introduced by Ho & Chung (2006), which is a function of the screw diameter, tensile strength of the steel and thickness of the steel strip. The derived load-slip behaviour was capped by the shear capacity of the connection $F_{u,v}$, for which predictions and test results are provided in Chapter 3. The adopted load-slip response of these springs in shear, determined based on the properties given in

Table 6.1 for a 4.8 mm diameter screw with a shear capacity $F_{u,v} = 5.15$ kN, is illustrated in Figure 6.13, where positive and negative values designate compression and tension of the springs respectively. For the axial behaviour of the screwed connection, a 2-noded linear translational spring, defined along the direction of the length of the screw, was used, with its stiffness set equal to the axial stiffness of the screw EA/L (where E is the Young's modulus of steel, A is the screw shank area and L is the sum of the thickness of the stud and track). Note that the ultimate tensile capacity of the screw $F_{u,s}$ was capped at $F_{u,s} = 9.16$ kN, in line with the results reported in Chapter 3 (Kyprianou et al. 2021*a*).

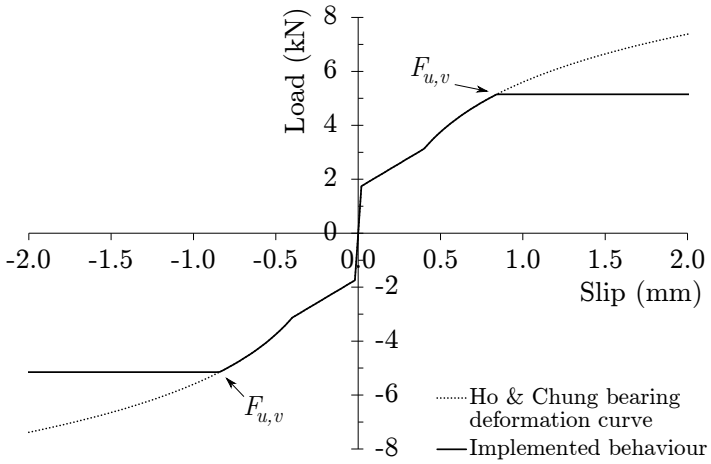


Figure 6.13: Adopted load-slip response for springs in the FE model for simulating steel-to-steel shear screwed connection behaviour

6.3.5 Geometrical imperfections

Cold-formed steel sections are particularly prone to cross-sectional instabilities, such as local and distortional buckling, as well as to global instabilities, such as flexural and flexural-torsional buckling, when unbraced. Initial imperfections that ensure that these modes of buckling are not inhibited were therefore incorporated into the developed FE models. The imperfections were introduced in the form of elastic buckling mode shapes obtained from a finite element strip analysis using the software CUFSM (Li & Schafer 2010) and extracted using a custom prepared Matlab script for the purposes of this study. Following their determination, the local and distortional modes were longitudinally distributed using sinusoidal functions with periods equal to their corresponding critical wavelengths. Similarly, the

global imperfection shapes were introduced using single half-sine and full cosine functions for the flexural and torsional buckling modes, respectively, as recommended by Zhao (2016) and illustrated in Figure 6.14. The distribution of all buckling mode shapes along the length of the steel columns is shown in Figure 6.15. All the cross-sectional and global buckling modes were then scaled to a prescribed amplitude and superimposed for implementation into the ABAQUS (2016) software as imperfection input files along with the main analysis input files.

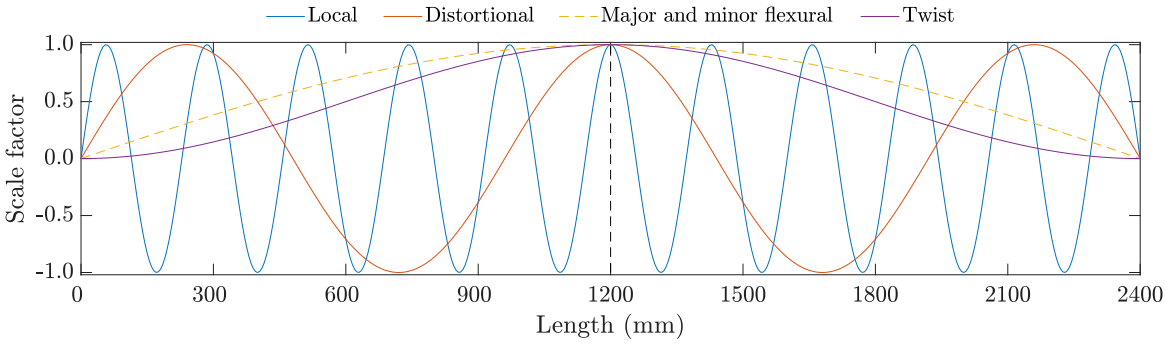
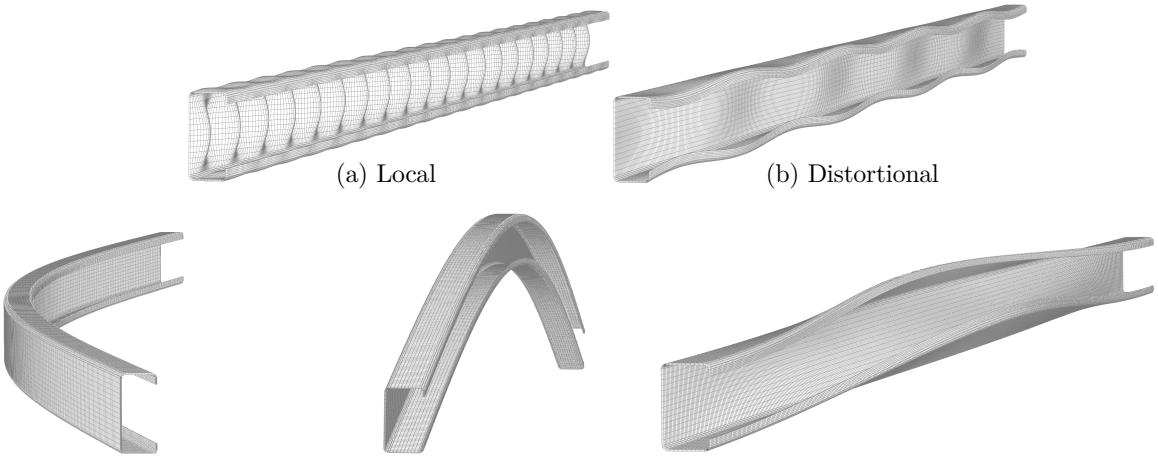


Figure 6.14: Shape of amplitude distribution along the length of the specimens for the different imperfection modes



(a) Local (b) Distortional

(c) Minor flexural (d) Major flexural (e) Torsional

Figure 6.15: Longitudinal distribution of: (a,b) cross-sectional and (c-e) global imperfections

For the validation studies presented in Section 6.4, the measured imperfection amplitudes reported by Young (1997), Vieira et al. (2011), Peterman (2012) and Kyprianou et al. (2021*c*) were used in the corresponding models, while for the parametric study presented in Section 6.5.2, the adopted imperfection amplitudes were based on the values presented

in Chapter 5. Note that for sheathed specimens, the sheathing boards were also modelled with major and minor flexural imperfections equal to those of the stud in order to ensure elimination of gaps between the steel and the board, as well as alignment of the the nodes on the board and steel used for the spring definitions (simulating the screws). The following notation is employed for the imperfection amplitudes: δ_L for local, δ_D for distortional, $\delta_{G,min}$ for minor axis flexural, $\delta_{G,maj}$ for major axis flexural and $\theta_{G,tor}$ for twist; these are illustrated in Figure 6.16.

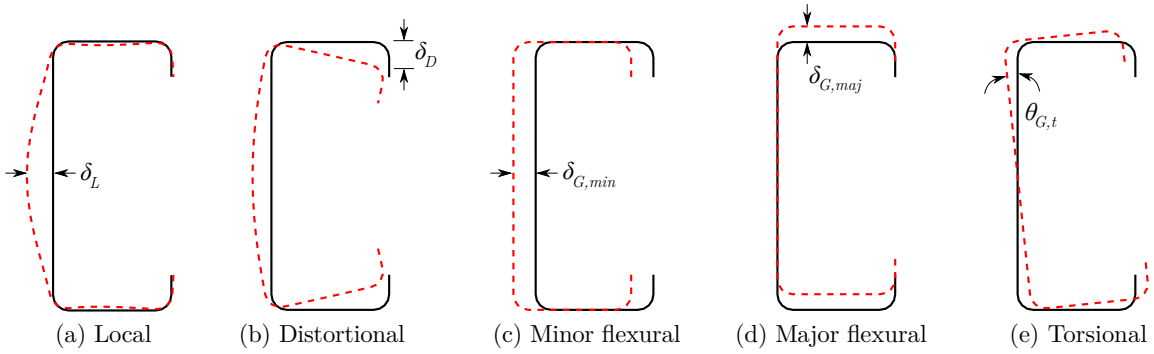


Figure 6.16: Mode shape and amplitude notation of: (a,b) cross-sectional and (c-e) global imperfections

6.3.6 Boundary and loading conditions

It is common practice for steel columns to be modelled under the assumption of idealised boundaries corresponding to either fully fixed or pinned end conditions. However, since in reality cold-formed steel studs are usually set in tracks, their actual boundary conditions dictate a different structural performance than that exhibited by the equivalent fully fixed or pinned studs. In order to investigate the influence of boundary conditions on the behaviour of the examined systems, two alternative sets of boundary conditions were modelled: idealised end conditions, corresponding to the idealised fully fixed and pinned configurations, and the actual end conditions, with the end tracks being explicitly modelled.

Idealised boundary conditions were implemented by binding all the cross-sectional nodes at both column ends to reference nodes located at the respective end centroids, using BEAM Multipoint Constraints (MPCs) (ABAQUS 2016) - see Figure 6.17. For the case of fully

fixed conditions, all translational and rotational degrees of freedom at the reference nodes were restrained except for vertical translation at the top end of the column where the loading was introduced. For the simulation of pinned conditions, the rotational degrees of freedom about the major and minor axes were released.

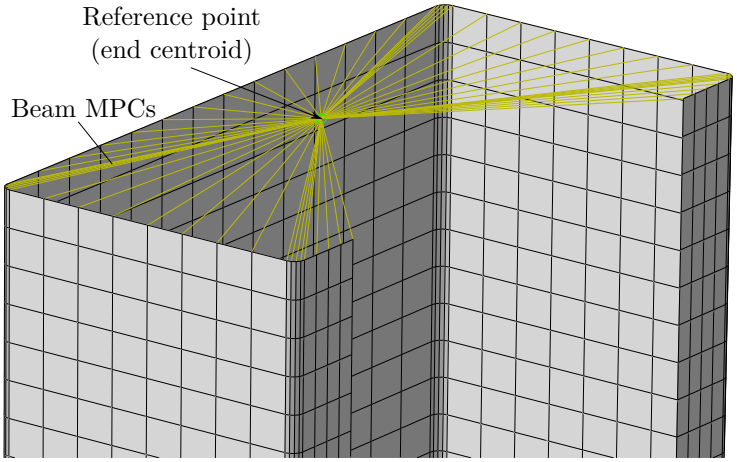
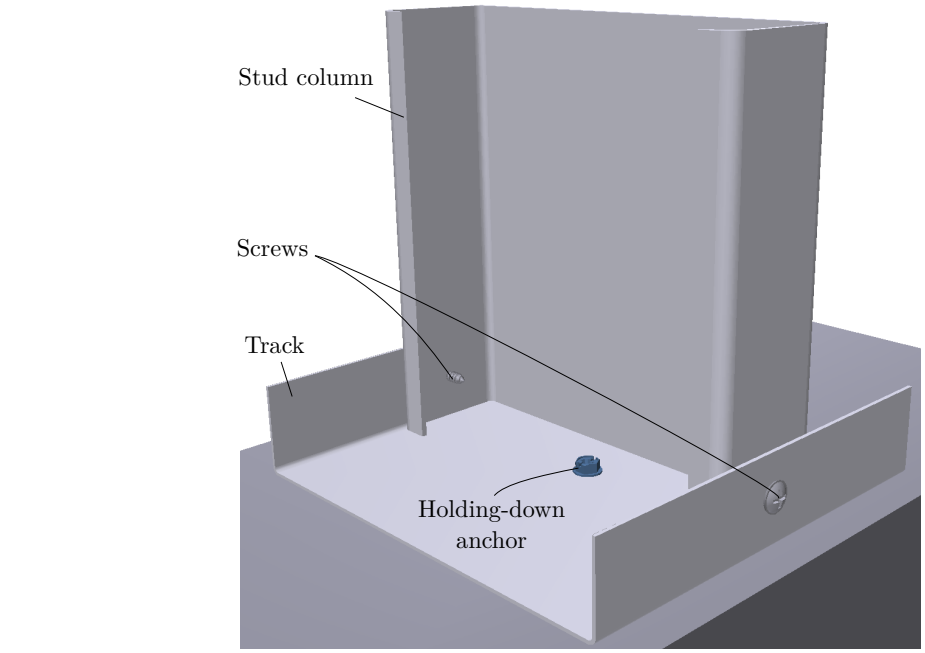


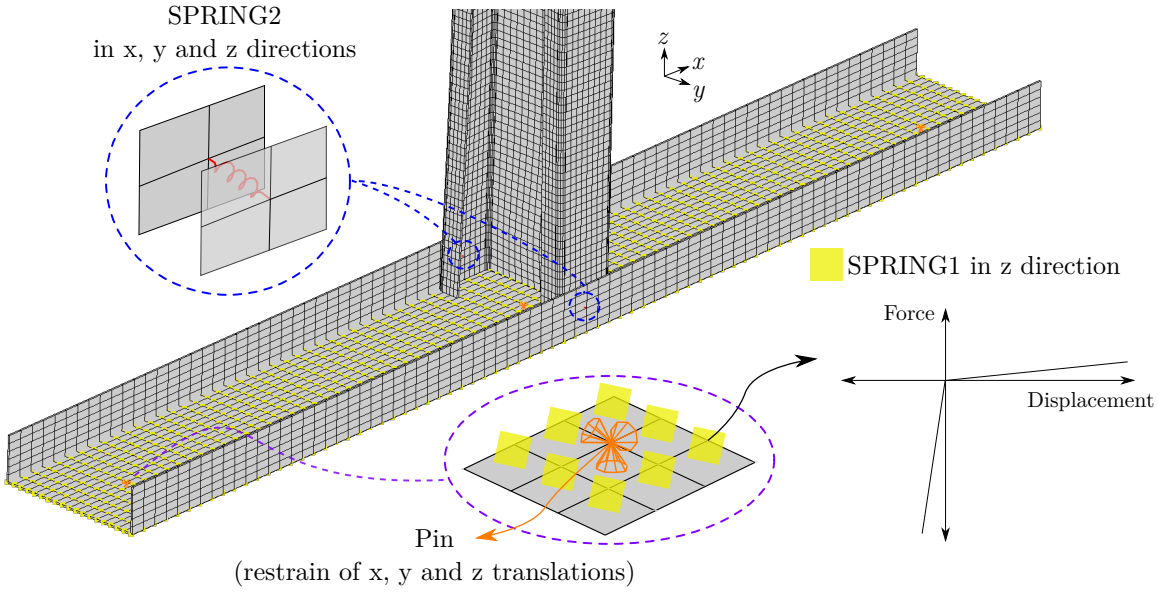
Figure 6.17: Idealised boundary implementation using MPCs

For the finite element models simulating the realistic boundary conditions at the column ends, as tested by Vieira et al. (2011), Peterman & Schafer (2014) and Kyprianou et al. (2021*c*), explicit modelling of the tracks as well as of the track-to-column connection was implemented, as shown in Figure 6.18, with the behaviour of the springs adopted for the simulation of the screwed connection modelled as described in Section 6.3.4.2.

Nonlinear translational springs (SPRING1 type) were positioned under the bottom track, simulating the ground, allowing upward but preventing downward movement. The holding-down anchor bolt shown in Figure 6.18 (a), used to secure the track to the ground, was simulated as a pinned constraint (restraining all three translations), as shown in Figure 6.18 (b). Similarly, the use of nonlinear springs at the top track allowed downward movement, by being freely extensible, but prevented upward movement, by being incompressible. Unlike the ground springs which were fixed into position (SPRING1 type), the top springs were 2-noded (SPRING2 type) and connected at their free ends by an MPC to a reference node located at the centre of the track as shown in Figure 6.19. For the specimens under pure compression and combined loading, axial loading was introduced through this reference node to the web of the track, only when the nonlinear springs were in compression,



(a) Drawing



(b) FE model

Figure 6.18: Column-to-track connection: (a) drawing and (b) FE model

simulating the effect of a rigid loading plate at the top of the track. Anchors on the top track used to secure it to the rigid loading plane were simulated with pinned constraints only in the x and y directions, while in the z direction, the *EQUATION command was used to keep the vertical distance between the anchors and the loading point constant.

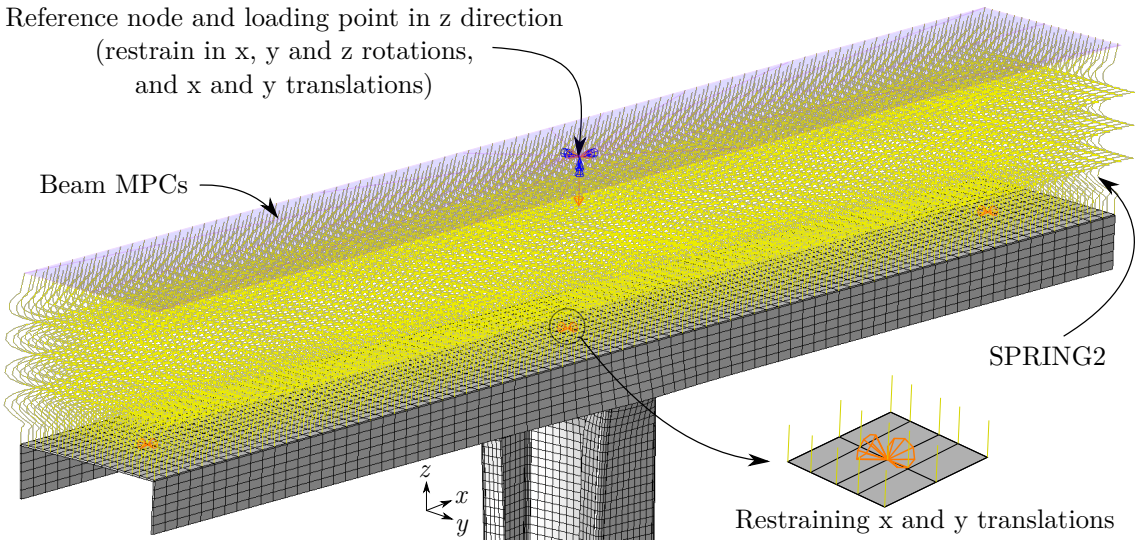


Figure 6.19: Column-to-top-track detail and axial loading

Similarly, lateral loading was applied to the board surface with the use of nonlinear 2-noded springs (with high stiffness defined when the springs were in compression). As for the springs on the top track, the free ends of the springs were connected with Beam MPCs to a single reference point, where the load was introduced. For the four-point loading scheme, the whiffletree used in the physical tests was modelled using stiff linear 2-noded springs (SPRINGA type) and Beam MPC elements, connected to a single reference point at mid-height and mid-width of the board, where the lateral load was applied. A schematic illustration of the implementation of the lateral four-point loading scheme is illustrated in Figure 6.20.

Note that, since the sheathing boards in the FE model were not directly loaded, their top and bottom ends were free to move, replicating the boundary conditions of the physical tests described by Vieira et al. (2011), Peterman & Schafer (2014) and the tests reported in Chapter 5. Also, it should be mentioned that the development of warping effects at the column ends, inside the tracks, was not prevented. Typical end deformations of a modelled column and track under pure compression and combined compression plus bending are shown in Figures 6.21 and 6.22 respectively. In Figure 6.22, the end deformations at various key stages of the loading are presented along with the board deformation. The boards, as described in the physical tests reported in Chapter 5, were not connected to the tracks but

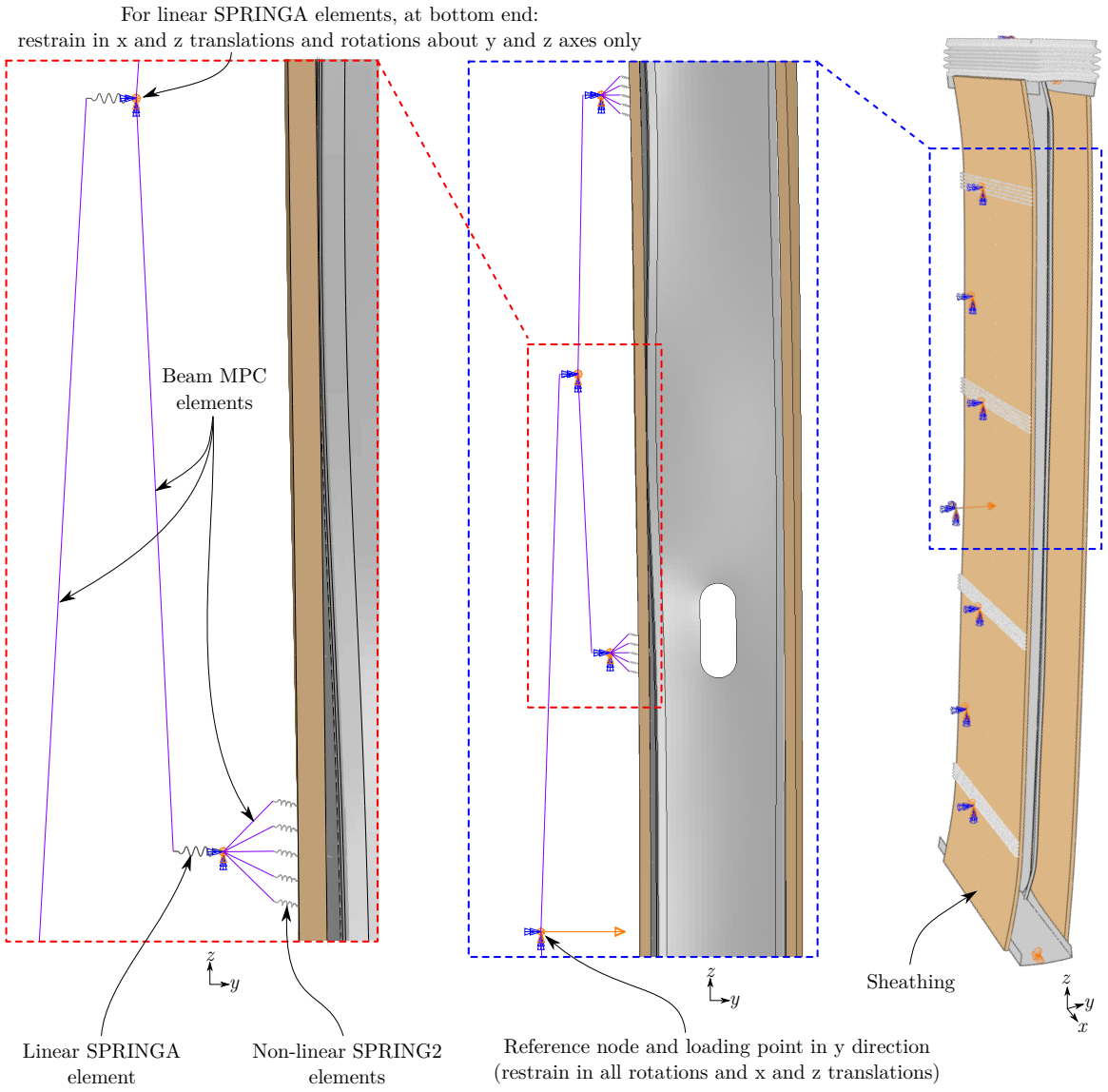


Figure 6.20: FE model of the four-point loading scheme

their contact interaction was simulated using springs, which prevented the boards moving towards the tracks but allowed their free movement away from them - see Figure 6.22 (c).

6.3.7 Contact interaction and solution scheme

The contact interaction between the column and the tracks was implemented using the generalised contact algorithm (*CONTACT INCLUSIONS) (ABAQUS 2016), while the interaction between the column and the boards was defined using the contact pair algorithm

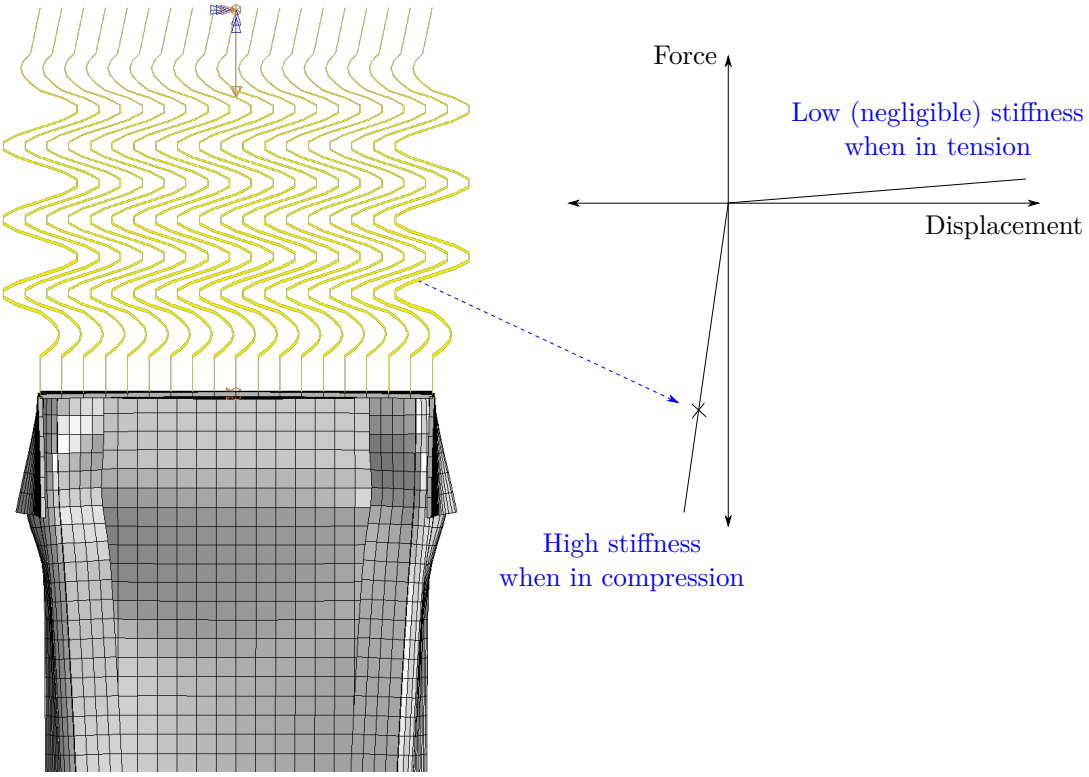
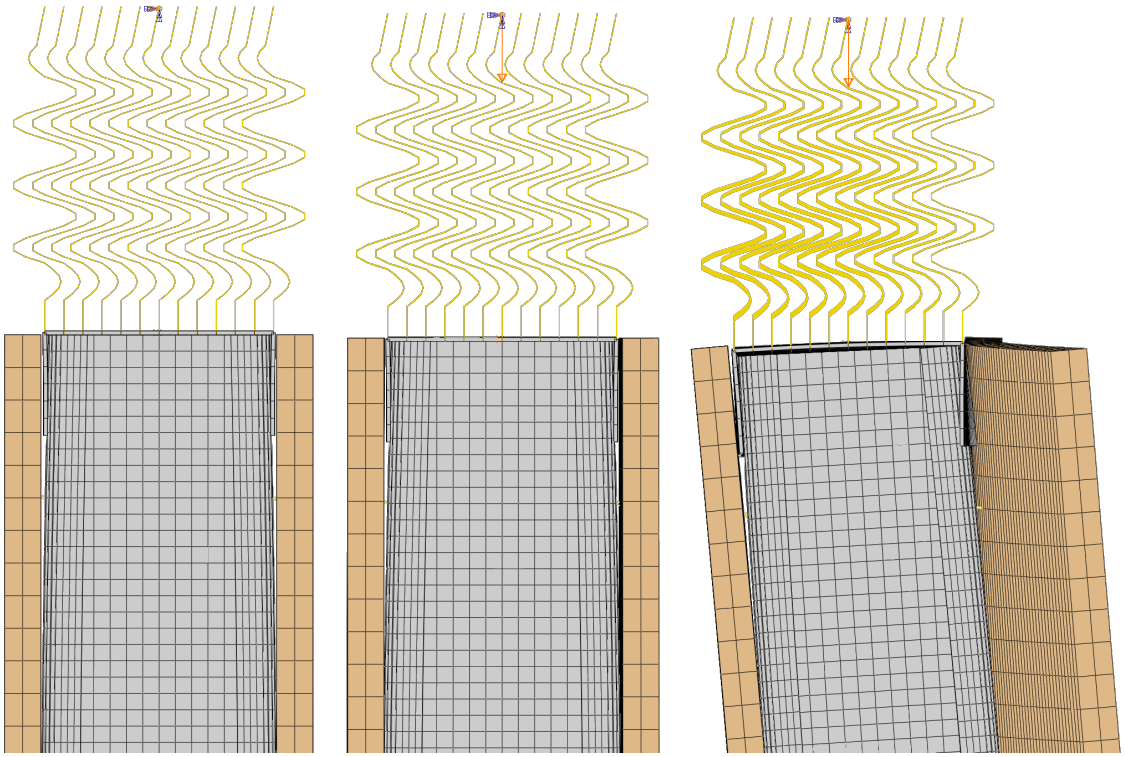


Figure 6.21: Typical end deformation from FE model of column and track under compression; indicative load-displacement path for the top track springs when in compression

(*CONTACT PAIR) (ABAQUS 2016). "Hard contact" was defined in the normal direction ensuring no surface overlapping with a friction coefficient of 0.2 (Gorst et al. 2003) in the tangential direction. Both geometric and material nonlinearities were accounted for in the analyses performed. For the finite element analyses where idealised fully fixed and pinned bare steel columns were modelled, the modified static Riks (ABAQUS 2016) solver was employed. However, for the simulation of the more complicated systems (i.e. specimens in tracks with single or double sheathing), the use of the general static solver with artificial stabilisation was necessary to achieve convergence due to the highly unstable nature of the examined systems.

For the combined load cases, compression was initially introduced using a geometrically nonlinear static analysis in load control, followed by a second load step where horizontal action was introduced using displacement control in conjunction with the general static solver using artificial stabilisation, with a set limit of stabilisation to strain energy equal



(a) (b) (c)

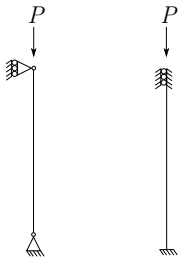
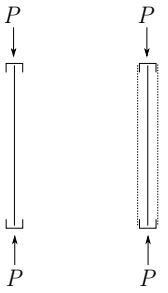
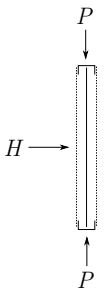
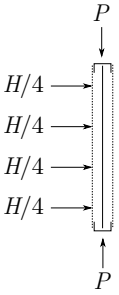
Figure 6.22: Typical FE model end deformation of column and track under combined loading at the (a) start of analysis (b) end of compression – Step 1 and (c) end of bending – Step 2

to 0.01. For the combined loading scenarios, the *MODEL CHANGE ADD and *MODEL CHANGE REMOVE commands were used between the two load steps (with the first load step corresponding to the axial loading of the column and the second to the lateral loading), to add the lateral springs associated with the whiffletree and to replace the top track springs with undeformed ones, but with the position of the top axial reference node remaining unchanged and with the compression load remaining constant during the second load step. Replacement of the top track springs was performed so that, with the onset of bending (i.e. load step 2), the top springs would not be in an already compressed phase (achieved during step 1) but in their neutral state. Note that the use of the Riks solver with the *MODEL CHANGE function is prohibited, therefore rendering the use of the general static solver with artificial stabilisation necessary.

6.4 Validation

Validation of the developed FE models against test results from four different studies, are presented herein. A summary of the configurations and loading conditions of the investigated specimens is presented in Table 6.6. In total, 56 physical tests were employed for the validation process.

Table 6.6: Summary of studies and type of specimens used for validation

Study	Loading	No. of tests	Configuration	
Young (1997)	Compression	14	Bare studs with ideal boundaries (pinned and fixed)	
Vieira (2011)	Compression	4 16	Bare studs set in tracks Sheathed studs set in tracks	
Peterman (2012)	Combined loading	5	Sheathed studs set in tracks	
Kyprianou et al. (2021*c*)	Compression Combined loading Bending	8 6 3	Sheathed studs set in tracks	

6.4.1 Bare cold-formed steel columns with ideal boundaries

For the first set of validation models, a series of tests on bare cold-formed steel C-lipped shaped columns of different lengths and cross-section sizes was simulated, with the end boundaries considered as either fully fixed or pinned. Measured material stress-strain curves, specimen dimensions and geometric imperfections, as reported by Young (1997), Young & Yan (2000), Young & Rasmussen (1998*a*) and Young & Rasmussen (1998*b*), were employed in the conducted finite element simulations. A brief description of the specimens used for the validation, along with a summary of the comparisons between the finite element and test results, is presented in Table 6.7.

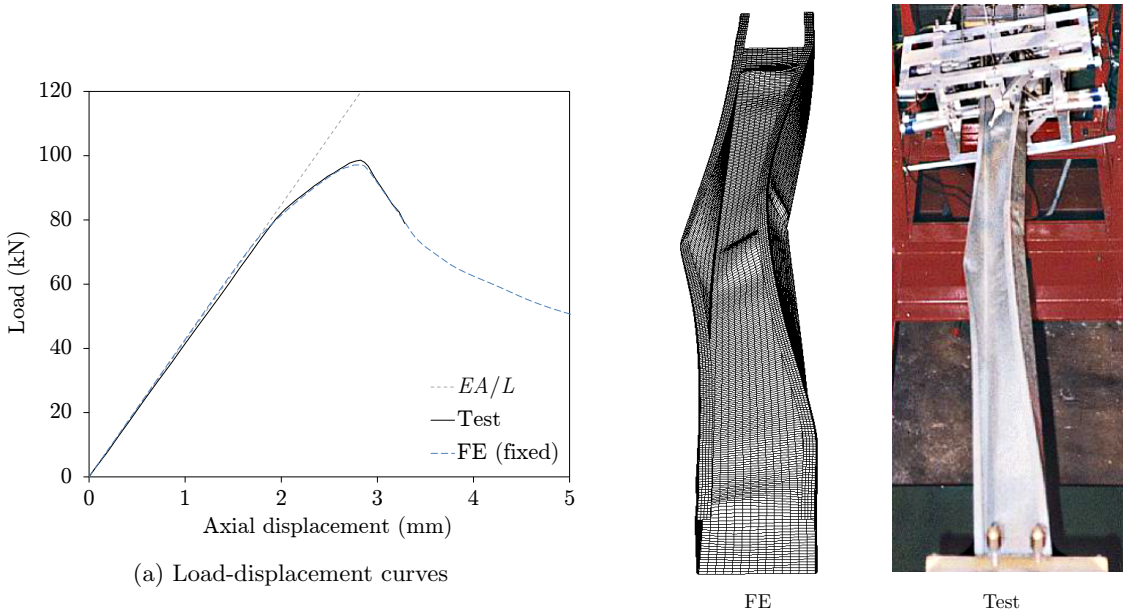
Table 6.7: Comparison between FE and test results reported in Young (1997)

Specimen	Flange width (mm)	Length (mm)	Boundaries	$P_{u,exp}$ (kN)	$P_{u,FE}$ (kN)	$P_{u,exp}/P_{u,FE}$
L36F1000	36	1000	Fixed-Fixed	89.6	93.6	0.96
L36F1500	36	1500	Fixed-Fixed	82.4	78.2	1.05
L36F2000	36	2000	Fixed-Fixed	70.1	64.4	1.09
L36F2500	36	2500	Fixed-Fixed	58.1	53.0	1.10
L36F3000	36	3000	Fixed-Fixed	39.3	41.2	0.95
L36P0815	36	815	Pinned-Pinned	70.7	69.4	1.02
L36P1315	36	1315	Pinned-Pinned	41.1	39.3	1.05
L48F1000	48	1000	Fixed-Fixed	102.3	100.6	1.02
L48F1500	48	1500	Fixed-Fixed	98.6	97.1	1.02
L48F2000	48	2000	Fixed-Fixed	90.1	88.0	1.02
L48F2500	48	2500	Fixed-Fixed	73.9	71.0	1.04
L48F3000	48	3000	Fixed-Fixed	54.3	51.7	1.05
L48P1065	48	1065	Pinned-Pinned	72.0	73.6	0.98
L48P1565	48	1565	Pinned-Pinned	53.2	52.3	1.02
					Mean	1.03
					COV	0.04

The labelling system of the specimens in Table 6.7 starts with the letter L, followed by the nominal width of the flange, then a letter corresponding to the employed boundary conditions (F = fixed; P = pinned) and finally the total measured length of the specimen in mm. The two different cross-sections are designated L36 and L48 and their mean measured dimensions are: b = 37.0 mm and 49.0 mm respectively, h = 97.2 mm, c = 12.5 mm,

$r = 0.85$ mm and $t = 1.48$ mm for both cross-sections – see Figure 6.6 for notations.

Comparisons between the ultimate compression capacities attained by the test specimens $P_{u,exp}$ (Young 1997) and those predicted by the finite elements models $P_{u,FE}$ are presented in Table 6.7, with a mean $P_{u,exp}/P_{u,FE}$ ratio of 1.03 and a coefficient of variation (COV) of 0.04. The finite element models were also found capable of accurately capturing the exhibited failure modes as well as the recorded load-axial shortening curves, shown in Figure 6.23.



(a) Load-displacement curves

(b) Failure mode

Figure 6.23: Typical comparison between the results from the developed FE model and the tests by Young (1997); example shown is L48F1500

6.4.2 Bare and sheathed cold-formed steel columns set in tracks

For the second set of validation models, tests on 20 cold-formed steel C-lipped studs of various lengths and sheathing configurations, as reported by Vieira et al. (2011), Vieira (2011), were utilised; a brief summary of these is presented in Table 6.8. Measured cross-sectional dimensions (Vieira et al. 2011), material properties (Vieira & Schafer 2016) and initial imperfections (Vieira et al. 2011) were incorporated into the numerical simulations, while for all sheathed specimens a connector spacing of 300 mm was employed. Finally,

since the studs were set in tracks in the physical tests (Vieira et al. 2011), finite element models explicitly simulating the end tracks, as described in Section 6.3.6, were employed. Comparisons between compression capacities obtained from FE models with simulated track boundaries $P_{u,FE,tr}$ and idealised fixed boundaries $P_{u,FE,fix}$ are presented in Table 6.8. The identification system of the specimens begins with two letters corresponding to the type of sheathing board on each side of the stud (with B – bare, G – gypsum and O – OSB), followed by the letter L and the measured length in mm. The measured mean yield strength f_y was reported as 383 MPa, while the mean measured cross-sectional dimensions were: $h = 93.6$ mm, $b = 42.0$ mm, $c = 13.0$ mm, $r = 4.37$ mm and $t = 1.86$ mm – see Figure 6.6.

Table 6.8: Comparison between FE and test results reported by Vieira et al. (2011)

Specimen	Length (mm)	Sheathing	$P_{u,exp}$ (kN)	$P_{u,FE,fix}$ (kN)	$P_{u,FE,tr}$ (kN)	$P_{u,exp}/P_{u,FE,fix}$	$P_{u,exp}/P_{u,FE,tr}$
BB-L610	610	Bare-Bare	87.9	94.6	94.2	0.93	0.93
BB-L1220	1220	Bare-Bare	84.6	87.3	87.2	0.97	0.97
BB-L1830	1830	Bare-Bare	60.5	72.8	71.9	0.83	0.84
BB-L2440	2440	Bare-Bare	57.1	58.6	58.0	0.97	0.98
OB-L610	610	OSB-Bare	95.4	99.7	98.1	0.96	0.97
OB-L1220	1220	OSB-Bare	94.0	97.5	96.5	0.96	0.97
OB-L1830	1830	OSB-Bare	80.1	81.8	81.1	0.98	0.99
OB-L2440	2440	OSB-Bare	69.5	67.8	66.8	1.03	1.04
GG-L610	610	Gyp-Gyp	96.7	98.2	97.7	0.99	0.99
GG-L1220	1220	Gyp-Gyp	99.6	99.6	98.9	1.00	1.01
GG-L1830	1830	Gyp-Gyp	88.7	103.6	102.2	0.86	0.87
GG-L2440	2440	Gyp-Gyp	95.0	104.1	103.5	0.91	0.92
OG-L610	610	OSB-Gyp	97.8	100.1	99.5	0.98	0.98
OG-L1220	1220	OSB-Gyp	96.2	103.2	101.7	0.93	0.95
OG-L1830	1830	OSB-Gyp	90.7	104.7	101.3	0.87	0.90
OG-L2440	2440	OSB-Gyp	99.9	104.7	103.1	0.95	0.97
OO-L610	610	OSB-OSB	101.6	103.2	100.1	0.98	1.01
OO-L1220	1220	OSB-OSB	99.0	101.0	99.4	0.98	1.00
OO-L1830	1830	OSB-OSB	99.5	103.8	99.6	0.96	1.00
OO-L2440	2440	OSB-OSB	102.7	106.1	105.3	0.97	0.98
					Mean	0.95	0.96
					COV	0.05	0.05

The observed failure modes were captured (including local, distortional, flexural and flexural-torsional buckling, as reported by Vieira et al. (2011)) by the finite element models.

Typical examples of comparisons between the finite element and test results are presented in Table 6.8, where a mean $P_{u,exp}/P_{u,FE,tr}$ ratio of 0.96 was obtained for all the examined systems. It should be mentioned that the axial load-shortening test curves reported by Vieira et al. (2011) display an initial nonlinearity which, as demonstrated by Kyprianou et al. (2021*c*) and presented in Chapter 5, are mainly attributable to gaps between the column and the end tracks, whereas, the equivalent curves obtained from the FE models captured the theoretical axial stiffness of the column (EA/L). Therefore, for these specimens, a comparison is provided only between the maximum capacities achieved by the FE models and the physical tests. Further discussion on this and comparisons between the relevant curves is provided by Kyprianou et al. (2018).

In order to examine the influence of the adopted boundary conditions (i.e. explicit modelling of the end tracks) on the load-carrying capacity of the studs, finite element analyses of the same specimens but with idealised fixed boundaries were also carried out. The relevant obtained results are presented in Table 6.8, with a mean $P_{u,exp}/P_{u,FE,fix}$ ratio of 0.95. The minor discrepancy of 1% in the mean values of ultimate capacities obtained for the two alternative boundary conditions indicates that, when under pure compression, the assumption of idealised fully fixed boundary conditions for a cold-formed steel stud in tracks is realistic.

6.4.3 Sheathed cold-formed steel beam-columns with a horizontal load at mid-height

Following the validation study of members under pure compression using the tests reported by Vieira et al. (2011), the finite element model was further developed so that the sheathed stud wall specimen could be loaded both axially and horizontally. Five tests from the study by Peterman & Schafer (2014) were utilised, which was a complementary investigation to the one presented by Vieira et al. (2011), examining the same type of stud section, boundary conditions (i.e. set in tracks), sheathing configuration and spacing of connectors but with a fixed length of 2440 mm and a different loading scheme. The specimens tested by Peterman & Schafer (2014) and Peterman (2012) were first axially loaded to a predeter-

mined load level, calculated based on the results obtained by Vieira et al. (2011), and then laterally loaded at mid-height until failure, using a line load across the board.

The five tests that were used for the validation presented herein were all sheathed on both sides with OSB, connected using screws of 4.8 mm diameter at a spacing of 300 mm, with each specimen subjected to a different combination of compressive and horizontal load. A summary of the examined specimens and a comparison between the compressive P_u and horizontal H_u forces attained by the test specimens and predicted by the FE models is provided in Table 6.9 and Figure 6.24. To account for the combined effect of compression and horizontal actions, a resultant force R was calculated using Equation (6.5) to allow for an easier comparison between the test and FE results. In Table 6.9, the subscripts 'exp' and 'FE' denote test and finite element results respectively.

$$R = \sqrt{{P_u}^2 + {H_u}^2} \tag{6.5}$$

The name designation of the specimens begins with the two letters OO, corresponding to the OSB-OSB sheathing boards (one on either side of the stud), followed by the approximate level of compressive load (expressed as a percentage of the compressive strength achieved by Vieira et al. (2011) - i.e. 100% designates pure compression), followed by the letter S, and, finally by the screw spacing in mm.

The horizontal line load at mid-height was simulated by a series of springs and a single BEAM MPC element, which is a simplified version of the 4-point loading scheme explained in Section 6.3.6. Also, the top and bottom edges of the boards were secured to the flanges of the tracks since in the tests, as reported by Peterman (2012), the boards were screwed to the tracks. The measured cross-sectional dimensions, initial imperfections and material stress-strain curves reported by Peterman (2012) were incorporated into the FE model. The mean measured yield strength f_y was 413 MPa, while the mean measured cross-sectional dimensions were reported as: $h = 93.5$ mm, $b = 43.1$ mm, $c = 15.3$ mm, $r = 8.25$ mm and $t = 1.82$ mm – see Figure 6.6.

Table 6.9: Comparison between FE and test results presented in Peterman & Schafer (2014)

Specimen	$P_{u,exp}$ (kN)	$P_{u,FE}$ (kN)	$H_{u,exp}$ (kN)	$H_{u,FE}$ (kN)	$H_{u,exp}/H_{u,FE}$	R_{exp} (kN)	R_{FE} (kN)	R_{exp}/R_{FE}
OO-100-S300	102.7	105.3	0.0	0.0	-	102.7	105.3	0.98
OO-80-S300	80.9	80.9	4.7	5.3	0.89	81.0	81.1	1.00
OO-60-S300	66.4	66.4	6.0	6.1	0.98	66.7	66.7	1.00
OO-50-S300	50.9	50.9	6.7	6.5	1.03	51.3	51.3	1.00
OO-30-S300	33.7	33.7	6.9	6.8	1.01	34.4	34.4	1.00
OO-10-S300	10.8	10.8	7.4	7.1	1.04	13.1	12.9	1.01
				Mean	0.99			1.00
				COV	0.06			0.01

As shown in Figure 6.24 and reflected by the mean $H_{u,exp}/H_{u,FE}$ and R_{exp}/R_{FE} ratios of 0.99 and 1.00 (see Table 6.9), there is excellent agreement between the test and finite element results. Note that the capacity of specimen OO-100-S300, subjected to pure compression, was reported by Vieira et al. (2011) and is included herein to provide the limit corresponding to pure compression for the examined beam-columns.

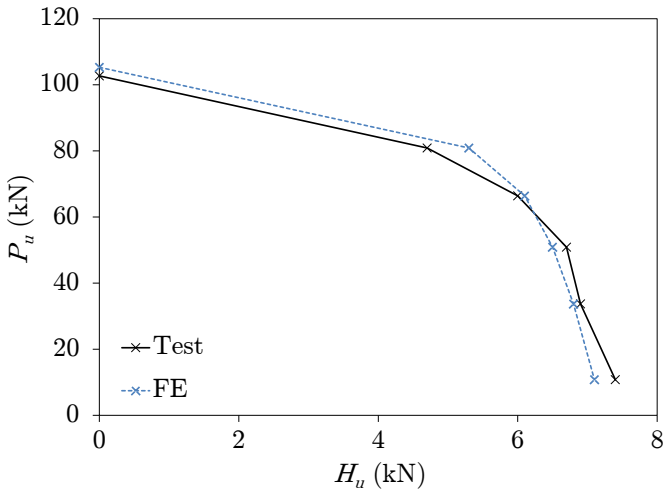
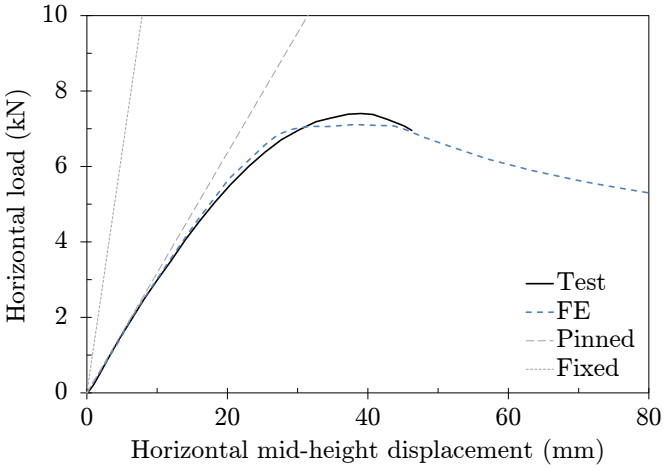


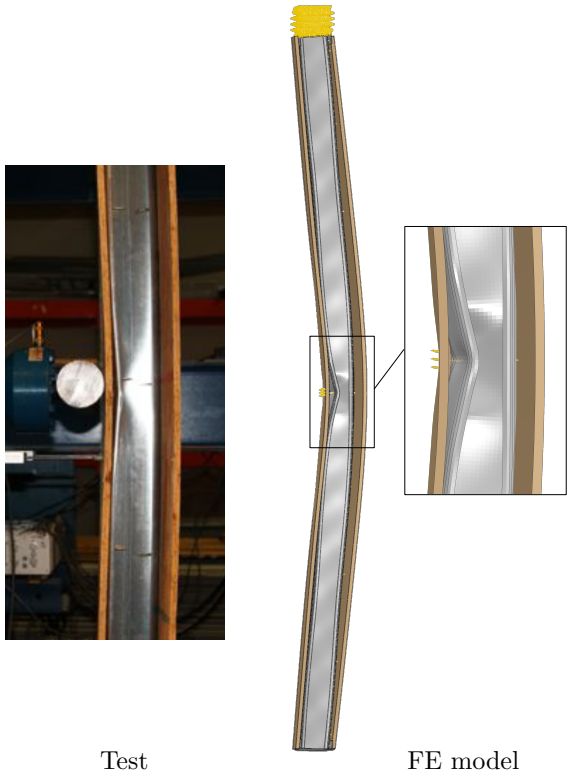
Figure 6.24: Comparison between the ultimate compression P_u and horizontal H_u loads from the developed FE model and the tests by Peterman (2012) for beam-columns sheathed with OSB and connected at 300 mm intervals

Accurate replication of the observed failure modes for all five specimens under combined loading (Peterman & Schafer 2014) was achieved by the finite element models - see Figure 6.25 (b). A typical comparison between the horizontal load-displacement curves achieved by the test specimens and the finite element models is presented in Figure 6.25 (a), where the initial stiffnesses of the curves match that of the theoretical response of the member with

pinned boundaries. Note that the screw connector between the loaded side of the sheathing and the steel column at mid-height, where local buckling occurred, suffered pull-through beyond the peak load level, as reported by Peterman & Schafer (2014) and illustrated in Figure 6.25 (b).



(a) Load-displacement curves



(b) Failure mode

Figure 6.25: Typical comparison between the results from the developed FE model and the tests by Peterman (2012); the example shown is OO-10-S300

6.4.4 Sheathed cold-formed steel beam-columns loaded with four horizontal point loads

The final set of validation models were based on the 17 tests reported by Kyprianou et al. (2021*c*) and also presented in Chapter 5. A summary of the examined specimens and a comparison between the test and finite element results is presented in Table 6.10, for which the adopted presentation style and reported results (i.e. P_u, H_u and R) are as in Table 6.9 - see Subsection 6.4.3. The name designation of the specimens is the same as the one given in Chapter 5, starting with the letter G or O corresponding to gypsum (plasterboard) and oriented strand board (OSB) respectively, followed by the level of the applied compressive load (expressed as a percentage of the stud compressive strength), followed by the letter S and the spacing between screws in mm and, finally, by the test number.

Material nonlinearity was implemented as described in Section 6.3.3.1 using the properties reported in Table 6.1. The dimensions of the steel cross-sections were based on the mean measurements reported in Chapter 5: $h = 149.15$ mm, $b = 43.92$, $c = 11.95$ mm, $r = 2.50$ mm and $t = 1.44$ mm – see Figure 6.6. Similarly, the adopted geometrical imperfections were based on the measurements reported in Chapter 5. Following a sensitivity study, it was found that increasing the distortional imperfection by a factor of three resulted in the most accurate predictions of ultimate capacities and the overall profiles of the load-displacement curves. This deviation in the magnitude of the distortional imperfection is considered to be reasonable, reflecting the fact that the imperfection measurements were taken on the bare steel sections, prior to any attachment of sheathing, and that screwing of the sheathing or of the track to the steel column would induce additional imperfections on the steel column. The latter point was observed visually, but not directly measured. Therefore, all finite element analyses were conducted using geometrical imperfections as described in Section 6.3.5, assuming the following imperfection magnitudes: $\delta_L = 0.21t$, $\delta_D = 1.56t$, $\delta_{G,min} = L/4380$, $\delta_{G,maj} = L/17700$ and $\theta_{G,t} = 0.15$ deg/m.

For the specimens sheathed with OSB under combined load, a comparison between the FE and test P_u and H_u values is presented in Figure 6.26, illustrating excellent agreement,

with a mean R_{exp}/R_{FE} ratio of 1.01 and a COV of 0.02 - see Table 6.10.

Table 6.10: Comparison between FE and test results for experiments carried out as part of the present study, as described in Chapter 5

Specimen	$P_{u,exp}$ (kN)	$P_{u,FE}$ (kN)	$\frac{P_{u,exp}}{P_{u,FE}}$	$H_{u,exp}$ (kN)	$H_{u,FE}$ (kN)	$\frac{H_{u,exp}}{H_{u,FE}}$	R_{exp} (kN)	R_{FE} (kN)	$\frac{R_{exp}}{R_{FE}}$
G-100-S600-1	69.0	76.2	0.91	0.0	0.0	-	69.0	76.2	0.91
G-100-S600-2	77.7	76.2	1.02	0.0	0.0	-	77.7	76.2	1.02
G-100-S300-1	76.5	78.4	0.98	0.0	0.0	-	76.5	78.4	0.98
G-100-S300-2	82.1	78.4	1.05	0.0	0.0	-	82.1	78.4	1.05
G-100-S150	85.5	89.8	0.95	0.0	0.0	-	85.5	89.8	0.95
G-100-S75	90.5	90.3	1.00	0.0	0.0	-	90.5	90.3	1.00
O-100-S600	79.5	82.7	0.96	0.0	0.0	-	79.5	82.7	0.96
O-75-S600	60.0	60.0	1.00	14.0	13.0	1.07	61.6	61.4	1.00
O-50-S600	40.0	40.0	1.00	17.4	16.5	1.05	43.6	43.3	1.01
O-25-S600	20.0	20.0	1.00	20.8	19.8	1.05	28.9	28.1	1.03
O-0-S600	0.0	0.0	-	20.8	20.4	1.02	20.8	20.4	1.02
O-100-S75	90.7	93.4	0.97	0.0	0.0	-	90.7	93.4	0.97
O-75-S75	67.5	67.5	1.00	15.5	14.7	1.05	69.3	69.1	1.00
O-50-S75	45.0	45.0	1.00	21.3	20.0	1.07	49.8	49.2	1.01
O-25-S75	22.5	22.5	1.00	23.5	22.7	1.03	32.5	32.0	1.02
O-0-S75-1	0.0	0.0	-	22.3	21.9	1.02	22.3	21.9	1.02
O-0-S75-2	0.0	0.0	-	20.8	21.9	0.95	20.8	21.9	0.95
		Mean	0.99 (0.98)*		Mean	1.04		Mean	0.99 (1.01)**
		COV	0.03 (0.04)*		COV	0.04		COV	0.04 (0.02)**

* values in brackets are for when only pure compression results are considered

** values in brackets are for when only combined load results are considered

A comparison between the FE and test axial load-displacement curves for the specimens under pure compression is presented in Figure 6.27, where it is demonstrated that the initial axial stiffness (EA/L) and the overall curve profile are accurately captured. Similarly, for the combined load cases, a comparison between the FE and test curves of horizontal load versus displacement of the column at mid-height is presented in Figures 6.28, 6.29 and 6.30 for specimens initially compressed at 75%, 50% and 25% of their compressive capacity

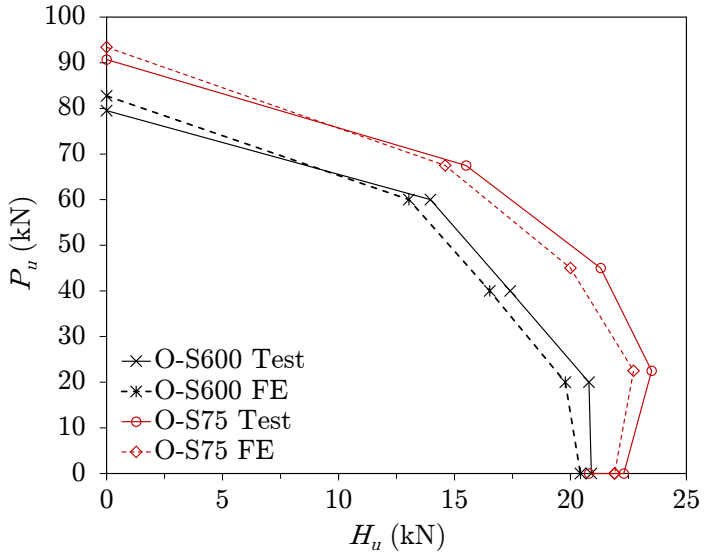
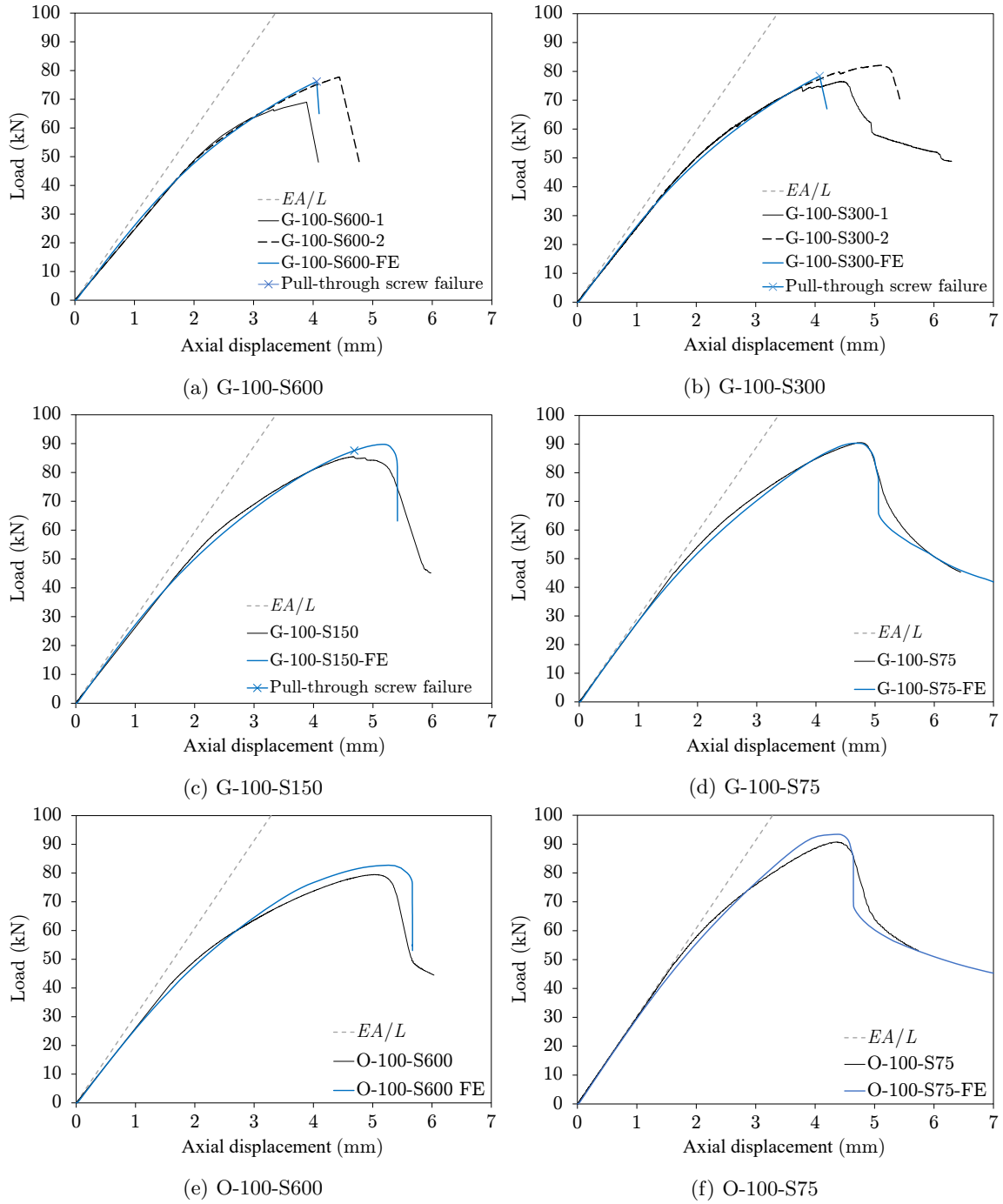


Figure 6.26: Comparison between the ultimate compressive P_u and horizontal H_u loads determined from the developed FE and the tests from the present study for beam-column specimens (sheathed with OSB and connected at 600 mm and 75 mm intervals)

respectively and then horizontally loaded until failure. Finally, the FE–test curves of the specimens under pure bending are presented in Figure 6.31. Overall, it can be observed that the horizontal load-deflection curves gathered from the FE model analyses and from the experimental studies compare well in terms of initial stiffnesses and peak capacities. It should be noted that the initial stiffness of the load-deflection curves is close to the theoretical pinned limits, while a slight increase in fixity is demonstrated with decreasing screw spacing (from 600 mm to 75 mm) and with increasing pre-compression.

The failure modes of the plasterboard specimens under pure compression are illustrated in Figure 6.32, while the failure modes of the specimens subjected to the combined load cases and connected to OSB sheathing at 600 mm and 75 mm intervals are illustrated in Figures 6.33 and 6.34 respectively. A summary of the observed failure modes is also provided in Table 6.11. The FE models were capable of capturing accurately the observed test failure modes. For the specimens sheathed with plasterboard and screw connected at spacings of 600 mm and 300 mm, the critical failure mode, both for the FE models and test specimens, was screw pull-through, followed by buckling of the column.

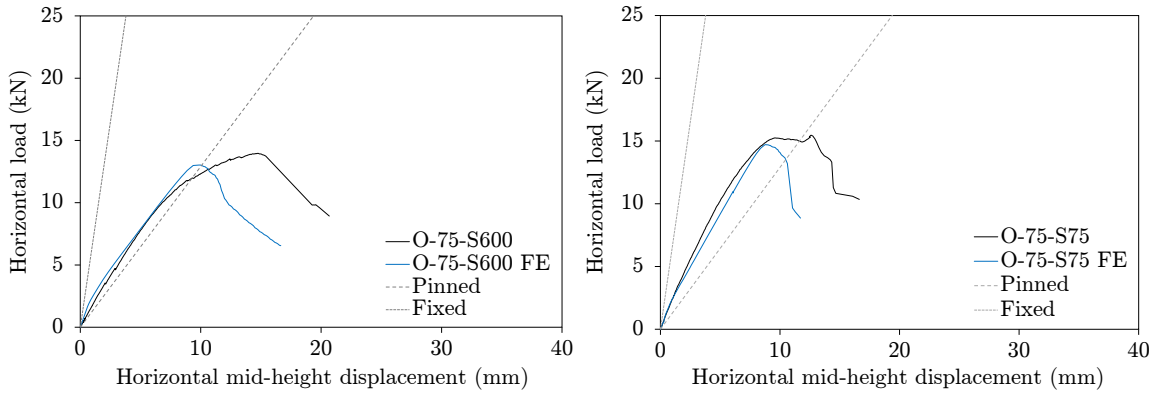


(a) G-100-S600 (b) G-100-S300

(c) G-100-S150 (d) G-100-S75

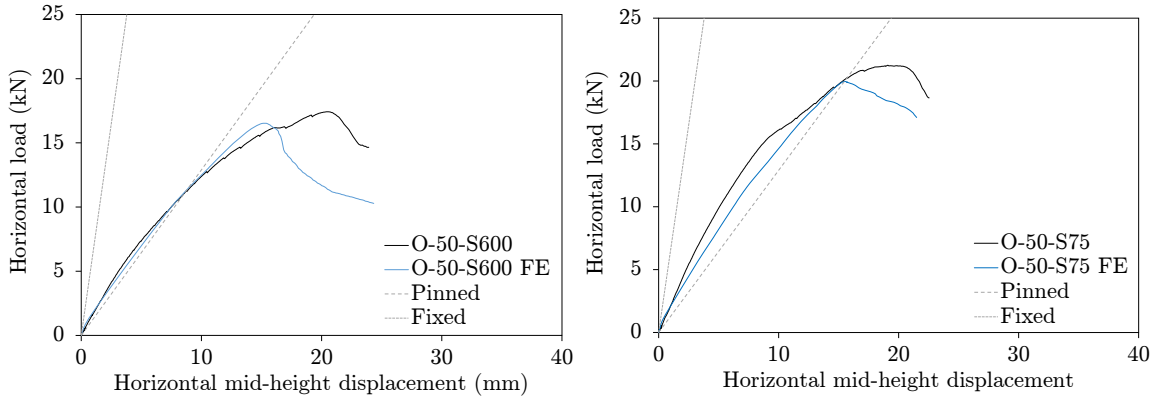
(e) O-100-S600 (f) O-100-S75

Figure 6.27: Comparison between the FE and test axial load-displacement curves for plasterboard sheathed specimens, connected with screws at a spacing of (a) 600 mm (b) 300 mm (c) 150 mm and (d) 75 mm, and for OSB sheathed specimens connected with screws at a spacing of (e) 600 mm and (f) 75 mm



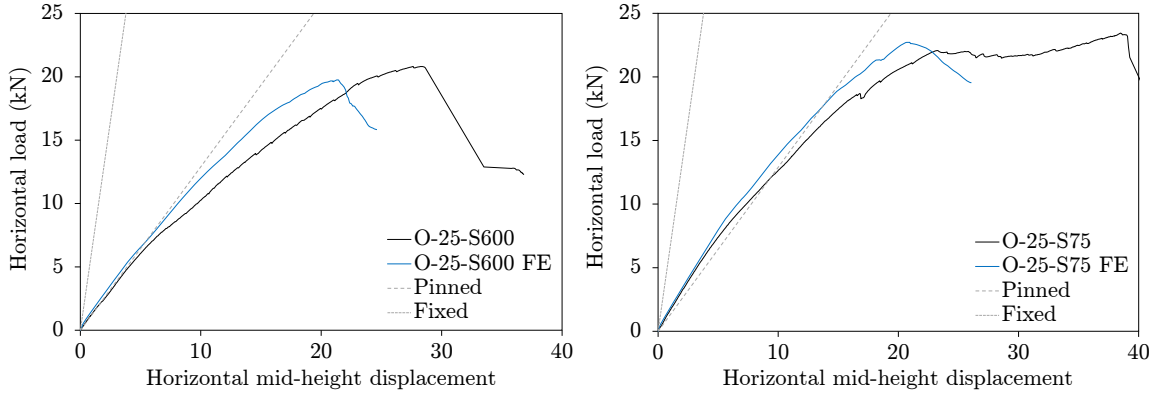
(a) O-75-S600 (b) O-75-S75

Figure 6.28: Comparison between the FE and test horizontal load-displacement curves for OSB sheathed specimens, connected with screws at a spacing of (a) 600 mm and (b) 75 mm after being axially loaded at 75% of their compressive capacity



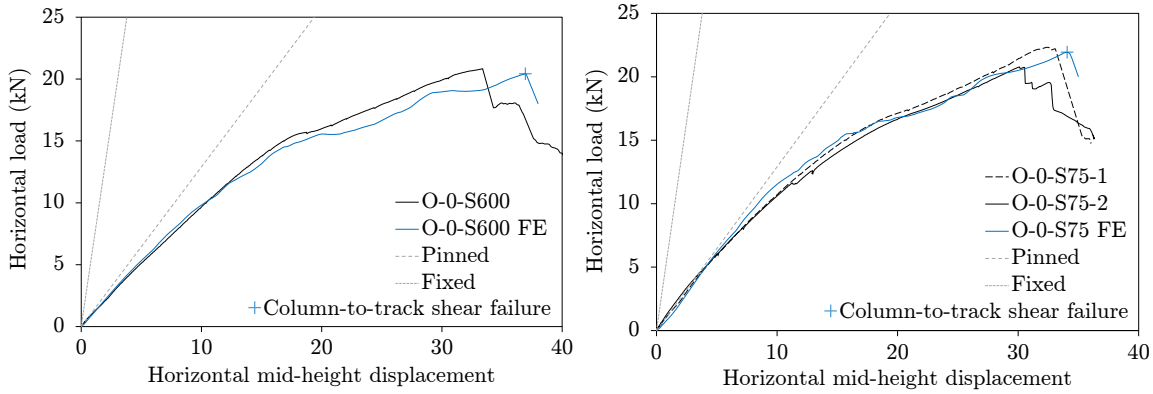
(a) O-50-S600 (b) O-50-S75

Figure 6.29: Comparison between the FE and test horizontal load-displacement curves for OSB sheathed specimens, connected with screws at a spacing of (a) 600 mm and (b) 75 mm after being axially loaded at 50% of their compressive capacity



(a) O-25-S600 (b) O-25-S75

Figure 6.30: Comparison between the FE and test horizontal load-displacement curves for OSB sheathed specimens, connected with screws at a spacing of (a) 600 mm and (b) 75 mm after being axially loaded at 25% of their compressive capacity



(a) O-0-S600 (b) O-0-S75

Figure 6.31: Comparison between the FE and test horizontal load-displacement curves for OSB sheathed specimens, connected with screws at a spacing of (a) 600 mm and (b) 75 mm subjected to pure bending



(a) G-100-S600 (b) G-100-S300 (c) G-100-S150 (d) G-100-S75

Figure 6.32: Comparison between the FE (left images) and test (right images) failure modes of specimens under pure compression sheathed with plasterboard screw connected at every (a) 600 mm, (b) 300 (mm), (c) 150 mm and (d) 75 mm (yielding in FE models is marked by grey)



(a) O-100-S600 (b) O-75-S600 (c) O-50-S600 (d) O-25-S600 (e) O-0-S600

Figure 6.33: Comparison between the FE and test failure modes of specimens screw connected at every 600 mm with OSB under (a) pure compression, (b) 75%, (c) 50%, (d) 25% and (e) 0% in compression followed by bending until failure (yielding in FE models is marked by grey)



(a) O-100-S75 (b) O-75-S75 (c) O-50-S75 (d) O-25-S75 (e) O-0-S75

Figure 6.34: Comparison between the FE and test failure modes of specimens screw connected at every 75 mm with OSB under (a) pure compression, (b) 75%, (c) 50%, (d) 25% and (e) 0% in compression followed by bending until failure (yielding in FE models is marked by grey)

Table 6.11: Comparison between the observed FE and test failure modes

Specimen	Test failure mode *	FE failure mode *
G-100-S600-1	D → CF → FT	D → CF
G-100-S600-2	D → CF → FT	D → CF
G-100-S300-1	(L + D (hole)) → CF	D + L (hole) → CF
G-100-S300-2	(D → CF) + L (end)	D + L (hole) → CF
G-100-S150	(L (end) + D) → CF	(L (end) + D) → CF
G-100-S75	L (end)	L
O-100-S600	L (end) + D	L (end) + D
O-75-S600	L (hole)	L (hole)
O-50-S600	L (hole)	L (hole)
O-25-S600	L (hole)	L + Y (ends)
O-0-S600	L + L (end)	L + Y (ends) + CF + CF (column-to-track)
O-100-S75	L (end)	L (end)
O-75-S75	L (hole)	L (hole)
O-50-S75	L (end) + L (hole)	L (hole)
O-25-S75	L (end) + L (hole)	L (hole)
O-0-S75-1	L (end) + CF (column-to-track)	L + Y (ends) + CF (column-to-track)
O-0-S75-2	L (end) + CF (column-to-track)	L + Y (ends) + CF (column-to-track)

* CF: connector failure, L: local buckling, D: distortional buckling,
FT: flexural torsional buckling, Y: yielding

Note that, in order to capture pull-through failure in the numerical simulations of the specimens with screw spacings of 600 mm and 300 mm, the pull-through load capacity of the 3.5 mm screws in plasterboard, provided in Table 6.5 and Figure 6.12 (b), was halved (from $F_{u,pt} = 0.48$ kN to $F_{u,pt} = 0.24$ kN). This decrease was employed to reflect the fact that, during axial loading of the column, initiation of global buckling about the minor axis results in shear slipping of the screws, causing loss of contact between one side of the screw shank and the inner core of the board. This effect gets magnified with decreasing numbers of screws and at the mid-height of the column where the resulting bow is at its maximum. The pull-through load-displacement behaviour of the critical screw at the mid-height of specimen G-100-S600 is illustrated in Figure 6.35, where the key stages are also highlighted

with regards to the overall axial load-displacement behaviour of the column.

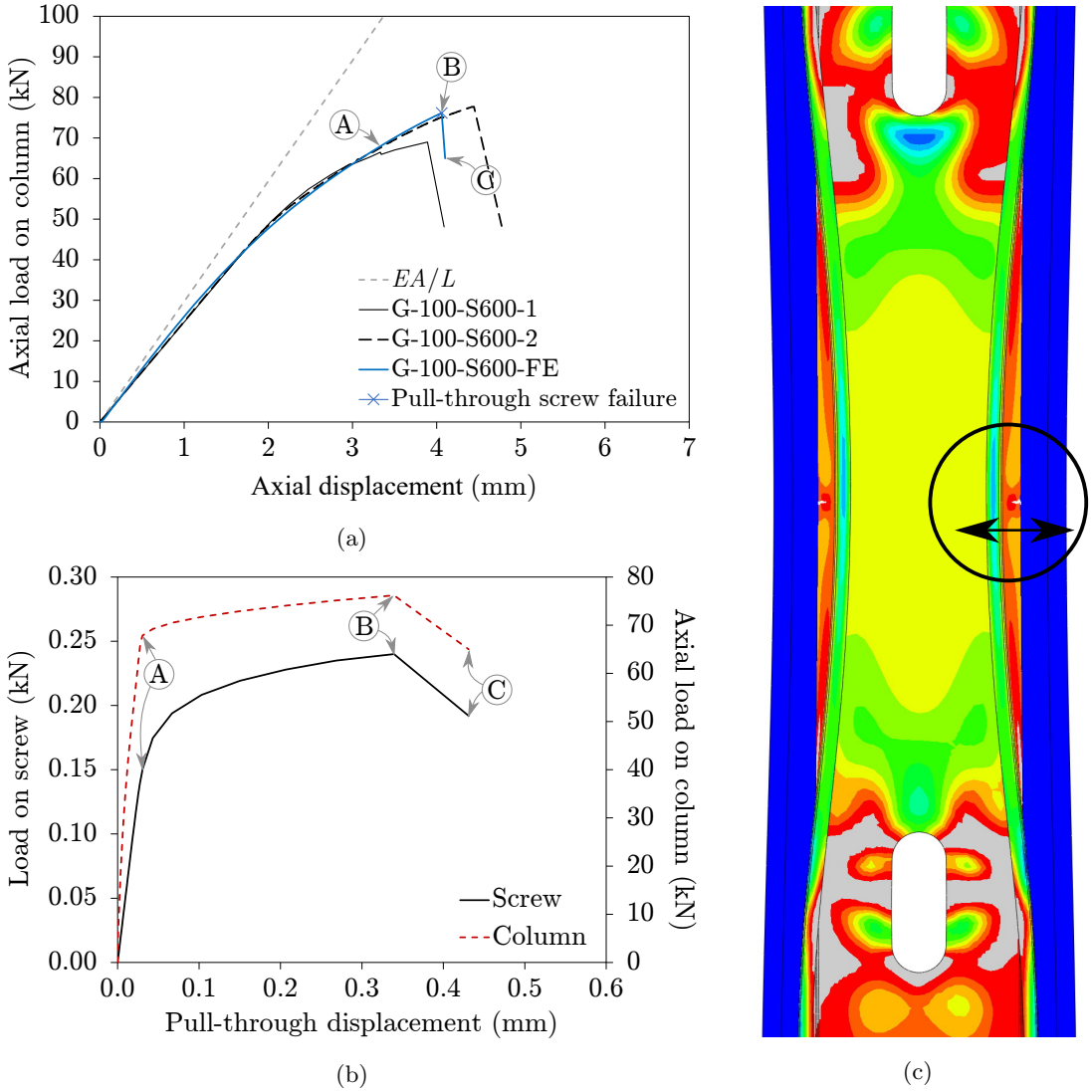


Figure 6.35: Illustration of pull-through connector failure of the screw at mid-height of specimen G-100-S600, where A to C stages are indicated on (a) an axial load-displacement FE curve of the column, (b) a combined graph of two curves consisting of the pull-through screw load and the axial load of the column, both plotted against the pull-though displacement of the screw and (c) an FE model of the relevant screw at failure

For the specimen connected to plasterboard with a screw spacing of 150 mm, pull-through failure of some screws occurred prior to the peak capacity and before the occurrence of local buckling at the end of the specimen. For the rest of the specimens under pure compression sheathed with plasterboard at 75 mm intervals or with OSB, no screw failure occurred and the peak capacity was limited by buckling of the column, as also observed in

the physical tests. Similarly, for the beam-column specimens which were connected to OSB sheathing, no screw connector failure was observed. Finally, for the two specimens under pure bending (Figure 6.31), the ultimate resistance from the FE model was limited by the shear capacity of the column-to-track screw, in agreement with the physical tests. The shear load-slip behaviour of the critical column-to-track screw is illustrated in Figure 6.36, where the key stages are highlighted with regard to the overall horizontal load-deflection behaviour of the column.

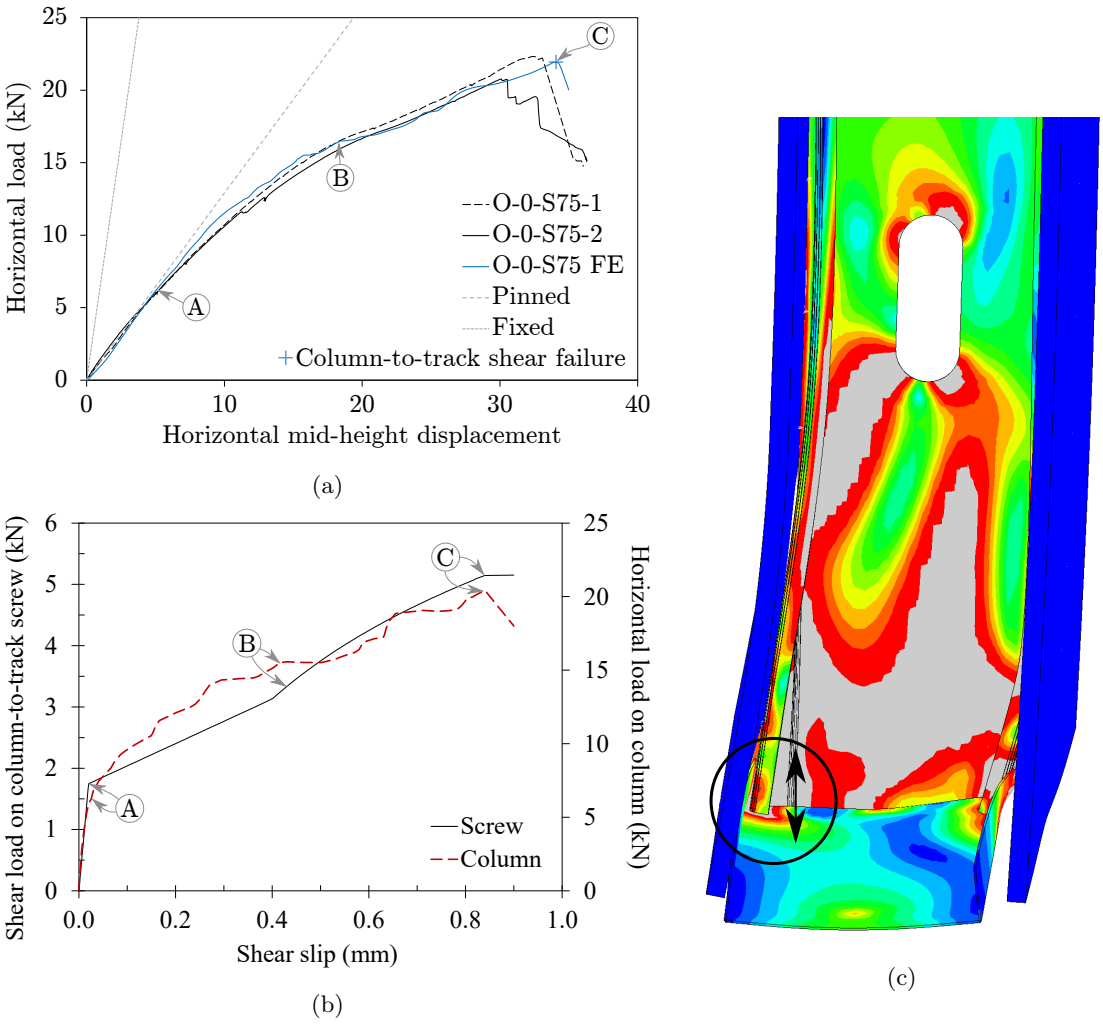


Figure 6.36: Illustration of shear connector failure of the screw at mid-height of specimen O-0-S75, where A to C stages are indicated on (a) a horizontal load-displacement FE curve of the column, (b) a combined graph of two curves consisting of the shear screw load and the horizontal load of the column, both plotted against the shear slip of the screw and (c) an FE model of the relevant screw at failure

6.5 Parametric study

Following validation of the developed FE models, parametric studies were undertaken to investigate the influence of the sheathing, spacing of sheathing-to-stud fasteners and section depth on the load-bearing capacity of the examined specimens under various loading scenarios.

6.5.1 Effect of sheathing

A numerical study has been carried out in order to investigate the impact of sheathing configuration and fastener spacing on the compression capacity of sheathed stud members. As shown in Table 6.12, three different sheathing configurations have been investigated, all benchmarked against their equivalent unsheathed response. All specimens were 2.7 m long, while their cross-sectional dimensions were set to: $h = 100$ mm, $b = 44$ mm, $c = 12$ mm, $r = 2.5$ mm and $t = 1.46$ mm - see Figure 6.6 for the adopted notation. The material properties of the cold-formed steel studs were taken from the study by Vieira & Schafer (2016), while the employed imperfection amplitudes, as shown in Figure 6.16, were taken as the recommended 50 %ile values by Zeinoddini & Schafer (2012). Therefore, with reference to Figure 6.16, $\delta_L = 0.31t$, $\delta_D = 0.75t$, $\delta_{G,min} = L/2910$, $\delta_{G,maj} = L/4010$ and $\theta_{G,tor} = 0.3$ deg/m, where t is the nominal thickness and L is 2.7 m. The material behaviour of the plasterboard and OSB was modelled as reported in Sections 6.3.3.2 and 6.3.3.3 respectively, while the modelling of the screw fasteners is described in Section 6.3.4.1. A description of the examined systems as well as a summary of the obtained results are presented in Table 6.12, while comparison of the load-axial shortening curves between the bare steel case and the plasterboard or OSB sheathed specimens are shown in Figures 6.37 and 6.38 respectively. The identification system of the specimens begins with two letters corresponding to the type of sheathing board on each side of the stud (with B – bare, G – gypsum (plasterboard) and O – OSB), followed by the employed spacing of fasteners in mm.

The FE results showed that adding sheathing to one side of the stud columns led to an increase in capacity of about 30% over that of the bare steel column $P_{FE,BB}$, while for

sheathing on both sides, the capacity rose by about 80% - 100%. The more robust OSB material yielded greater gains than the plasterboard. The primary reason for the increase in capacity was the restraint against minor axis flexural and flexural-torsional buckling afforded to the columns through the sheathing and fasteners. Greater gains were achieved however for the closer connector spacing (i.e. moving from 300 mm to 100 mm); this is attributed to the mobilisation of composite action between the boards and the column as well as to a reduction in the wavelength of the distortional buckles.

Table 6.12: Description of parametric examined systems and obtained FE results.

Specimen	Sheathing	Spacing of fasteners (mm)	P_{FE} (kN)	$P_{FE}/P_{FE,BB}$
BB	Bare-Bare	-	43.2	1.00
GB-S300	Gypsum-Bare	300	53.0	1.23
GB-S100	Gypsum-Bare	100	58.0	1.34
OB-S300	OSB-Bare	300	58.2	1.35
OB-S100	OSB-Bare	100	63.4	1.47
GG-S300	Gypsum-Gypsum	300	76.7	1.78
GG-S100	Gypsum-Gypsum	100	82.0	1.90
OO-S300	OSB-OSB	300	82.0	1.90
OO-S100	OSB-OSB	100	88.1	2.04

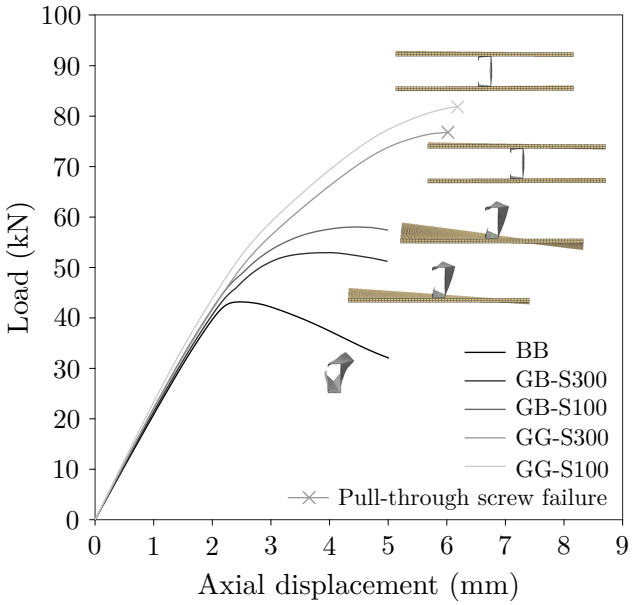


Figure 6.37: Comparisons of FE load-axial shortening curves for bare steel stud and plasterboard sheathed systems

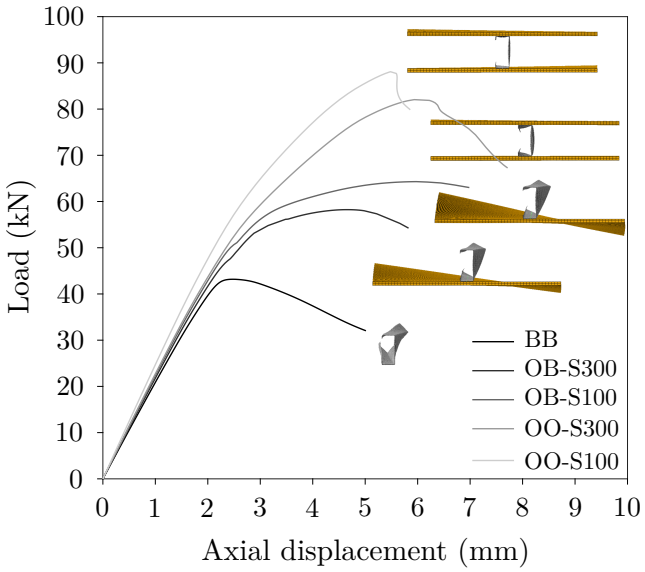


Figure 6.38: Comparisons of FE load-axial shortening curves for bare steel stud and OSB sheathed systems

6.5.2 Effect of connector spacing and section depth

The influence of fastener spacing and section depth on the response of specimens set in tracks and sheathed on both sides with OSB boards is reported in this subsection. The modelled members were studied in pure compression, pure bending and under various combinations of axial and horizontal loading (with the axial load applied up to 25%, 50% and 75% of the compression stud capacity, followed by bending until failure). All specimens were 2.4 m long, while their cross-sectional dimensions were set to $b = 44$ mm, $c = 12$ mm, $r = 2.5$ mm and $t = 1.46$ mm, with a varying section depth $h = 68, 100, 150, 201$ and 252 mm - see Figure 6.5 for the employed mesh and Figure 6.6 for the adopted notation. Note that for the members with deeper section sizes (i.e. $h = 150, 201$ and 252 mm), three service holes were modelled along the stud length, with a spacing of 600 mm between them and with the first one 300 mm away from the end of the stud. The employed connectors were screws of 4.8 mm in diameter, while the three different connector spacings that were examined were 300 mm, 150 mm and 75 mm, resulting to 9, 17 and 33 screws respectively on each side of the specimen, connecting an OSB board of 11 mm thickness to the steel stud. The material properties assigned to the cold-formed steel members and OSB boards were as described in

Section 6.3.3. The modelled tracks were 800 mm long and the boards were 600 mm wide, while the lateral load was introduced using the 4-point loading scheme described in Section 6.3.6. Modelling of imperfections was implemented as described in Section 6.3.5 using the magnitudes provided in Section 6.4.4, while the screw fasteners were modelled as described in Section 6.3.4.

A summary of the obtained results is provided in Table 6.13, where P_u is the ultimate compressive load and H_u is the ultimate horizontal load. The adopted specimen notation starts with the section depth in mm, followed by the nominal thickness of the cold-formed steel member in mm multiplied by 10, then by a hyphen (-) and the letter S and, finally, by the connector spacing in mm. Note that, for simplicity, in the notation of the specimens with depths of 68 mm, 201 mm and 252 mm, these were rounded to 70, 200 and 250 respectively. The following subsections describe the effect of section depth and connector spacing on the response of the examined systems subjected to different loading configurations.

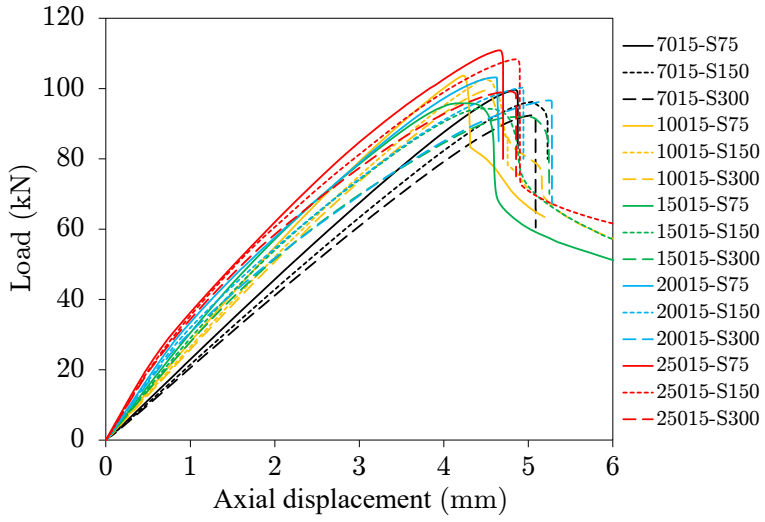
Table 6.13: Results of parametric studies

Specimen	Pure compression	$0.75P_u$ followed by bending		$0.5P_u$ followed by bending		$0.25P_u$ followed by bending		Pure bending
	P_u (kN)	$0.75P_u$ (kN)	H_u (kN)	$0.5P_u$ (kN)	H_u (kN)	$0.25P_u$ (kN)	H_u (kN)	H_u (kN)
7015-S300	92.5	69.4	3.2	46.2	5.8	23.1	7.2	8.3
7015-S150	96.2	72.2	3.8	48.1	6.3	24.1	8.0	9.3
7015-S75	99.7	74.8	4.1	49.8	6.8	24.9	8.9	10.5
10015-S300	99.5	74.6	6.1	49.7	10.1	24.9	13.2	15.3
10015-S150	102.8	77.1	6.6	51.4	11.0	25.7	14.3	16.5
10015-S75	103.7	77.8	7.8	51.9	13.1	25.9	16.6	18.8
15015-S300	92.0	69.0	9.5	46.0	15.8	23.0	20.2	23.1
15015-S150	94.3	70.7	10.4	47.1	17.4	23.6	22.1	25.1
15015-S75	95.8	71.9	11.8	47.9	19.6	24.0	24.5	27.9
20015-S300	96.6	72.5	12.6	48.3	21.0	24.2	26.2	29.4
20015-S150	100.3	75.2	13.6	50.2	22.6	25.1	28.8	32.8
20015-S75	103.2	77.4	14.9	51.6	24.9	25.8	31.7	36.1
25015-S300	99.2	74.4	15.1	49.6	25.1	24.8	31.7	35.9
25015-S150	108.3	81.2	16.4	54.2	27.3	27.1	34.5	39.0
25015-S75	110.9	83.2	17.7	55.4	29.6	27.7	37.5	42.5

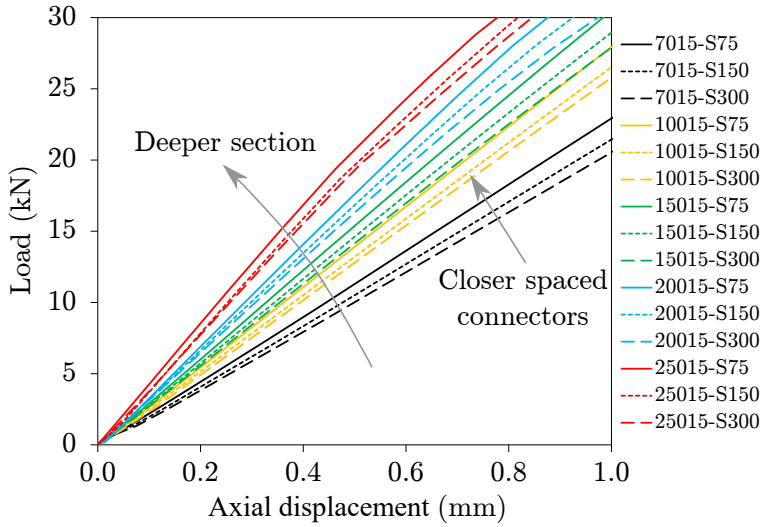
6.5.2.1 Pure compression results

The axial load-displacement curves of all specimens under pure compression are presented in Figure 6.39. It can be observed that the axial stiffness (EA/L) increases with in-

creasing section depth and decreasing connector spacing. For deeper sections, whose axial stiffness is higher, after about 25 kN of compression where the elasticity limits of the material are reached, the gradient of the curves decreases, becoming approximately equal to the gradient of the curves of shorter sections, up to about 85 kN. The influence of the connector



(a)

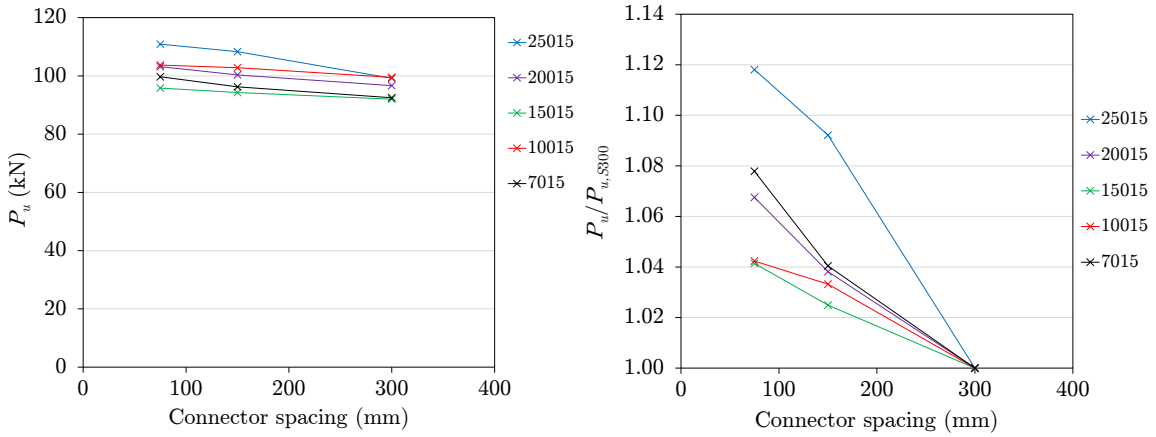


(b)

Figure 6.39: FE parametric axial load-displacements curves: (a) full spectrum and (b) initial detail

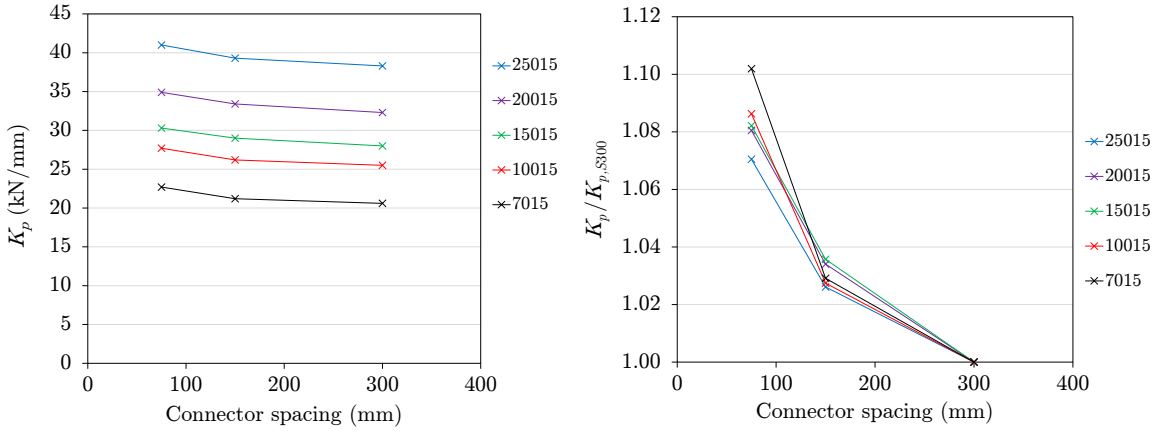
spacing on the ultimate axial capacity P_u and measured initial axial stiffness K_p of the examined systems is schematically illustrated in Figures 6.40 and 6.41 respectively, where the ultimate capacity P_u and initial stiffness K_p of each system is presented both in absolute values and normalised by the capacity and stiffness of the equivalent system with the

widest (i.e. 300 mm) spacing of connectors ($P_{u,S300}$ and $K_{p,S300}$ respectively). Up to 12% increases in strength and 10% increases in stiffness were achieved for the systems employing the closest connector spacing (i.e. 75 mm) - see Figures 6.40 and 6.41 respectively. As shown in Figures 6.39 and 6.40, the ultimate capacity P_u is not significantly affected by changes in section depth as local buckling limits the capacity of the specimens with the more slender cross-sections (classified as Class 4 per EN 1993-1-1 (2005)).



(a) (b)

Figure 6.40: Influence of connector spacing on ultimate compression capacity: (a) absolute values and (b) normalised by the compression capacity of the equivalent system with 300 mm spacing

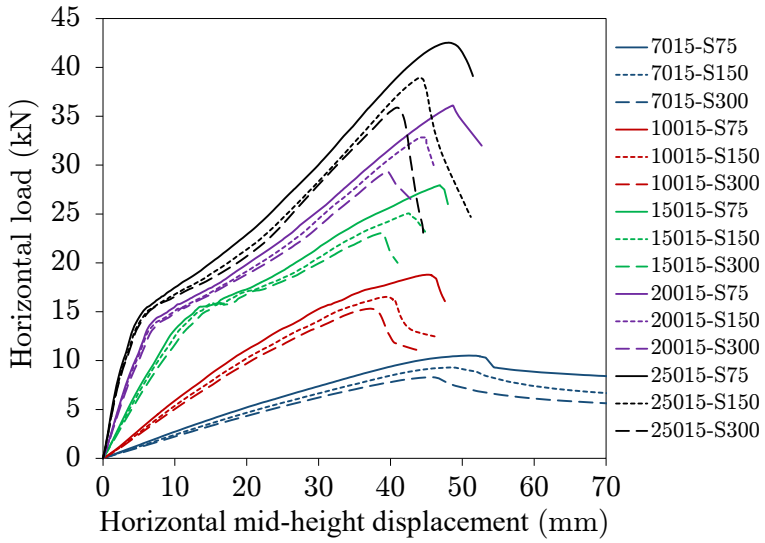


(a) (b)

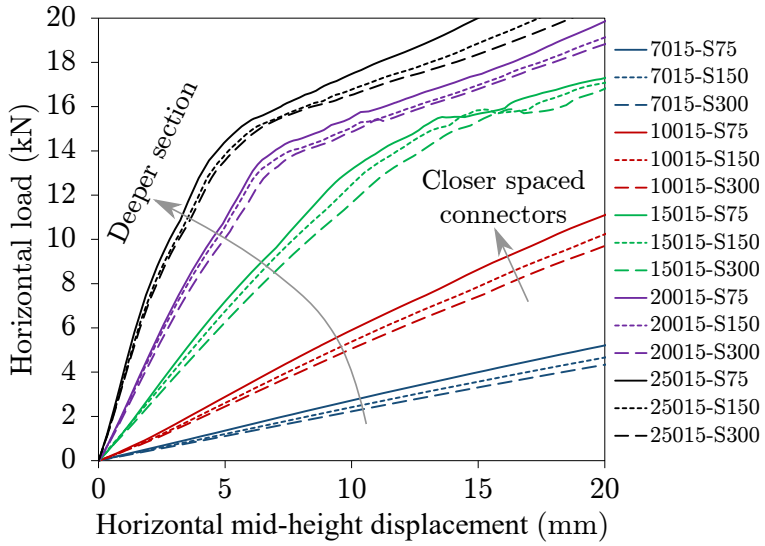
Figure 6.41: Influence of connector spacing on measured initial axial stiffness: (a) absolute values and (b) normalised by the stiffness of the equivalent system with 300 mm spacing

6.5.2.2 Pure bending results

The horizontal load-displacement curves of all specimens under pure bending are presented in Figure 6.42. As expected, the bending stiffness and ultimate bending capacity (indicated in terms of the ultimate horizontal load H_u) were found to increase with increasing section depth, with up to four times higher strength and 13 times higher stiffness achieved when increasing the section depth from 68 mm to 252 mm. The maximum horizontal load



(a)



(b)

Figure 6.42: FE parametric results of horizontal load vs mid-height at mid-depth deflections: (a) full spectrum and (b) initial detail

H_u and initial flexural stiffness K_h attained by each specimen are presented in Figures 6.43 and 6.44 respectively, both in absolute values and normalised by the maximum horizontal load and stiffness of the equivalent specimen with the widest (i.e. 300 mm) screw spacing ($H_{u,S300}$ and $K_{h,S300}$ respectively). Up to 26% increases in horizontal capacity H_u and 22% increases in bending stiffness K_h were achieved by decreasing the connector spacing from 300 mm to 75 mm, largely due to the effects of composite action - see Figures 6.43 and 6.44 respectively.

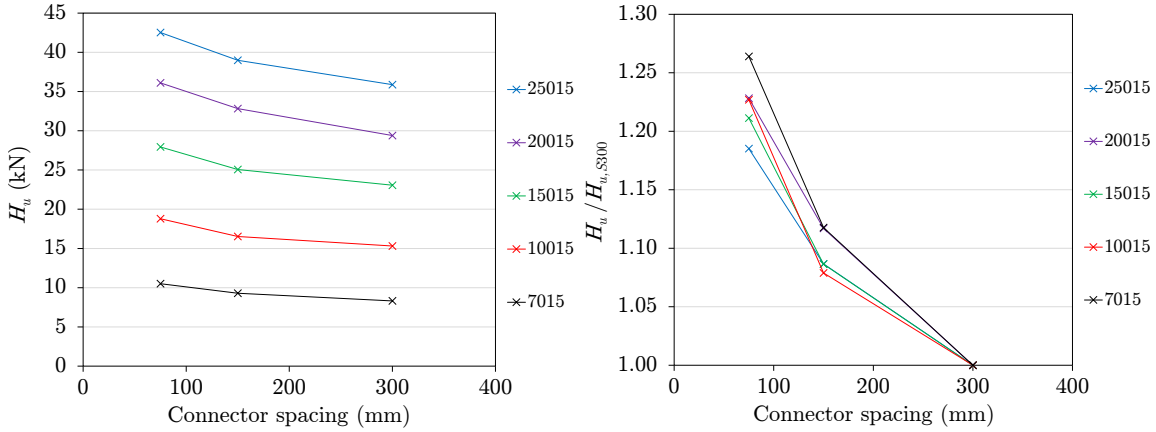


Figure 6.43: Influence of connector spacing on ultimate bending capacity in terms of horizontal loads H_u: (a) absolute values and (b) normalised by the loads of the equivalent system with 300 mm spacing

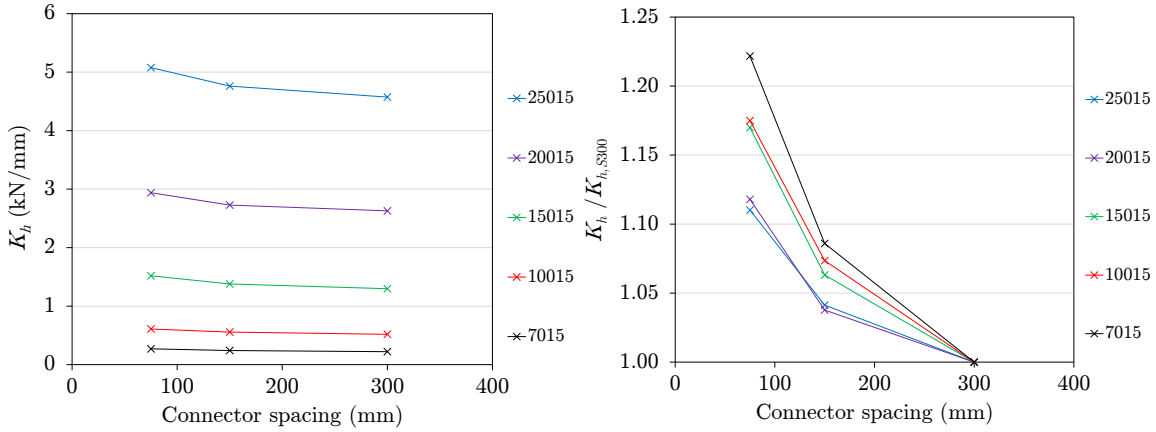


Figure 6.44: Influence of connector spacing on flexural stiffness for the examined systems under pure bending: (a) absolute values and (b) normalised by the stiffness of the equivalent system with 300 mm spacing

In Figure 6.42, a pronounced change in gradient can be observed for the specimens with a depth equal to or deeper than 150 mm, which is attributed to material yielding and to the development of buckling at the stud ends. This has been verified by the findings of a case study, the results of which are presented in Figure 6.45. In the conducted case study, two different FE models of specimen 15015-S300 were developed and subjected to pure bending: one model with the nonlinear material response that was used in all parametric studies and one with an idealised perfectly elastic material behaviour. No sudden change in gradient or buckling near the member ends occurred for the perfectly elastic model, as shown in Figure 6.45. Note also that the shape, thickness and material strength of the end track, as well as its connection to the column, was found to affect slightly the degree of gradient change, as well as the roundedness of the load-displacement curve and its smoothness beyond this change (with smoother curves corresponding to stronger column-to-track connections). Therefore, the column-to-track connection of all modelled specimens was strengthened for system failure to not be limited by failure of the connection between the column and track (as was the case for the validation studies presented in Section 6.4.4). Further commentary on the effect of the track is provided in Section 6.5.3.

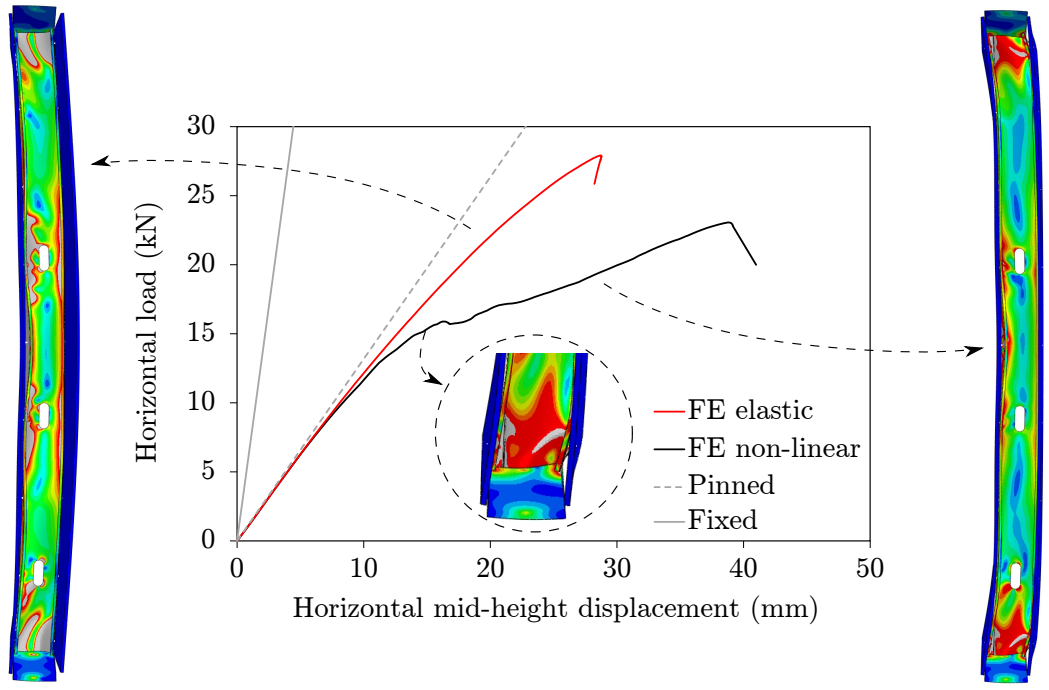


Figure 6.45: Case study results of specimen 15015-S300 under pure bending modelled with (i) perfectly elastic and (ii) actual nonlinear material behaviour

6.5.2.3 Combined loading results

The FE results of the specimens subjected to combined loading (i.e. axially loaded up to a percentage of the compressive capacity of the stud and then laterally loaded until failure) are reported in terms of axial load P_u and ultimate horizontal load H_u in Table 6.13. It is apparent that the $P_u - H_u$ relationship is not linear, since the specimens initially loaded up to 25%, 50% and 75% of P_u failed at about 90%, 70% and 40%, respectively, of the ultimate horizontal load H_u attained when under pure bending (whilst for a linear relationship this would have been 75%, 50% and 25% respectively). The capacities of the specimens under combined loading were found to increase with decreasing connector spacing and increasing section depth, while the influence of the section depth was found to be higher for lower levels of initial compression. A typical example of the influence of the connector spacing on the ultimate horizontal capacity H_u is provided in Figure 6.46, where capacity improvements of up to 29% were achieved when shifting to closer spaced connectors (from 300 mm to 75 mm) for the specimens initially compressed at 50% of P_u.

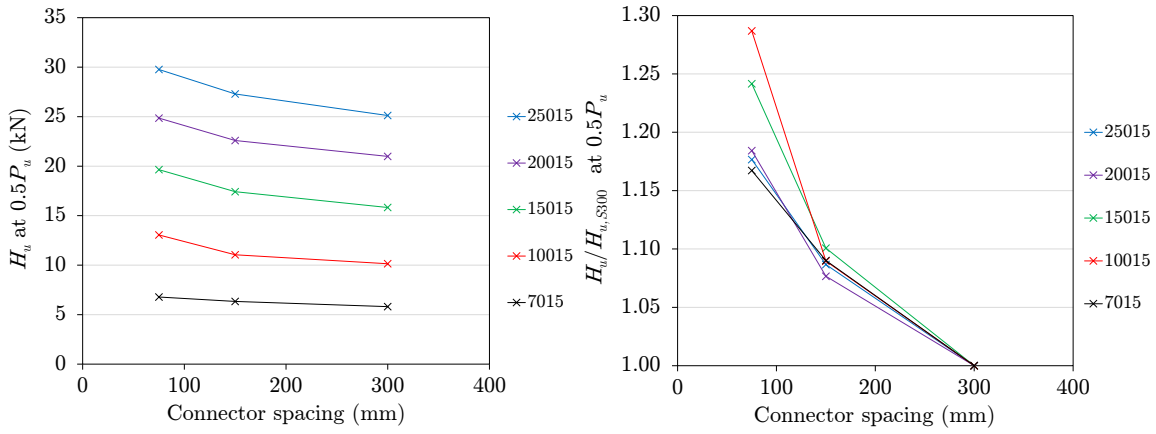


Figure 6.46: Influence of connector spacing on bending capacity for specimens initially compressed at 50% of their compression capacity, in terms of horizontal loads H_u: (a) absolute values and (b) normalised by the loads of equivalent systems with 300 mm spacing

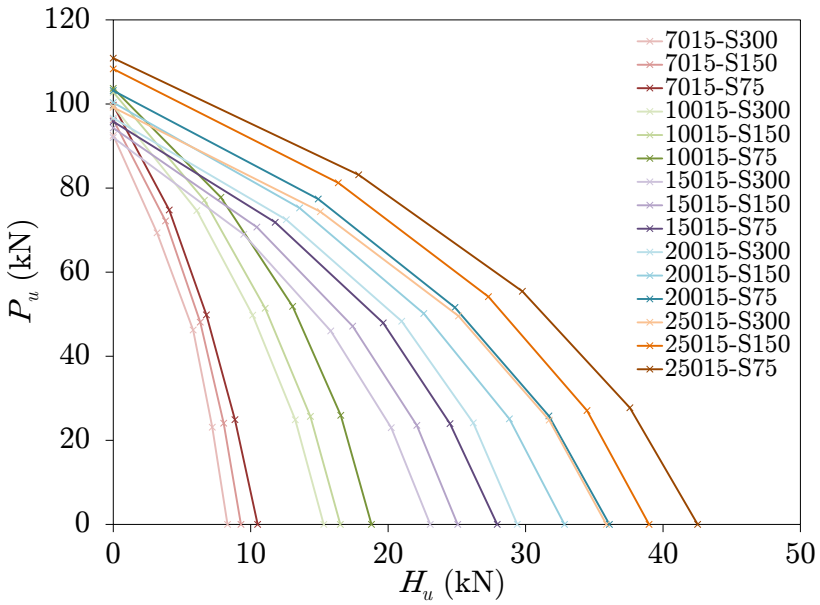
The interaction curves of the examined specimens under combined loading are presented in Figure 6.47 (a), where the compressive load P_u is plotted against the horizontal load H_u (in terms of absolute values), while in Figure 6.47 (b), the same set of data is presented

in a normalised format, which allows the convex shape of the interaction curves to become more apparent. The normalisation used in in Figure 6.47 (b) was realised using Equations (6.6) and (6.7), where $N_{c,Rd}$ is the axial cross-section resistance in compression, A_{eff} is the effective area in compression and f_y is the yield strength, taken as 482 MPa. In Equation (6.7), $H_{c,y,Rd}$ is the horizontal load resistance corresponding to pinned boundary conditions, $M_{c,y,Rd}$ is the moment resistance about the major axis and $W_{eff,y,Rd}$ is the elastic section modulus of the effective cross-section about the major axis. Note that the effective section properties were calculated using the effective width method, in accordance with the provisions in Eurocode EN 1993-1-3 (2006).

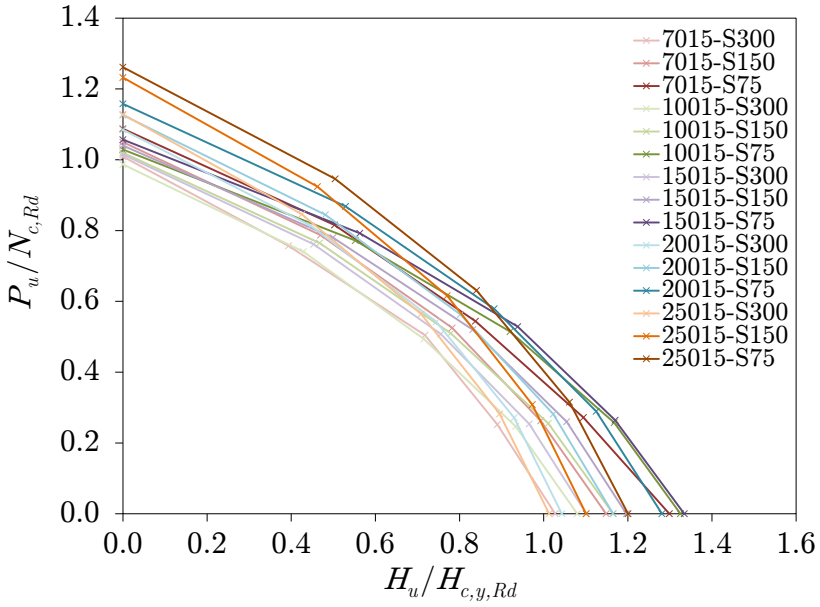
$$N_{c,Rd} = A_{eff} f_y \tag{6.6}$$

$$H_{c,y,Rd} = M_{c,y,Rd} \times 8/L = W_{eff,y,Rd} f_y \times 8/L \tag{6.7}$$

In order to examine more clearly the influence of the connector spacing on the response of specimens of different section depths, the interaction curves of each different cross-section are plotted separately and presented in both absolute and normalised formats in Figure 6.48. All interaction curves are of a convex profile, with decreasing connector spacing resulting in increased capacities. This effect gets more pronounced as bending becomes the predominant loading action, with the $H_u/H_{c,y,Rd}$ values corresponding to pure bending shown to be more than 1.0 for specimens connected at 300 mm intervals, then increasing to more than 1.1 for specimens with 150 mm connector spacings and, finally, for the specimens with 75 mm connector spacings, values greater than 1.2 are achieved.

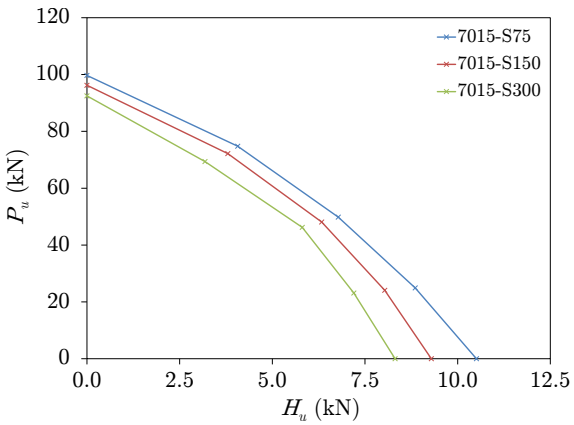


(a)

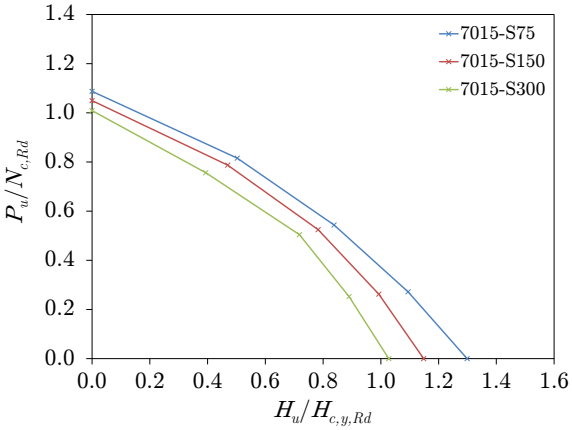


(b)

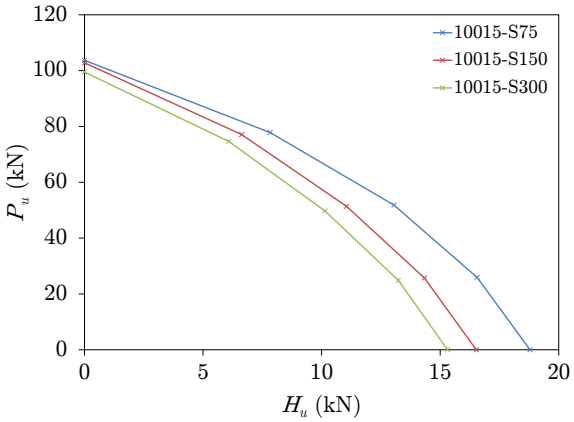
Figure 6.47: Summary of interaction curves of the FE parametric results in terms of (a) P_u vs H_u and (b) normalised capacities with effective cross-sectional properties determined using EN 1993-1-3 EN 1993-1-3 (2006)



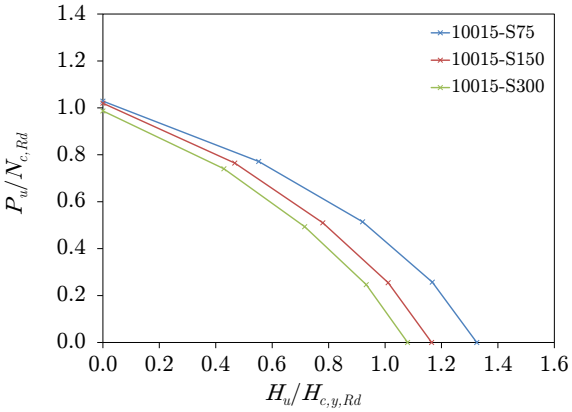
(a1)



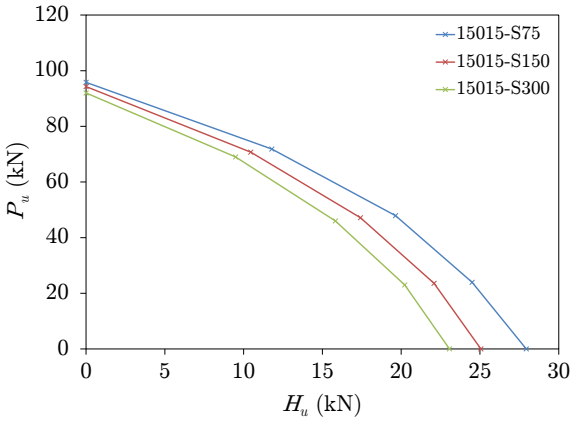
(a2)



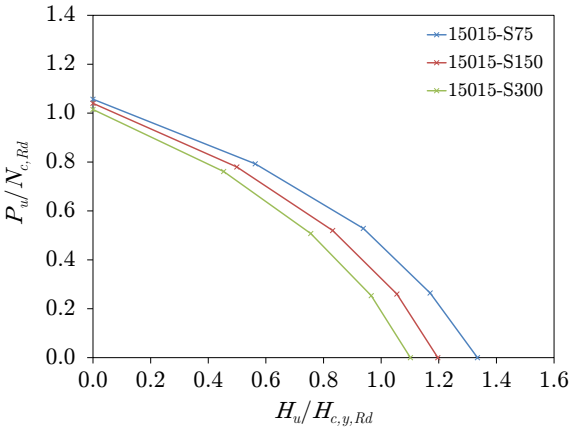
(b1)



(b2)



(c1)



(c2)

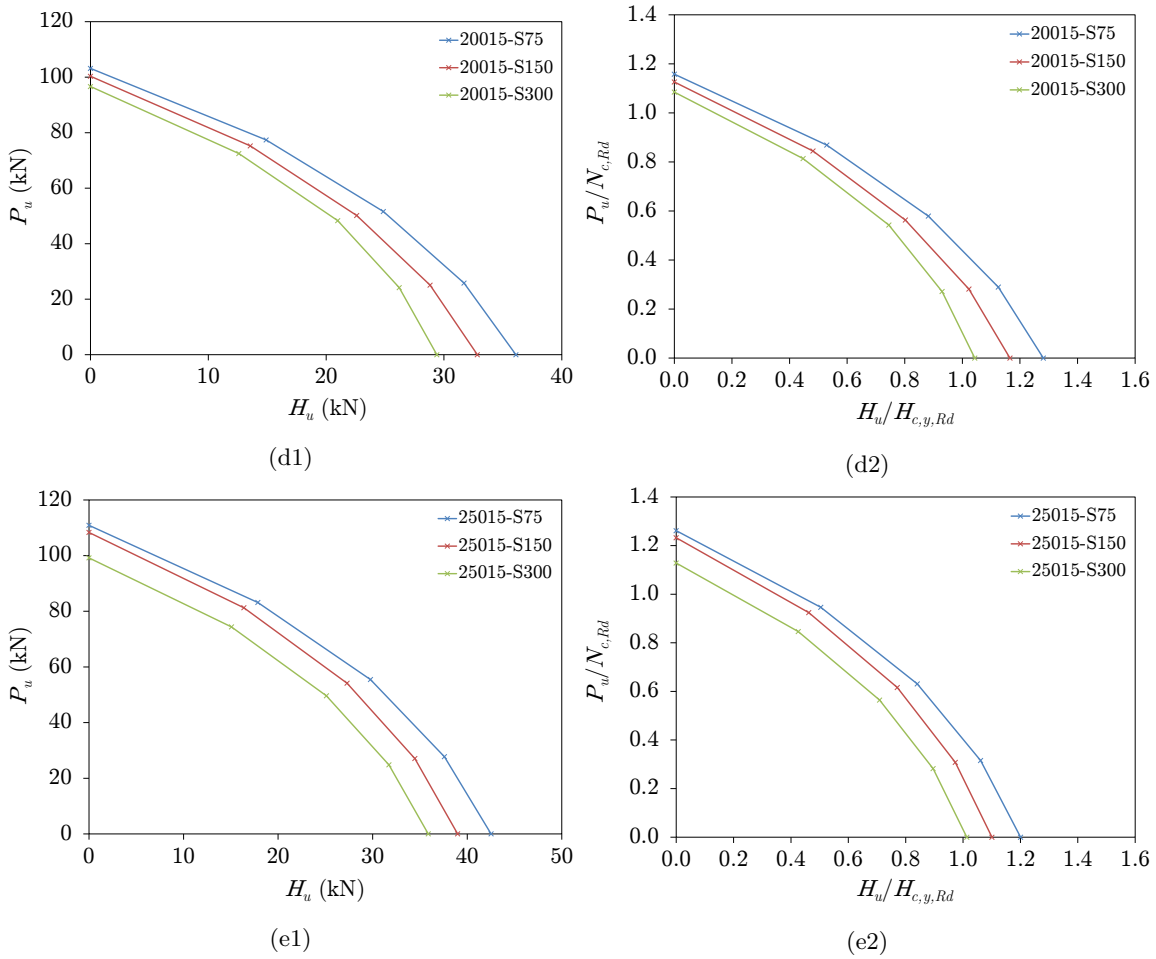
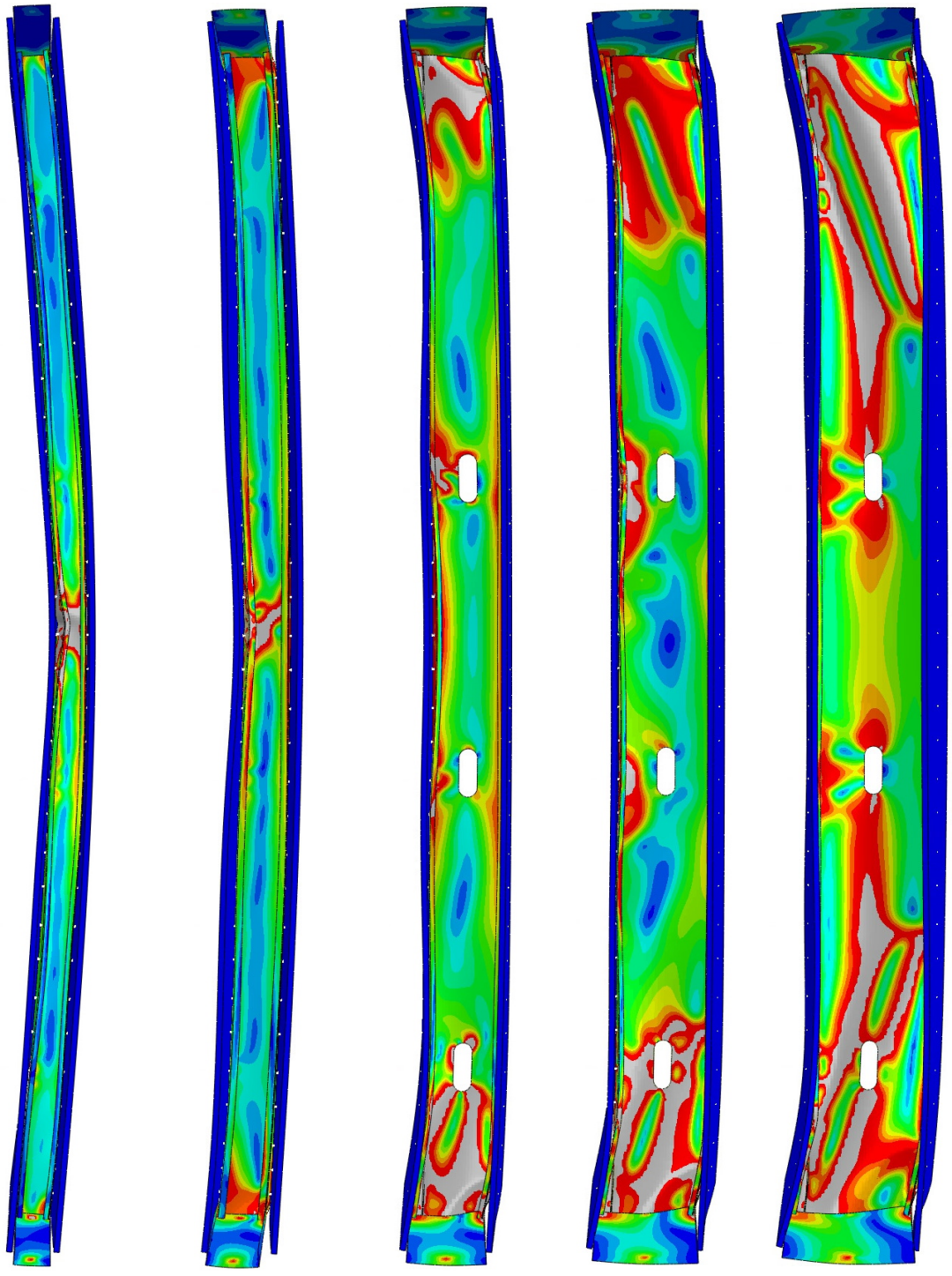


Figure 6.48: Interaction curves of FE parametric results in terms of (1) P_u vs H_u and (2) normalised capacities with effective cross-sectional properties determined using EN 1993-1-3 EN 1993-1-3 (2006) for specimens with section depths of: (a) 70 mm, (b) 100 mm, (c) 150 mm, (d) 200 mm and (e) 250 mm

6.5.3 Commentary on the effect of the track

Based on the conducted parametric studies reported in Section 6.5.2, the tracks at the stud ends were found to affect the response of the sheathed stud wall specimens depending on their geometric features as well as on the overall loading configuration. When under pure compression, the column-to-track boundaries behave more like fully fixed connections, while when under pure bending, they behave like pinned connections. When bending is predominant, the structural behaviour and failure mode of the examined systems are affected by the section depth, and, as a result, by the track depth. In Figure 6.49, the failure

modes of specimens of different section depths with 75 mm connector spacing under pure bending are presented. It can be observed that for the two smaller sections of 68 mm and



(a) 68 mm (b) 100 mm (c) 150 mm (d) 201 mm (e) 252 mm

Figure 6.49: Failure modes for specimens in pure bending with 75 mm screw spacing and a section depth of (a) 68 mm, (b) 100 mm, (c) 150 mm (d) 201 mm and (e) 252 mm

100 mm depth, the main failure mode was local buckling at mid-height, while for the deeper specimens, buckling near the stud ends became predominant. For sections with a depth equal to or greater than 150 mm, the thickness of the track had to be increased to 2.5 mm in order to obtain a smooth load-displacement curve beyond the point at which the column ends started to buckle. A stronger column-to-track connection was also required to not limit the system capacity. Therefore, the use of tracks of sufficient thickness in order to secure a smooth response not limited by the strength of the connection is recommended along with the use of a stronger connection between the column and the track, which can be achieved either with a larger diameter screw or by using more than one screw connector.

6.6 Conclusions

Finite element models simulating sheathed cold-formed steel studs set in tracks and subjected to various loading configurations (i.e. compression, bending and combinations of the two) were developed and validated against experimental data reported in the literature. The FE models included geometrical imperfections, while geometrical and material nonlinearities were also taken into account in the analyses. The finite element simulations were found to be capable of realistically describing the column-to-track boundary conditions, while the contact interaction between the cold-formed steel columns and the boards, as well as the nonlinear behaviour of the employed connectors, were explicitly replicated.

Following successful validation, the FE models were employed to investigate the influence of the sheathing, section depth and fastener spacing on the load-bearing capacity of the columns under various loading scenarios. It was found that the addition of sheathing leads to significant increases in the load-carrying capacity of the system over the bare steel column; sheathing on both sides of the cold-formed steel studs with the more robust OSB panels led to about a 100% increase in capacity. The main reason for the gains in capacity is the restraint of global buckling modes, while further increases due to closer connector spacing are attributed to a reduction of the wavelength of the distortional buckles and to the mobilisation of composite action between the boards and the column.

Decreasing the fastener spacing was found to lead to significant improvements in terms of ultimate capacity and stiffness under all loading configurations, with up to about 7% and 8% increase in capacity and stiffness respectively for specimens in pure compression and up to about 20% and 15% increase in capacity and stiffness respectively for specimens in pure bending when decreasing connector spacing from 600 mm to 75 mm. Finally, the characteristics of the end tracks as well as the strength of the stud-to-track connections were found to have the potential to significantly affect the response of the examined systems, limiting their ultimate capacity. Recommendations on the choice of the end tracks and stud-to-track connection were therefore made to secure the efficient performance of sheathed cold-formed steel stud wall systems. Development of preliminary design rules that recognise the restraint, end fixity and potential composite action present in sheathed cold-formed steel wall systems, supported by the test results from Chapter 5 and the findings presented in this chapter, are presented in the next Chapter 7.

Chapter 7

Preliminary design recommendations for sheathed cold-formed steel beam-columns

7.1 Introduction

STRUCTURAL design rules for sheathed cold-formed steel studs under combined compression and major axis bending are devised, presented and assessed in the current chapter, based on the experimental and numerical findings. The set of rules provided offers a preliminary design methodology for cold-formed steel wall systems, which is based on the design methodology of EN 1993-1-3 (2006), but harnesses structurally the presence of sheathing. In the proposed approach, the additional capacity gains brought by a stronger connection (due to increased number of fixings) between the sheathing and the stud are also recognised. The increased capacities predicted by the proposed design are attributed to the recognition of four factors: restraint to the global buckling modes, fixity of boundary conditions under compression, a convex shape for the interaction curve under combined loading and potential for mobilisation of composite action between the sheathing and steel under pure bending. Limitations on the system capacity depend on the demand and resistance of the screw connectors between the sheathing and the steel; recommendations are provided.

The chapter begins by introducing the current design methodologies, with the main focus being on the Eurocode approach, where a detailed overview of the effective width method and member design is provided, but also with a brief discussion on the direct strength method (Schafer 2008) and its application to sheathed stud walls as described in the research work by Vieira & Schafer (2013) and Peterman & Schafer (2014). Assessment of these existing design methodologies against the test data reported in Chapter 5 is provided. The design rules proposed herein are then introduced and comparisons against the experimental and parametric finite element (FE) results reported in Chapters 5 and 6 respectively are made.

7.2 Existing design methods

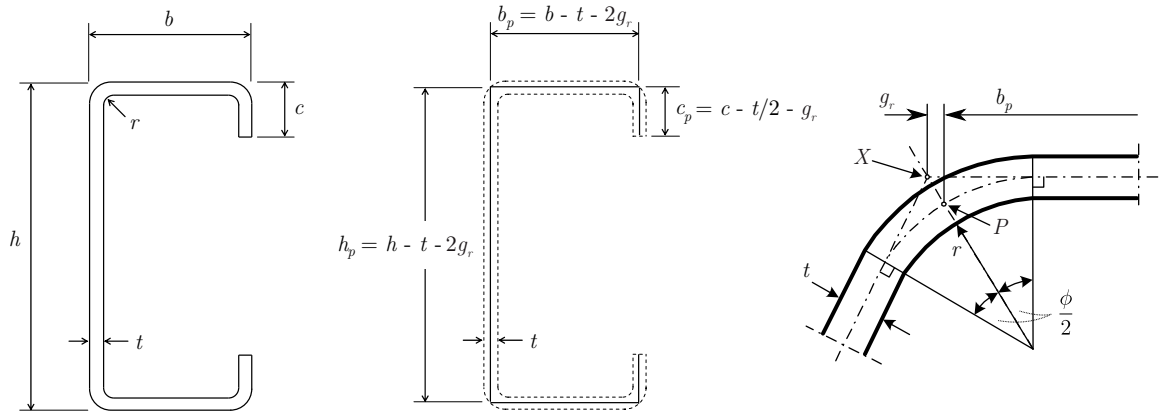
7.2.1 Design of cold-formed steel sections to Eurocode 3

In accordance with Eurocode 3 'Design of Steel Structures' (EN 1993-1-1 2005), where the general design rules for structural steel are described, the design of cold-formed steel members should be undertaken in line with the supplementary EN 1993-1-3 (2006) code, which very frequently refers to EN 1993-1-5 (2006) for details regarding the approach of the effective width method used for the design of steel plated elements suffering local instabilities. Therefore, for the design of cold-formed steel members, consideration of all three standards is required (and of their respective National Annexes), while it is worth mentioning that the presence of sheathing and its influence on the capacity of cold-formed steel members is ignored.

Eurocode 3 (EN 1993-1-3 2006) allows determination of the capacity of cold-formed steel members either through the use of the provided design rules or by physical testing. Although design by the provided rules is relatively complex and leads to conservative results, it remains the preferred design method for cold-formed steel members of relatively simple shape, such as C-shaped lipped studs (Way & Heywood 2012).

7.2.1.1 Effective section properties

In accordance with the EN 1993-1-3 (2006) design guidance rules, when calculating effective section properties from the gross section properties the three following issues need to be addressed: the core steel thickness, the use of midline theory and the impact of the corner radii on the sections. Cold-formed steel sections are typically galvanised with a zinc coating of 275 g/m^3 (referred to as Z275) but under the design rules of EN 1993-1-3 (2006), cross-sectional capacities should be calculated using the core thickness t of the member, excluding the thickness of the zinc coating surface. In design, the nominal (specified) thickness is reduced to the core thickness by subtracting 0.04 mm (EN 1993-1-3 2006). Following calculation of the core thickness, the section properties of cold-formed steel members can be determined based on an idealised sharp-corner cross-section composed of flat elements concentrated along the mid-lines of the actual plate elements. The idealised cross-section and respective notations for a lipped channel section are illustrated in Figure 7.1. To avoid



(a) Actual section (b) Idealised section (b) Rounded corner

Figure 7.1: Mid-line theory for a C-lipped section where (a) is the actual section, (b) is the idealised section and (c) is a detail of the rounded corner. Adapted from EN 1993-1-3 (2006)

double counting the overlapping of corner regions, the notional flat widths (such h_p, b_p and c_p shown in Figure 7.1 (b)) should be measured to the true intersection point P between adjacent elements, a distance g_r from X, given by Equation (7.1), as illustrated in Figure 7.1 (c), where r is the radius, t is the core thickness and ϕ is the angle illustrated in Figure

7.1 (c).

$$g_r = \left(r + \frac{t}{2}\right)\left(\left(\tan\frac{\phi}{2}\right) - \sin\left(\frac{\phi}{2}\right)\right) \tag{7.1}$$

In accordance with EN 1993-1-3 (2006), the influence of rounded corners may be ignored if $r \leq 5t$ and $r \leq 0.1b_p$, where b_p is the notional width. Since the midline theory assumes an idealised cross-section, the impact of the corner radii can be significant if ignored, therefore when the influence of radii is deemed significant (where the stated limits above are exceeded) then a reduction of the area, the second moment of area and the warping constant is performed by applying the factors reported in Clause 5.1(4) of EN 1993-1-3 (2006). This is also applicable to the calculation of the respective effective properties, assuming the notional flat widths of the plane elements are measured to the points of intersection of their midlines.

7.2.1.1.1 Local buckling

The local buckling mode shapes of a lipped channel section under pure compression and pure bending about the major axis are illustrated in Figures 7.2 (a) and 7.3 (a) respectively. In accordance with EN 1993-1-3 (2006), local buckling of cold-formed steel sections is treated by adopting the effective width concept. The cross-section is divided into elements, as illustrated in Figure 7.1, with each element treated as a flat plate. For each element subjected to compressive stress, either due to axial compression or bending, the effective width (h_{eff}, b_{eff} and c_{eff} for the web, flange and lip respectively) is determined by multiplying the appropriate width of each element (h_p, b_p and c_p for the web, flange and lip respectively) with the reduction factor ρ. Details of the method and the relevant equations can be found in EN 1993-1-5 (2006). For an internal element (such as a flange or a web for the shapes shown in Figures 7.2 and 7.3), ρ is given by Equation (7.2):

$$\rho = \frac{\overline{\lambda}_p - 0.055(3+\psi)}{\overline{\lambda}_p^2} \leq 1.0 \tag{7.2}$$

while for an outstand element (such as a lip for the shapes shown in Figures 7.2 and 7.3), ρ is given by Equation (7.3):

$$\rho = \frac{\overline{\lambda}_p - 0.188}{\overline{\lambda}_p^2} \leq 1.0 \tag{7.3}$$

where ψ is the stress ratio between the edges of the element and $\overline{\lambda}_p$ is the slenderness of the element calculated using Equation (7.4).

$$\overline{\lambda}_p = \sqrt{\frac{f_y}{\sigma_{cr}}} = \frac{\overline{b}/t}{28.4\varepsilon\sqrt{k_\sigma}} \tag{7.4}$$

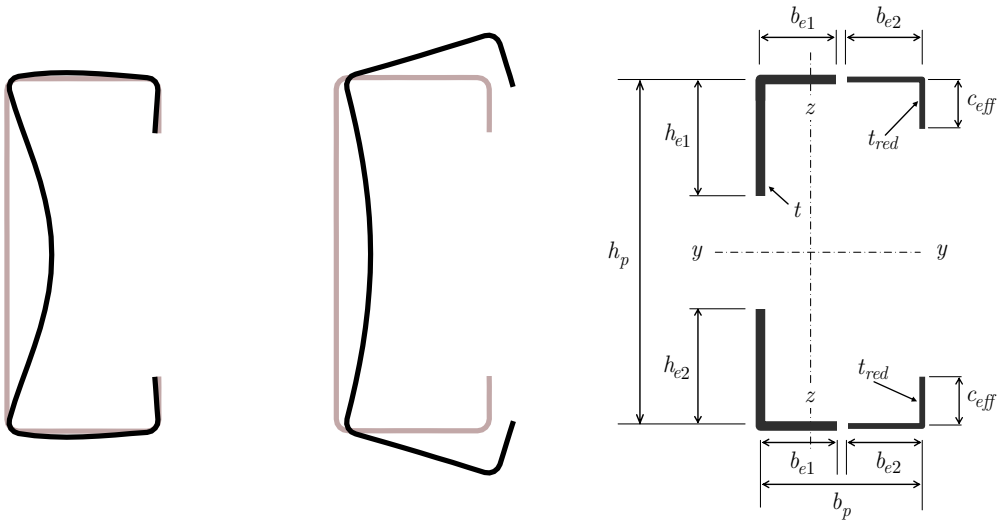
In Equation (7.4), f_y is the design yield strength, σ_{cr} is the elastic buckling stress, $\overline{b}$ is the appropriate width of the element in compression (with respect to Table 5.2 of EN 1993-1-1 (2005)), t is the core thickness, $\varepsilon = \sqrt{235/f_y}$ and k_σ is a buckling factor accounting for the stress ratio ψ and the element boundary conditions (i.e. internal or an outstand element). Values of k_σ should be obtained from Tables 4.1 and 4.2 of EN 1993-1-5 (2006), while background theory is provided by Trahair et al. (2008) and Timoshenko & Gere (1961).

The effective section properties of a member subjected to compression will differ from those subjected to bending due to the different distribution of compressive stresses across the section between these two cases. Illustrations of effective cross-sectional geometries under pure compression and major axis bending are provided in Figures 7.2 (c) and 7.3 (c) respectively. Note, that $b_{e1} = b_{e2} = 0.5b_{eff}$ and $h_{e1} = h_{e2} = 0.5h_{eff}$ for cross-sections under pure compression, while for cross-sections under bending h_{e1} and h_{e2} are dependent on the position of the neutral axis (N.A.) which shifts towards the part of cross-section in tension as shown in Figure 7.3 (c).

7.2.1.1.2 Distortional buckling

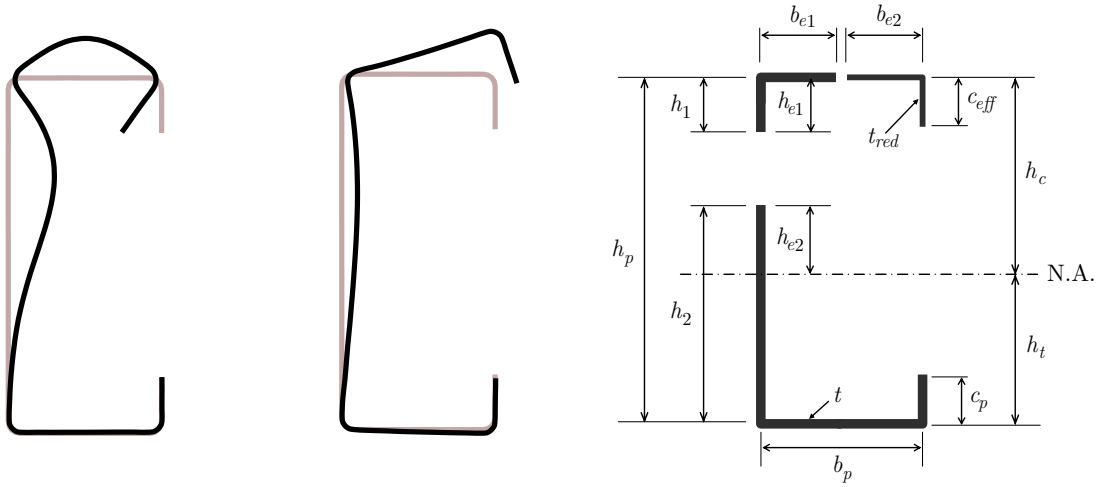
The distortional buckling mode shapes of a lipped channel section under pure compression and pure bending about the major axis are illustrated in Figures 7.2 (b) and 7.3 (b) respectively. In accordance with EN 1993-1-3 (2006), distortional buckling of cold-formed steel sections is treated by adopting an effective thickness approach, imposed on the stiffened region of the cross-section susceptible to this form of buckling.

To prevent or delay local and distortional buckling in cold-formed steel members, stiffeners are typically introduced by manufacturers, to permit the use of even thinner gauge steel (Way & Heywood 2012). For a channel section (stud), stiffeners are typically introduced in



(a) Local buckling mode (b) Distortional buckling mode (c) Effective cross-section

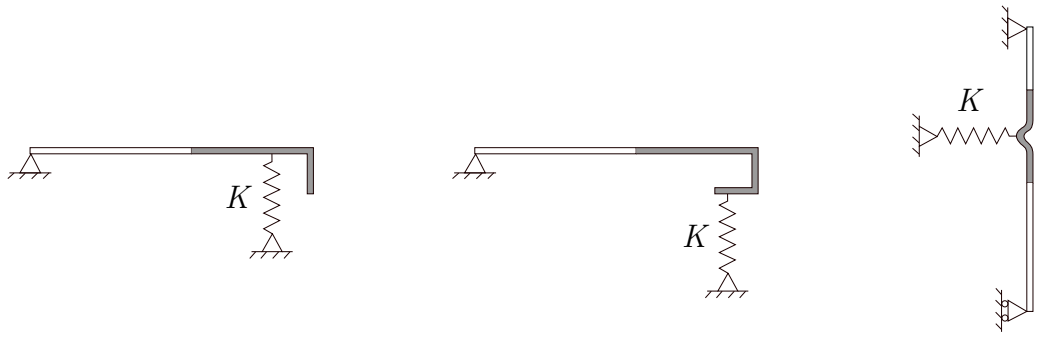
Figure 7.2: The (a) local and (b) distortional buckling modes of a C-lipped section under compression and (c) the theoretical effective cross-section



(a) Local buckling mode (b) Distortional buckling mode (c) Effective cross-section

Figure 7.3: The (a) local and (b) distortional buckling modes of a C-lipped section under bending about major axis and (c) the theoretical effective cross-section

the form of 'lips' at the ends of free flanges to stiffen them up. Stiffening the end flanges is usually performed either with single fold lips (which is the most common practice) or double fold lips as shown in Figures 7.4 (a) and (b) respectively. Intermediate stiffeners (see Figure 7.4 (c)) for the web or flanges are not as common for members used in framing applications but are readily employed in deep purlin members or floor joists (Kyvelou et al. 2017*b*, 2020, Way & Heywood 2012).



(a) Single fold edge stiffener (b) Double fold edge stiffener (c) Intermediate stiffener

Figure 7.4: Equivalent linear spring model assumed by EN 1993-1-3 (2006) to replicate the distortional mode at (a) an edge lip, (b) an edge double lip and (c) an intermediate stiffener

EN 1993-1-3 (2006) design caters for all types of stiffeners presented in Figure 7.4 by assuming that a compression element with a stiffener behaves like a compression member with a continuous partial restraint to displacement. This restraint is represented by a linear spring of stiffness K as illustrated in Figure 7.4. The spring stiffness depends on the boundary conditions and the flexural stiffness of the adjacent plate elements, while the spring with a stiffness K is assumed to be acting on the centroid of the stiffener.

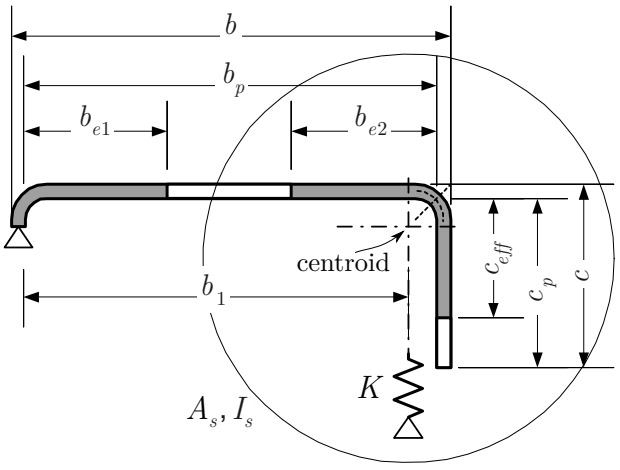


Figure 7.5: Equivalent dimensions for a flange with a single edge stiffener in compression. Adapted from EN 1993-1-3 (2006).

For the case of a single fold edge stiffener, as shown in Figure 7.5, the spring stiffness

K can be obtained using Equation (7.5):

$$K = \frac{Et^3}{4(1-v^2)(b_1^2\, h_p + b_p^3 + 0.5\, b_1 b_2\, h_p\, k_f)} \tag{7.5}$$

where

E is the Young's modulus of steel

t is the core thickness

v is the Poisson's ratio of steel (taken as 0.3)

b_1 and b_2 are the respective distances for the two flanges of a channel section, from the web-to-flange junction to the centroid of the effective area of the edge stiffener (which includes the lip of length c_{eff} and the effective area of the flange adjacent to the stiffener of length b_{e2}), as illustrated in Figure 7.5.

h_p is the depth of the web, as shown in Figures 7.2 and 7.3.

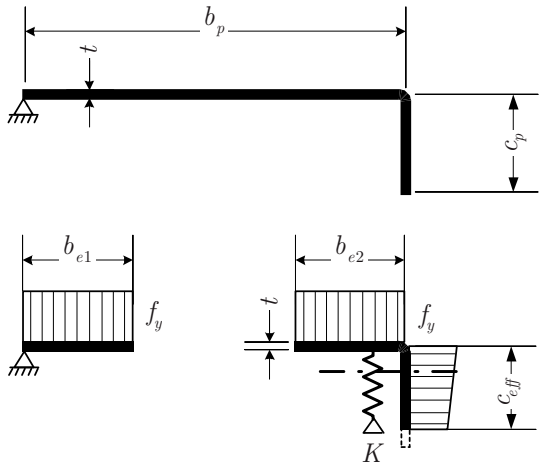
k_f is the ratio of the effective areas of the two edge stiffeners (including the effective portion of the flange), i.e. $k_f = A_{s2}/A_{s1}$, where A_{s2} and A_{s1} are the effective areas of the two edge stiffeners in a channel lipped cross-section. For symmetric channel lipped sections in compression, as shown in Figure 7.2, $k_f = 1$. For symmetric channel lipped sections in bending about the major axis, as shown in Figure 7.3, $k_f = 0$.

Following the guidance of EN 1993-1-3 (2006), once the equivalent spring stiffness K of the stiffener is calculated, the elastic critical stress for the stiffener $\sigma_{cr,s}$ can then be calculated, followed by the determination of the relative distortional slenderness $\overline{\lambda}_d$ and the reduction factor of the distortional buckling resistance χ_d. Finally, the reduction factor χ_d is used to determine a reduced effective area of the stiffener, which is implemented by means of a reduced thickness t_{red}. A detailed procedure for determining t_{red} follows.

The procedure described below is for a flange with a single fold edge stiffener (a lip). It is divided into three steps, the last of which involves an optional iteration in order to refine the value of the reduction factor χ_d.

Step 1: Calculation begins with the determination of effective widths, as described in Section 7.2.1.1.1. At this step (see Figure 7.6), the edge stiffener is assumed to be infinitely

stiff and, as such, to provide full restraint to the free end of the flange. The corners are therefore assumed fixed in position and failure is due to local buckling only. The maximum compressive stress $\sigma_{com,Ed}$ in the flange is assumed to be equal to the design strength f_y of the material.



Gross cross-section and boundary conditions

Step 1: Effective cross-section for K = ∞ based on $\sigma_{com,Ed} = f_y$

Figure 7.6: Effective properties of an edge stiffener, Step 1. Adapted from EN 1993-1-3 (2006).

Step 2: In the second step (See Figure 7.7), the edge stiffener is considered in isolation. The infinitely stiff spring in Step 1 is replaced by a spring with a stiffness K, which can be calculated by Equation (7.5), using the initial effective cross-section determined in Step 1. Then, the elastic critical buckling stress $\sigma_{cr,s}$ of the stiffener can be calculated using Equation (7.6), where I_s is the effective second moment of area of the stiffener and A_s is the effective cross-sectional area of the stiffener.

$$\sigma_{cr,s} = \frac{2\sqrt{KEI_s}}{A_s} \tag{7.6}$$

Once the critical buckling stress $\sigma_{cr,s}$ of the stiffener is calculated, the relative slenderness of the stiffener for distortional buckling $\overline{\lambda}_d$ may be determined using Equation (7.7).

$$\overline{\lambda}_d = \sqrt{\frac{f_y}{\sigma_{cr,s}}} \tag{7.7}$$

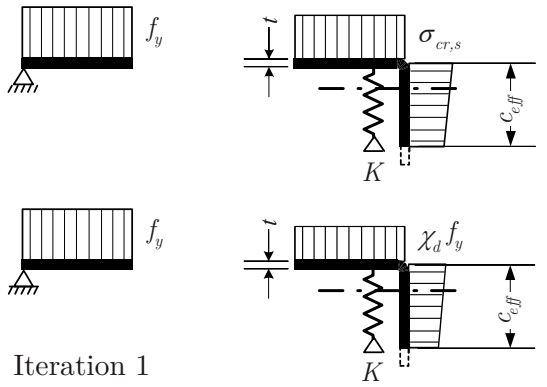
Based on the calculated $\overline{\lambda}_d$, the reduction factor for distortional buckling χ_d can then be

determined using Equations (7.8) - (7.10).

$$\text{For} \quad \overline{\lambda}_d \leq 0.65, \quad \chi_d = 1.0 \tag{7.8}$$

$$\text{For} \quad 0.65 \leq \overline{\lambda}_d \leq 1.38, \quad \chi_d = 1.47 - 0.723\overline{\lambda}_d \tag{7.9}$$

$$\text{For} \quad \overline{\lambda}_d > 1.38, \quad \chi_d = 0.66/\overline{\lambda}_d \tag{7.10}$$



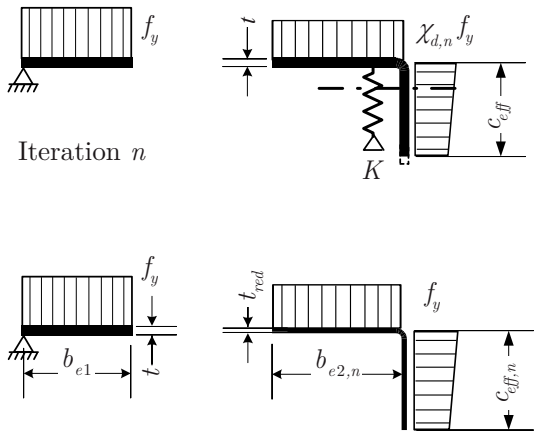
Step 2: Calculation of elastic critical buckling stress $\sigma_{cr,s}$ based on K and properties of stiffener I_s and A_s

Reduced strength $\chi_d f_y$ for effective stiffener of area A_s

Figure 7.7: Effective properties of an edge stiffener, Step 2. Adapted from EN 1993-1-3 (2006).

Step 3: As shown in Figure 7.8, the value of χ_d may be refined by returning to Step 1 and calculating modified effective widths (b_{eff} and c_{eff}) based on a revised compressive stress $\sigma_{com,Ed} = \chi_d f_y$. This is achieved by calculating modified values of ρ for Equations (7.2) and (7.3), using a reduced element slenderness $\overline{\lambda}_{p,red}$ given by Equation (7.11).

$$\overline{\lambda}_{p,red} = \overline{\lambda}_p \sqrt{\chi_d} \tag{7.11}$$



Step 3: Optionally repeat step 1 by calculating modified effective widths with a reduced element slenderness, calculated with $\sigma_{com,Ed,i} = \chi_d f_y$ with χ_d from previous, iteration and continuing until:

$$\chi_{d,n} \approx \chi_{d,(n-1)} \text{ but } \chi_{d,n} \leq \chi_{d,(n-1)}$$

Adopt an effective cross-section with b_{e2}, c_{eff} and reduced thickness t_{red} corresponding to $\chi_{d,n}$

Figure 7.8: Effective properties of an edge stiffener, Step 3. Adapted from EN 1993-1-3 (2006).

Then, Step 2 may be repeated to obtain a modified effective section and a new value of χ_d. The whole process can be repeated again, for n times, until the desired degree of convergence on the value χ_d has been achieved.

Finally, once the final value of χ_d has been calculated to the desired accuracy, the reduced effective cross-sectional area of the stiffener is implemented by means of a uniformly reduced thickness t_{red} using Equation (7.12).

$$t_{red} = \chi_d t \tag{7.12}$$

In Appendix A, the calculation of gross and effective properties for a set of typical lipped channel sections in accordance with the Eurocode 3 methodology (EN 1993-1-3 2006) is presented. Recommended sources of worked examples illustrating in detail the calculation of effective properties for lipped channel sections include the guidance of ECCS (2008) and Way & Heywood (2012).

7.2.1.2 Design resistances

7.2.1.2.1 Compression resistance

The resistance of a Class 4 (as per EN 1993-1-1 (2005) classification) cross-section under compression $N_{c,Rd}$ is calculated with Equation (7.13), where A_{eff} is the effective area of the cross-section calculated as described in the previous section so that the effects of local and distortional buckling are taken into account, and f_y is the yield strength of steel (EN 1993-1-3 2006).

$$N_{c,Rd} = A_{eff} f_y \tag{7.13}$$

An unrestrained member under compression may be prone to flexural, torsional and flexural-torsional buckling, depending on its geometry and member slenderness. The design buckling resistance of a ('Class 4' as per EN 1993-1-1 (2005)) member under compression is

given by Equation (7.14), where χ is the reduction factor for the relevant buckling mode.

$$N_{b,Rd} = \chi A_{eff} f_y \tag{7.14}$$

The reduction factor χ is used to determine the reduction in resistance below the cross-sectional compression capacity (or the squash load) of a member due to global buckling. The value of χ may be obtained from EN 1993-1-1 (2005) using the appropriate buckling curve in conjunction with the value of non-dimensional slenderness $\overline{\lambda}$ corresponding to either flexural, torsional or flexural-torsional buckling. EN 1993-1-1 (2005) offers five different buckling curves depending on the imperfection factor assumed, but this choice, in accordance with EN 1993-1-3 (2006), is restricted to only three curves (a, b and c) for cold-formed steel members. The relationship between the reduction factor χ and non-dimensional slenderness $\overline{\lambda}$ for buckling curves a, b and c is shown in Figure 7.9.

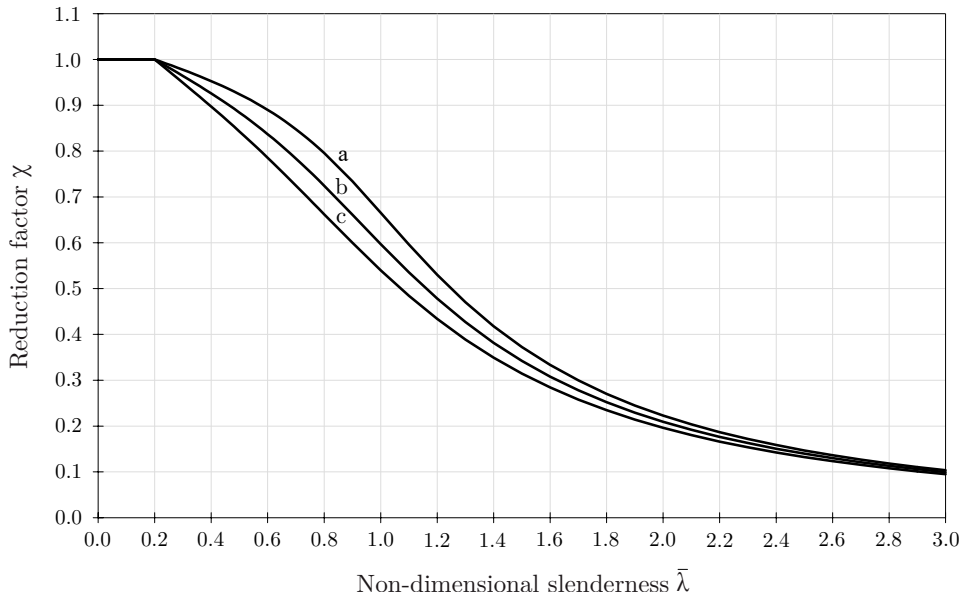


Figure 7.9: Buckling curves a, b and c. Adapted from EN 1993-1-3 (2006).

The value of χ may be calculated directly using Equations (7.15) and (7.16), where α is the imperfection factor corresponding to the relevant buckling curve. For buckling curves a, b and c, $\alpha = 0.21$, 0.34 and 0.49 respectively (EN 1993-1-3 2006). For cold-formed steel channel lipped sections, the appropriate buckling curve to use, for buckling about any axis

in accordance with EN 1993-1-3 (2006), is b and as such $\alpha = 0.34$.

$$\chi = \frac{1}{\Phi + \sqrt{\Phi^2 - \overline{\lambda}^2}} \qquad \text{but} \quad \chi \leq 1.0 \tag{7.15}$$

$$\text{where} \qquad \Phi = 0.5\left[1 + \alpha\left(\overline{\lambda} - 0.2\right) + \overline{\lambda}^2\right] \tag{7.16}$$

The non-dimensional slenderness $\overline{\lambda}$ is given by Equation (7.17), where N_{cr} is the elastic critical load.

$$\overline{\lambda} = \sqrt{\frac{A_{eff} f_y}{N_{cr}}} \tag{7.17}$$

For flexural buckling, N_{cr} is equal to the Euler load and is given by Equation (7.18), where E is the Young's modulus of steel, I is the appropriate second moment of area and L_{cr} is the effective buckling length considered. To calculate the flexural buckling resistance about the major axis $N_{b,y,Rd}$, $N_{cr} = N_{cr,y}$, the gross second moment of area about the major axis I_y is considered and the effective buckling length about the major axis is defined as $L_{cr,y}$. To calculate the flexural buckling resistance about the minor axis $N_{b,z,Rd}$, $N_{cr} = N_{cr,z}$, the gross second moment of area about the minor axis I_z is considered and the effective buckling length about the minor axis is defined as $L_{cr,z}$. The effective lengths $L_{cr,y}$ and $L_{cr,z}$ are dependant on the boundary conditions and the presence of restraints about the relevant axis.

$$N_{cr} = \frac{\pi^2 EI}{L_{cr}^2} \tag{7.18}$$

For torsional buckling, $N_{cr} = N_{cr,T}$ and can be calculated using Equation (7.19):

$$N_{cr,T} = \frac{1}{i_o^2}\left(GI_t + \frac{\pi^2 EI_w}{L_T^2}\right) \tag{7.19}$$

$$\text{with} \qquad i_o^2 = i_y^2 + i_z^2 + y_o^2 + z_o^2 \tag{7.20}$$

For flexural-torsional buckling, $N_{cr} = N_{cr,FT}$ and can be calculated using Equation (7.21):

$$N_{cr,FT} = \frac{i_o^2}{2\left(i_y^2 + i_z^2\right)}\left(N_{cr,y} + N_{cr,T} - \sqrt{\left(N_{cr,y} + N_{cr,T}\right)^2 - 4N_{cr,y}N_{cr,T}\frac{i_y^2 + i_z^2}{i_o^2}}\right) \tag{7.21}$$

In Equations (7.19), (7.20) and (7.21), G is the shear modulus of steel, I_t is the torsional constant, I_w is the warping constant, L_T is the buckling length regarding the torsional mode (typically taken as equal to the system length L in the absence of restraints and for pinned ends or as $0.7L$ when significant restraint against torsion and warping exists at the ends (EN 1993-1-3 2006)), i_y and i_z are the radii of gyration of the cross-section about the major and minor axis respectively, and finally y_o and z_o are the horizontal and vertical coordinates, respectively, of the shear centre with respect to the centroid (for a doubly symmetric section, the centroid coincides with the shear centre, i.e. $y_o = 0$ and $z_o = 0$, while for a singly symmetric section, like a channel lipped section, only $z_o = 0$). Further information on the critical axial load for torsional and flexural-torsional buckling can be found in NCCI SN001a (2005), EN 1993-1-3 (2006) and in the work of Timoshenko & Gere (1961).

Note that in accordance with EN 1993-1-1 (2005), $N_{c,Rd}$ and $N_{b,Rd}$ are also divided by a γ_M safety factor, which is not included in the above expressions. In accordance with the UK national annex provisions, the γ_M safety factor, for these expressions is equal to unity.

The buckling resistance of a member in compression can also be expressed in terms of Equation 7.22:

$$N_{b,Rd} = \min(N_{c,Rd}, N_{b,y,Rd}, N_{b,z,Rd}, N_{b,T,Rd}, N_{b,FT,Rd}) \tag{7.22}$$

7.2.1.2.2 Bending resistance

The cross-sectional resistance of a Class 4 (as per EN 1993-1-1 (2005) classification) cold-formed steel member subjected to bending is given by Equation (7.23), where W_{eff} is the elastic section modulus of the effective cross-section about the relevant axis in accordance with the guidance in Section 7.2.1.1 so that the effects of local and distortional buckling are taken into account.

$$M_{c,Rd} = W_{eff} f_y \tag{7.23}$$

For the cross-sectional bending resistance about the major axis, as shown in Figure

7.3 (c), $M_{c,Rd} = M_{c,y,Rd}$ and $W_{eff} = W_{y,eff}$, which is the elastic section modulus of the effective cross-section calculated with respect to the most extreme fibre from the neutral axis (i.e. the minimum value of $W_{y,eff}$, given by $I_{y,eff}/h_c$, where $I_{y,eff}$ is the second moment of area of the effective cross-section in bending about the major axis and h_c is the distance from the neutral axis to the most extreme fibre as shown in Figure 7.3 (c)). Likewise, to calculate the cross-sectional bending resistance about the minor axis, $M_{c,Rd} = M_{c,z,Rd}$ and $W_{eff} = W_{z,eff}$, with the elastic effective section modulus calculated with respect to the fibre with the maximum elastic stress.

A member that is subjected to major axis bending and is not adequately restrained may be prone to lateral-torsional buckling, depending on its geometry and its member slenderness. The essential feature of this global mode of failure, for a member in major axis bending, is that the compression flange becomes unstable and, since it is not restrained, it attempts to buckle laterally but, because it is attached to the flange in tension, through its web, it cannot move freely. The resistance offered by the flange in tension results to a combination of both lateral and torsional buckling. This effect only occurs when the member is under major axis bending. Lateral-torsional buckling is analogous to a column under compression and, as such, the buckling curves shown in Figure 7.9 are equally applicable. The buckling resistance $M_{b,Rd}$ of a member in major axis bending is given by Equation (7.24),

$$M_{b,Rd} = \chi_{LT} W_{y,eff} f_y \tag{7.24}$$

where χ_{LT} is the reduction factor due to lateral-torsional buckling given by Equations (7.25) and (7.26).

$$\chi_{LT} = \frac{1}{\Phi_{LT} + \sqrt{\Phi_{LT}^2 - \overline{\lambda}_{LT}^2}} \qquad \text{but} \quad \chi_{LT} \leq 1.0 \tag{7.25}$$

$$\text{where} \qquad \Phi_{LT} = 0.5 \left[1 + \alpha_{LT} \left(\overline{\lambda}_{LT} - 0.2\right) + \overline{\lambda}_{LT}^2\right] \tag{7.26}$$

In accordance with Clause 6.2.4 of EN 1993-1-3 (2006), cold-formed steel members in bending should use buckling curve b and as such the imperfection factor $a_{LT} = 0.34$. The non-dimensional slenderness due to lateral-torsional buckling $\overline{\lambda}_{LT}$ may be calculated using

Equation (7.27), where M_{cr} is the elastic critical moment for lateral-torsional buckling.

$$\overline{\lambda}_{LT} = \sqrt{\frac{W_{y,eff} f_y}{M_{cr}}} \tag{7.27}$$

A general expression for the elastic critical moment for lateral torsional buckling M_{cr} is given by Equation (7.28):

$$M_{cr} = C_1 \frac{\pi^2 E I_z}{(kL_{LT})^2 g} \left(\sqrt{\left(\frac{k}{k_w}\right)^2 \frac{I_w}{I_z} + \frac{(kL_{LT})^2 G I_t}{\pi^2 E I_z} + (C_z z_g)^2} - C_2 z_g \right) \tag{7.28}$$

where

C_1 and C_2 are coefficients dependent on the shape of the bending moment diagram. For a uniform bending moment diagram in pinned boundary conditions $C_1 = 1.127$ and $C_2 = 0.454$ – see NCCI SN003b (2005).

k is an effective length parameter for end rotation on plan, taken as one when both flanges are free to rotate on plan (as assumed for a stud set in tracks in pure bending).

k_w is an effective length parameter for end warping, typically taken as one (as assumed for a stud set in tracks in pure bending).

I_z is the gross second moment of area about the minor axis of the section

L_{LT} is the member length (assumed unrestrained)

g allows for in-plane curvature of the beam prior to buckling and is given by $g = \sqrt{1 - \frac{I_z}{I_y}}$ or may conservatively be taken as unity.

z_g is the distance between the point of the applied load and the shear centre of the section; the value is positive for destabilizing loads applied above the shear centre. For singly-symmetric channel lipped sections, z_g is taken as half the depth of the cross-section.

For more details on the elastic critical moment M_{cr} and its parameters, information can be found in the non-conflicting and complementary information technical documents NCCI SN003b (2005) and NCCI SN002a (2005), as well as in the work by Gardner (2011). The LTBeamN software (Kyprianou 2015) may also be used to calculate the elastic critical bending moment for a variety of complex scenarios, including variable load on the member,

change of geometry along the member length and the presence of restraints.

It is worth noting that sheathing attached to a stud member subjected to bending is typically able to restrain lateral-torsional buckling, assuming the sheathing-to-steel connection does not fail. Nevertheless, checks should be made for the length of the spacing between connectors.

Similarly to the compression resistances, in accordance with design in EN 1993-1-1 (2005), the bending resistances stated above, are divided by a γ_M safety factor, which is not included in the expressions above; in accordance with the UK national annex provisions, this γ_M factor is equal to one.

7.2.1.2.3 Shear buckling resistance

Following the guidance in Clause 6.1.5 of EN 1993-1-3 (2006), the shear buckling resistance $V_{b,Rd}$ of a member is given by Equation (7.29), where h_w is the height of the web between the mid-lines of the flanges, ϕ is the slope of the web relative to the flanges (for a channel lipped section this is orthogonal, i.e. 90°), t is the steel core thickness and f_{bv} is the shear strength allowed for buckling of the web.

$$V_{b,Rd} = \frac{h_w}{\sin\phi} t f_{bv} \tag{7.29}$$

The susceptibility of a cold-formed steel section to shear buckling is dependent on the slenderness of its web $\overline{\lambda}_w$; deeper members are therefore more prone to this form of buckling. Shear buckling is considered in design by the use of f_{bv}, which is a function of the yield strength f_y and the relative web slenderness $\overline{\lambda}_w$; values of f_{bv} can be obtained from Table 6.1 of EN 1993-1-3 (2006). The γ_M safety factor is not included in Equation (7.29) since it is equal to 1, as per the UK national annex provisions.

7.2.1.2.4 Combined compression and bending

In accordance with EN 1993-1-3 (2006), the cross-sectional combined compression and bending resistance should be determined using Equation (7.30), where N_{Ed} is the effective

design force, $M_{y,Ed}$ is the effective design bending moment about the major axis, $M_{z,Ed}$ is the effective design bending moment about the minor axis and e_N is the shift of the centroid after the calculation of effective properties when the cross-section is subjected to pure compression. For a singly-symmetric section such a channel lipped section $e_{N,y} = 0$, while $e_{N,z}$ is the difference of the position of the minor axis $z - z$ running through the centroid calculated between the gross-sectional area and the effective cross-sectional area, as shown in Figure 7.2 (c) - the centroid shifts towards the web.

$$\frac{N_{Ed}}{N_{c,Rd}} + \frac{M_{y,Ed} + N_{Ed}e_{Ny}}{M_{c,y,Rd}} + \frac{M_{z,Ed} + N_{Ed}e_{Nz}}{M_{c,z,Rd}} \leq 1.0 \tag{7.30}$$

The interaction between axial force and bending moment may be obtained from a second-order analysis of the member based on the properties of the effective cross-section, calculated as described in Section 7.2.1.1. As an alternative though, EN 1993-1-3 (2006) provides Equation (7.31) for the calculation of interaction between compression and bending.

$$\left(\frac{N_{Ed}}{N_{b,Rd}}\right)^{0.8} + \left(\frac{M_{Ed}}{M_{b,Rd}}\right)^{0.8} \leq 1.0 \tag{7.31}$$

Detailed worked examples of the all-steel design of a channel lipped stud member under combined compression and bending, including calculations with all of the above expressions, can be found in the work of Way & Heywood (2012).

7.2.1.3 Comparison with the beam-column test results of the present study

A comparison between the beam-column test results, presented in Chapter 5, and the EN 1993-1-3 (2006) interaction curve given by Equation (7.31) using the resistances calculated as described above, under three different assumptions of restraint, is presented. The interaction curves presented in Figure 5.37 of Chapter 5 are replicated in a normalised format (see Figure 7.10), and with the horizontal test results H_u converted to their equivalent moments M_u (see Figure 7.11).

In Figures 7.10 and 7.11, the axial compressive load P_u is normalised by the squash

load $N_{c,Rd}$, given by Equation (7.13), while the bending moment M_u is normalised by the cross-sectional bending resistance about the major axis $M_{c,y,Rd}$, given by Equation (7.23). In Figure 7.10, where results are presented in terms of axial and horizontal loads, the design moment resistances were converted to their equivalent horizontal loads, for comparison with the test loads, by multiplying them with $8/L$, i.e. $H = M \times 8/L$. The cross-sectional resistances, with geometries as described in Chapter 5, were calculated as follows: $N_{c,Rd} =$ 88.4 kN, $M_{c,y,Rd} = 6.10$ kNm and the equivalent conversion to horizontal force $H_{c,y,Rd} = 20.3$ kN.

In Figure 7.11, where results are presented in an axial load-moment ($P-M$) interaction format, in contrast with the presentation in Figure 7.10 - the test results are those which are converted to equivalent moments for comparison with the bending resistances. The conversion to moments considered the measured fixities presented in Chapter 5 from mid-height deflections shown in Figure 5.31 and from rotations shown in Figure 5.34. Based on the average fixity relationship between fixity and amount of compression load, determined between the two sets of measured fixities, a linear interpolation for the resultant moment between the pinned ($M = HL/8$) and fixed ($M = 5HL/128$) boundary conditions (for the four-point loading scheme - see Figure 5.16), was performed for all the horizontal test results H_u loads at 75%, 50%, 25% of P_u and at pure bending.

As already described in Section 5.5 of Chapter 5, three cases of effective critical lengths about the minor axis $L_{cr,z}$ are considered: the full length of the specimen (2400 mm) and the connector spacings of 600 mm and 75 mm. The torsional buckling length L_T for the calculation of the critical axial force given by Equation (7.19) and the lateral-torsional buckling length L_{LT} for the calculation of the critical moment given by Equation (7.28) are assumed to be equal to $L_{cr,z}$. As shown in both Figures 7.10 and 7.11, assuming no restraint is provided from the sheathing yields, overconservative results, while recognising the restraints provided at the positions of the connectors leads to much more accurate predictions. The accuracy of the resistance predictions, even when the restraint by the sheathing is recognised, is however limited due to lack of recognition of the end fixity in pure compression and of the mobilisation of composite action in pure bending, as well as due

to the concave shape of the interaction resistance curve (arising from the power coefficients). Note that the convex shape of the $P-M$ test results in Figure 7.11 is not as convex when compared to the $P-H$ test results in Figure 7.10, due to the values of the moment being reduced because of the recognition of increased fixity with increasing compression load.

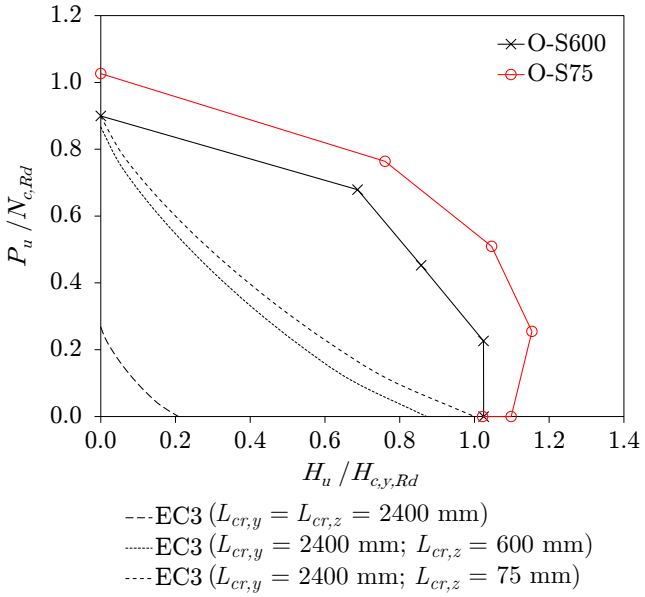


Figure 7.10: Comparison between the beam-column test results from Chapter 5 and EN 1993-1-3 (2006) predictions assuming various effective lengths in a normalised format, in terms of $P_u/N_{c,Rd}$ vs $H_u/H_{c,y,Rd}$

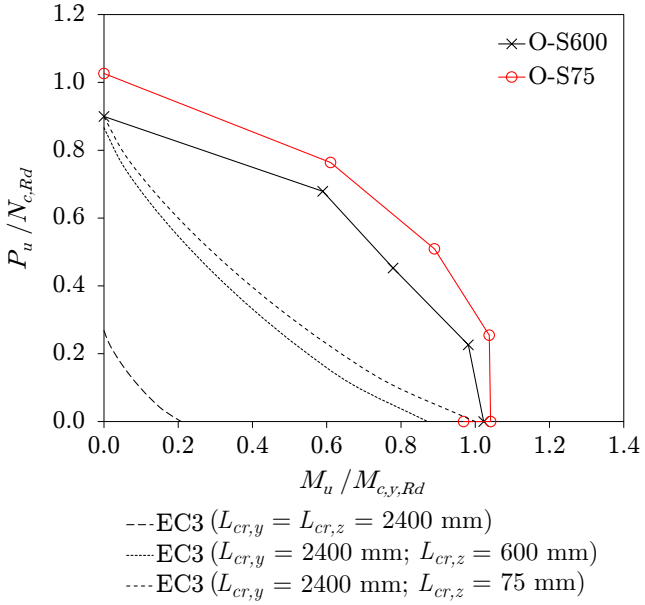


Figure 7.11: Comparison between the beam-column test results from Chapter 5 and EN 1993-1-3 (2006) predictions assuming various effective lengths in a normalised format, in terms of $P_u/N_{c,Rd}$ vs $M_u/M_{c,y,Rd}$

7.2.2 Design of sheathed studs with DSM and recommendations from the literature

According to Vieira & Schafer (2013) and Peterman & Schafer (2014) the restraining effect of the sheathing to the stud can be recognised through the use of linear springs in an elastic buckling analysis when determining compression and bending buckling capacities. The direct strength method can then be used to provide member capacity predictions (Schafer 2013, 2008).

The direct strength method requires the determination of elastic buckling loads (P_{crl} for local, P_{crd} for distortional and P_{cre} for global) and moments (M_{crl} for local, M_{crd} for distortional and M_{cre} for global) through a rational analysis for the subsequent determination of nominal compression P_n and bending M_n capacities respectively. The nominal capacity for compression P_n can be determined by taking the minimum of the nominal axial strength for global buckling P_{ne}, local-global buckling interaction P_{nl} and distortional buckling P_{nd}. The expression for the nominal axial strength for global buckling P_{ne} is given by Equation (7.32), where $P_y = Af_y$, A is the gross cross-sectional area and f_y is the yield strength.

$$P_{ne} = \begin{cases} 0.658^{\lambda_c^2} P_y & \text{for} \quad \lambda_c \leq 1.5 \\ 0.877 P_{cre} & \text{for} \quad \lambda_c > 1.5 \end{cases} \qquad \text{where} \qquad \lambda_c = \sqrt{P_y / P_{cre}} \tag{7.32}$$

The nominal axial strength for local-global buckling interaction P_{nl} is given by Equation (7.33).

$$P_{nl} = \begin{cases} P_{ne} & \text{for} \quad \lambda_l \leq 0.776 \\ \left(1 - 0.15 \left(\frac{P_{crl}}{P_{ne}}\right)^{0.4}\right) \left(\frac{P_{crl}}{P_{ne}}\right)^{0.4} P_{ne} & \text{for} \quad \lambda_l > 0.776 \end{cases} \qquad \text{where} \quad \lambda_l = \sqrt{\frac{P_{ne}}{P_{crl}}} \tag{7.33}$$

The nominal axial strength for distortional buckling P_{nd} is given by Equation (7.34).

$$P_{nd} = \begin{cases} P_y & \text{for} \quad \lambda_d \leq 0.561 \\ \left(1 - 0.25 \left(\frac{P_{crd}}{P_y}\right)^{0.6}\right) \left(\frac{P_{crd}}{P_y}\right)^{0.6} P_y & \text{for} \quad \lambda_d > 0.561 \end{cases} \qquad \text{where} \quad \lambda_d = \sqrt{\frac{P_y}{P_{crd}}} \tag{7.34}$$

The nominal flexural strength M_n is the minimum of M_{ne}, M_{nl} and M_{nd}, which are given below. The expression for the nominal flexural strength for lateral-torsional buckling M_{ne} is given by Equation (7.35), where $M_y = W f_y$, W is the gross elastic cross-section modulus at the extreme fibre and f_y is the yield strength.

$$M_{ne} = \begin{cases} M_{cre} & \text{for} \quad M_{cre} < 0.56 M_y \\ \dfrac{10}{9} M_y \left(1 - \dfrac{10 M_y}{36 M_{cre}}\right) & \text{for} \quad 2.78 M_y \geq M_{cre} \geq 0.56 M_y \\ M_y & \text{for} \quad M_{cre} > 2.78 M_y \end{cases} \tag{7.35}$$

The nominal flexural strength for local-global buckling interaction M_{nl} is given by Equation (7.36).

$$M_{nl} = \begin{cases} M_{ne} & \text{for} \quad \lambda_l \leq 0.776 \\ \left(1 - 0.15 \left(\dfrac{M_{crl}}{M_{ne}}\right)^{0.4}\right) \left(\dfrac{M_{crl}}{M_{ne}}\right)^{0.4} M_{ne} & \text{for} \quad \lambda_l > 0.776 \end{cases} \quad \text{where} \quad \lambda_l = \sqrt{\frac{M_{ne}}{M_{crl}}} \tag{7.36}$$

The nominal flexural strength for distortional buckling M_{nd} is given by Equation (7.37).

$$M_{nd} = \begin{cases} M_y & \text{for} \quad \lambda_d \leq 0.673 \\ \left(1 - 0.22 \left(\dfrac{M_{crd}}{M_y}\right)^{0.5}\right) \left(\dfrac{M_{crd}}{M_y}\right)^{0.5} M_y & \text{for} \quad \lambda_d > 0.673 \end{cases} \quad \text{where} \quad \lambda_d = \sqrt{\frac{M_y}{M_{crd}}} \tag{7.37}$$

For the interaction between compression and bending, a simple linear relationship is adopted (as employed in AISI S100 (2016)) ignoring second-order effects, given by Equation (7.38), where P and M are the applied load and moments respectively.

$$\frac{P}{P_n} + \frac{M}{M_n} \leq 1 \tag{7.38}$$

The method employed to determine the elastic buckling loads (P_{crl} for local, P_{crd} for distortional and P_{cre} for global) and moments (M_{crl} for local, M_{crd} for distortional and M_{cre} for global) is through the use of the finite strip method CUFSM (Li & Schafer 2010). The stiffnesses of the linear springs employed are reported in the work by Peterman & Schafer (2014) and have been derived based on the studies by Peterman (2012) and Vieira & Schafer

(2013). These stiffnesses are appropriate for use with the tests reported in Chapter 5 since the same screw type and size has been employed, as well as the same type and thickness of OSB board, while the steel section is of a similar thickness. Therefore the stiffnesses per fastener, for the lateral and rotational springs adopted, are as follows: $k_x = 971$ N/mm, $k_y = 0.374$ N/mm and $k_\phi = 95,309$ Nmm/rad. The relevant springs (k_x, k_y and k_ϕ) and their positions on the cross-section are illustrated in Figure 7.12.

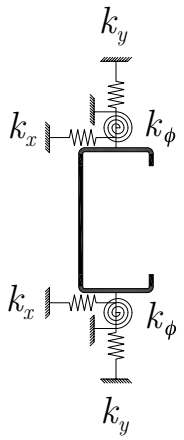


Figure 7.12: Spring on cross-section to simulated the effect of sheathing for use in elastic buckling analysis

7.2.2.1 Comparison with the beam-column test results of the present study

In accordance with the guidance reported by Peterman & Schafer (2014), the per fasteners values need to be divided by the connector spacing for use in CUFSM (Li & Schafer 2010). For the four screw spacings considered of 600 mm, 300 mm, 150 mm and 75 mm, the resultant spring stiffnesses are reported in Table 7.1. The predictions with the equivalent spring stiffnesses are benchmarked against a bare steel DSM prediction, where no stiffeners were employed.

In the elastic buckling analysis, for both compression and bending, pinned end boundary conditions were assumed, to allow for a direct comparison against the results presented in Section 7.2.1.3, yielded using the EN 1993-1-3 (2006) guidance. The cross-sectional geometry and yield strength employed is as reported in Chapter 5.

Table 7.1: Spring stiffnesses for different screw spacings for use in CUFSM of a steel-to-OSB 4.8 mm in diameter screw connection

Description	Screw spacing mm	k_x (N/mm)/mm	k_y (N/mm)/mm	k_ϕ (Nmm/rad)/mm
Bare steel, unbraced	-	-	-	-
600 mm screw spacing	600	1.62	0.000623	159
300 mm screw spacing	300	3.24	0.00125	318
150 mm screw spacing	150	6.47	0.00249	635
75 mm screw spacing	75	12.95	0.00499	1271

Table 7.2: Axial member predictions using CUFSM (Li & Schafer 2010) and DSM

Description	P_{crl}/P_y	L_{crl} mm	P_{crd}/P_y	L_{crd} mm	P_{cre}/P_y	L_{cre} mm	P_y kN	P_n kN
Bare steel, unbraced	0.21	110	0.35	440	0.17	2400	173.0	24.5
600 mm screw spacing	0.21	110	0.38	455	2.15	2400	173.0	75.3
300 mm screw spacing	0.21	110	0.44	470	2.20	2400	173.0	75.5
150 mm screw spacing	0.21	110	0.55	500	2.23	2400	173.0	75.7
75 mm screw spacing	0.21	110	2.96	1150	2.26	2400	173.0	75.8

Table 7.3: Flexural member capacity predictions using CUFSM (Li & Schafer 2010) and DSM

Description	M_{crl}/M_y	L_{crl} mm	M_{crd}/M_y	L_{crd} mm	M_{cre}/M_y	L_{cre} mm	M_y kNm	M_n kNm	H_n kN
Bare steel, unbraced	1.12	80	0.94	340	0.27	2400	7.56	2.05	6.8
600 mm screw spacing	1.12	80	1.00	320	9.85	2400	7.56	5.90	19.7
300 mm screw spacing	1.12	80	1.05	310	10.94	2400	7.56	6.00	20.0
150 mm screw spacing	1.12	80	1.14	290	12.78	2400	7.56	6.18	20.6
75 mm screw spacing	1.12	80	1.27	260	15.73	2400	7.56	6.41	21.4

Results for both compression and bending are provided in Tables 7.2 and 7.3 respectively which summarise the critical loads and moments gathered from the signature curves presented in Figures 7.13 and 7.14 correspondingly. The critical buckling half-wave lengths for local L_{crl}, distortional L_{crd} and global buckling L_{cre} are also reported. Predictions of nominal capacity P_n and M_n using the DSM expressions are also provided in the respect-

ive tables, while for bending, an equivalent horizontal force H_n is also calculated using $H_n = M_n \times 8/L$.

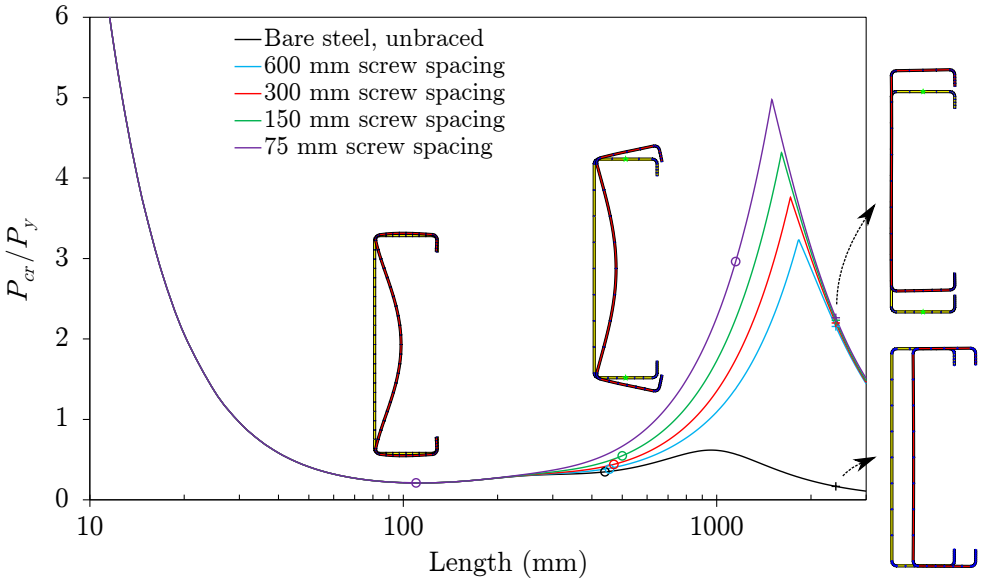


Figure 7.13: Signature curve and deformed shapes for the specimen with geometries and properties tested in Chapter 5 using CUFSM; illustrating critical compression loads versus length for different stiffnesses in accordance with the properties given in Table 7.1

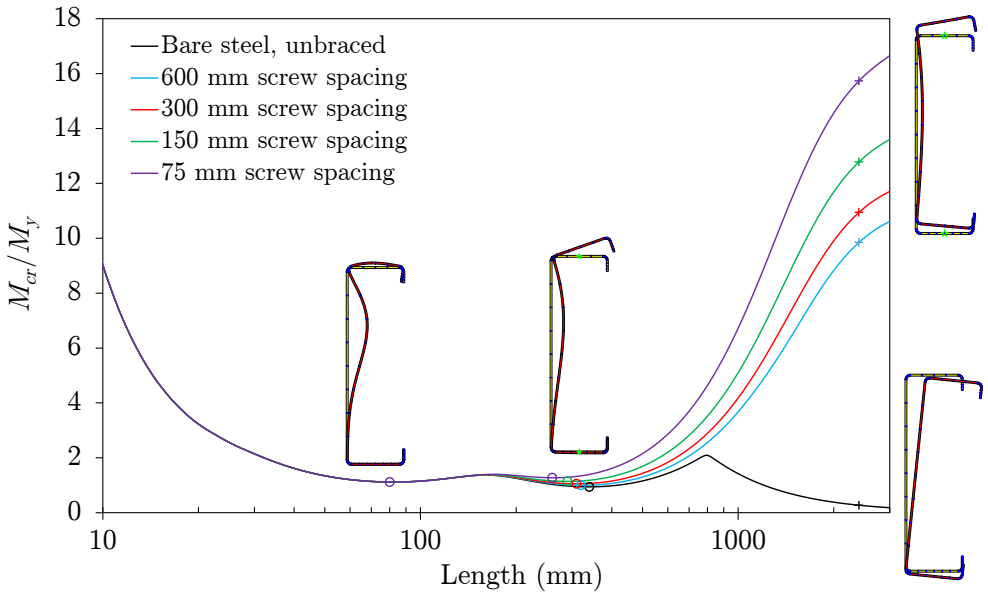


Figure 7.14: Signature curve and deformed shapes for the specimen with geometries and properties tested in Chapter 5 using CUFSM; illustrating critical moments versus length for different stiffnesses in accordance with the properties given in Table 7.1

The DSM linear interaction predictions are compared against the beam-column test data reported in Chapter 5, in terms of axial P_u and horizontal H_u load in Figure 7.15, in a normalised $P_u - H_u$ format in Figure 7.16 and in a normalised axial and bending $P_u - M_u$ format in Figure 7.17. Normalisation and conversion of the test data to bending moments was performed as described in Section 7.2.1.3, to allow for a direct comparison with the EN 1993-1-3 (2006) predictions.

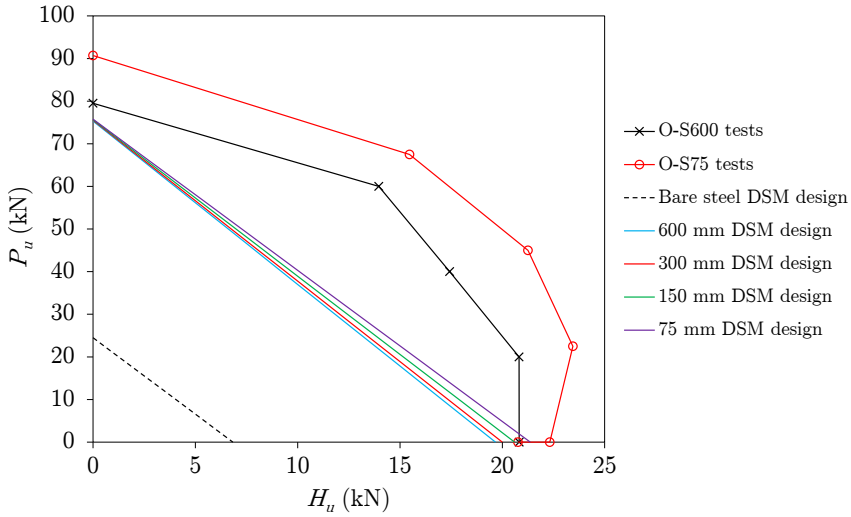


Figure 7.15: Comparisons between linear interaction curves predicted with DSM and Table 7.1 spring stiffnesses in elastic buckling analysis with the beam-column test results from Chapter 5 in terms of axial loads P_u vs horizontal loads H_u

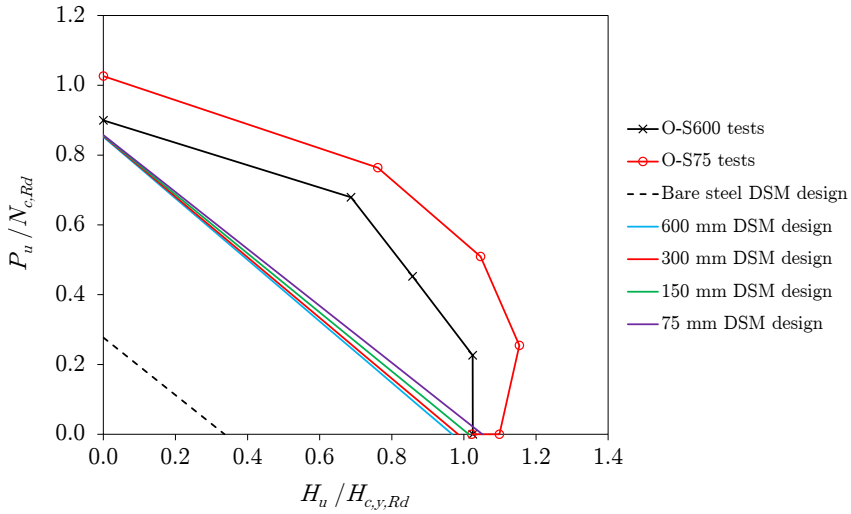


Figure 7.16: Comparisons between linear interaction curves predicted with DSM and Table 7.1 spring stiffnesses in elastic buckling analysis with the beam-column test results from Chapter 5 in a normalised format, in terms of $P_u/N_{c,Rd}$ vs $H_u/H_{c,y,Rd}$

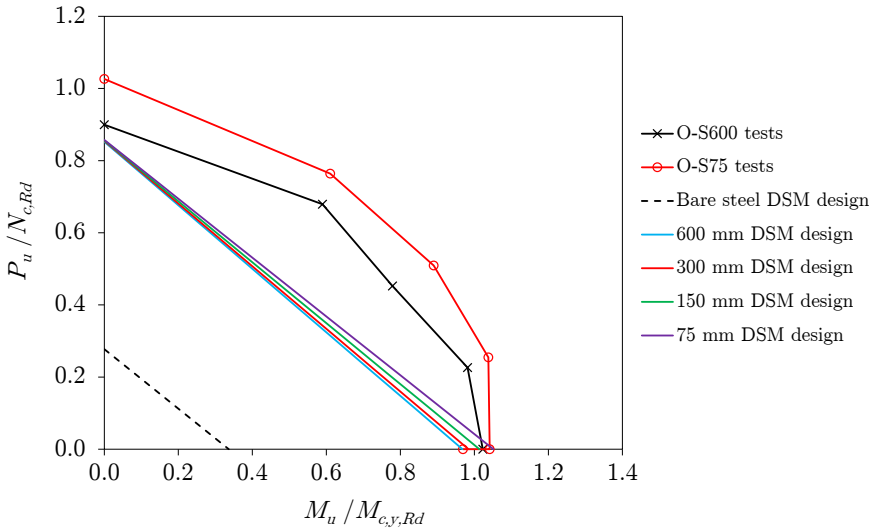


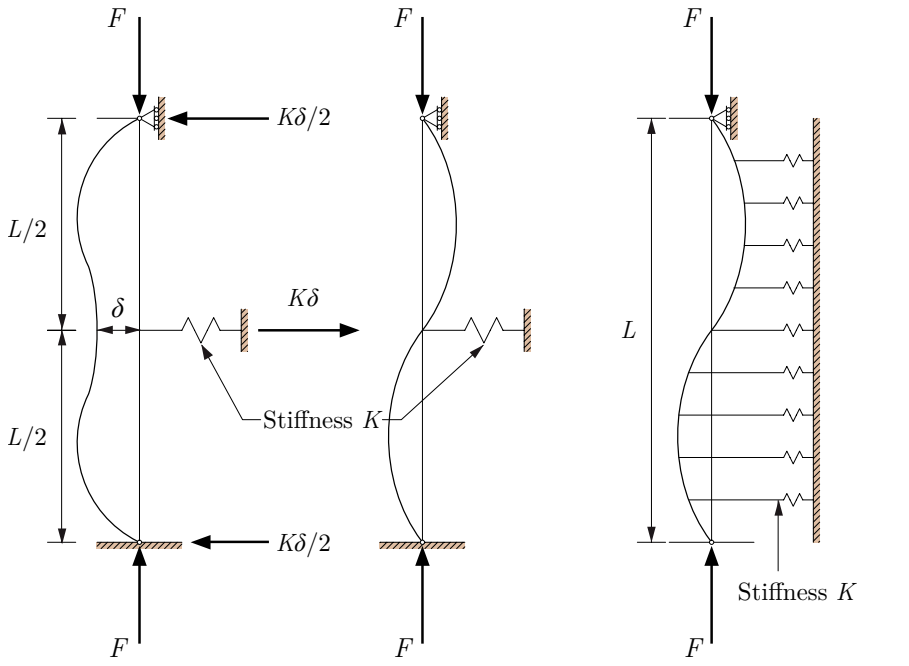
Figure 7.17: Comparisons between linear interaction curves predicted with DSM and Table 7.1 spring stiffnesses in elastic buckling analysis with the beam-column test results from Chapter 5 in a normalised format, in terms of $P_u/M_{c,Rd}$ vs $M_u/M_{c,y,Rd}$

As illustrated by Figures 7.15, 7.16 and 7.17, DSM capacity predictions with the use of springs of appropriate stiffnesses yield much more accurate results compared to the predictions corresponding to the bare steel case. Results are similar to those predicted by EN 1993-1-3 (2006) when restraint was recognised, as reported in Section 7.2.1.3, although DSM predictions indicate sightly higher flexural capacity predictions for both the bare steel and restrained (simulated with springs) cases. As with the results reported in Section 7.2.1.3, there is the potential for the accuracy of the resistances to be improved if the end fixity in compression and mobilisation of composite action in bending are recognised. Also, note that although the linear interaction relationship is an improvement to the concave profile recommended by the EN 1993-1-3 (2006) method, it does not capture the convex profile of the test data and, as such, predictions for combined compression-bending are limited.

7.3 Design recommendations

7.3.1 Restraint in minor axis

For both columns and beams, when intermediate lateral restraints, of some form, are introduced, depending on their stiffness K and location along the length of the member, they can alter both the buckled shape of the member and its critical buckling load. Given the example of a column under compression with a single mid-height lateral restraint, as illustrated in Figure 7.18 (a) and (b), the restraint may or may not constrain the deformation at its location (Gardner 2011). When the restraint prevents the member from deflecting at



(a) Braced first mode (b) Second mode (c) Column with elastic restraints

Single discrete restraint Continuous restraint

Figure 7.18: Column with intermediate elastic restraints. Adapted from Gardner (2011).

its mid-height (when $\delta = 0$), as shown in Figure 7.18 (b), then the column is 'forced' to buckle into its second mode (two half sine waves). As a result, the effective length L_{cr} of the member becomes $L/2$, and replacing that in Equation 7.18 for elastic flexural buckling, results in a four times higher load ($4\pi^2 EI/L^2$) compared to that of an unrestrained member ($\pi^2 EI/L^2$). Further discussion on imperfect columns with intermediate elastic restraints

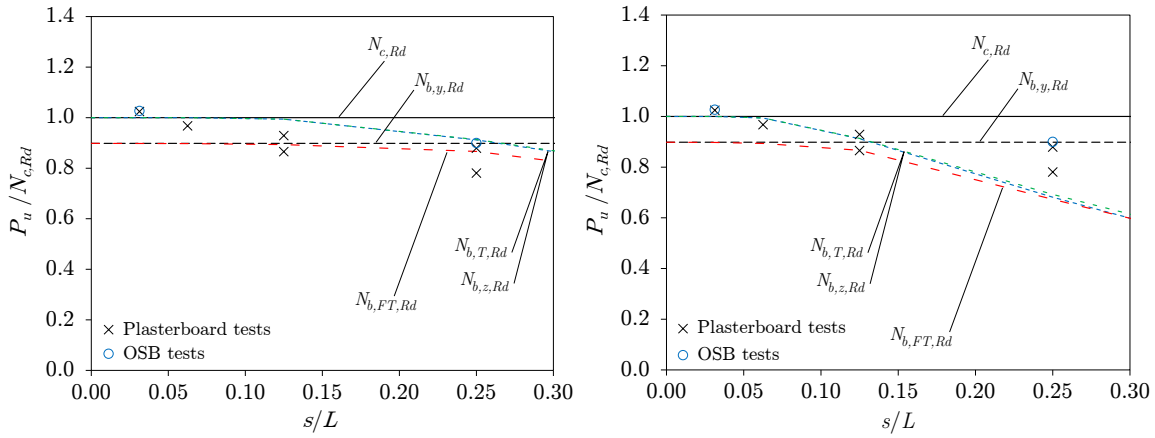
and relationships between the forces experienced by the restraints and the load on the column, are provided in the works of Gardner (2011), Trahair et al. (2008), Timoshenko & Gere (1961)

Given the presence of sheathing, the member may be considered as a column with continuous elastic restraints, as shown in Figure 7.18 (c), and, depending on the rigidity of the restraints (assumed as linear springs), the buckled shape and elastic buckling loads or moments can be determined. Such an approach is presented in Section 7.2.2.1 based on the work of Vieira & Schafer (2013) and Peterman & Schafer (2014), where appropriate spring stiffnesses were determined and subsequently the use of DSM was performed to determine capacities. Note that the effect of bracing about the minor axis was achieved with the reported k_x stiffness in Section 7.2.2.1.

The effects of variations in the restraint conditions on the buckling resistance of members in compression $N_{b,Rd}$ and bending $M_{b,Rd}$, may be accounted for by replacing the actual length of the member L by an effective length L_{cr} in the calculation of the elastic buckling load N_{cr} or the elastic lateral-torsional buckling moment M_{cr} and hence the slenderness $\overline{\lambda}$ or $\overline{\lambda}_{LT}$, which is used throughout the resistance equations, as given in Section 7.2.1.2 (Trahair et al. 2008). As illustrated in Figures 7.10, and 7.11 of Section 7.2.1.3, employing an effective length for the minor axis buckling mode $L_{cr,z}$, the torsional mode L_T and the lateral-torsional mode L_{LT} equal to that of the connector spacing results in significant improvements in capacities calculated in accordance with EN 1993-1-1 (2005), by as much as three to four times more for both compression and bending, and a much closer comparison with the test results.

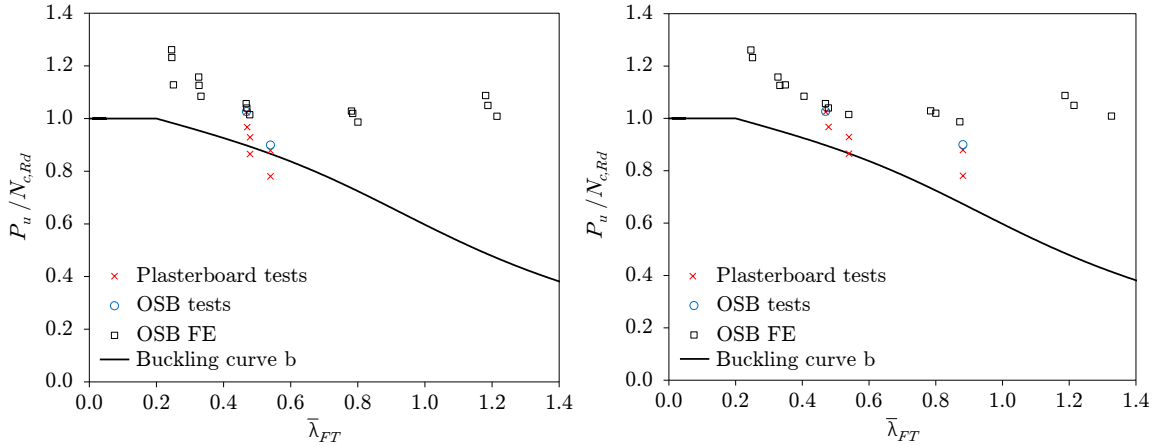
The tests results of the specimens sheathed with plasterboard and OSB under pure compression, reported in Chapter 5, are compared against the EN 1993-1-1 (2005) buckling curves for flexure about both axes, torsional and flexural-torsional buckling, as described in Section 7.2.1.2.1. Figures 5.36 (b) and (c), presented in Chapter 5, are replicated here as Figures 7.19 (a) and (b) respectively in a normalised format. Compression is normalised by the cross-sectional compression resistance (allowing for local buckling) and the connector spacing s, plotted on the horizontal axis, is normalised by the actual length L of the member

($L = 2400$ mm). The test results are compared against predictions made with two different considerations for the effective length about the minor axis $L_{cr,z}$; (i) $L_{cr,z}$ = connector spacing s in Figure 7.19 (a) and (ii) $L_{cr,z}$ = two times the connector spacing $2s$ in Figure 7.19 (b). The effective length about the major axis $L_{cr,y}$ is taken as the full member length, while the effective torsional buckling length L_T is taken equal to $L_{cr,z}$. As shown in Figure 7.19, the



(a) For EC3 predictions: $L_{cr,y} = L$, $L_{cr,z} = s$ (b) For EC3 predictions: $L_{cr,y} = L$, $L_{cr,z} = 2s$

Figure 7.19: Comparisons between normalised compression test results with EN 1993-1-3 (2006) resistance prediction limits assuming $L_T = L_{cr,z}$ and $L_{cr,z}$ is equal to (a) the connector spacing s and (b) two times the connector spacing s. $L_{cr,y}$ was taken as the full member length for both cases.

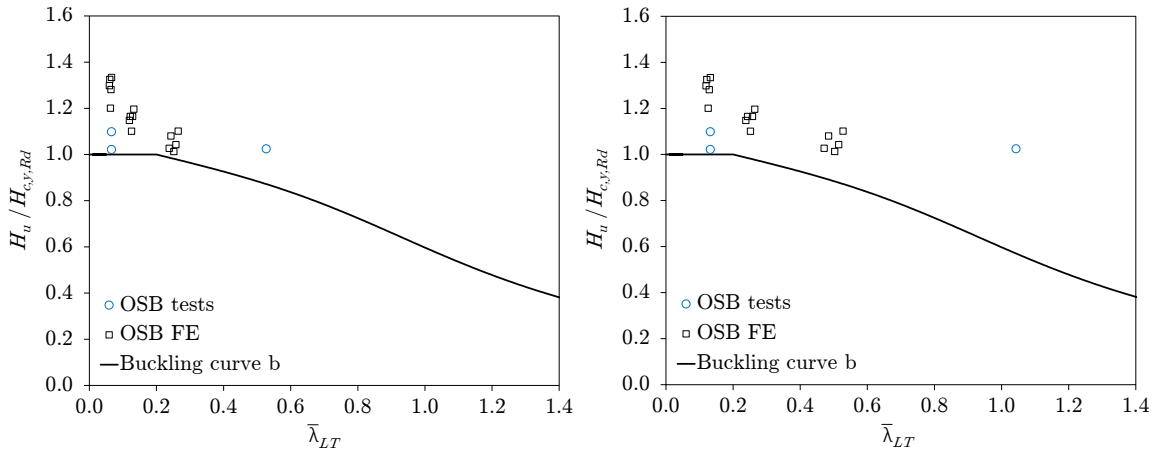


(a) $L_{cr,y} = L$, $L_{cr,z} = s$ (b) $L_{cr,y} = L$, $L_{cr,z} = 2s$

Figure 7.20: Comparisons between normalised compression test and FE results with EN 1993-1-3 (2006) flexural-torsional buckling curve assuming $L_T = L_{cr,z}$ and $L_{cr,z}$ is equal to (a) the connector spacing s and (b) two times the connector spacing s. $L_{cr,y}$ was taken as the full member length L for both cases.

critical limit is the flexural-torsional buckling $N_{b,FT,Rd}$ resistance. Therefore, the normalised compression capacities ($P_u/N_{c,Rd}$) of all tests under pure compression, reported in Chapter 5, along with the FE results, reported in Chapter 6, are plotted against the non-dimensional slenderness $\overline{\lambda}$ calculated with $N_{cr,FT}$, given by Equation (7.21), in Figures 7.20 (a) and (b) for the two cases of effective length considered. Although all of the predictions for the OSB test and FE data are on the safe side when the effective length about the minor axis is taken as equal to the connector spacing, unsafe predictions are yielded for the plasterboard sheathed specimens connected at 300 mm and 600 mm spacings, which suffered connector failure. Nevertheless, taking the effective length about the minor axis as equal to two times the connector spacing, effectively assuming every other connector fails and thus does not provide restraint, led to safe results for all of the plasterboard sheathed specimens, as shown in both Figure 7.19 (b) and 7.20 (b).

Similarly to the compression test and FE results, the normalised bending capacities for specimens under pure bending, from tests and FE simulations, are plotted against the non-dimensional slenderness for lateral torsional buckling, assuming an effective length L_{LT} equal to the connector spacing s and twice the connector spacing $2s$, in Figures 7.21 (a) and (b), respectively. In both cases, safe predictions are yielded, indicating that sheathing is able to restrain lateral-torsional buckling for specimens under bending effectively.



(a) L_{LT} = connector spacing

(b) L_{LT} = 2 × connector spacing

Figure 7.21: Comparisons between normalised bending test and FE results with EN 1993-1-3 (2006) lateral-torsional buckling curve assuming L_{LT} is equal to (a) the connector spacing s and (b) two times the connector spacing s

7.3.2 End fixity in compression

In the previous section, it was shown that the effect of the restraint conditions can be accounted for through the effective length. In a similar way, the effects of the variations in the end support conditions may be accounted for - see Figure 7.22. In the previous section, the effective length about the major axis $L_{cr,y}$ was assumed to be equal to the actual length L, essentially treating the member as pin ended about the major axis. It has

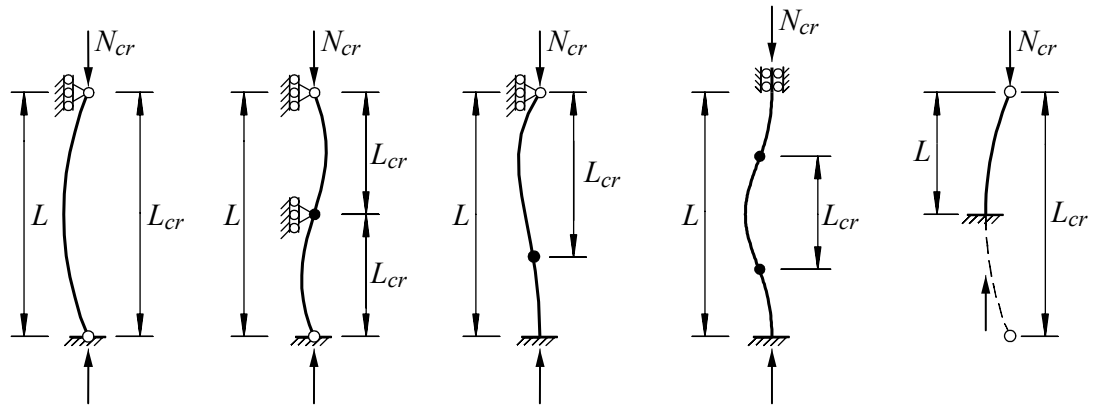
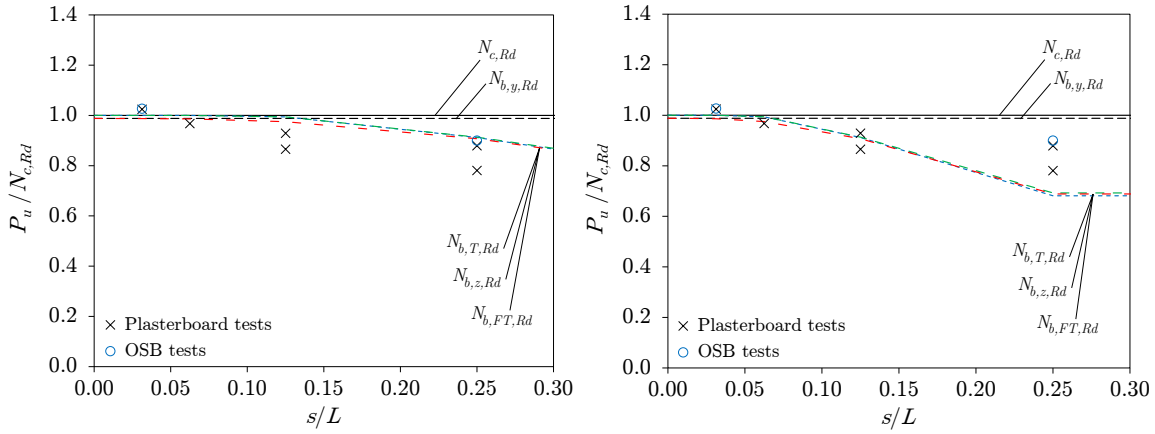


Figure 7.22: Effective lengths L_{cr} of columns with various end boundary conditions. From Trahair et al. (2008).

been shown though, in Chapters 5 through tests in pure compression and in Chapters 6 through numerical studies when the finite element model was validated against test data from the literature, as well as results from the parametric studies, that sheathed specimens under pure compression behave more like fully fixed specimens, with their effective length corresponding to the illustration of Figure 7.22 (d).

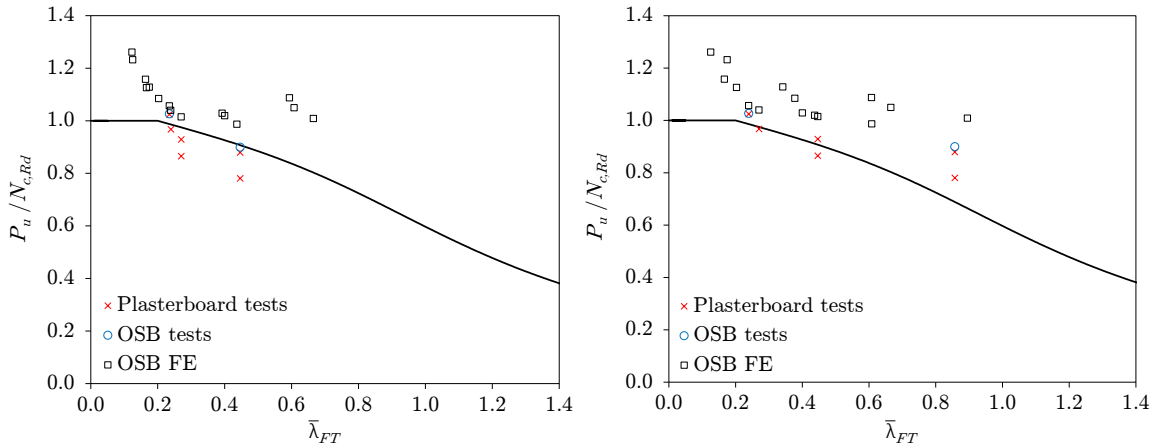
Therefore, end fixity of a compression member can be recognised by calculating the buckling resistance about the major axis $N_{b,y,Rd}$ with an effective length $L_{cr,y} = L/2$, while $L_{cr,z}$ which is associated with the connector spacing, as established in the previous section, remains unaffected. Note that it is not uncommon to consider the member behaviour in each principal plane independently with effective lengths $L_{cr,y}$ and $L_{cr,z}$ differing, since the radii of gyration i_y and i_z also differ (Trahair et al. 2008).

The scenarios presented in Figures 7.19 and 7.20, in the previous section, are repeated with an effective length about the major axis equal to $0.5L$, with the results presented in Figures 7.23 and 7.24 respectively. For the OSB test and FE results, the yielded predictions are safe-sided (even with $L_{cr,y} = 0.5L$ and $L_{cr,z}$ equal to the connector spacing), but close to the buckling curve, indicating improved accuracy. On the other hand, as shown in



(a) For EC3 predictions: $L_{cr,y} = 0.5L$, $L_{cr,z} = s$ (b) For EC3 predictions: $L_{cr,y} = 0.5L$, $L_{cr,z} = 2s$

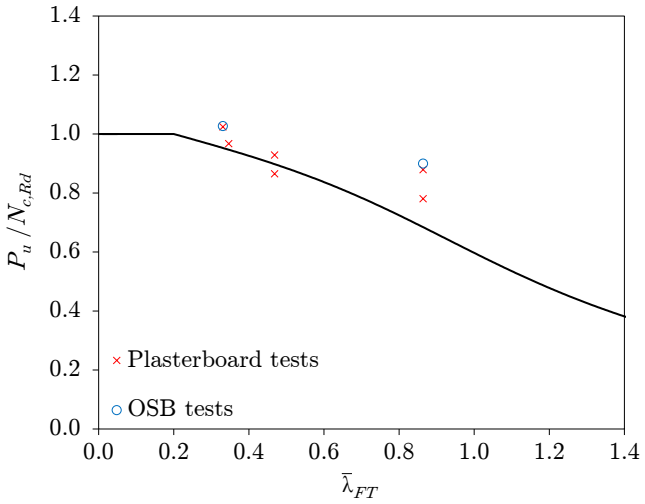
Figure 7.23: Comparisons between normalised compression test results with EN 1993-1-3 (2006) resistance prediction limits assuming $L_T = L_{cr,z}$ and $L_{cr,z}$ is equal to (a) the connector spacing s and (b) two times the connector spacing s. $L_{cr,y}$ was taken as the half the member length for both cases.



(a) $L_{cr,y} = 0.5L$, $L_{cr,z} = s$ (b) $L_{cr,y} = 0.5L$, $L_{cr,z} = 2s$

Figure 7.24: Comparisons between normalised compression test and FE results with EN 1993-1-3 (2006) flexural-torsional buckling curves assuming $L_T = L_{cr,z}$ and $L_{cr,z}$ is equal to (a) the connector spacing s and (b) two times the connector spacing s. $L_{cr,y}$ was taken as the half member length $0.5L$ for both cases.

Figures 7.23 (a) and 7.24 (a), all of the plasterboard data except those connected at 75 mm spacings are unconservatively predicted; note that for all of these specimens, connector failure was observed in the tests. When $L_{cr,z} = 2s$ is used in conjunction with $L_{cr,y} = 0.5L$, safer predictions for the specimens sheathed with plasterboard are provided, as shown in Figures 7.23 (b) and 7.24 (b). Nevertheless, there are still two specimens, sheathed with plasterboard, which are unsafely predicted since they lie below the buckling curve. Therefore, a third scenario is considered with an effective length about the major axis equal to $0.7L$ and an effective length about the minor axis equal to twice the connector spacing; the results are illustrated in Figure 7.25. It can be observed that the yielded predictions are more accurate, with only one specimen (connected at 300 mm spacings) slightly unsafely predicted.



$L_{cr,y} = 0.7L$, $L_{cr,z} = 2s$

Figure 7.25: Comparisons between normalised compression test results with EN 1993-1-3 (2006) flexural-torsional buckling curve assuming $L_T = L_{cr,z}$ and $L_{cr,z}$ is equal to two times the connector spacing s. $L_{cr,y}$ was taken as $0.7L$.

In Figures 7.26 and 7.27, the beam-column OSB test results reported in Chapter 5 are compared with the EN 1993-1-3 (2006) interaction curve, determined considering fixed ends when in compression by taking $L_{cr,y} = 0.5L$ (in terms of normalised horizontal loads and moments as described in Section 7.2.1.3). About a 10% increase in compression capacity is achieved for the specimens with the closest connector spacing (75 mm), yielding accurate predictions when compared with the test data.

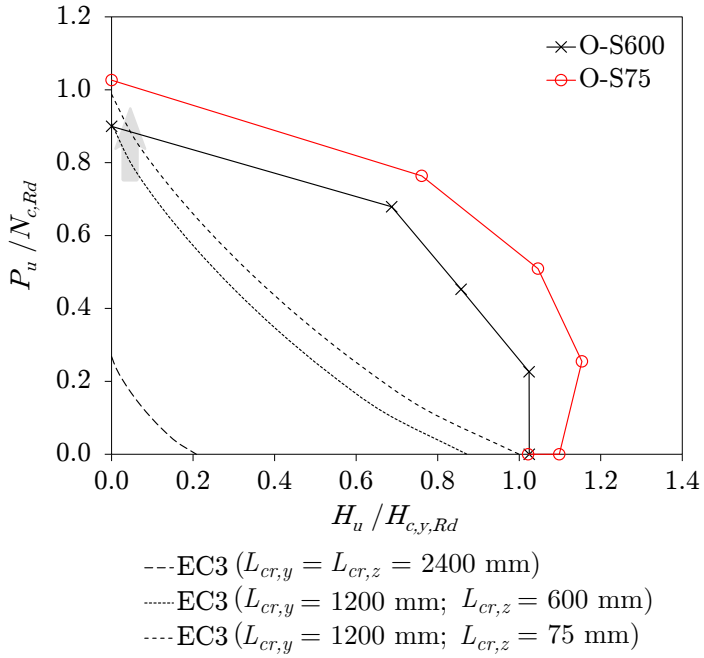


Figure 7.26: Comparison between the beam-column test results from Chapter 5 and EN 1993-1-3 (2006) predictions assuming fixity in compression and effective lengths about the minor axis equal to connector spacing in a normalised format, in terms of $P_u/N_{c,Rd}$ vs $H_u/H_{c,y,Rd}$

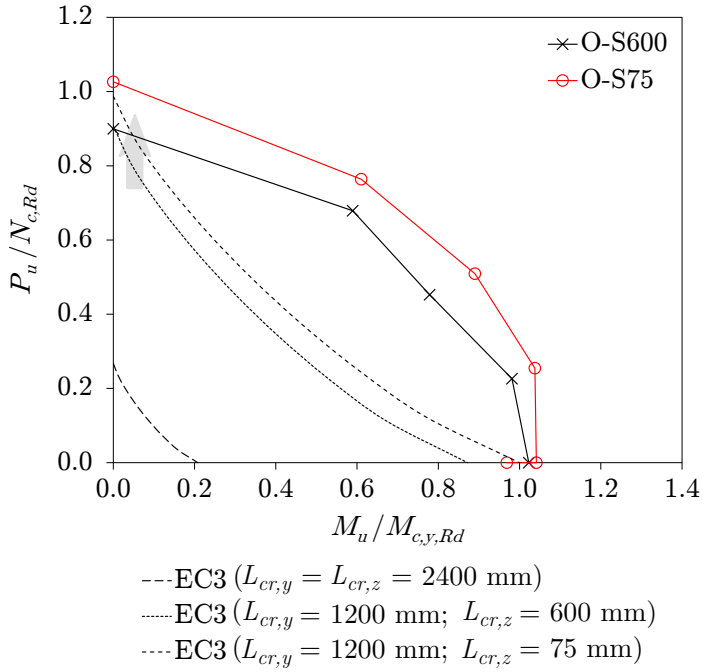


Figure 7.27: Comparison between the beam-column test results from Chapter 5 and EN 1993-1-3 (2006) predictions assuming fixity in compression and effective lengths about the minor axis equal to connector spacing in aa normalised format, in terms of $P_u/N_{c,Rd}$ vs $M_u/M_{c,y,Rd}$

Recommendations for effective lengths of sheathed specimens in pure compression, are provided in Table 7.4. A minimum of 300 mm spacing between connectors is recommended. For members in bending sheathed with OSB, as already established in the previous section, an effective length for lateral torsional buckling L_{LT} equal to the connector spacing, is appropriate.

Table 7.4: Recommended effective lengths in compression

	Effective length about the major axis $L_{cr,y}$	Effective length about the minor axis $L_{cr,z}$	Effective torsional length L_T	Maximum connector spacing s (mm)
Oriented strand board 4.8 mm screw diameter	$0.5L$	s	s	300
Plasterboard 3.5 mm screw diameter	$0.7L$	$2\times s$	$2\times s$	300

7.3.3 Composite action

The efficiency of a composite structural system is dependent on the strength and stiffness of the employed shear connection between the components comprising the system (Nethercot 2003, Johnson 2004, Davison & Owens 2012, Kyvelou et al. 2017*a*). Mobilisation of composite action, which prevents the system components acting independently is dependent on the connection at the shear interface, which can reduce or even completely eliminate the relative slip between the components of a structural system. For a composite system with full shear connection between the components, the employed connection is strong enough so that the ultimate capacity is not limited by the shear strength of the connection. A system whose strength is limited by the shear connection between its components, is said to have partial shear connection. In accordance with Oehlers & Bradford (1995) and Kyvelou et al. (2017*a*), a distinction should be made between full shear connection and full shear interaction, since the former is related to the shear strength of the longitudinal connection while the latter is related to its stiffness. A system with full shear interaction behaves in a monolithic way since no slip whatsoever occurs between the interface of the system components when under load. As such, although a full shear connection can be achieved

with a sufficient number of shear connectors, it is unrealistic to assume that a full shear interaction is achievable, since the connectors between the components of the system will always undergo some degree of deformation. In fact, for a composite system to be designed with partial shear connection, in accordance with EN 1994-1-1 (2004), the employed shear connectors need to be ductile.

Based on the test and finite element results presented in Chapters 5 and 6, specimens under bending exceeded their cross-sectional bending resistances (assuming no composite action). It is therefore anticipated that considering the mobilisation of composite action between the board and the steel when in flexure, is realistic and would enhance the capacity of the system. Based on the provisions of EN 1994-1-1 (2004) and the design methodology developed by Kyvelou et al. (2017*a*), a set of guidelines is outlined in the following subsections for considering composite action between the sheathing and the column for stud walls in major axis bending. Note that in the guidelines that follow, when the sheathing board is in tension its contribution is ignored.

It should be mentioned that, although the FE results presented in Chapter 6 indicated that there is potential for composite action also arising within the sheathed studs under axial compression, a design method to account for this has not been devised herein and is therefore recommended as a topic for future research.

7.3.3.1 Degree of shear connection

For a composite system in bending, the strength from the available shear connectors needs to be first established to determine whether the shear connection between the components of the system is full or partial, so that the bending resistance of the composite member can be determined accordingly.

Expressions for the prediction of the load carrying capacity $F_{u,po}$ per shear plane of a screw connector in a sheathing-to-steel connection were established in Section 4.4.2.2 of Chapter 4, for plasterboard and OSB. Thus, in design, the strength of s screw failing in the board P_b is given by Equation (7.39), where γ_V is a partial safety factor with a recommended

value of 1.25 (EN 1994-1-1 2004).

$$P_b = F_{u,po}\frac{1}{\gamma_V} \tag{7.39}$$

The shear strength of the screw connector is limited though by its shear capacity, given by Equation (7.40), where $d_{s,sh}$ is the diameter of the shank, typically taken as 0.75 of the screw diameter d, $f_{u,s}$ is the ultimate tensile strength of the screw and γ_V is a partial safety factor with a recommended value of 1.25 (EN 1994-1-1 2004).

$$P_v = \pi\frac{d_{s,sh}^2}{4}\frac{f_{u,s}}{\sqrt{3}}\frac{1}{\gamma_V} \tag{7.40}$$

Therefore, the shear strength of a steel-to-sheathing fixing is given by Equation (7.41).

$$P_{Rd} = \min(P_v, P_v) \tag{7.41}$$

The total longitudinal shear force transferred by the shear connectors N_c of the composite system along the shear interface is given by Equation (7.42),

$$N_c = nP_{Rd} \tag{7.42}$$

where n is the the total number of shear connectors from the edge of the beam up to the point of maximum moment and can be determined using Equation (7.43), assuming all connectors are in line along the length of the member and at a constant spacing s.

$$n = L_{sh,cr}/s \tag{7.43}$$

$L_{sh,cr}$ is the critical distance between points of zero and maximum moment, i.e. for a member in bending under uniform distributed loading that point is at mid-length, hence in this scenario the critical length is taken as $L_{sh,cr} = L/2$, where L is the total length of the member.

For a fully composite member, the total force $N_{c,f}$ that can be transferred is the minimum between the axial strength of the steel member $N_{pl,a}$ and the compressive strength of

the board $N_{c,board}$, given by Equation (7.44)

$$N_{c,f} = \min(N_{c,board}, N_{pl,a}) \tag{7.44}$$

The axial strength of the steel member $N_{pl,a}$ is given by Equation (7.45), where A is the gross area of the steel cross-section and f_y is the yield strength.

$$N_{pl,a} = Af_y \tag{7.45}$$

The compressive strength of the board $N_{c,board}$ is given by Equation (7.46), where f_{cbd} is the design compressive strength of the board material, t_b is the board thickness and b_{eff} is the effective width of the board, taken as the minimum of two times the $L/8$ and the stud spacing, in accordance with Clause 5.4.1.2 of EN 1994-1-1 (2004), with consideration for shear lag (for the cases examined herein, b_{eff} is taken as 600 mm).

$$N_{c,board} = f_{cbd}b_{eff}t_b \tag{7.46}$$

The design compressive strength of the board material f_{cbd} is given by Equation (7.47), where f_{cb} is the compressive strength of the board material; for plasterboard this value may be taken from Table 4.2 of Chapter 4 and for OSB from Table 4.3 of Chapter 4. γ_M is a partial safety factor and may be taken as 1.3 for the OSB (based on Table 2.3 of EN 1993-1-5 (2006)) and 1.5 for the plasterboard (based on the recommended safety factor for concrete (EN 1994-1-1 2004), since plasterboard and concrete share similar material characteristics).

$$f_{cbd} = \frac{f_{cb}}{\gamma_M} \tag{7.47}$$

Hence, the degree of shear connection η can be expressed in terms of the strength of the available shear connection over the strength that would be needed for full shear connection, given by Equation 7.48. The degree of shear connection η can also be expressed in terms of total number of shear connectors n along the critical length over the total number of shear

connectors required for full shear connection n_f, given by Equation (7.49).

$$\eta = N_c/N_{c,f} \leq 1.0 \tag{7.48}$$

$$\eta = n/n_f \leq 1.0 \tag{7.49}$$

7.3.3.2 Moment capacity

In accordance with Clause 6.2.1.3 of EN 1994-1-1 (2004), the relationship between the composite moment capacity M_{Rd}, of a Class 1 or 2 cross-section under bending, and the degree of partial shear connection η, is illustrated in Figure 7.28, with M_{Rd} varying between the plastic bending resistance of the bare steel member $M_{pl,a,Rd}$ and that of a fully composite system $M_{pl,Rd}$. M_{Rd} can either be calculated using the stress-block equilibrium method, (by determining the plastic neutral axis for the given partial shear connection and determining the equivalent bending resistance from stress-blocks), or by carrying out linear interpolation between $M_{pl,a,Rd}$ and $M_{pl,Rd}$, leading to a simpler, but more conservative prediction.

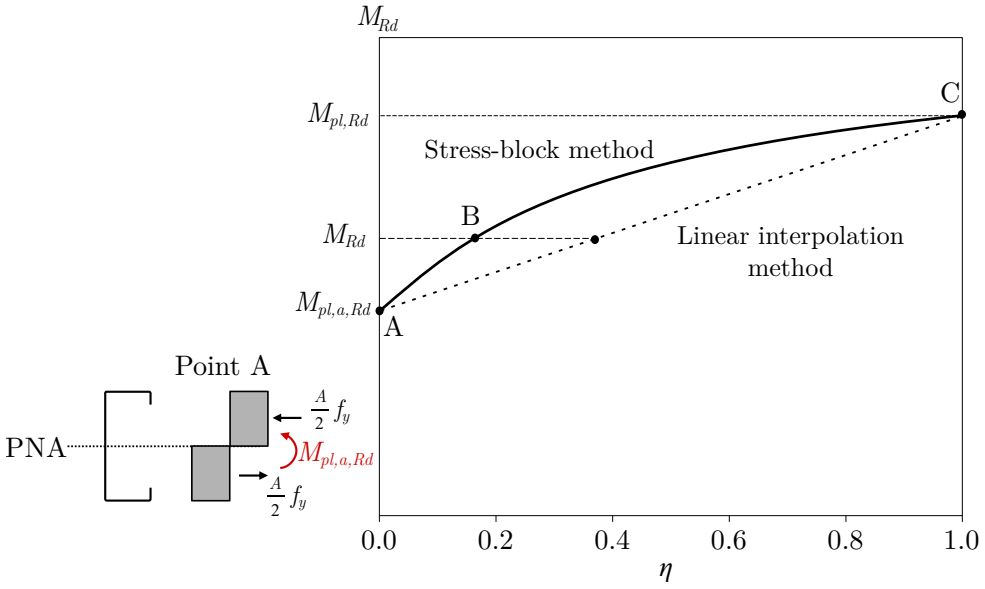


Figure 7.28: Relationship between moment resistance and degree of shear connection η in composite systems under bending in accordance with EN 1994-1-1 (2004)

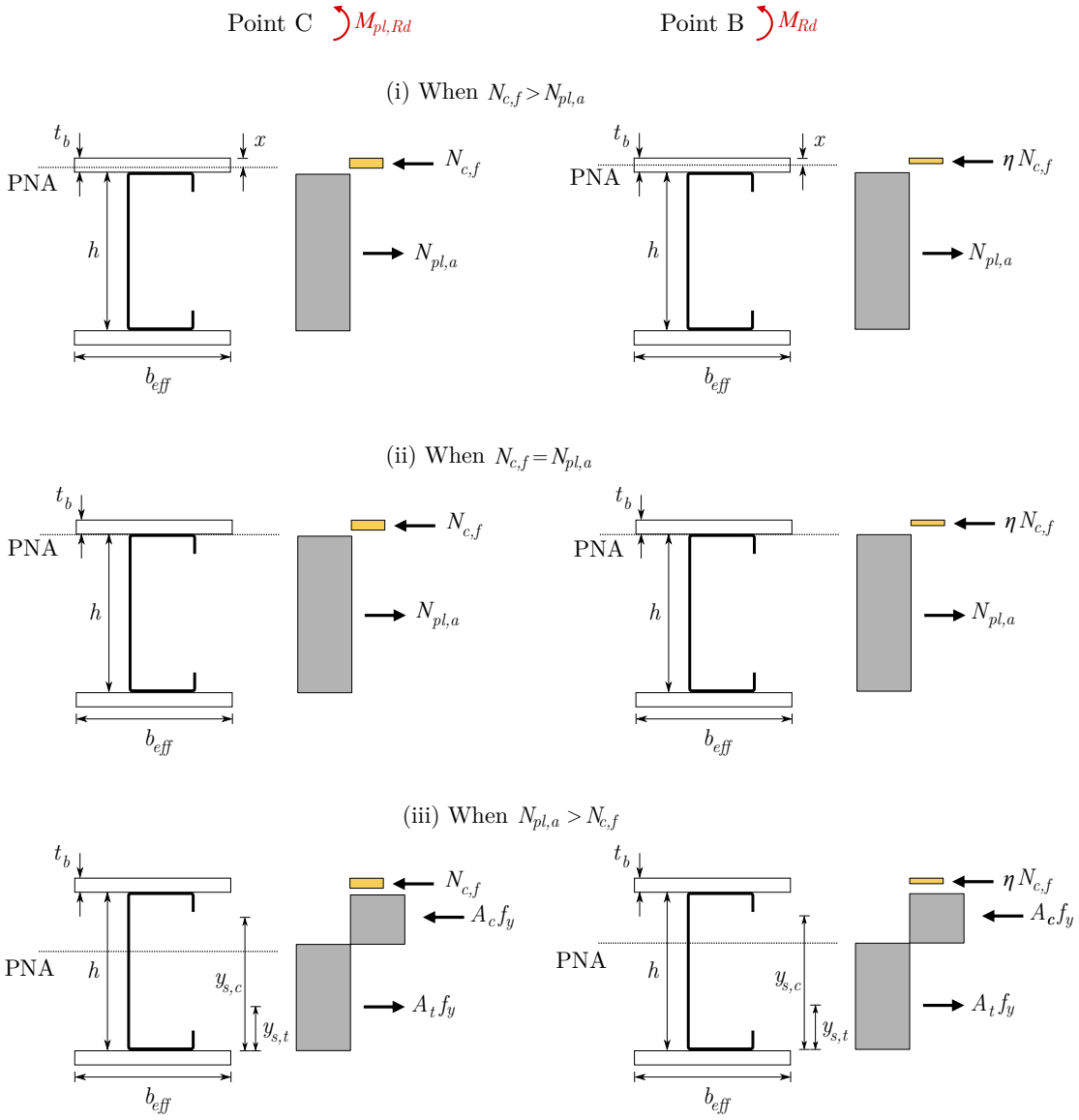


Figure 7.29: Plastic stress distributions for full shear connection (Point C) and partial shear connection (Point B)

The equivalent forces at the critical cross-section of the member (i.e. at mid-length) at point B (with partial shear connection) and point C (with full shear connection) shown in Figure 7.28, can be visualised in terms of stress blocks, for three different scenarios, as illustrated in Figure 7.29. The three scenarios considered are (i) $N_{c,f} > N_{pl,a}$ and, as such, the plastic neutral axis (PNA) lies in the board, (ii) $N_{c,f} = N_{pl,a}$ and, as such, the PNA lies at the steel-board interface and (iii) $N_{c,f} < N_{pl,a}$ and, as such, the PNA lies in the steel member. For these three scenarios, based on the equivalent stress blocks and dimensions illustrated in Figure 7.29, the following plastic bending resistances can be determined for a

fully composite system (i.e. point C on Figure 7.28).

(i) Plastic neutral axis within the board, $N_{c,f} > N_{pl,a}$:

$$M_{pl,Rd} = N_{c,f}\left(\frac{h}{2} + t_b - \frac{x}{2}\right) \tag{7.50}$$

where x is the distance of the PNA from the top fibre of the composite section.

(ii) Plastic neutral axis at the interface, $N_{c,f} = N_{pl,a}$:

$$M_{pl,Rd} = N_{pl,a}\left(\frac{h}{2} + \frac{t_b}{2}\right) \tag{7.51}$$

(iii) Plastic neutral axis in the steel section, $N_{c,f} < N_{pl,a}$:

$$M_{pl,Rd} = N_{c,f}\left(\frac{t_b}{2} + h - y_{s,t}\right) + A_c f_y \left(y_{s,c} - y_{s,t}\right) \tag{7.52}$$

where A_c and A_t are the cross-sectional areas of the steel member in compression and in tension, respectively, while $y_{s,t}$ and $y_{s,c}$ are the distances from the bottom fibre of the steel section to the centroids of the parts of the steel section in tension and compression respectively.

Note that the cross-sectional plastic resistance $M_{pl,a,Rd}$ is given by Equation 7.53, where z is the distance between the centroids of the steel member under tension and compression.

$$M_{pl,a,Rd} = \frac{A}{f_y} z \tag{7.53}$$

Since Class 4 cold-formed steel cross-sections suffer local instabilities under flexure, as illustrated in Figure 7.3, their plastic moment resistance $M_{pl,a,Rd}$ cannot be attained due loss of effectiveness. However, in accordance with Kyvelou et al. (2017*a*), composite cold-formed steel members with full shear connection are typically reclassified as Class 1 or 2, since most of the compression is carried by the board. Therefore, when this assumption is valid, the methodology developed by Kyvelou et al. (2017*a*) can be adopted and the moment resistance $M_{comp,Rd}$ of a composite cold-formed steel member under flexure can be determined using

Equation (7.54), as illustrated in Figure 7.30.

$$M_{comp,Rd} = M_{Rd} - (1 - \eta)\,(M_{pl,a,Rd} - M_{c,Rd}) \tag{7.54}$$

Note that M_{Rd} (at point B) is the composite moment capacity of a system with the same degree of shear connection as the examined system, derived based on the stress-block method (point B) assuming a plastic distribution of stresses (Kyvelou et al. 2017*a*), while $M_{c,Rd}$ is the bending resistance of the cold-formed steel member accounting for loss of effectiveness due to cross-sectional instabilities.

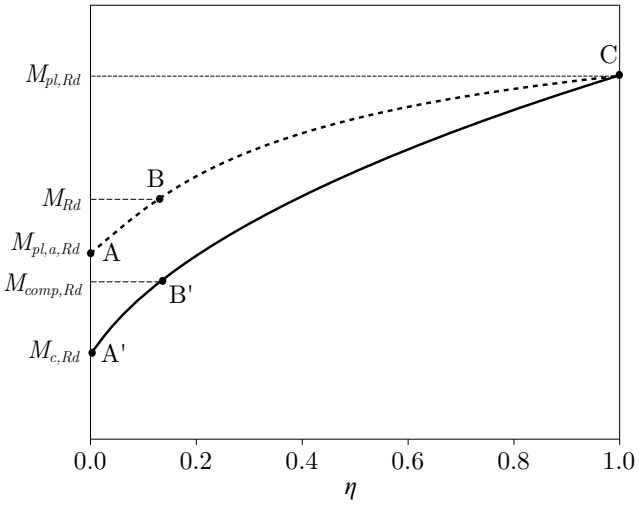


Figure 7.30: Variation of moment capacity of composite systems against degree of shear connection η according to the proposed method by Kyvelou et al. (2017*a*). Adapted from Kyvelou et al. (2017*a*).

A more conservative approach is to calculate the moment resistance using linear interpolation between points A' and C, given by Equation (7.55).

$$M_{comp,linear,Rd} = M_{c,Rd} + \eta\,(M_{pl,Rd} - M_{c,Rd}) \tag{7.55}$$

It is necessary to emphasise that the above expressions were derived based on the fact that under full shear connection the members can be reclassified as Class 1 or 2. For cross-sections which are classified as Class 3 or 4, even when full shear connection is assumed, the effects of local buckling will need to be considered. Further research is required to establish whether composite action can be taken into consideration for such systems.

7.3.3.3 Interaction between bending and shear

When high levels of shear force develop within the system (i.e. a shear force higher than 50% of the shear resistance), appropriate allowance should be made to the resulting degradation of moment resistance. For Class 1 or 2 cross-sections, the design bending moment resistance should be reduced in accordance with the provisions of Clause 6.2.8 of EN 1993-1-1 (2005), while for Class 3 or 4 cross-sections, the design bending moment resistance should be reduced in accordance with the provisions of Clause 7.1 of EN 1993-1-5 (2006).

7.3.3.4 Final bending capacity

The minimum degree of shear connection as given in EN 1994-1-1 (2004) is to ensure that the shear connectors have adequate deformation capacity. For establishing limits of minimum allowed degree of shear connection for sheathed stud specimens in bending, further research is needed. Nevertheless, based on the test and the FE parametric results presented in Chapters 5 and 6 respectively, a limit expressed in terms of minimum connector spacing can be suggested. Connecting OSB sheathing to the stud members with fixings at a spacing of equal to or less than 300 mm, was shown to lead to capacities in excess of the cross-sectional resistances, while with spacings of 150 mm, resistances were at least 10% improved. Therefore, for specimens, of a length of 2.4 m, sheathed with OSB, it is suggested that the minimum allowed degree of shear connection for composite action to be considered, is with at least 150 mm connector spacings.

In Figures 7.31, 7.32 and 7.33 the beam-column interaction test and FE results are grouped by the employed connector spacing, for 300 mm, 150 mm and 75 mm respectively. Results are presented in a normalised format to emphasise the gains in bending resistance relative to the cross-sectional bending resistance (expressed in terms of equivalent horizontal forces).

It can be observed that for specimens connected with screws at every 300 mm, the cross-sectional bending resistance (expressed as $H_{c,y,Rd}$) was attained by all specimens and

gains of up to 10% greater than $H_{c,y,Rd}$ were achieved. For specimens connected with screws at 150 mm spacings, the gains in bending capacity were between 10% and 20% higher than the cross-sectional bending resistance, while for specimens connected at every 75 mm the gains in bending capacity were between 20% and 33% greater.

Note that the test results of the OSB sheathed specimens with 600 mm screw spacings are not presented since the number of connectors is too limited to consider mobilisation of composite action. Also, note that the Peterman & Schafer (2014) test results, which are included in Figure 7.31 within the 300 mm group, demonstrate a more 'pronounced' convex shape than the FE results, while the results of the test specimens connected with 75 mm spacings (included in Figure 7.33), of the current study, did not attain their full bending capacity due to failure of the stud-to-column connection.

As shown by the results in Figures 7.31, 7.32 and 7.33, considering effective restraint about the minor axis, fixity in compression and composite action in bending can result to much more accurate design predictions for pure compression and bending. However, the accuracy of the resistance prediction for combined loading using the EN 1993-1-3 (2006) interaction curve is limited by the concave shape of the curve. A methodology for adopting a more representative shape for the design interaction curve, is reported in the next section.

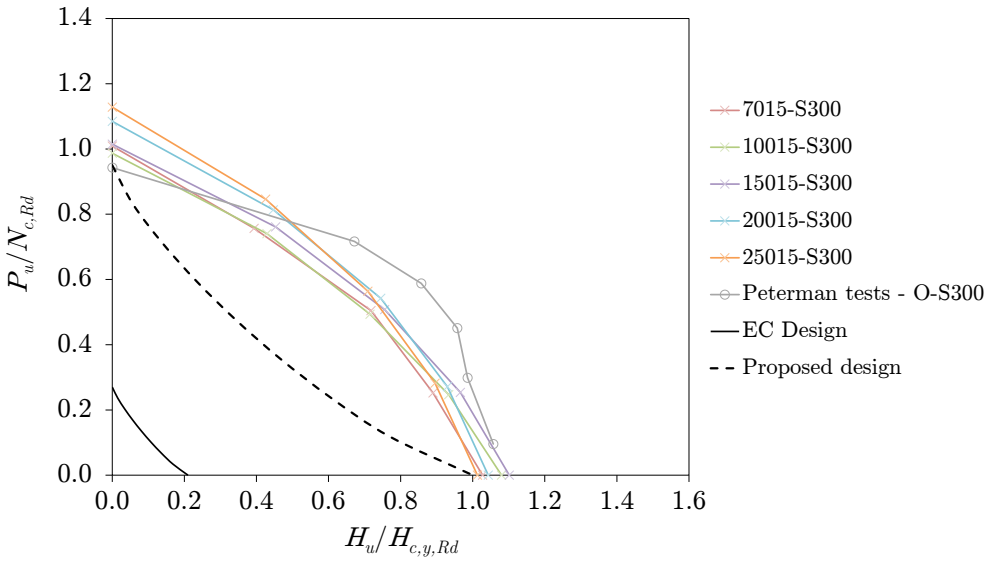


Figure 7.31: Illustrating increase in bending for FE and test data with fixings spaced at 300 mm

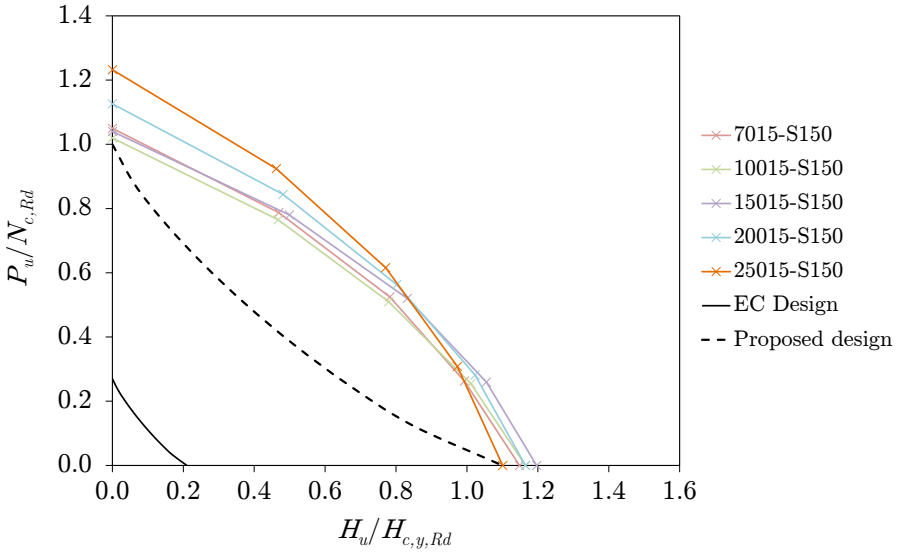


Figure 7.32: Illustrating increase in bending for FE and test data with fixings spaced at 150 mm

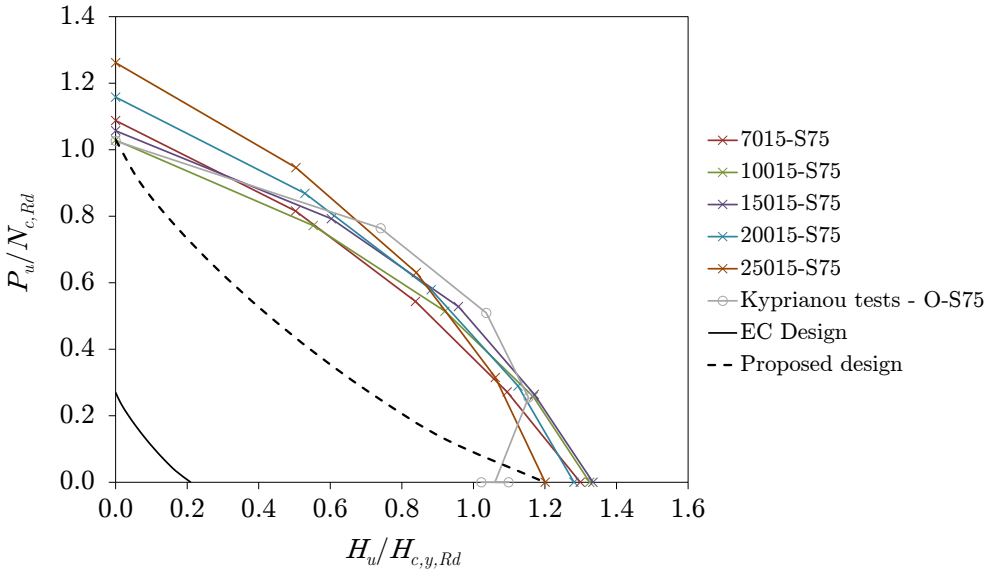


Figure 7.33: Illustrating increase in bending for FE and test data with fixings spaced at 75 mm

7.3.4 Interaction curve profile

To determine more appropriate power coefficients ω for the EN 1993-1-3 (2006) interaction curve between compression and bending, Equation (7.56) was fitted with each individual interaction curve from the beam-column parametric FE results, by manually changing the ω value to best fit the respective curves.

$$\left(\frac{N_{Ed}}{N_{b,Rd}}\right)^{\omega} + \left(\frac{M_{Ed}}{M_{b,Rd}}\right)^{\omega} \leq 1.0 \tag{7.56}$$

The values of $N_{Ed}/N_{b,Rd}$ and $M_{Ed}/M_{b,Rd}$ for each fitted curve were taken from the respective FE results, normalised against the cross-sectional capacities in compression and bending, respectively. The empirically determined ω power coefficients are presented in Table 7.5, where designation of specimens corresponds to the depth of the member in mm followed by the thickness in mm multiplied by 10 (i.e. 7015 is a member which is 70 mm deep and 1.5 mm thick). As indicated by the ω results presented in Table 7.5, where the coefficient of variation was less than 0.03 and a mean value of 1.30 was found to be appropriate for describing the shape of the interaction curves for all three cases of connector spacings (i.e. 300 mm, 150 mm and 75 mm).

A second, more refined, approach for determining the power coefficient and allowing more flexibility in changing the shape of the interaction curve is expressed by having the power coefficient ω described in terms of Equation (7.57), where ω_1 and ω_2 are two new empirical coefficients that need to be determined by fitting Equation (7.56) to the data. The determined ω_1 and ω_2 power coefficients are presented in Table 7.5. Use of the mean values of ω_1 and ω_2 from Table 7.5 in Equation (7.57) and then in the design Equation (7.56) are presented along with the beam-column interaction curves in Figures 7.34, 7.35 and 7.36 for specimens with connector spacings of 300 mm, 150 mm and 75 mm respectively. It can be observed that improved convex-shaped design interaction curves were derived using the new power coefficients, yielding much more accurate predictions and leading to an improvement of about 100% in bending capacity for specimens loaded at about 50% of their compressive

capacity, when compared to the equivalent resistance achieved with the 0.8 power coefficient.

$$\omega = \omega_1 - \omega_2 \frac{N_{Ed}}{N_{b,Rd}} \tag{7.57}$$

Table 7.5: Empirically determined power coefficients ω and the refined ω_1 and ω_2 when fitting the employed interaction curves to the FE data

Designation of specimens	Connector spacing								
	75 mm			150 mm			300 mm		
	ω	ω_1	ω_2	ω	ω_1	ω_2	ω	ω_1	ω_2
7015	1.25	1.22	0.00	1.3	1.31	0.05	1.26	1.30	0.06
10015	1.31	1.35	0.05	1.29	1.29	0.05	1.25	1.30	0.07
15015	1.35	1.38	0.04	1.32	1.32	0.04	1.31	1.32	0.03
20015	1.30	1.35	0.10	1.28	1.32	0.05	1.33	1.40	0.08
25015	1.31	1.35	0.05	1.33	1.38	0.07	1.32	1.38	0.10
Mean	1.30	1.33	0.05	1.30	1.32	0.05	1.29	1.34	0.07
COV	0.03	0.05	0.74	0.02	0.03	0.21	0.03	0.04	0.38

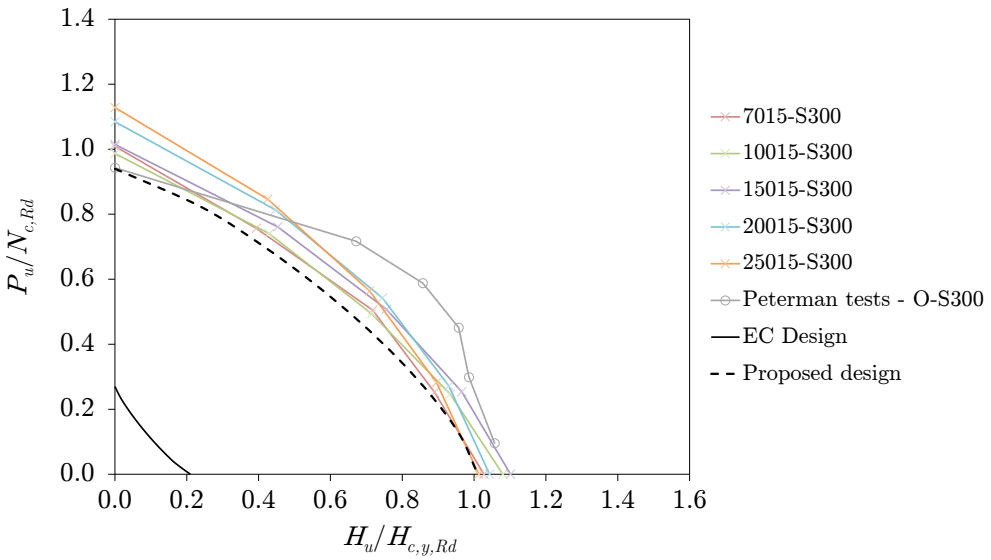


Figure 7.34: Interaction curve fitted to the FE and test data with fixings spaced at 300 mm

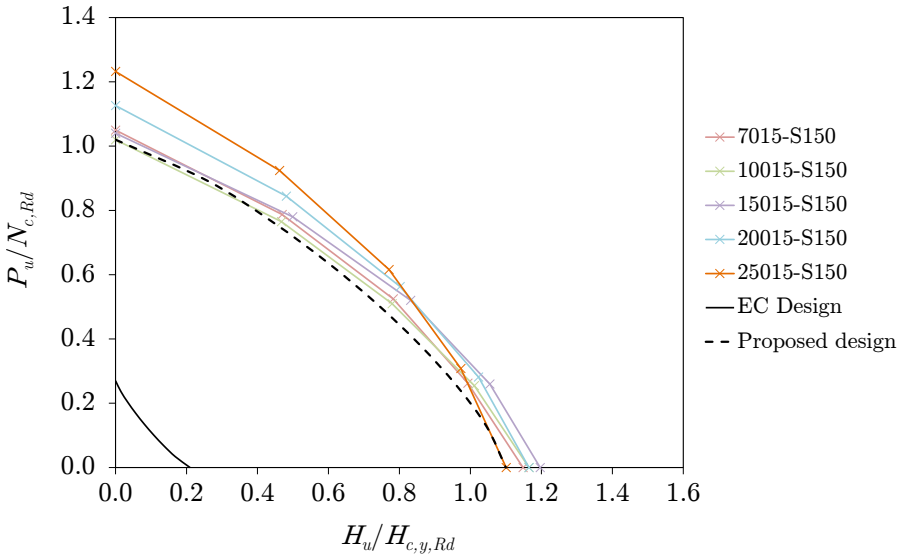


Figure 7.35: Interaction curve fitted to the FE and test data with fixings spaced at 150 mm

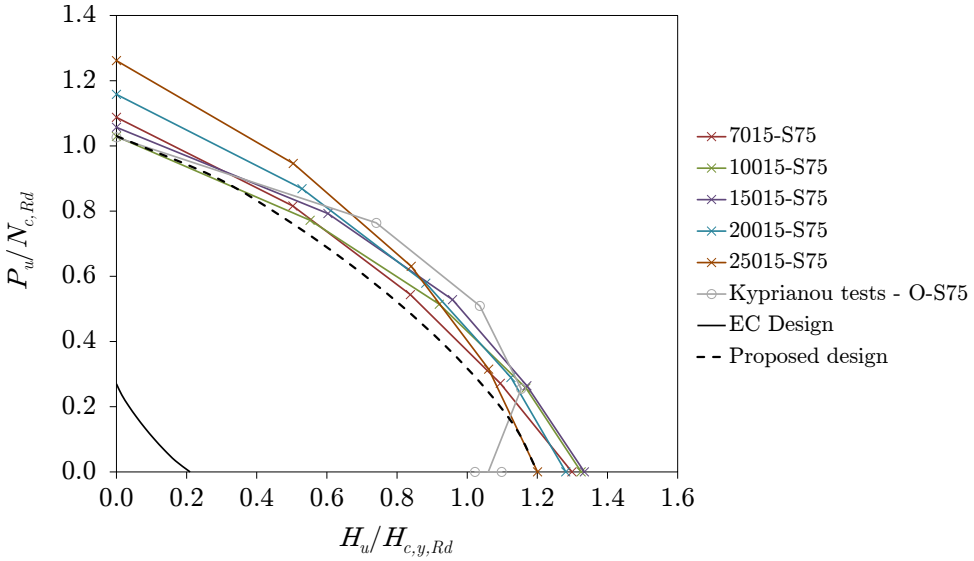


Figure 7.36: Interaction curve fitted to the FE and test data with fixings spaced at 75 mm

7.3.5 Connector limits

Limitations on the system capacity may arise from connector failure, hence relevant demands and resistances of the sheathing-to-steel connection assemblies need to be established.

7.3.5.1 Sheathing-to-column

7.3.5.1.1 Required demands for axial stability bracing

In accordance with Schafer (2013), the following expressions are provided for estimating the demand on the screws attaching similar sheathing on both flanges of the stud.

For the bearing demand $F_{Ed,br}$ on each screw, Equation (7.58) is given:

$$F_{Ed,br} = \frac{0.02 N_{Ed}}{L/s} \tag{7.58}$$

where N_{Ed} is the axial force applied to the stud member, L is the length of the member and s is the connector spacing.

For the pull-through demand $F_{Ed,pt}$ on each screw, Equation (7.58) is given:

$$F_{Ed,pt} = \frac{0.02 N_{Ed}(h/b)}{(L/s)(1+n)} \tag{7.59}$$

$$\text{where} \qquad n = \frac{k_x(h^2/4)}{k_\phi} \tag{7.60}$$

and h and b is the depth and width of the cross-section, respectively, while k_x is the lateral stiffness of the fastener-sheathing assembly and k_ϕ is the rotational stiffness of the fastener-sheathing assembly. The latter values are typically determined by testing; according to Peterman & Schafer (2014), for a 4.8 mm diameter screw connected to OSB: $k_x = 0.97$ kN/mm and $k_\phi = 95.3$ kNmm/rad, while for a 3.5 mm diameter screw connected to plasterboard: $k_x = 0.43$ kN/mm and $k_\phi = 96.0$ kNmm/rad.

However, when Equation (7.59) is compared against the results of the test specimens of the current study, predictions are not accurate. The expression failed to recognise failure in connection for the test specimens sheathed with plasterboard under compression (presented in Chapter 5) where a connector failure occurred for specimens with connector spacings at 600 mm, 300 mm and 150 mm intervals. As such, an empirical formula, based on the observed test results has been developed; this is given by Equation (7.61), where $\overline{\lambda}_d$ is the

non dimensional distortional slenderness of the cross-section given by Equation (7.7).

$$F_{Ed,pt,new} = \frac{0.008 N_{Ed} \overline{\lambda}_d}{\left(\frac{L}{s} + 1\right)^{0.3}} \tag{7.61}$$

Resistance estimations for screw connections between cold-formed steel and OSB or plasterboard in pull-through and bearing are provided in Section 4.4.1.2 and 4.4.2.2 of Chapter 4, respectively. A summary of these resistances is provided in Table 7.6.

Table 7.6: Summary of pull-through $F_{u,pt}$ and bearing $F_{u,po}$ capacities for certain configurations determined in Chapter 4

Configuration	$F_{u,pt}$ (kN)	$F_{u,po}$ (kN)
3.5 mm screw diameter in 12.5 mm thick plasterboard (for steel thicknesses 0.8 - 2.5 mm)	0.48	0.54
4.8 mm screw diameter in 11.1 mm thick OSB (for steel thicknesses 0.8 - 2.5 mm)	1.44	1.90

For use in design, the resistances given in Table 7.6 should be divided by a partial safety factor, as given by Equation (7.62), where 1.25 is the typical safety factor (γ_{M2}) adopted for connectors as per EN 1993-1-1 (2005).

$$F_{Rd,pt} = F_{u,pt}/1.25 \tag{7.62}$$

Rearranging Equation (7.61) in terms of the pull-through resistance and making the required axial force $N_{Rd,pt,fixing}$ the subject, results to Equation (7.63).

$$N_{Rd,pt,fixing} = \frac{F_{Rd,pt}\left(\frac{L}{s} + 1\right)^{0.3}}{0.008\overline{\lambda}_d} \tag{7.63}$$

In Tables 7.7 and 7.8, the accuracy of the proposed Equation (7.61) for predicting pull-through connection failure is assessed. Comparisons between the resistances and predictions of connector failure are presented in Table 7.7, while in Table 7.8, the axial resistance N_{Rd},

which is determined based on the recommendations provided in the previous sections by considering both restraint and fixity, is compared against $N_{Rd,pt,fixing}$ and the test results P_u, indicating accurate comparisons. Note that $N_{Rd,pt,fixing}$ is predicting connector failures without compromising the improved resistance prediction offered by N_{Rd}.

Table 7.7: Comparison between the proposed formula for pull-through demand, calculated based on the test results and the resistances; a value above one in the last column indicates a valid prediction of pull-though connector failure

Designation	P_u (kN)	Note	$F_{Ed,pt,new}$ (kN)	$F_{Rd,pt}$ (kN)	$F_{Ed,pt,new}/F_{Rd,pt}$
G-100-S600-1	69.0	Connector failure	0.42	0.384	1.09
G-100-S600-2	77.7	Connector failure	0.47	0.384	1.23
G-100-S300-1	76.5	Connector failure	0.39	0.384	1.01
G-100-S300-1	82.1	Connector failure	0.42	0.384	1.09
G-100-S150	85.5	Connector failure	0.36	0.384	0.94
G-100-S75	90.5	Local buckling	0.31	0.384	0.81
O-100-S600	79.5	Local buckling	0.48	1.152	0.42
O-100-S75	90.7	Local buckling	0.31	1.152	0.27

Table 7.8: Comparison between the axial resistance calculations, based on the design recommendation from the previous sections N_{Rd}, the axial resistance from the pull-though screw resistance $N_{Rd,pt,fixing}$ and the test results P_u

Designation	P_u (kN)	Note	N_{Rd} (kN)	$N_{Rd,pt,fixing}$ (kN)	$\min(N_{Rd}, N_{Rd,pt,fixing})/P_u$
G-100-S600-1	69.0	Connector failure	60.5	63.2	0.88
G-100-S600-2	77.7	Connector failure	60.5	63.2	0.78
G-100-S300-1	76.5	Connector failure	79.3	75.4	0.99
G-100-S300-1	82.1	Connector failure	79.3	75.4	0.92
G-100-S150	85.5	Connector failure	83.7	91.3	0.98
G-100-S75	90.5	Local buckling	84.2	111.4	0.93
O-100-S600	79.5	Local buckling	79.8	189.7	1.00
O-100-S75	90.7	Local buckling	87.3	334.2	0.96

It should be noted that the established expression for the required demand of screw pull-through has been based on the presented test data, and further research would be required for its wider application.

7.3.5.1.2 Required demands to resist torsion

In accordance with Schafer (2013), the required torsion T_{Ed} at a fastener location that develops due to the transverse actions on a sheathed member, may be determined, for a uniform distributed load w, by Equation (7.64), where s is the connector spacing and e is the eccentricity as shown in Figure 7.37.

$$T_{Ed} = wse \tag{7.64}$$

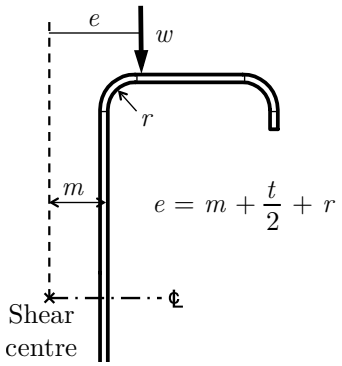


Figure 7.37: Assumed final location of horizontal load for twisting. From Peterman & Schafer (2014)

The eccentricity e depends on the cross-section characteristics and the rigidity of the section as twist progresses. The assumed value of the eccentricity is given by Equation 7.65:

$$e = m + t/2 + r \tag{7.65}$$

where m is the distance between the shear centre of the cross section and the midline of the web, t is the thickness of the steel member and r is the internal corner radius of the cross-section.

Based on the guidance provided by Peterman & Schafer (2014), the torsional demand is carried by the screw fixings in a combination of pull-through and bearing resistances. The torsional pull-through resistance is given by Equation (7.66), where $F_{Rd,pt}$ is the design pull-through resistance given by Equation 7.62, b is the width of the member and i is a

subscript referring to the two faces of the stud.

$$T_{pt,i} = F_{Rd,pt}(b/2) \tag{7.66}$$

Similarly, the torsional bearing resistance is determined by Equation (7.67) where h is the depth of the member and $F_{Rd,br}$ is the equivalent design resistance of bearing strength by considering an appropriate partial safety factor with the $F_{u,po}$ values presented in Table 7.6.

$$T_{br,i} = F_{Rd,br}(h/2) \tag{7.67}$$

Therefore, the total torsional resistance T_{Rd} of the screw fixing is given by Equation (7.68).

$$T_{Rd} = T_{pt,1} + T_{br,1} + T_{pt,2} + T_{br,2} \tag{7.68}$$

The method developed by Peterman & Schafer (2014) is supported by test data, for more information please refer to the work by Peterman & Schafer (2014) and Schafer (2013).

7.3.5.2 Column-to-track

As shown in the tests presented in Chapter 5, the 4.8 mm diameter screw connecting the stud to the track failed for OSB sheathed specimens with 75 mm spacings under pure bending. The screw connectors failed in shear due to significant slip between the track and the stud column during lateral loading. As already discussed in Section 6.5.3 of Chapter 6, a thicker track, of at least 2.5 mm thickness, and a stronger connection would be required to prevent such failure. Therefore, the use of tracks of sufficient thickness and a stronger connection, which can be achieved with a larger diameter screw or by using more than one screw fixings, is recommended. Further research is required in order to establish accurate demand capacities for the screw connectors between column and track in order to provide more precise design recommendations.

7.3.6 Deflection checks

A serviceability check for the maximum lateral deflection from lateral loads, such as wind, should be performed. The midspan deflection of a simply supported member in pure bending under a uniformly distributed load w is given by Equation (7.69):

$$\delta_{max} = \frac{5wL^4}{384(EI)_{comp}} \tag{7.69}$$

where $(EI)_{comp}$ is the stiffness of the steel stud and of the two sheathing boards on either side. This may be calculated by taking into consideration the shear connection effect; guidance is provided in Kyvelou (2017). A more conservative determination of $(EI)_{comp}$ is given by Equation (7.70), assuming no composite action:

$$(EI)_{comp} = EI_{y,eff} + 2E_{board}I_{y,board} \tag{7.70}$$

where E is the steel Young's modulus, $I_{y,eff}$ is the effective second moment of area of the steel member about its major axis, E_{board} is the Young's modulus of the board, which for plasterboard may be taken from Table 4.2 of Chapter 4 and for OSB from Table 4.3 of Chapter 4. The second moment of area of the board may be calculated as $I_{y,board} = b_{board}t_b^3/12$, where b_{board} is the width of the board equal to the spacing between studs in wall frames and t_b is the thickness of the board.

The deflection limit δ_{limit} for wall stud frames should be taken as the length of the member divided by 360, in accordance with Way & Heywood (2012).

$$\delta_{limit} = L/360 \tag{7.71}$$

7.4 Concluding remarks

Existing design standards are very conservative in predicting capacities for sheathed stud wall systems under compression, bending and combined loading. The contributing effects of sheathing on the structural stability of the stud wall are typically ignored or

very conservatively considered in the current design codes (EN 1993-1-1 2005, AISI S100 2016). A detailed overview of the effective width method, for determining the cross-sectional resistance of a member, in accordance with the provisions of EN 1993-1-3 (2006) is provided, which is followed by the member design methodology.

It has been shown, with safe predictions against test results, that an assumed minor axis and twist restraint equal to the spacing of connectors results in accurate predictions for the specimens sheathed with OSB. However, for the plasterboard-sheathed specimens, which are more prone to connection failure, an assumed restraint of equal to two times the connector spacing is more appropriate. Considering this bracing effect leads to gains in capacities in both pure compression and bending in excess of 300% when compared to the equivalent bare steel resistances without any restraint assumed. Employing the direct strength method for determining member strengths, based on an elastic buckling analysis with linear springs of particular stiffnesses for simulating the effects of the sheathing, as recommended in the literature, also yields to improved capacities comparable to those achieved with the assumed minor axis restraint using the Eurocode approach.

Further capacity gains can be achieved by considering end fixity for buckling about the major axis in pure compression, potential for the mobilisation of composite action in pure bending and an improved profile for the beam-column interaction design curve. Considering end fixity about the major axis leads to additional increases in compression capacity, from that already achieved with minor axis restraint, of about 10%, while composite action can lead to up to 30% improvement in the cross-sectional bending capacity with the closest 75 mm spacings. Note, in order to recognise end fixity, for OSB sheathed specimens, under compression, an effective length about the major axis of $0.5L$ is recommended, while for the equivalent system with plasterboard sheathing an effective length $0.7L$ was determined as more appropriate. A new convex shape for the interaction curve has been proposed, which is achieved with empirically determined power coefficients, based on the results of the finite element parametric results presented in Chapter 6. This contribution leads to up to 100% improvement in bending capacities for specimens loaded at 50% of their compressive capacity when compared to the equivalent resistance achieved with the current interaction

equation given by EN 1993-1-3 (2006).

Recommendations on the screw connector demand for pull-through and bearing for when the system is in compression or bending were also provided based on available expressions found in the literature (Schafer 2013), as well as developing an empirical expression for pull-through demand for when the stud is in compression. Although it is recognised that further research is required to establish a more rigorous approach in determining fixing demands under different loads, the recommendations presented herein have shown good agreement with the test results of the current study. The design recommendations presented herein, are straightforward to adopt within the current EN 1993-1-3 (2006) design framework.

Chapter 8

Conclusions and future research

IN the current chapter, a summary of the research presented in this thesis is provided and the principal conclusions from each chapter are outlined. Furthermore, a discussion on future research directly associated with the work presented in this thesis is provided as well as recommendations on further areas of research on stud wall systems.

8.1 Summary and conclusions

Wall systems made from cold-formed steel lipped channel vertical members (studs) set in tracks and sheathed with wood-based boards or gypsum plasterboards are becoming increasingly common in the construction industry. The versatility, practicality and economy associated with the quick construction process of these systems allows for their use both as non-structural and load-bearing wall systems. Although it has been recognised that bracing the member can result to enhanced capacities, the use of sheathing for this purpose is not considered systematically in design and as a result its structural contribution is typically ignored in the design of wall stud frames. The scope of this thesis was to illustrate that the impact of sheathing on wall studs can be structurally considered and highlight in what areas this contribution may be.

The first step in studying the behaviour of sheathed stud wall systems was to have a thorough understanding of the material behaviour of the individual components and of

the interaction between them. As a result, an experimental investigation into the material response of, and interaction between, the different components of a typical sheathed cold-formed steel wall system was performed, with results presented in Chapter 3. A total of 103 material and component tests was performed, covering tensile tests on cold-formed steel coupons, compressive and tensile material tests on OSB and plasterboard coupons (extracted from both the longitudinal and transverse board directions), tensile and shear screw connector tests and, finally, pull-through and push-out (shear) tests to examine the behaviour of screwed steel-to-board connections. Mechanical properties for plasterboard and OSB were established, with the longitudinal properties from both materials demonstrating the highest strength, with that of OSB in compression being as much as three times than that of plasterboard.

The pull-through experiments featured different types of screws and sheathing boards such as OSB and plasterboard, with the latter board type studied in both single and double layer arrangements. It was observed that the shape of the underside of the screw head had a significant influence on the pull-through response, with flatter heads resulting in improved capacity and ductility. Also, using two layers of plasterboard led to average increases of 60% in stiffness and 30% in strength, when compared to a single plasterboard layer. Push-out tests were undertaken to investigate the shear behaviour of screwed connections between cold-formed steel sections and sheathing boards. The varied parameters were the screw size, the number of board layers and the steel thickness. The shear strength of the connection was found to increase with increasing steel thickness, screw diameter and number of plasterboard layers. The main failure modes were screw tilting and screw bending, with the latter mode being more prominent in the specimens with the stronger and thicker boards. At the end of Chapter 3, experimental data from the literature, to complement the reported test data, were collected and discussed, while setting the scene for their assessment and development of analytical models to describe the observed mechanical responses of the material and components comprising sheathed cold-formed steel wall systems in Chapter 4.

An experimental dataset comprising the results of more than 400 physical tests, were used as the basis for underpinning the development of predictive analytical expressions in

Chapter 4. The two models employed to describe the material behaviour of plasterboard and OSB were the single stage Ramberg-Osgood expression up to the ultimate material stress and the Mander et al. (1988) model; both models were found to be capable of accurately capturing the response of plasterboard and OSB, while the latter one was also able to account for the post peak decreasing capacity, observed in compression. A modified version of the Ramberg-Osgood expression was employed for modelling the pull-through behaviour of screwed connections in plasterboard or OSB up to the ultimate capacity, while the observed post-peak behaviour was modelled with linear functions. An expression, based on the geometric and material properties of the components, was developed for determining the pull-through capacity, while stiffness and ultimate deformation were expressed as functions of the screw diameter and board thickness. The shear behaviour of screwed connections between steel and either plasterboard or OSB was accurately captured, up to their ultimate capacity, using a model consisting of two single Ramberg-Osgood expressions. It was found that the EN 1993-1-5 (2006) equations for screw tilting could accurately predict the ultimate capacity of a connection with plasterboard while, for OSB, the expressions corresponding to failure due to screw bending for thin steel plates combined with pull-through yielded consistent and accurate capacity predictions. A new empirical expression for the calculation of the embedment strength of plasterboard was also developed.

Experimental studies on full-scale sheathed cold-formed-steel studs, investigating the influence of board type and connector spacing under various loading conditions were presented in Chapter 5. Seventeen sheathed studs, comprising eight specimens under pure compression, six specimens under combined loading and three under pure bending, were carried out, along with supporting material tests and imperfection measurements. The tested specimens were sheathed with either plasterboard or OSB, on both sides, with various stud-to-sheathing connector spacings ranging from 600 mm to 75 mm.

For the test specimens subjected to pure compression, the controlling failure mode exhibited by the studs connected to plasterboards at the wider spacings (i.e. 600 mm and 300 mm) was pull-through of the connectors, while for the studs with the closest spaced connectors of 75 mm, local buckling was the dominant failure mode. For the OSB-sheathed

beam-column specimens local failure at the service openings was observed, while for the specimens subjected to pure bending, local buckling and stud-to-track connector failure occurred. Reducing the spacing of the connectors from 600 mm to 75 mm resulted in up to 20% increases in the capacity of the specimens sheathed with OSB under both compression and bending. For the specimens sheathed with plasterboards and subjected to pure compression, reducing the connector spacing from 600 mm to 75 mm resulted in up to 30% increases in capacity while pull-through connector failure was also prevented.

In Chapter 6, the methodology for developing a sophisticated finite element model, which can simulate the behaviour of sheathed cold-formed steel studs set in tracks and subjected to various loading configurations (i.e. compression, bending and combinations of the two) is presented. The finite element models included geometrical imperfections, while both geometric and material nonlinearities were accounted for in the analysis. Nonlinear material behaviour for both steel and sheathing was employed with material models used to describe the behaviour provided in Chapter 4. The finite element simulations were found to be capable of realistically describing the column-to-track boundary conditions, while the contact interaction between the cold-formed steel columns and the boards, as well as the nonlinear behaviour of the employed connectors, were explicitly replicated.

The finite element models were validated against physical tests from four different studies in the literature, including the experiments reported in Chapter 5. In total, 56 physical tests were employed for the validation process. Following successful validation, the finite element models were employed to investigate the influence of the sheathing, section depth and fastener spacing on the load-bearing capacity of the columns under various loading scenarios. It was found that the addition of sheathing leads to significant increases in the load-carrying capacity of the system over the bare steel column; sheathing on both sides of the cold-formed steel studs with the more robust OSB panels led to about a 100% increase in capacity. The main reason for the gains in capacity is the restraint of the global buckling modes, while further increases due to closer connector spacing are attributed to a reduction of the wavelength of the distortional buckles and to the mobilisation of composite action between the boards and the column.

The parametric studies in the finite element simulations demonstrated that decreasing the fastener spacing led to improvements in terms of ultimate capacity and stiffness under all loading configurations, with up to about 7% and 8% increase in capacity and stiffness, respectively, for specimens in pure compression and up to about 20% and 15% increase in capacity and stiffness, respectively, for specimens in pure bending when decreasing connector spacing from 600 mm to 75 mm. The characteristics of the end tracks as well as the strength of the stud-to-track connections were found to have the potential to significantly affect the response of the examined systems, limiting their ultimate capacity. Recommendations based on the numerical results for having thicker end tracks (of up to 2.5 mm thick) and a stronger stud-to-track connection achieved either with a larger diameter screw or by using more than one screw connector were therefore made to secure the efficient performance of sheathed cold-formed steel stud wall systems.

Preliminary design recommendations for sheathed cold-formed steel studs under combined compression and major bending axis are provided in Chapter 7. The set of rules provided are based on the design methodology of EN 1993-1-3 (2006), but leading to significantly higher capacity predictions achieved by harnessing structurally the presence of the sheathing. Hence, at the start of Chapter 7 a detailed overview of the effective width method, for determining the cross-sectional resistance of a member, in accordance with the provisions of EN 1993-1-3 (2006) is provided, which is followed by a description of the member design methodology.

In the proposed approach, the additional capacity gains brought by a stronger connection (due to increased number of fixings) between the sheathing and the stud are also recognised. The increased capacities predicted by the proposed design are attributed to the recognition of four factors: (i) restraint in the minor axis based on the connector spacings, (ii) end fixity of boundary conditions under compression, (iii) potential for mobilisation of composite action between the sheathing and steel under pure bending and (iv) a convex shape for the interaction curve under combined loading. Gains in capacities when compared to the resistances achieved by an assumed unrestrained bare steel design is more than 4-5 times. Demand and resistance calculations on the connection between sheathing and

steel should be evaluated as they could limit the system capacity; recommendations were provided, but it is recognised that further research is needed for determining accurately connector demands for any given stud wall system.

8.2 Potential impact

Owing to their enhanced load-carrying capacity, sheathed cold-formed studs can provide solutions to even higher building construction with light steel frames, as well as the use of less material, by using thinner steel members, and fewer members such as the elimination of horizontal mid-height bracing sections. The horizontal bracing members, typically used in an all-steel design, would no longer be necessary since all bracing can be assumed to be taken by the sheathing, assuming adequate connection exists with the column.

It should of course be noted that additional fixings come at a cost and that there is a tradeoff between structural performance and practicality of installation. It is recognised though that the increased cost is not so much associated with the amount of screws in terms of material volume but with the time spent by the worker in the construction process. Thus, it is envisaged in the future, where automation is increased and pre-assembled panels are manufactured in a factory setting, before being delivered at the construction site, that the screws are inserted robotically rather than by a worker, as such, the cost associated with increased connection is driven considerably down.

8.3 Future research

8.3.1 Directly related to the present study

One of the most complex problems in the design of sheathed stud specimens is determining accurately the demand on the sheathing-to-column connectors. The finite element models developed in Chapter 6 can be used to determine the bracing demand on the connector (which were simulated as nonlinear springs in terms of the pull-through and shear behaviour) by extracting the demand force from each connector and comparing to the re-

spective load on the system. Assembling a large dataset with such results, from a series of parametric studies, can then lead to empirically determined expressions.

In Chapter 6, the finite element parametric simulations were carried out only for specimens of 2.4 m length and one thickness, these parametric studies can be extended for longer specimens and a wider spectrum of thicknesses.

In Chapter 7, where the basic steps for considering composite action were outlined, there is need for further investigation for cross-sections classified as Class 3 or 4 when full-composite action is considered, as well as accurately determining the minimum degree of shear connection for sheathed stud wall systems when under bending.

8.3.2 Further areas of research

Further work could be based on designing improved screw connectors for use in sheathed stud frames so that they can withstand higher bearing and pull-through forces. An example of such a connector, with an embedded washer, is illustrated in Figure 8.1, which in accordance with the design resistance calculations developed in Chapter 4 could result in a considerable increase in the pull-through capacity in a given sheathing-to steel connection assembly.

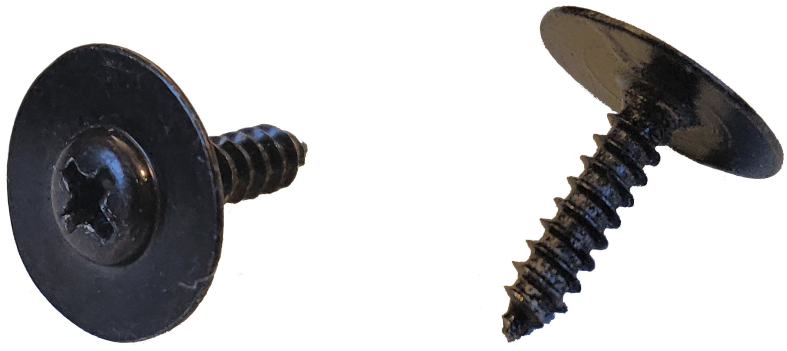


Figure 8.1: Screw connectors with a large flat head

Other avenues of recommended research include, investigation of:

(i) Different sheathing material on each side of the stud under combined compression and bending.

(ii) One sided sheathed stud in compression, bending and combined loading.

(iii) The behaviour of a wall stud frame consisting of five studs under combined loads.

(iv) The behaviour of sheathed back-to-back stud columns under combined compression and bending.

(v) The behaviour of a sheathed stud wall under dynamic loads.

(vi) Optimisation of the cross-section geometry of the stud.

References

ABAQUS (2016) *Version 6.19*, Dassault Systèmes Simulia Corp., Johnston, RI, USA.

Abdel-Rahman, N. & Sivakumaran, K. S. (1997) 'Material properties models for analysis of cold-formed steel members', *Journal of Structural Engineering* **123**(9), 1135–1143.

Abu-Hamd, M. (2019) 'Experimental study on screw connections in cold-formed steel walls with cement sheathing', *Advances in Structural Engineering* **22**(9), 2033–2047.

Afshan, S., Rossi, B. & Gardner, L. (2013) 'Strength enhancements in cold-formed structural sections — Part I: Material testing', *Journal of Constructional Steel Research* **83**, 177–188.

AISI (1962) *Light Gage Cold-formed Steel Design Manual*, American Iron and Steel Institute, Washington, D.C.

AISI (1980) *Light Gage Cold-formed Steel Design Manual*, American Iron and Steel Institute, Washington, D.C.

AISI (1996) *Cold-Formed Steel Design Manual*, American Iron and Steel Institute, Washington, D.C.

AISI S100 (2016) *North American specification for the design of cold-formed steel structural members*, American Iron and Steel Institute, Washington, D.C.

AISI S211 (2012) *North American standard for cold-formed steel framing — Wall stud design (including Supplement 1)*, American Iron and Steel Institute, Washington, D.C.

Allwood, J. M., Cullen, J. M., Carruth, M. A., Cooper, D. R., McBrien, M., Milford, R. L.,

Moynihan, M. C. & Patel, A. C. H. (2012) *Sustainable materials: with both eyes open*, UIT Cambridge Ltd, Cambridge, UK.

Arrayago, I., Real, E. & Gardner, L. (2015) 'Description of stress–strain curves for stainless steel alloys', *Materials & Design* **87**, 540–552.

Ashraf, M., Gardner, L. & Nethercot, D. A. (2006) 'Finite element modelling of structural stainless steel cross-sections', *Thin-Walled Structures* **44**(10), 1048–1062.

AS/NZS 4600 (2018) *Cold-formed steel structures*, Standards Australia/Standards New Zealand.

B1M (2020) 'How to build more homes, faster'. [Accessed: 1st of December 2020].
URL: *https://www.theb1m.com/video/how-we-can-build-more-homes-faster*

Becque, J. & Rasmussen, K. J. (2009*a*) 'Experimental investigation of local-overall interaction buckling of stainless steel lipped channel columns', *Journal of Constructional Steel Research* **65**(8), 1677–1684.

Becque, J. & Rasmussen, K. J. (2009*b*) 'A numerical investigation of local–overall interaction buckling of stainless steel lipped channel columns', *Journal of Constructional Steel Research* **65**(8), 1685–1693.

Bernard, E. S. (1993) Flexural behaviour of cold-formed profiled steel decking, PhD thesis, University of Sydney, Sydney, Australia.

Bleich, F. (1952) *Buckling strength of metal structures*, Mc Graw-Hill, New York.

Bluehill (2019) *Data acquisition system*, Instron.

Bonada, J., Casafont, M., Roure, F. & Pastor, M. M. (2012) 'Selection of the initial geometrical imperfection in nonlinear fe analysis of cold-formed steel rack columns', *Thin-Walled Structures* **51**, 99–111.

BS 5950-5 (1998) *British Standard 5950: Structural use of steelwork in building — Part 5: Code of practice for design of cold formed thin gauge sections*, BSI.

BS EN 10143 (2006) *Continuously hot-dip coated steel sheet and strip — Tolerances on dimensions and shape*, BSI.

BS EN 10346 (2015) *Continuously hot-dip coated steel flat products for cold forming — Technical delivery conditions*, BSI.

Bulson, P. S. (1970) *The stability of flat plates*, Chatto & Windus, London.

Cai, J., Schafer, B. D. & Moen (2017) CUFSM elastic buckling analysis software module for quantifying hole effects in thin-walled structural members, *in* 'Proceedings of the Annual Stability Conference Structural Stability Research Council', San Antonio, Texas, USA.

Camotim, D., Dinis, P. B. & Martins, A. D. (2016) Direct strength method — a general approach for the design of cold-formed steel structures, *in* C. Yu, ed., 'Recent trends in cold-formed steel construction', Woodhead Publishing, chapter 4, pp. 69–105.

Camotim, D., Silvestre, N. & Dinis, P. B. (2005) 'Numerical analysis of cold-formed steel members', *Steel Structures* **5**(1), 63–78.

Chajes, A., Britvec, S. J. & Winter, G. (1963) 'Effects of cold-straining on structural sheet steels', *Journal of the Structural Division* **89**(2), 1–32.

Chen, B., Roy, K., Uzzaman, A., Raftery, G. & Lim, J. B. P. (2020) 'Axial strength of back-to-back cold-formed steel channels with edge-stiffened holes, un-stiffened holes and plain webs', *Journal of Constructional Steel Research* **174**, 106313.

Chen, G. & He, B. (2017) 'Stress-strain constitutive relation of osb under axial loading: An experimental investigation', *BioResources* **12**(3), 6142–6156.

Chen, W., Ye, J. & Chen, T. (2016) 'Design of cold-formed steel screw connections with gypsum sheathing at ambient and elevated temperatures', *Applied Sciences* **6**(9), 248.

Chou, S. M., Chai, G. B. & Ling, L. (2000) 'Finite element technique for design of stub columns', *Thin-Walled Structures* **37**(2), 97–112.

Dat, D. T. & Peköz, T. (1980) The strength of cold-formed steel columns, Report No. 80-4, Department of Structural Engineering, Cornell University, Ithaca, New York, USA.

Datascan (2019) *Datascan acquisition system*, Carollton, Texas, USA.

DaVis (2019) *Version 10.0.5.4259*, LaVision, Göttingen, Germany.

Davison, B. & Owens, G. W., eds (2012) *Steel designers' manual*, 7^{th} edn, John Wiley & Sons.

Dawson, R. G. & Walker, A. C. (1972) 'Post-buckling of geometrically imperfect plates', *Journal of the Structural Division* **98**(1), 75–94.

Dinis, P. B., Camotim, D. & Silvestre, N. (2007) 'FEM-based analysis of the local-plate/distortional mode interaction in cold-formed steel lipped channel columns', *Computers & Structures* **85**(19-20), 1461–1474.

Dubina, D., Ungureanu, V. & Landolfo, R. (2012) *Design of Cold-formed Steel Structures: Eurocode 3: Design of Steel Structures. Part 1-3 Design of cold-formed Steel Structures*, European Convention for Constructional Steelwork (ECCS).

ECCS (2008) Technical Committee 7 Cold-formed steel — Worked examples according to EN 1993-1-3, Technical Report 123, European Convention for Constructional Steelwork.

Ellobody, E. (2014) *Finite element analysis and design of steel and steel–concrete composite bridges*, Butterworth-Heinemann.

EN 12369-1 (2001) *Wood-based panels — Characteristic values for structural design — Part 1: OSB, particleboards and fibreboards*, European Committee for Standardization, Brussels, Belgium.

EN 1383 (2016) *Timber structures — Test methods — Pull through resistance of timber fasteners*, European Committee for Standardization, Brussels, Belgium.

EN 14566:2008+A1 (2009) *Mechanical fasteners for gypsum plasterboard systems — Definitions, requirements and test methods*, European Committee for Standardization, Brussels, Belgium.

EN 1993-1-1 (2005) *Eurocode 3: Design of steel structures — Part 1-1: General rules and rules for buildings*, European Committee for Standardization, Brussels, Belgium.

EN 1993-1-3 (2006) *Eurocode 3: Design of steel structures — Part 1-3: General rules — Supplementary rules for cold-formed members and sheeting*, European Committee for Standardization, Brussels, Belgium.

EN 1993-1-5 (2006) *Eurocode 3: Design of steel structures — Part 1-5: Plated structural elements*, European Committee for Standardization, Brussels, Belgium.

EN 1994-1-1 (2004) *Eurocode 4: Design of composite steel and concrete structures — Part 1-1: General rules and rules for buildings*, European Committee for Standardization, Brussels, Belgium.

EN 1995-1-1 (2004) *Eurocode 5: Design of timber structures — Part 1-1: General - Common rules and rules for buildings*, European Committee for Standardization, Brussels, Belgium.

EN 300 (2006) *Oriented Strand Boards (OSB) — Definitions, classification and specifications*, European Committee for Standardization, Brussels, Belgium.

EN 520 (2009) *Gypsum plasterboards — Definitions, requirements and test methods*, European Committee for Standardization, Brussels, Belgium.

EN 789 (2005) *Timber structures. Test methods. Determination of mechanical properties of wood based panels*, European Committee for Standardization, Brussels, Belgium.

EN ISO 6892 (2016) *Metallic materials - Tensile testing. Part 1: Method of test at room temperature*, European Committee for Standardization, Brussels, Belgium.

Feng, M., Wang, Y. C. & Davies, J. M. (2003) 'Structural behaviour of cold-formed thin-walled short steel channel columns at elevated temperatures, Part 1: Experiments', *Thin-Walled Structures* **41**(6), 543–570.

Fiorino, L., Della Corte, G. & Landolfo, R. (2007) 'Experimental tests on typical screw connections for cold-formed steel housing', *Engineering Structures* **29**(8), 1761–1773.

Fiorino, L., Pali, T., Bucciero, B., Macillo, V., Terracciano, M. T. & Landolfo, R. (2017) 'Experimental study on screwed connections for sheathed CFS structures with gypsum or cement based panels', *Thin-Walled Structures* **116**, 234–249.

Fratamico, D. C. & Schafer, B. W. (2014) Numerical studies on the composite action and buckling behavior of built-up cold-formed steel columns, *in* '22nd International Specialty Conference on Cold-formed Steel Structures', St. Louis, Missouri, USA, pp. 213–228.

Fratamico, D. C., Torabian, S., Zhao, X., Rasmussen, K. J. R. & Schafer, B. W. (2018) 'Experiments on the global buckling and collapse of built-up cold-formed steel columns', *Journal of Constructional Steel Research* **144**, 65–80.

Fülöp, L. A. & Dubina, D. (2004) 'Performance of wall-stud cold-formed shear panels under monotonic and cyclic loading: Part I: Experimental research', *Thin-Walled Structures* **42**(2), 321–338.

Gardner, L. (2011) Stability of steel beams and columns, SCI Publication: P360, The Steel Construction Institute, UK.

Gardner, L. & Ashraf, M. (2006) 'Structural design for non-linear metallic materials', *Engineering Structures* **28**(6), 926–934.

Gardner, L. & Nethercot, D. (2004*a*) 'Numerical modeling of stainless steel structural components—a consistent approach', *Journal of Structural Engineering* **130**(10), 1586–1601.

Gardner, L. & Nethercot, D. A. (2004*b*) 'Experiments on stainless steel hollow sections—part 1: Material and cross-sectional behaviour', *Journal of Constructional Steel Research* **60**(9), 1291–1318.

Gardner, L., Saari, N. & Wang, F. (2010) 'Comparative experimental study of hot-rolled and cold-formed rectangular hollow sections', *Thin-Walled Structures* **48**(7), 495–507.

Gardner, L. & Yun, X. (2018) 'Description of stress-strain curves for cold-formed steels', *Construction and Building Materials* **189**, 527–538.

Gorst, N. J. S., Williamson, S. J., Pallett, P. F. & Clark, L. A. (2003) Friction in temporary works, Research Report 71, University of Birmingham, Birmingham, U.K.

Green, G. G., Winter, G. & Cuykendall, T. R. (1947) Light gage steel columns in wall-braced panels, Bulletin 35 Part 2, Engineering Experiment Station, Cornell University, Ithaca, NY, USA.

Grubb, J. P., Gorgolewksi, T. M. & Lawson, M. R. (2001) Building design using cold formed steel sections: Light steel framing in residential constuction, SCI Publication: P301, The Steel Construction Institute, UK.

Grubb, J. P., Thepaut, R. & Mettem, C. (2003) Lightweight steel/timber composite solutions: Information and guidance for new product development, SCI Electronic Publication: ED002, The Steel Construction Institute, UK.

Hadjipantelis, N., Gardner, L. & Wadee, M. A. (2019) 'Finite-element modeling of prestressed cold-formed steel beams', *Journal of Structural Engineering* **145**(10), 04019100.

Haidarali, M. R. (2011) Local and distortional buckling behaviour of cold-formed steel Z section beams, PhD thesis, Imperial College London, London, UK.

Hancock, G. J. (2003) 'Cold-formed steel structures', *Journal of Constructional Steel Research* **59**(4), 473–487.

Hancock, G. J., Kwon, Y. B. & Bernard, E. S. (1994) 'Strength design curves for thin-walled sections undergoing distortional buckling', *Journal of Constructional Steel Research* **31**(2-3), 169–186.

Hancock, G., Wilkinson, T. J. & Zhao, X. (2005) *Cold-formed tubular members and connections: Structural behaviour and design*, Elsevier.

Heywood, M. D., Lawson, M. R. & Way, A. G. J. (2012) *Light steel structures and modular construction in Steel designers' manual*, 7^{th} edn, John Wiley & Sons, chapter 8, pp. 238–270.

Hill, H. N. (1944) Determination of stress-strain relations from "offset" yield strength values, National Advisory Committee for Aeronautics, Technical Notes: No. 927, Aluminum Company of America.

Hill, R. (1950) *The mathematical theory of plasticity*, Oxford University Press.

Ho, H. C. & Chung, K. F. (2006) 'Analytical prediction on deformation characteristics of lapped connections between cold-formed steel Z sections', *Thin-Walled Structures* **44**(1), 115–130.

Hui, C. (2014) Moment redistribution in cold-formed steel purlin systems, PhD thesis, Imperial College London, London, UK.

Ingvarsson, L. (1977) Cold-forming residual stresses and box columns built up by two cold-formed channel sections welded together, Bulletin of the Department of Building Statics and Structural Engineering - 121, The Royal Institute of Technology, Stockholm, Sweden.

Jandera, M., Gardner, L. & Machacek, J. (2008) 'Residual stresses in cold-rolled stainless steel hollow sections', *Journal of Constructional Steel Research* **64**(11), 1255–1263.

Johnson, R. P. (2004) *Composite structures of steel and concrete: beams, slabs, columns, and frames for buildings*, 3^{rd} edn, Wiley-Blackwell.

Karren, K. W. (1967) 'Corner properties of cold-formed shapes', *Journal of the Structural Division, ASCE Proceedings* **93**(1), 401–432.

Karren, K. W. & Winter, G. (1967) 'Effects of cold-forming on light-gage steel members', *Journal of the Structural Division, ASCE Proceedings* **93**(1), 433–469.

Kechidi, S., Fratamico, D. C., Bourahla, N., Castro, J. M. & Schafer, B. W. (2017) Numerical study of screw fasteners in built-up CFS chord studs, *in* '8th European Conference on Steel and Composite Structures - Eurosteel 2017', Vol. 1, Copenhagen, Denmark, pp. 1543–1552.

Kechidi, S., Fratamico, D. C., Schafer, B. W., Castro, J. M. & Bourahla, N. (2020) 'Simulation of screw connected built-up cold-formed steel back-to-back lipped channels under axial compression', *Engineering Structures* **206**, 110109.

Kulatunga, M. P. & Macdonald, M. (2013) 'Investigation of cold-formed steel structural members with perforations of different arrangements subjected to compression loading', *Thin-Walled Structures* **67**, 78–87.

Kwon, Y. B. & Hancock, G. J. (1992) 'Tests of cold-formed channels with local and distortional buckling', *Journal of Structural Engineering* **118**(7), 1786–1803.

Kyprianou, C. (2015) 'Use of LTBeamN', *New Steel Construction* (January 2015), 25–27.

Kyprianou, C., Kyvelou, P., Gardner, L. & Nethercot, D. A. (2018) Numerical study of sheathed cold-formed steel columns, *in* 'Proceedings of the ninth international conference on Advances in Steel Structures', Hong Kong, China.

Kyprianou, C., Kyvelou, P., Gardner, L. & Nethercot, D. A. (2021*a*) 'Characterisation of material and connection behaviour in sheathed cold-formed steel wall systems - Part 1: Experimentation and data compilation', *Structures* **30**, 1161–1183.

Kyprianou, C., Kyvelou, P., Gardner, L. & Nethercot, D. A. (2021*b*) 'Characterisation of material and connection behaviour in sheathed cold-formed steel wall systems - Part 2: Analytical modelling', *Structures* **30**, 1184–1199.

Kyprianou, C., Kyvelou, P., Gardner, L. & Nethercot, D. A. (2021*c*) 'Experimental study of sheathed cold-formed steel beam-columns', *Thin-Walled Structures [Accepted]* .

Kyprianou, C., Kyvelou, P., Gardner, L. & Nethercot, D. A. (2021*d*) Experiments on sheathed cold-formed steel beam-columns, *in* 'Eurosteel 2021', Sheffield, UK.

Kyvelou, P. (2017) Structural behaviour of composite cold-formed steel systems, PhD thesis, Imperial College London, London, UK.

Kyvelou, P., Gardner, L. & Nethercot, D. A. (2015) 'Composite action between cold-formed steel beams and wood-based floorboards', *International Journal of Structural Stability and Dynamics* **15**(8), 1540029.

Kyvelou, P., Gardner, L. & Nethercot, D. A. (2017*a*) 'Design of composite cold-formed steel flooring systems', *Structures* **12**, 242–252.

Kyvelou, P., Gardner, L. & Nethercot, D. A. (2017*b*) 'Testing and analysis of composite cold-formed steel and wood-based flooring systems', *Journal of Structural Engineering* **143**(11), 04017146.

Kyvelou, P., Gardner, L. & Nethercot, D. A. (2018) 'Finite element modelling of composite cold-formed steel flooring systems', *Engineering Structures* **158**, 28–42.

Kyvelou, P., Kyprianou, C., Gardner, L. & Nethercot, D. A. (2019) 'Challenges and solutions associated with the simulation and design of cold-formed steel structural systems', *Thin-Walled Structures* **141**, 526–539.

Kyvelou, P., Nethercot, D., Hadjipantelis, N., Kyprianou, C. & Gardner, L. (2020) 'The evolving basis for the design of light gauge steel systems', *International Journal of Structural Stability and Dynamics* **20**(13), 2041008.

Lange, J. & Naujoks, B. (2006) 'Behaviour of cold-formed steel shear walls under horizontal and vertical loads', *Thin-Walled Structures* **44**(12), 1214–1222.

Lau, S. C. W. (1988) Distortional buckling of thin-walled columns, PhD thesis, University of Sydney, Sydney, Australia.

Lau, S. C. W. & Hancock, G. J. (1987) 'Distortional buckling formulas for channel columns', *Journal of Structural Engineering* **113**(5), 1063–1078.

Lawson, R. M. & Ogden, R. G. (2008) ''Hybrid' light steel panel and modular systems', *Thin-Walled Structures* **46**(7-9), 720–730.

Lawson, R. M., Way, A. G., Heywood, M., Lim, J. B. P., Johnston, R. & Roy, K. (2019) 'Stability of light steel walls in compression with plasterboards on one or both sides', *Proceedings of the Institution of Civil Engineers-Structures and Buildings* pp. 1–19.

Lee, Y. & Miller, T. H. (2001) 'Axial strength determination for gypsum-sheathed, cold-formed steel wall stud composite panels', *Journal of Structural Engineering* **127**(6), 608–615.

Li, Z. & Schafer, B. W. (2010) Buckling analysis of cold-formed steel members with general boundary conditions using CUFSM: conventional and constrained finite strip methods, *in* 'Twentieth International Speciality Conference on Cold-Formed Steel Structures', St. Louis, Missouri.

Lian, Y., Uzzaman, A., Lim, J. B. P., Abdelal, G., Nash, D. & Young, B. (2016) 'Effect of web holes on web crippling strength of cold-formed steel channel sections under end-one-flange loading condition – part i: Tests and finite element analysis', *Thin-Walled Structures* **107**, 443–452.

Liang, Y., Manninen, T., Zhao, O., Walport, F. & Gardner, L. (2019) 'Elevated temperature material properties of a new high-chromium austenitic stainless steel', *Journal of Constructional Steel Research* **152**, 261–273.

Mander, J. B., Priestley, M. J. N. & Park, R. (1988) 'Theoretical stress-strain model for confined concrete', *Journal of Structural Engineering* **114**(8), 1804–1826.

Miller, T. H. & Peköz, T. (1993) 'Behavior of cold-formed steel wall stud assemblies', *Journal of Structural Engineering* **119**(2), 641–651.

Miller, T. H. & Peköz, T. (1994) 'Behavior of gypsum-sheathed cold-formed steel wall studs', *Journal of Structural Engineering* **120**(5), 1644–1650.

Mirambell, E. & Real, E. (2000) 'On the calculation of deflections in structural stainless steel beams: an experimental and numerical investigation', *Journal of Constructional Steel Research* **54**(1), 109–133.

Moen, C. D., Igusa, T. & Schafer, B. W. (2008) 'Prediction of residual stresses and strains in cold-formed steel members', *Thin-Walled Structures* **46**(11), 1274–1289.

Moen, C. D., Padilla-Llano, D. A., Corner, S. & Ding, C. (2014) Towards load-deformation models for screw-fastened cold-formed steel-to-steel shear connections, *in* 'Twenty-Second International Specialty Conference on Cold-Formed Steel Structures', St. Louis, Missouri, USA.

Moen, C. D. & Schafer, B. W. (2009) 'Elastic buckling of cold-formed steel columns and beams with holes', *Engineering Structures* **31**(12), 2812–2824.

Moen, C. D., Tao, F. & Cole, R. (2016) Monotonic and cyclic backbone response of single shear cold-formed steel screw-fastened connections, *in* 'The international colloquium on stability and ductility of steel structures'.

Moreyra, M. E. & Peköz, T. (1994) Finite element studies on lipped channel flexural members, *in* 'Twelfth International Specialty Conference on Cold-Formed Steel Structures: Recent Research and Developments in Cold-Formed Steel Design and Construction', University of Missouri–Rolla, St. Louis, Missouri, USA.

Mulligan, G. P. & Peköz, T. (1984) 'Locally buckled thin-walled columns', *Journal of Structural Engineering* **110**(11), 2635–2654.

NCCI SN001a (2005) *Critical axial load for torsional and flexural torsional buckling modes*, SCI/CTICM.

NCCI SN002a (2005) *Determination of non-dimensional slenderness of I and H sections*, SCI.

NCCI SN003b (2005) *Elastic critical moment for lateral torsional buckling*, SCI/CTICM.

Nethercot, D. A., ed. (2003) *Composite construction*, Spon Press.

Nithyadharan, M. & Kalyanaraman, V. (2011) 'Experimental study of screw connections in cfs-calcium silicate board wall panels', *Thin-Walled Structures* **49**(6), 724–731.

Oehlers, D. J. & Bradford, M. A. (1995) *Composite Steel and Concrete Structural Members. Fundamental Behaviour*, Pergamon Press, Oxford, UK.

Peterman, K. D. (2012) Experiments on the stability of sheathed cold-formed steel studs under axial load and bending, MSc thesis, Johns Hopkins University, Baltimore, Maryland, USA.

Peterman, K. D., Nakata, N. & Schafer, B. W. (2014) 'Hysteretic characterization of cold-formed steel stud-to-sheathing connections', *Journal of Constructional Steel Research* **101**, 254–264.

Peterman, K. D. & Schafer, B. W. (2013) Hysteretic shear response of fasteners connecting sheathing to cold-formed steel studs, Research report, CFS-NEES, RR04.

Peterman, K. D. & Schafer, B. W. (2014) 'Sheathed cold-formed steel studs under axial and lateral load', *Journal of Structural Engineering* **140**(10), 04014074.

Petrone, C., Magliulo, G. & Manfredi, G. (2016) 'Mechanical properties of plasterboards: experimental tests and statistical analysis', *Journal of Materials in Civil Engineering* **28**(11), 04016129.

Pham, C. H. & Hancock, G. J. (2010) 'Numerical simulation of high strength cold-formed purlins in combined bending and shear', *Journal of Constructional Steel Research* **66**(10), 1205–1217.

Plenzler, R., Ludwiczak-Niewiadomska, L. & Strzelecki, P. (2017) 'Elastic and strength properties of OSB layers', *Drvna industrija: Znanstveni časopis za pitanja drvne tehnologije* **68**(1), 3–9.

Ramberg, W. & Osgood, W. R. (1943) Description of stress-strain curves by three parameters, Technical Notes 902, National Advisory Committee for Aeronautics, Washington.

Rasmussen, K. J., Burns, T., Bezkorovainy, P. & Bambach, M. R. (2003) 'Numerical modelling of stainless steel plates in compression', *Journal of Constructional Steel Research* **59**(11), 1345–1362.

Rasmussen, K. J. R. (2003) 'Full-range stress–strain curves for stainless steel alloys', *Journal of constructional steel research* **59**(1), 47–61.

Rhodes, J., ed. (1991) *Design of cold formed steel members*, Elsevier Applied Science.

Rogers, C. A. & Hancock, G. J. (1997) 'Ductility of g550 sheet steels in tension', *Journal of Structural Engineering* **123**(12), 1586–1594.

Rossi, B., Afshan, S. & Gardner, L. (2013) 'Strength enhancements in cold-formed structural sections — Part II: Predictive models', *Journal of Constructional Steel Research* **83**, 189–196.

Sadovskỳ, Z., Kriváček, J., Ivančo, V. & Ďuricová, A. (2012) 'Computational modelling of geometric imperfections and buckling strength of cold-formed steel', *Journal of Constructional Steel Research* **78**, 1–7.

Schafer, B. W. (2002) 'Local, distortional, and Euler buckling of thin-walled columns', *Journal of Structural Engineering* **128**(3), 289–299.

Schafer, B. W. (2008) 'Review: the direct strength method of cold-formed steel member design', *Journal of constructional steel research* **64**(7), 766–778.

Schafer, B. W. (2013) Sheathing Braced Design of Wall Studs, Technical report.

Schafer, B. W., Li, Z. & Moen, C. D. (2010) 'Computational modeling of cold-formed steel', *Thin-Walled Structures* **48**(10), 752–762.

Schafer, B. W. & Peköz, T. (1998*a*) 'Computational modeling of cold-formed steel: characterizing geometric imperfections and residual stresses', *Journal of Constructional Steel Research* **47**(3), 193–210.

Schafer, B. W. & Peköz, T. (1998*b*) 'Direct strength prediction of cold-formed steel members using numerical elastic buckling solutions'.

Schafer, B. W. & Peköz, T. (1999) 'Laterally braced cold-formed steel flexural members with edge stiffened flanges', *Journal of Structural Engineering* **125**(2), 118–127.

Selvaraj, S. & Madhavan, M. (2018*a*) 'Geometric imperfection measurements and validations on cold-formed steel channels using 3D noncontact laser scanner', *Journal of Structural Engineering* **144**(3), 04018010.

Selvaraj, S. & Madhavan, M. (2018*b*) 'Studies on cold-formed steel stud panels with gypsum sheathing subjected to out-of-plane bending', *Journal of Structural Engineering* **144**(9), 04018136.

Selvaraj, S. & Madhavan, M. (2019*a*) 'Bracing effect of sheathing in point-symmetric cold-formed steel flexural members', *Journal of Constructional Steel Research* **157**, 450–462.

Selvaraj, S. & Madhavan, M. (2019*b*) 'Investigation on sheathing effect and failure modes of gypsum sheathed cold-formed steel wall panels subjected to bending', *Structures* **17**, 87–101.

Selvaraj, S. & Madhavan, M. (2019*c*) 'Investigation on sheathing-fastener connection failures in cold-formed steel wall panels', *Structures* **20**, 176–188.

Selvaraj, S. & Madhavan, M. (2019*d*) 'Sheathing braced design of cold-formed steel structural members subjected to torsional buckling', *Structures* **20**, 489–509.

Serrette, R. L., Encalada, J., Juadines, M. & Nguyen, H. (1997) 'Static racking behavior of plywood, osb, gypsum, and fiberbond walls with metal framing', *Journal of Structural Engineering* **123**(8), 1079–1086.

Shahi, R., Lam, N., Saifullah, I., Gad, E. F. & Wilson, J. L. (2013) Realistic modelling of cold-formed steel in domestic constructions for performance based design, *in* 'Proceedings of the 2013 Australian Earthquake Engineering Society Conference', pp. 1–10.

Shifferaw, Y., Vieira, J. L. C. M. & Schafer, B. W. (2010) Compression testing of cold-formed steel columns with different sheathing configurations, *in* 'Proceedings of the Structural Stability Research Council - Annual Stability Conference', Orlando, Florida, USA, pp. 593–612.

Simaan, A. & Peköz, T. (1976) 'Diaphragm braced members and design of wall studs', *Journal of the Structural Division, ASCE* **102**(1), 77–92.

Sivakumaran, K. S. (1987) 'Analysis for local buckling capacity of cold-formed steel sections with web opening', *Computers & Structures* **26**(1-2), 275–282.

Solidworks (2017) *Version 25*, Dassault Systèmes Solidworks Corp.

Stergiopoulos, M., Lawson, R. M. & Lopez, P. (2019) 'Composite action of fixings to gypsum boards acting in shear based on material properties', *Proceedings of the Institution of Civil Engineers-Construction Materials* pp. 1–56.

Swensen, S., Deierlein, G. G. & Miranda, E. (2015) 'Behavior of screw and adhesive connections to gypsum wallboard in wood and cold-formed steel-framed wallettes', *Journal of Structural Engineering* **142**(4), E4015002.

Telue, Y. & Mahendran, M. (2004) 'Behaviour and design of cold-formed steel wall frames lined with plasterboard on both sides', *Engineering Structures* **26**(5), 567–579.

Telue, Y. & Mahendran, M. (2006) 'Design of cold-formed steel wall frames lined with plasterboard on one side under axial compression', *International Journal of Steel Structures* **6**(1), 1–12.

Thomasson, P.-O. (1978) Thin-walled C-shaped panels in axial compression, Technical report, Swedish Council for Building Research.

Tian, Y. S., Wang, J. & Lu, T. J. (2007) 'Axial load capacity of cold-formed steel wall stud with sheathing', *Thin-Walled Structures* **45**(5), 537–551.

Timoshenko, S. P. & Gere, J. M. (1961) *Theory of Elastic Stability*, 2nd edn, McGraw-Hill, New York.

Torabian, S. & Schafer, B. W. (2018) 'Development and experimental validation of the direct strength method for cold-formed steel beam-columns', *Journal of Structural Engineering* **144**(10), 04018175.

Torabian, S., Zheng, B. & Schafer, B. W. (2015) 'Experimental response of cold-formed steel lipped channel beam-columns', *Thin-Walled Structures* **89**, 152–168.

Trahair, N. S., Bradford, M. A., Nethercot, D. & Gardner, L. (2008) *The behaviour and design of steel structures to EC3*, 4^{th} edn, Taylor & Francis.

Uzzaman, A., Lim, J. B., Nash, D., Rhodes, J. & Young, B. (2012*a*) 'Web crippling behaviour of cold-formed steel channel sections with offset web holes subjected to interior-two-flange loading', *Thin-Walled Structures* **50**(1), 76–86.

Uzzaman, A., Lim, J. B. P., Nash, D., Rhodes, J. & Young, B. (2012*b*) 'Cold-formed steel sections with web openings subjected to web crippling under two-flange loading conditions—part I: Tests and finite element analysis', *Thin-Walled Structures* **56**, 38–48.

Vella, N., Gardner, L. & Buhagiar, S. (2020) 'Experimental analysis of cold-formed steel-to-timber connections with inclined screws', *Structures* **24**, 890–904.

Vieira, J. L. C. M. (2011) Behavior and design of sheathed cold-formed steel stud walls under compression, PhD thesis, Johns Hopkins University, Baltimore, Maryland, USA.

Vieira, J. L. C. M. & Schafer, B. W. (2009) Experimental results for translational stiffness of stud-sheathing assemblies, Technical report, AISI-COFS Project on Sheathing Braced Design of Wall Studs.

Vieira, J. L. C. M. & Schafer, B. W. (2012) 'Lateral stiffness and strength of sheathing braced cold-formed steel stud walls', *Engineering Structures* **37**, 205–213.

Vieira, J. L. C. M. & Schafer, B. W. (2013) 'Behavior and design of sheathed cold-formed steel stud walls under compression', *Journal of Structural Engineering* **139**(5), 772–786.

Vieira, J. L. C. M. & Schafer, B. W. (2016) 'Fastener demands for sheathing-braced cold-formed steel stud gravity walls', *Latin American Journal of Solids and Structures* **13**(6), 1167–1185.

Vieira, J. L. C. M., Shifferaw, Y. & Schafer, B. W. (2011) 'Experiments on sheathed cold-formed steel studs in compression', *Journal of Constructional Steel Research* **67**(10), 1554–1566.

Von Kármán, T. (1932) 'The strength of thin plates in compression', *Trans. ASME* **54**, 53–57.

Way, A. G. J. & Heywood, M. D. (2012) Design of light steel sections to Eurocode 3, SCI Electronic Publication: ED005 (Technical Report), The Steel Construction Institute, UK.

Weng, C. C. & Peköz, T. (1990) 'Residual stresses in cold-formed steel members', *Journal of Structural Engineering* **116**(6), 1611–1625.

Winter, G. (1947) 'Strength of thin steel compression flanges', *Transactions of the American Society of Civil Engineers* **112**(1), 527–554.

Winter, G. (1952) Light gauge (thin-walled) steel structures for building in the USA, *in* 'Fourth Congress of the International Association for Bridge and Engineering', pp. 523–538.

Winter, G. (1960) 'Lateral bracing of columns and beams', *Transactions No. 125* .

World Steel Association (2020) *World Steel in Figures 2020*.

Yamaki, N. (1960) 'Postbuckling behavior of rectangular plates with small initial curvature loaded in edge compression—(continued)', *Journal of Applied Mechanics* **27**(2), 335–342.

Ye, J. & Rasmussen, K. J. (2008) 'Compression strength of unstiffened elements in cold-reduced high strength steel', *Journal of Structural Engineering* **134**(2), 189–197.

Ye, J., Wang, X. & Zhao, M. (2016) 'Experimental study on shear behavior of screw connections in CFS sheathing', *Journal of Constructional Steel Research* **121**, 1–12.

Young, B. (1997) The behaviour and design of cold-formed channel columns, PhD thesis, University of Sydney, Sydney, Australia.

Young, B. & Hancock, G. J. (2003) 'Compression tests of channels with inclined simple edge stiffeners', *Journal of Structural Engineering* **129**(10), 1403–1411.

Young, B. & Rasmussen, K. J. R. (1998*a*) 'Design of lipped channel columns', *Journal of Structural Engineering* **124**(2), 140–148.

Young, B. & Rasmussen, K. J. R. (1998*b*) Tests of cold-formed channel columns, *in* 'Fourteenth International Specialty Conference on Cold-Formed Steel Structures', St. Louis, Missouri, USA.

Young, B. & Rasmussen, K. J. R. (1998*c*) 'Tests of fixed-ended plain channel columns', *Journal of Structural Engineering* **124**(2), 131–139.

Young, B. & Yan, J. (2000) Finite element analysis of cold-formed channel columns, *in* 'Fifteenth International Specialty Conference on Cold-Formed Steel Structures', St. Louis, Missouri, USA.

Yu, C. & Schafer, B. W. (2003) 'Local buckling tests on cold-formed steel beams', *Journal of Structural Engineering* **129**(12), 1596–1606.

Yu, C. & Schafer, B. W. (2006) 'Distortional buckling tests on cold-formed steel beams', *Journal of structural engineering* **132**(4), 515–528.

Yu, C. & Schafer, B. W. (2007) 'Simulation of cold-formed steel beams in local and distortional buckling with applications to the direct strength method', *Journal of Constructional Steel Research* **63**(5), 581–590.

Yu, W. & LaBoube, R. A. (2010) *Cold-formed steel design*, 4^{th} edn, John Wiley & Sons.

Yun, X. & Gardner, L. (2017) 'Stress-strain curves for hot-rolled steels', *Journal of Constructional Steel Research* **133**, 36–46.

Yun, X. & Gardner, L. (2018) 'The continuous strength method for the design of cold-formed steel non-slender tubular cross-sections', *Engineering Structures* **175**, 549–564.

Zeinoddini, V. M. & Schafer, B. W. (2012) 'Simulation of geometric imperfections in cold-formed steel members using spectral representation approach', *Thin-Walled Structures* **60**, 105–117.

Zeinoddini, V. & Schafer, B. W. (2011) 'Global imperfections and dimensional variations in cold-formed steel members', *International Journal of Structural Stability and Dynamics* **11**(05), 829–854.

Zhao, X. (2016) Measurement and application of geometric imperfections in cold-formed steel members, PhD thesis, Johns Hopkins University, Baltimore, Maryland, USA.

Zhao, X. & Hancock, G. J. (1992) 'Square and rectangular hollow sections subject to combined actions', *Journal of Structural Engineering* **118**(3), 648–667.

Zhu, E. C., Guan, Z. W., Rodd, P. D. & Pope, D. J. (2005) 'A constitutive model for OSB and its application in finite element analysis', *Holz als Roh-und Werkstoff* **63**(2), 87–93.

Appendix A

Section dimensions, gross and effective section properties

Calculated gross and effective section properties for a set of channel lipped sections are presented. The geometric dimensions of these sections are provided in Table A.1; illustrative notation of these section dimensions is shown in Figure 5.3. Gross section properties are provided in Table A.2, while effective section properties are provided in Table A.3; illustrations of the effective shapes of the cross-section are shown in Figure 7.2 (c) for pure compression and Figure 7.3 (c) for major axis bending. These properties can be used for the design of wall stud frames. Calculations were carried out in accordance with the EN 1993-1-3 (2006) methodology, summarised in Chapter 7. For the calculation of these properties, a yield strength f_y of 450 MPa and a Young's modulus E of 205 GPa were considered.

The calculation of these properties included iteration of effective properties and, as such, refinement of the reduction factor for buckling of the stiffener. This was achieved by code using *Visual Basic for Applications*, purposefully build for the needs of the current study.

Table A.1: Section dimensions

Section	Depth, h	Width, b_1	Width, b_2	Lip, c	Thickness, t	Internal radius, r	Area, A	Weight
	mm	mm	mm	mm	mm	mm	mm^2	kg/m
CS7012	68	44	44	12	1.2	2.5	197.1	1.55
CS7015	68	44	44	12	1.5	2.5	245.9	1.94
CS7020	68	44	44	12	2.0	2.5	325.3	2.57
CS10012	100	44	44	16	1.2	2.5	243.5	1.92
CS10015	100	44	44	16	1.5	2.5	304.3	2.40
CS10020	100	44	44	16	2.0	2.5	403.7	3.19
CS15012	150	44	44	12	1.2	2.5	292.2	2.30
CS15015	150	44	44	12	1.5	2.5	365.6	2.89
CS15020	150	44	44	12	2.0	2.5	486.1	3.84
CS20012	201	44	44	12	1.2	2.5	351.3	2.77
CS20015	201	44	44	12	1.5	2.5	440.1	3.47
CS20020	201	44	44	12	2.0	2.5	586.0	4.63
CS25012	252	44	44	12	1.2	2.5	410.5	3.24
CS25015	252	44	44	12	1.5	2.5	514.5	4.06
CS25020	252	44	44	12	2.0	2.5	686.0	5.43
CS29015	290	44	44	12	1.5	4.0	566.3	4.50
CS29020	290	44	44	12	2.0	4.0	755.4	6.01
CS34020	341	44	44	12	2.0	4.0	855.4	6.81

Table A.2: Gross section properties

Section	Radius of gyration for major axis, i_y mm	Radius of gyration for minor axis, i_z mm	Centroid from midline of bottom flange, C_z mm	Centroid from midline of web, C_y mm	Shear centre, horizontal distance from centroid, y_0 mm	Shear centre, vertical distance from centroid, z_0 mm	Torsion constant, I_t mm^4	Warping constant, I_w cm^6	Second moment of area about major axis, I_y cm^4	Second moment of area about minor axis, I_z cm^4	Elastic section modulus for major axis, W_y cm^3	Elastic section modulus for minor axis, W_z cm^3
CS7012	27.87	16.51	33.40	15.86	-38.19	0.00	88.39	58.38	15.31	5.37	4.58	1.99
CS7015	27.73	16.37	33.25	15.70	-37.82	0.00	174.72	70.60	18.91	6.59	5.69	2.46
CS7020	27.50	16.14	33.00	15.43	-37.20	0.00	416.61	88.57	24.60	8.47	7.46	3.19
CS10012	39.66	16.88	49.40	14.47	-36.51	0.00	109.20	160.47	38.30	6.93	7.75	2.45
CS10015	39.51	16.74	49.25	14.32	-36.16	0.00	216.21	195.38	47.51	8.52	9.65	3.02
CS10020	39.26	16.50	49.00	14.07	-35.57	0.00	517.01	248.03	62.25	11.00	12.70	3.94
CS15012	57.28	15.46	74.40	10.69	-28.64	0.00	131.05	303.92	95.86	6.99	12.88	2.18
CS15015	57.10	15.32	74.25	10.56	-28.31	0.00	259.78	370.79	119.21	8.58	16.06	2.68
CS15020	56.80	15.07	74.00	10.33	-27.76	0.00	622.42	472.30	156.83	11.03	21.19	3.48
CS20012	74.21	14.66	99.90	8.89	-24.96	0.00	157.59	585.93	193.47	7.55	19.37	2.23
CS20015	74.01	14.51	99.75	8.77	-24.65	0.00	312.69	716.24	241.03	9.27	24.16	2.75
CS20020	73.67	14.26	99.50	8.57	-24.14	0.00	750.42	915.27	318.06	11.92	31.97	3.56
CS25012	90.58	13.92	125.40	7.61	-22.17	0.00	184.12	978.55	336.78	7.95	26.86	2.26
CS25015	90.36	13.77	125.25	7.50	-21.88	0.00	365.59	1197.43	420.08	9.76	33.54	2.79
CS25020	89.99	13.52	125.00	7.32	-21.40	0.00	878.42	1532.88	555.51	12.55	44.44	3.62
CS29015	101.95	13.13	144.25	6.68	-19.99	0.00	402.34	1601.06	588.50	9.77	40.80	2.73
CS29020	101.55	12.89	144.00	6.51	-19.53	0.00	967.33	2049.26	779.04	12.55	54.10	3.54
CS34020	117.28	12.29	169.50	5.75	-17.71	0.00	1095.34	2965.56	1176.54	12.92	69.41	3.56

Table A.3: Effective section properties

Section	Effective area, (when in pure compression) A_{eff}	Effective elastic section modulus for bending about y axis, $W_{y,eff}$	Effective elastic section modulus for bending about z axis, $W_{z,eff}$	Effective centroid from midline of bottom flange (due to compression), $C_{z,eff,comp}$	Effective centroid from midline of web (due to compression), $C_{y,eff,comp}$	Second moment of area about major axis (due to bending), $I_{y,eff}$
	mm^2	cm^3	cm^3	mm	mm	cm^4
CS7012	134.08	3.78	1.89	33.40	15.54	13.61
CS7015	195.43	5.13	2.40	33.25	15.51	17.77
CS7020	295.31	7.10	3.22	33.00	15.04	23.93
CS10012	147.43	6.61	2.24	49.40	16.92	34.75
CS10015	214.93	8.95	2.85	49.25	16.62	45.44
CS10020	328.51	12.37	3.85	49.00	15.82	61.36
CS15012	129.07	9.15	1.95	74.40	13.28	78.03
CS15015	194.43	13.42	2.48	74.25	13.52	107.24
CS15020	307.02	19.87	3.35	74.00	13.02	150.95
CS20012	127.41	12.25	1.96	99.90	12.65	146.09
CS20015	191.53	18.07	2.50	99.75	12.76	203.06
CS20020	306.48	27.97	3.38	99.50	12.37	294.63
CS25012	126.51	15.32	1.98	125.40	12.27	236.63
CS25015	188.53	22.74	2.52	125.25	12.13	332.19
CS25020	304.73	35.40	3.40	125.00	11.86	486.83
CS29015	185.82	25.87	2.49	144.25	11.81	444.67
CS29020	301.11	40.44	3.37	144.00	11.54	656.03
CS34020	299.04	47.98	3.39	169.50	11.16	941.02